

International School for Advanced Studies

THE ROLE OF SYNCHROTRON  
AND SELF-COMPTON RADIATION  
IN ACTIVE GALACTIC NUCLEI

*by*

Annalisa Celotti

A thesis submitted for the degree

*of Doctor Philosophiae*

Trieste – October 1992

*Supervisors*

Prof. A.C. Fabian

Prof. A. Treves



*“Dissi soltanto: “ Quando di sera  
le luna piena rimane impigliata  
tra i rami dell’ albero di kadam  
qualcuno non potrebbe prenderla? ”*

*(Tagore, L’astronomo)*

*“Ed ecco c’è in noi un desiderio  
per qualcosa, pure se ignoriamo  
che cosa al mondo questo qualcosa sia ”*

*(Traherne)*





## Acknowledgments

My deepest thanks to Andy Fabian. He has taught me a great deal of astrophysics (and physics) and has been patient with my ignorance (and terrible English!). He has been generous with his ideas but encouraged me to follow mine. More important he inspired a way of doing research and of being scientifically 'curious' in more general sense. He also had to fight against my lack of confidence, and fortunately his enthusiasm sometimes was contagious. I am also grateful to him for the friendly care he has shown toward me as he has shown to all members of the X-ray group.

I acknowledge the invaluable discussions of Prof. Martin Rees, who as director of the Institute of Astronomy accepted me, so kindly, to work in this stimulating environment.

I thank Prof. Dennis Sciama, director of the Astrophysics Sector of S.I.S.S.A. for having allowed, and constantly encouraged, my stay in Cambridge.

My thanks to Aldo Treves, my internal supervisor for availability, discussions and encouragement (and spending part of his holidays reading my thesis).

I am very grateful to Laura Maraschi. She helped me to find the way to research. I benefit from many scientific discussions with her and from constant scientific (and personal) support and advice.

Deep thanks are due to Gabriele Ghisellini for many fruitful interactions, for having been friendly available and for some 'injections' of scientific enthusiasm.

Many friends helped me and made life more enjoyable in various ways...Ian George (with unforgettable table tennis matches and his patient friendship), Carolin Crawford (with vivacity, wittiness and care), Alastair Edge (with attention and many incredible shirts), Giorgio Matt (with a lot of Italian chat, support in the last period of the thesis and 'excellent' food), Paul Nandra, Dave White, Roderick Johnston, Malcolm Bremer and all the other members of the 'X-ray group'. Thanks are also due to Monica Colpi (for her friendship and generosity), Martin Haehnelt, Silvano Molendi (the dear 'Duca') and Nicola Caon.

I am deeply grateful to my dear friends Tobi Barnett and all the Corbella.

Endless thanks to my mother, without whom I could never have followed this way (she knows why) and to my brother.

I would like to dedicate this thesis to myself (...at least nobody can be offended).



# Table of contents

INTRODUCTION	1
1. ACTIVE GALACTIC NUCLEI	5
1.1 Spectral observations	5
1.1.1 Radio-quiet objects	6
1.1.1.a Radio-UV continuum	6
1.1.1.b X-ray spectrum	8
1.1.1.c Iron line and cold matter	8
1.1.1.d $\gamma$ -ray spectrum	10
1.1.1.e Optically-UV line emission	11
1.1.2 Blazars	13
1.1.2.a Radio-UV continuum	13
1.1.2.b BL Lac objects	14
1.1.2.c $\gamma$ -ray emission	16
1.1.3 Variability	16
1.1.3.a Timescales	17
1.1.3.b Amplitude	18
1.1.3.c Correlated variability	19
1.1.3.d Power spectrum	21
1.2 Spatial observations	21
1.2.1 Large and small scale jets	22
1.2.1.a Optical and X-ray jets	24
1.2.1.b Polarization	24
1.2.2 Superluminal sources	25
1.2.3 Blazars	26

<b>2. NON-THERMAL PROCESSES IN COMPACT SOURCES</b>	<b>28</b>
<b>2.1 General constraints</b>	<b>28</b>
2.1.1 The compactness parameter	28
2.1.2 Pair production	29
2.1.3 Variability limits	33
<b>2.2 SSC radiation mechanism</b>	<b>34</b>
2.2.1 Synchrotron and self-Compton emission	34
2.2.2 Energy density estimates	39
2.2.3 Beaming	40
2.2.4 Estimates of the source parameters	43
2.2.5 Brightness temperature	45
 <b>3. THE CENTRAL REGION: REPROCESSED SSC RADIATION</b>	 <b>47</b>
<b>3.1 The magnetic energy density</b>	<b>48</b>
3.1.1 Primary X-ray radiation	48
3.1.2 Constraints on the magnetic field	49
3.1.3 The sample	51
3.1.4 Results	53
3.1.5 Parameters	55
3.1.6 Effects of beaming	57
3.1.7 Discussion	58
<b>3.2 Cold matter and reprocessing</b>	<b>59</b>
3.2.1 Cold matter	59
3.2.1.a <i>Observational evidence</i>	59
3.2.1.b <i>Estimates of matter density</i>	60
3.2.1.c <i>Radiative equilibrium</i>	61
3.2.1.d <i>Spectral effects</i>	62
3.2.2 The properties of cold gas in the central engine	63
3.2.2.a <i>'Macrophysics'</i>	63
3.2.2.b <i>'Microphysics'</i>	68
<b>3.3 Discussion</b>	<b>69</b>
 <b>4. THE INNER JET: HIGH ENERGY EMISSION</b>	 <b>73</b>
<b>4.1 Emission from jets</b>	<b>74</b>
4.1.1 Observations	76
4.1.2 The stationary model	78
4.1.3 Time dependent emission in the presence of a perturbation	80
4.1.3.a <i>Time dependent spectra</i>	82
4.1.3.b <i>Light curves at different frequencies</i>	85
4.1.3.c <i>Normalized variability parameter</i>	87
4.1.4 The case of a relativistic shock wave	87

<b>4.2 The gamma-ray emitting blazar 3C279</b>	90
4.2.1 Observations	91
4.2.2 General constraints	91
4.2.2.a <i>Beaming factor and <math>\gamma</math>-ray variability</i>	92
4.2.2.b <i>Magnetic and radiation energy density</i>	92
4.2.2.c <i>Maximum electron energy</i>	93
4.2.3 The jet model	94
4.2.4 Other $\gamma$ -ray sources	95
<b>4.3 Discussion</b>	96
 <b>5. PC-SCALE JETS</b>	 101
<b>5.1 The sample</b>	102
<b>5.2 The SSC formalism</b>	104
<b>5.3 Beaming indicators</b>	105
5.3.1 The Doppler factors	110
5.3.2 Distributions of brightness temperature	111
5.3.3 Superluminal motion	111
5.3.4 Derivation of the bulk Lorentz factor and viewing angle	112
5.3.5 The core dominance parameter	114
5.3.6 Comparison of the derived beaming parameters with other estimates	116
5.3.6.a <i>The jet to counterjet intensity ratio</i>	116
5.3.6.b <i>Beaming and <math>\gamma</math>-ray emission</i>	116
5.3.6.c <i>Parent population statistic</i>	116
5.3.7 Conclusions	117
<b>5.4 Matter content</b>	119
5.4.1 Particle density	122
5.4.2 Pair plasma jets	123
5.4.2.a <i>The dynamics of <math>e^\pm</math> pairs</i>	124
5.4.2.b <i>Number density of surviving pairs</i>	126
5.4.2.c <i>The effect of the assumptions</i>	129
5.4.2.d <i>Results</i>	130
5.4.3 Particle number flux	131
5.4.4 Kinetic and radiative power in pc-scale jets	132
5.4.4.a <i>Kinetic luminosity</i>	132
5.4.4.b <i>Kinetic vs radiative luminosity</i>	133
5.4.5 Kinetic power on pc- and Mpc-scales	134
5.4.6 Conclusions	146
<b>5.5 Confinement and acceleration</b>	137
5.5.1 Magnetic field estimates	138

<b>6. UNIFIED MODEL FOR BL LAC OBJECTS</b>	<b>150</b>
<b>6.1 Unification models</b>	<b>150</b>
6.1.1 FRI radio galaxies and BL Lacs	151
<b>6.2 The luminosity function of ‘wide’ jets objects</b>	<b>153</b>
6.2.1 The luminosity enhancement	154
6.2.2 The luminosity function	156
6.2.3 Spectra and number densities in the X-ray and radio bands	159
<b>6.3 Observational constraints</b>	<b>160</b>
6.3.1 Luminosity functions of FRI radio galaxies and BL Lacs	160
6.3.2 Constraints on parameters	161
6.3.2.a <i>Relative number of XBL and RBL</i>	162
6.3.2.b <i>Relative number of FRI and BL Lacs</i>	163
6.3.2.c <i>Maximum luminosity of the beamed population</i>	163
<b>6.4 Results and discussion</b>	<b>163</b>
 <b>SUMMARY AND FUTURE WORK</b>	 <b>166</b>
 <b>Appendix A</b>	 <b>170</b>
 <b>Appendix B</b>	 <b>172</b>
 <b>List of symbols</b>	 <b>174</b>
 <b>References</b>	 <b>176</b>

## Introduction

Active Galactic Nuclei (AGN) contain some of the most spectacular phenomena in the Universe. They produce luminosities between  $10^{39}$ – $10^{48}$  erg s $^{-1}$  (if emitted isotropically) from regions smaller than 1 pc. They are therefore the most luminous and compact (quasi steady) sources known. The power is released both as electromagnetic radiation and as the kinetic energy of a plasma outflow. In general terms they show continuum emission which can exceed the total stellar contribution of a host galaxy, but the term ‘active’ can refer to one or more very different characteristics, which cannot be attributed to stellar evolution: strong continuum, at least partly non-thermal, strong and broad emission lines (FWHM  $> 500$  km/s) of high ionization, strong and fast variability timescales in all frequency bands (and particularly in X-rays where the timescales can be as short as 50 s), polarized radiation and collimated structures which sometimes show relativistic motion.

Despite any definitive proof, most astrophysicists are in favour of the presence of massive ( $10^6$ – $10^{10}$   $M_{\odot}$ ) black holes in the core of AGN, mainly because of their efficiency, compactness, stability and inevitability. The above phenomena of ‘activity’ support this picture. In particular the strong and fast variability, the large velocities inferred from emission lines, the central position in the host galaxy, the presence of jets aligned on pc to Mpc scales and the motion of plasma at relativistic speed, all suggest the presence of a very deep and stable gravitational potential with a large and compact mass at the centre of the galaxies.

The huge power can be produced by the release of gravitational energy of the matter falling into a black hole or by the extraction of its rotational energy (which can be more efficient than accretion) (*e.g.* Rees 1984; Blandford 1990).

If on one hand it is ‘encouraging’ that so many ‘speculations’ (theories and models) have survived the observational test for so long (at least on a general level), on the other hand we are still missing fundamental pieces of the whole picture. The knowledge of the physical processes operating in AGN is limited and fundamental problems remain open. Furthermore, AGN comprise a zoo of different objects and classes, the number of which increases with the accuracy of the observations. However there are some indications that we are looking at the same basic mechanisms for all the sources. Indeed one of the most striking facts is just that the global properties of AGN seem quite similar over more than eight orders of magnitude in luminosity (and even more if the similarity with galactic black hole candidates is considered).

Furthermore it is becoming evident that the AGN phenomenon is quite common (*e.g.* Woltjer 1990) and there is some continuity in the level of activity between ‘normal’ and active galaxies, and among active galaxies themselves suggesting that only quantitative

limits on the ‘degree of activity’ distinguish different sources and the basic physical structure is substantially the same for all the objects.

Different phenomenological aspects can contribute to infer the properties of the ‘central machine’. In particular in this thesis we concentrate on the shape of the high energy continuum, the luminosity and variability, which probably gives information on the smallest accessible scales, and on the relativistic jets. The radiative and kinetic luminosity contain the major power output. Despite the enormous difference in the physical conditions of these regions, it is plausible that magnetic fields play a dominant rôle in both cases. Measurements or limits on its presence can then give important clues on the operation of the central engine.

In fact the observed high energy radiation requires the presence of relativistic emitting electrons. In compact sources the radiative cooling timescales are extremely short, implying that a continuous supply of energetic particles is necessary. Magnetic fields can be responsible for their (re)acceleration and the consequent synchrotron and self-Compton (SSC) emission. SSC can therefore be a primary radiative process in compact regions.

Ordered magnetic field components can also be important for the dynamic of the plasma and for the collimation and acceleration of jets: it has been suggested that the field can be anchored in the inner parts of the accreting flow, where it could confine the material present bringing about jets and accelerate them to relativistic bulk velocities.

We therefore adopt the SSC mechanism as a working hypothesis and use it to infer properties of the physical conditions in the emitting plasma on different scales.

The outline of the thesis is the following.

Chapter 1 concerns observations and the general physical interpretation to which we refer in the following Chapters. Due to the variety of topics it ranges widely. In the first part we refer to spectral observations of radio-quiet sources and blazars. As discussed in the thesis there is increasing and convincing evidence that most (if not all) the observed radiation is due to reprocessing, which therefore hides the direct radiation from the central source, but can give clues on its geometry. Particular emphasis is given to the fact that the ‘standard’ accretion disc picture seems to account for new observational results, even if the radiative role of the accreting material is somewhat changed. The other interesting aspect is the observations in the  $\gamma$ -ray band: several blazars are strong  $\gamma$ -ray emitters, supporting the importance of beaming effects, and (few) radio quiet sources show a turnover in the high energy spectrum, possibly confirming the role of pair production in affecting the whole  $\gamma$ -ray spectrum. One section is devoted to variability, which, especially at high energies, is becoming an extremely powerful test for models (Chapters 3 and 4). In the second part of the Chapter we briefly describe the spatial observations, maps of radio sources and jets on small and large scales (Chapters 5 and 6).

The theoretical background is summarized in Chapter 2, where general constraints on radiative processes are presented. Compact sources are characterized by a high radiation energy density, which both implies rapid cooling of the relativistic electrons by inverse



Compton and a high optical depth for pair production through photon-photon interaction for  $\gamma$ -ray photons. The X-ray and  $\gamma$ -ray spectrum can be significantly modified by pair reprocessing. If an intense magnetic field is present in the compact region, synchrotron and self-Compton can be the dominant emission mechanisms. We recall the standard theory of SSC (which we adopt in Chapters 3, 4 and 5), with emphasis on the beaming effects and their dependence on the structure of the source.

Chapter 3 deals in the X-ray emitting region. We discuss the importance of the magnetic field and the cold matter in the compact region. For a non-thermal distribution of relativistic electrons upper limits on the intensity of the magnetic field can be determined by the relative importance of inverse Compton emission on the EUV and synchrotron radiation fields in producing the X-ray flux. An intense magnetic field (in equipartition with the radiation energy density) would require that part of the optical-UV SSC radiation is absorbed. The results support the idea that the presence of cold matter in or around the compact region could be responsible for reprocessing most of the primary radiation. Even a small fraction of the matter expected to be present in the central region, can be in the right physical conditions to free-free absorb part of the primary emission, due to the combined effect of the radiation and the magnetic field itself, which then ‘masks’ its own presence.

Moving to larger dimensions, in Chapter 4 we concentrate on the inner part of relativistic jets, the SSC emission of which presumably dominates the high energy radiation in blazars. In particular we discuss the constraints imposed by variability observations on inhomogeneous jet models. Firstly we study how the variability observed at different frequencies can be qualitatively accounted for, in models developed for stationary emission from jets of plasma, involving the presence of perturbations propagating along the jet. Secondly we show that the extreme variable  $\gamma$ -ray emission from the blazar 3C 279 imposes limits on the amount of beaming at high energies, by the constraint that the  $\gamma$ -ray emitting region is optically thin to pair production. The relativistic jet model can account for the  $\gamma$ -ray radiation of 3C 279 as SSC emission from the flowing plasma, and possibly of blazars at large.

Parsec-scale jets are the subject of Chapter 5. The increasing number of radio maps with milliarcsecond resolution gives some insight onto the physical condition of jets on pc scale. In particular it is possible, using SSC theory, to infer the relativistic Doppler factor, the emitting particle density and the intensity of the magnetic field. We use this information at different levels. At first we consider the correlation and consistency of some beaming indicators for different classes of AGN, finding that they are in significant agreement with and support the unification models.

We then use the derived particle density to constrain the matter content of jets, *i.e.* the possibility that such structures could be mostly composed of an electron-positron pair plasma, instead of ordinary electron-proton plasma. We combine and compare results on different scales: the limit on the electron-positron pair number produced in the compact region which could be channeled into the jet; the amount of accreting matter in the central source; the kinetic power and radiative dissipation on pc scales; and the kinetic luminosity

on kpc or larger scales. Jets appear to transport most of the energy in kinetic form; the radiative output on pc scales is a negligible fraction of the total emitted power.

Finally the derived magnetic field intensity, at least in our simple assumptions, is shown to be not dynamically important on these scales.

In Chapter 6 we consider the ‘unification’ problem posed by the beaming hypothesis. In particular we discuss a model which can account for the observed differences both in the spectral properties and in number densities between radio-selected and X-ray-selected BL Lacs, in the frame of the unification scheme of FR I radio galaxies and BL Lacs. The model explores the possibility that the differences can be due to a decrease in beaming at increasing emitted frequencies caused by an increasing degree of collimation of the relativistic flow.

Conclusions and discussion are presented in each Chapter. At the end of the thesis we summarize the results.

In the ‘List of symbols’ we define the most common symbols used in the different Chapters of the thesis.

The content of this thesis is partially based on the work by Celotti, Ghisellini & Fabian (1991a) and Celotti, Fabian & Rees (1992) [Chapter 3]; Celotti, Maraschi & Treves (1991), Tagliaferri *et al.* (1991) and Maraschi, Ghisellini & Celotti (1992) [Chapter 4]; Ghisellini, Padovani, Celotti & Maraschi (1992), Ghisellini, Celotti, George & Fabian (1992), Celotti & Fabian (1992b) [Chapter 5]; Celotti, Maraschi, Ghisellini & Caccianiga (1992) [Chapter 6].

## Chapter 1. Active Galactic Nuclei

In this Chapter we just present the observational background and the basic physical interpretations of the radiative mechanisms and spatial distribution of the emitting plasma to which we refer for further discussion in the following Chapters, in a schematic way. Emphasis is given to observations, ignoring for the present the many problems related with current interpretations and other unanswered questions.

In the first Section we concentrate on spectral information, while in the second one the maps of collimated structures are considered.

### 1.1 SPECTRAL OBSERVATIONS

AGN intriguingly radiate approximately the same power in equal logarithmic energy intervals over 8–10 decades of photon energy. More precisely and despite the variety in the detailed energy spectral distributions, the emission peaks between the IR and UV or in the  $\gamma$ -ray band in most of the observed objects. From 10 to 30 % of the total luminosity is emitted as X-rays (2–20 keV) (*e.g.* Padovani & Rafanelli 1988).

Recent observations in new energy bands (mm, far and near IR, UV, soft X-ray and  $\gamma$ -ray radiation), of fast and multiwavelengths variability and of high resolution spectra (*e.g.* in the X-ray band) give results which are particularly relevant for understanding the physical conditions and geometrical structures in AGN.

Despite the complex phenomenology and taxonomy of AGN, a gross division can be based on the prevalence of apparently thermal (radio-quiet objects) or non-thermal (blazars) emission in the continuum spectra (*e.g.* Lawrence 1987; Bregman 1990), which extend from radio to  $\gamma$ -ray energies. In Fig. 1.1 the average spectral distributions of objects belonging to these two classes are shown. It is not yet clear if the dominance of thermal or non-thermal emission reflects an intrinsic difference in the sources, *e.g.* related to the power production mechanism (accretion or rotational energy) or if it is due, for example, to reprocessing and/or to geometrical-orientational effects. It is worth mentioning that radio-quiet sources appear in the nucleus of spiral galaxies, while blazars have elliptical host galaxies, but the effect of the environment and/or angular momentum of the galaxy

on the central activity is not clear. The structure of this Section reflects this classification. (In the following we do not discuss the phenomenology of particular classes of sources like LINERS, IRAS sources, Starburst galaxies, etc.).

It should be remembered that the taxonomy of AGN is complex due to at least two reasons: it is difficult to reconcile classifications based on properties observed in different spectral bands; furthermore if the properties of a source vary with time, it is possible that the classification varies accordingly and depends on the number of observations.

For more complete reviews we refer to Bregman (1990), Lawrence (1987), Netzer (1990), Woltjer (1990).

### 1.1.1 Radio-quiet objects

This class includes quasars, Seyfert 1 galaxies, which are probably the low luminosity counterparts of radio quiet quasars, Seyfert 2 galaxies, Broad Absorption Line quasars (see *e.g.* Woltjer 1990).

#### 1.1.1.a Radio-UV continuum

Their continuum is quite complex and the presence of features at the same rest frame frequency implies that thermal or atomic processes are important.

Most of the objects present a steep ( $-1.1 < \alpha < -0.5$ , hereafter  $F(\nu) \propto \nu^{-\alpha}$ ) radio spectrum, the emission of which, even if stronger than the radio emission from an ordinary spiral galaxy, is not relevant in term of contribution to the bolometric luminosity. Radio-quiet AGN show a turnover in the submillimeter region with slopes sometimes steeper than  $\alpha = -2.5$  (Chini, Kreysa & Biermann 1989).

The peak of the emission is concentrated between  $10\mu\text{m}$  and  $100\mu\text{m}$ . The widely accepted interpretation is that the near IR emission is thermal emission from dust, which must intercept and reprocess from 10 to 50 % of the UV radiation.

A minimum is observed around  $1\mu\text{m}$  (Sanders *et al.* 1989), consistent with a cut-off in the emission from dust, which is destroyed at temperatures greater than  $\sim 2000\text{ K}$ .

At higher frequencies the contribution from the Balmer continuum ( $2700\text{--}3800\text{ \AA}$ ) and the pseudo-continuum created by the forest of Fe II lines ( $1800\text{--}3500\text{ \AA}$ ) (Wills, Netzer & Wills 1985) make the spectrum to rise (the ‘3000  $\text{\AA}$ ’ bump) up to the ‘big bump’, visible shortwards of  $1200\text{ \AA}$ .

Some objects show a decrease in flux at high UV frequencies, suggesting that perhaps the peak of the emission has been observed (Sun & Malkan 1989), while in most objects the

spectrum continues to rise, providing a contribution to the total power between 1200 Å and 100 eV which possibly dominates the bolometric luminosity (Elvis, Wilkes & McDowell 1990). Indirect evidence of radiation between 10 and 100 Å is provided by the observation of high ionization emission lines, requiring a ionizing continuum at these wavelengths (*e.g.* Collin-Souffrin 1991).

The UV–soft X–ray radiation is commonly attributed to the quasi–blackbody emission from (dynamically) cold material, probably accreting onto the central black hole.

Spherical accretion has low radiative efficiency because the cooling timescales are probably longer than the free fall timescales (*e.g.* Rees 1984). If material with angular momentum cool, it can form a thin, centrifugally supported disc (Shields 1978). The optically thick and geometrically thin ‘ $\alpha$ ’–disc model proposed by Shakura & Sunyaev (1973) and Pringle & Rees (1972) leads to simple analytical solutions, by assuming that the disc radiates locally as a blackbody. The maximum temperature of the accreting gas is of the order of  $T_{max} \simeq 10^7 (M/M_\odot)^{-1/4} (\dot{M}/\dot{M}_E)^{1/4}$  K and the convolution of the locally emitted blackbodies produces a  $F(\nu) \propto \nu^{1/3}$  frequency dependence. A non–thermal power law component, extending between IR and X–rays, is invoked to account for the fact that the observed spectra instead decrease with  $\nu$ .

Despite a qualitative global agreement with observations (*e.g.* Malkan 1983) and the initial hope of determining the black hole mass and the accretion rate modelling the observed spectra, some difficulties raised and a more detailed comparison requires a more sophisticated model (Courvoisier & Clavel 1991).

In fact the expected anticorrelation between the temperature of the bump and the mass/luminosity is not observed (*e.g.* Koratan & Gaskell 1991). Furthermore a HI Lyman edge feature is expected in the emission spectra, but has not been observed. Compton scattering opacity in the disc also implies linear polarization at the level of few percent ( $\lesssim 10\%$ ), while typically the observed optical polarization in quasars does not exceed 2 % (Stockman, Moore & Angel 1984).

More realistic assumptions include the effects due to electron scattering, inclination of the disc, relativistic corrections, rotation of the black hole, geometrically thick structures (radiation or ion supported torii), lines opacity (*e.g.* Sun & Malkan 1989; Laor, Netzer & Piran 1990; Abramowicz, Calvani & Nobili 1980; Treves, Maraschi & Abramowicz 1989; Begelman, Blandford & Rees 1984; Ross, Fabian & Mineshige 1992).

But recently a more fundamental problem emerged: the delay between optical and UV variations observed in NGC 4151 (with delays less than 2 days, Ulrich *et al.* 1991), NGC 5548 (Clavel *et al.* 1991) Fairall 9 and 3C 273 (Courvoisier 1992) are much shorter than the minimum delay expected if the variations are induced by a perturbation moving at the sound speed in the disc (in this case the expected delay would be of the order of months to years). It has been suggested that the emission is due to reprocessed X–ray radiation which impinges on the disc and is thermalized (§1.1.1.c). Time delays of the order

of light-crossing times are therefore expected (Collin-Souffrin 1991; Molendi, Maraschi & Stella 1991). Consequently the bulk of the emitted luminosity would not be produced by viscous dissipation in the accreting matter, but by an external high energy source, the emission of which must extend in some sources at least up to 100 keV, in order to account for the optical–UV luminosity.

Alternative models to reproduce the UV emission have been proposed: it can be non-thermal emission (Jones & Stein 1990) or, at least partly, bremsstrahlung emission from dense gas clouds with temperature  $\sim 10^4$ – $10^5$  K, which reprocess non-thermal X-rays (Guilbert & Rees 1988; Barvainis 1990; Ferland, Korista & Peterson 1990; §3.2).

#### 1.1.1.b X-ray spectrum

In the soft X-ray (0.5–1 keV) band, intrinsic absorption by cold material is sometimes observed, with column densities up to  $N_H \simeq 10^{22} \text{ cm}^{-2}$  (Turner & Pounds 1989). Recently it has been observed also in high redshift quasars (Wilkes 1992).

After correction for absorption many sources show a ‘soft excess’ (at energies  $< 1$ – $2$  keV) with respect to the extrapolation of the higher energies power-law (Arnaud *et al.* 1985; Turner & Pounds 1989). This soft radiation can be the high energy tail of the ‘big bump’, emitted from gas at a few hundred thousand K or can constitute a different (maybe thermal) component. The fact that it varies rapidly (on timescales of minutes-hours) indicates that it is produced close to the central region (Mkn 841, Arnaud *et al.* 1985; NGC 5548, Kaastra & Barr 1989).

At energies above 1-2 keV, or at all X-ray energies if the soft excess is not present, the spectrum can be best-fitted by a power-law with  $\alpha \sim 0.6$ – $0.8$  and a small dispersion in the spectral index. Turner & Pounds (1989) found  $\alpha = 0.7 \pm 0.17$  in the 2–10 keV band for 42 Seyfert galaxies. For the few objects observed up to 120 keV the spectrum is also consistent with such slope (Rothschild *et al.* 1983; NGC 4151, Maisak *et al.* 1992). Lawson *et al.* (1992) found average values of  $\alpha = 0.66 \pm 0.07$  for the radio loud and  $\alpha = 0.90 \pm 1.1$  for radio quiet quasars in the 2–10 keV band.

#### 1.1.1.c Iron line and cold matter

Observations of Seyfert 1 galaxies in the 2–30 keV band by GINGA revealed that an emission line at  $\sim 6.4$  keV and a hump (flattening) in the hard X-ray spectrum above 15 keV (Pounds *et al.* 1990; Matsuoka *et al.* 1990; Nandra 1991) are common features.

A natural explanation of the flattening is that it is due the scattering of hard X-ray photons on a cold and optically thick surface (Guilbert & Rees 1988; Lightman & White

1988). Hard X-rays ( $\gtrsim 40$  keV) are Compton scattered and decrease their energy by Compton recoil, while soft photons ( $< 10$  keV) are photoelectrically absorbed by high  $Z$  ions. Consequently a reflected component which peaks around 30 keV can add to the direct spectrum hardening it to the observed  $\alpha = 0.7$ . If so the primary spectrum has to be intrinsically steeper than the observed one, with typically  $\alpha \simeq 0.9$  (Pounds 1992). This in turn implies that the excess in the soft band is reduced up to 30% (Piro, Yamauchi & Matsuoka 1990; Pounds 1992).

In the context of the X-ray emission region, ‘cold’ material means at temperatures of about  $10^6$  K or less, so that the matter is not fully ionized. In this case iron atoms are not totally ionized ( $< \text{Fe XVII}$ ) and have K and L shell electrons. The fluorescence of iron can be responsible for the observed line emission. The  $K_\alpha$  energy is 6.4 keV.

The observed equivalent width of the line is typically 100–300 eV. Because the  $\text{EW} \simeq 300 (\Delta\Omega/4\pi)(Z/Z_\odot)\tau_T$  eV (where  $Z/Z_\odot$  is the metallicity in solar units,  $\tau_T$  the Thomson optical depth and  $\Delta\Omega$  the solid angle subtended by the cold plasma) an optically thick medium ( $N_H \simeq 10^{23-25} \text{ cm}^{-2}$ ) subtending a large angle ( $\simeq 2\pi$  sr) with the ionizing source is required.

The geometry is uncertain, although a disc-like structure, with the X-rays emitted from above and below the disc, is plausible (the hard X-ray source must be outside the disc in order to avoid photoelectric absorption features in the spectrum and intercept a large solid angle with the disc surface). Typical densities predicted by standard accretion disc models are sufficient to keep it cold and relatively neutral avoiding Compton heating (George & Fabian 1991). The X-ray emission could be for example associated with the release of energy stored in a strong magnetic field (*e.g.* Begelman & DeKool 1990).

Support for the whole picture comes from the quasi-simultaneous variability of the line and continuum in NGC 6814: Kunieda *et al.* (1990) measured a delay less than 250 s and a X-ray variability of  $\sim 50$  s, suggesting an upper limit of  $10^{13}$  cm for the size of the iron line emitting and reprocessing regions. It is therefore plausible that the X-rays can be produced at the surface of the disc. More generally the (non-simultaneous) fast variability of all the above spectral components (soft excess, Arnaud *et al.* 1985; iron line and hard continuum, Kunieda *et al.* 1990) suggests that the cold gas does lie in the central engine. Together with the UV bump these features are in fact strong indications of the presence of cold ( $T \simeq 10^5$  K) matter close to the central source.

Monte Carlo simulations of the reflection process of a primary X-ray power-law spectrum (with  $\alpha \sim 0.9$ ) in the described geometry (Fig. 1.2) reproduce the observed global features (George & Fabian 1991; Matt, Perola & Piro 1991) and the ratio of direct and reflected continuum (Fig. 2.2). An alternative picture is given by the ‘partial covering’ model (*e.g.* Matsuoka *et al.* 1990), which invokes the presence of cold material maybe comprised in clouds with  $N_H > 10^{24} \text{ cm}^{-2}$ , covering the central source. The quality of data do not allow to clearly discriminate between the two models (but see Fabian 1992).

Another predicted spectral signature of the presence of cold iron is a K edge, at energies ranging between 7.1–9.3 keV, depending on the ionization state. Some evidence of an edge has been observed at an energy consistent with neutral matter, but the spectral resolution does not allow it to be determined with confidence. Indeed, an absorption edge at  $\sim 8\text{--}9$  keV in 50 % of a large sample of Seyfert galaxies has been recently observed (Nandra 1991). The energy is typical of partially-ionized material with  $T \sim 10^6 - 10^7$  K and it has been suggested that it is produced by the so called ‘warm absorber’, having typical column density  $10^{23}\text{cm}^{-2}$  (Pounds *et al.* 1990). Remarkably observations with ROSAT have revealed the presence of an absorption edge at  $\sim 0.8$  keV in NGC 5548 and MGC 6–30–15, more naturally interpreted as an oxygen K-edge of warm material (Nandra *et al.* 1992; Nandra & Pounds 1992). Variations in the ionization degree of this absorber could also be responsible for some soft X-ray variability (*e.g.* NGC 5548, Nandra *et al.* 1991; NGC 4051) even if variations in the intrinsic spectral index are probably the cause of variations in some sources (NGC 4151, Perola *et al.* 1986; Yaqoob & Warwick 1991). The warm matter can also produce very broad wings in the optical lines (Mkn 509, Ferland, Korista & Peterson 1990).

Finally the iron line profiles could be a powerful means to investigate the geometry of the inner region of an accretion disc (at  $\sim 10R_s$ ) and determine the mass of the compact object if relativistically widened (*e.g.* Fabian *et al.* 1988). High resolution X-ray spectra may eventually be provided by AXAF.

It should be noted that the same ‘universal’ X-ray slope ( $\alpha \sim 0.7$ ), the reflection component and the iron line emission characterize also the spectrum of Galactic black hole candidates, suggesting a similarity in the physical processes, in particular accretion, for a ‘rescaling’ of  $10^6$  order of magnitude in the black hole mass (White, Fabian & Mushotzky 1984; Tanaka 1991; Sunyaev 1992; Fabian 1992).

For a recent review of the subject see Treves, Perola & Stella (1991).

An important consequence of this picture is that the primary X-ray spectrum has an intrinsic ‘universal’ slope of  $\alpha \simeq 0.9 - 1.0$  (Pounds 1992). As pointed out by Zdziarski *et al.* (1990), this value is naturally explained by pair plasma models for compact sources, as result when saturated pair cascades develop (§2.1.2).

#### 1.1.1.d $\gamma$ -ray spectrum

Before the launch of the Gamma Ray Observatory (GRO) and *Sigma* instruments, only five AGN have been detected above 100 keV.

A strong limit on the high energy emission of AGN is imposed by the steep  $\gamma$ -ray background (Fichtel *et al.* 1979): if their spectrum extend with a spectral index of  $\alpha = 0.7$ , it would exceed the diffuse emission at about 3 MeV (Bignami *et al.* 1979; Rothschild *et*



*al.* 1983). Therefore the AGN spectrum is expected to turnover below 2–3 MeV. Note the assumption of a steeper intrinsic power law  $\alpha \sim 0.9$  (§1.1.1.c) would increase this maximum energy.

One interesting feature between 100 keV and 2–3 MeV could be the detection of the electron–positron annihilation line (at rest energy  $\sim 511$  keV). In NGC 4151 and Cen A limits on its equivalent width are set at  $EW \sim 400$  and 300 keV, respectively (Baity *et al.* 1984). It is difficult to observe an annihilation line, because the greater the annihilation optical depth, the greater is the Compton downscattering, which smears the line. Also Doppler shifts contribute to broaden it. One situation in which the line could be seen is in a wind of pairs, which annihilate outside the source. However in a steady spherically symmetric geometry the wind can carry less than 10% of the injected luminosity (Svensson 1990; §5.4.2).

Recently a break in the spectrum of NGC 4151 at about 50 keV has been observed by *Sigma* (Jourdain *et al.* 1990), which has been interpreted as due to downscattering in a pair-dominated source (Coppi & Zdziarski 1992). A similar break has been observed in Cen A (at  $\sim 170$  keV, Johnson 1992). NGC 1275 and MGC 8–11–11 have been observed up to few MeV and their spectra steepen. So far some radio-quiet objects have been pointed but not detected by the EGRET instrument, probably indicating that sources belonging to this class are highly variable in  $\gamma$ -rays with short periods of emission or are not strong  $\gamma$ -ray emitters, possibly because pair reprocessing (§2.1.2). Observations between 20 keV to 1 MeV to determine if a break is a common feature in radio-quiet sources are a crucial test for pairs theories.

#### 1.1.1.e Optically-UV line emission

Line emission is a powerful diagnostic of the physical conditions of the plasma on m.a.s. scale and even if it can be considered of second order to understand the global energy output, being most probably reprocessed radiation, it gives information on the ionizing (maybe obscured) primary emission.

Generally two systems of emission lines are observed: a broad (FWHM  $\simeq 1000$ – $10000$  km/s) and a narrow (FWHM  $\simeq 200$ – $1000$  km/s) component. Type 1 Seyfert galaxies spectra show permitted lines (*e.g.* CIV) with width larger than the forbidden ones (*e.g.* [OIII], [NII]). In Seyfert 2 they are both narrow.

Most commonly (but see *e.g.* Blandford & Rees 1992) it is assumed that they are produced by clouds or filaments in two different regions, with typical parameters:

- Broad Line Region :  $R \simeq 0.1$ – $1$  pc,  $T \simeq 10^4$  K,  $n_e \simeq 10^{8-10}$  cm $^{-3}$  and covering factor  $\simeq 0.1$ .
- Narrow Line Region :  $R \simeq 0.1$ – $1$  kpc,  $T \simeq 10^4$  K,  $n_e \simeq 10^{3-6}$  cm $^{-3}$

Variability timescales, delays between continuum and line emission and estimates of the ionization parameter allow to estimate the BLR size, while the NLR has been optically resolved in some near Seyfert galaxies. The temperature  $T$  is inferred from the line ratios. Thermal broadening is smaller than the typical line width, suggesting dynamical motion at high velocity. The electron density  $n_e$  is constrained by the collisional transitions (recent evidences suggest that the density of the BLR clouds is in fact  $n_e \sim 10^{11}$ , Peterson 1992).

Photoionization by the central source continuum can produce ionized atoms at low temperatures. The amount of UV–X ray photons estimated extrapolating the optical continuum is consistent with the ratios of high ionization lines (Davidson & Netzer 1979, see however Mathews & Ferland 1987 and Netzer 1990). The photoionization model is strongly supported by the observed correlation between the continuum and broad lines intensities in Seyfert galaxies.

The fact that the filling factor is  $\ll 1$  in both regions suggests that the emitting gas is clumped in clouds, filaments or shell. Standard photoionization models predict  $N_H \sim 10^{22} - 10^{23} \text{ cm}^{-2}$  for the BLR clouds.

The width of the broad lines can be due to the high velocity dispersion of the clouds in in-outflowing motion. In fact, at the distance of the BLR, the clouds cannot be gravitationally bound at the speed inferred from the line width.

The self-gravity in the cloud is negligible and therefore a confining mechanism is required. The clouds are thought to be in pressure equilibrium with a hot, low density external medium ('two phases model', Krolik, McKee & Tarter 1981; Guilbert, Fabian & McCray 1983; Ferland & Rees 1988). At low densities Compton equilibrium is reached (with typical Compton temperatures  $T_C = (h/4k) \int F(\nu)\nu d\nu / \int F(\nu)d\nu \simeq 10^7\text{--}8 \text{ K}$ ), while at high densities optically thick gas tends to reprocess radiation and reach a phase equilibrium at the blackbody temperature ( $T \simeq 10^4\text{--}5 \text{ K}$ ). At intermediate densities, corresponding to similar radiation and gas energy densities, the gas is thermally unstable, but for proper values of density (or ionization parameters) both phases can coexist in pressure equilibrium (in agreement with the fact that similar ionization parameters were found for sources with different luminosity).

However detailed observations of the continuum shape including the UV contribution imply a Compton temperature too low to confine the clouds in a two phases equilibrium (Netzer 1990). For some range of parameters the optical depth in the hot medium may be large, but no effects on the spectrum have been observed. Recent long term monitoring of Seyfert galaxies in optical and UV (*e.g.* Clavel *et al.* 1991) shows that line emission lags variations in the continuum intensity from few days to months depending on the element and ionization state. This kind of studies ('reverberation') show that the 'standard' picture of the BLR is inadequate and that it probably extends closer to the central source, with  $N_H > 10^{24} \text{ cm}^{-2}$  in a stratified configuration (Ferland & Persson 1989; Rees, Netzer & Ferland 1989; Peterson 1992).

Moreover the velocity of the BLR clouds deduced from the lines width is probably greater than their sound velocity with consequent problems of stability during the motion.

Another possible confining mechanism is given by the magnetic field (with intensity of about 1 G) transported *e.g.* in a wind or accretion flow, in which case the matter tends to be in filamentary structures (Rees 1987; §3.2)

Lines (at least lines of low ionization) could be produced directly in the outer part of an accretion disc (Collin-Souffrin 1992). This possibility supports the picture that optical-UV radiation is due to reprocessing of a high energy flux impinging on the disc. Some evidences of asymmetric double peak lines, as predicted in such geometry, have been indeed observed (*e.g.* 3C390.3, Pérez *et al.* 1988), even if asymmetrical variations in the shape (*e.g.* in NGC 5548), suggest that part of the Balmer line emission is produced outside the disc (Ulrich 1990).

### 1.1.2 Blazars

The ‘blazar’ class includes BL Lac objects, Optically-Violent-Variable quasars (OVV), Highly Polarized Quasar (HPQ) (which are about 10 % of the radio loud quasars) and at least some, if not all, flat spectrum radio loud objects (Bregman 1990). By definition (*e.g.* Miller 1989) they have a smooth IR-optical-UV continuum from a point-like nucleus, a linear optical polarization  $p_{max} > 3\%$  (but up to 45%, Mead *et al.* 1990) variable in both degree and polarization angle; strong optical variability on timescale of days or less, and strong, polarized and variable radio emission. The flux-frequency dependence can be roughly approximated by a power-law with  $\alpha = 1$ . A strong correlation has been found between high polarization and optical variability of OVVs and HPQs (Moore & Stockman 1984; Impey 1992). The main difference between BL Lac objects and HPQs is the absence in the former of the UV excess and strong emission lines (usually a BL Lac has, by definition, lines with equivalent width less than 5 Å). Some objects appeared to belong to different classes during different observations (*e.g.* 3C446, 3C279, AO 0235+164, Visvanathan 1973; Cohen *et al.* 1987): when the continuum flux increased the lines intensity remained constant. BL Lacs show also a distribution in redshift and an average luminosity lower than HPQs.

#### 1.1.2.a Radio-UV continuum

The radio spectra are flat ( $-0.5 < \alpha < 0.5$ ) and no radio quiet (F(5 GHz) ; F(5500Å )) blazar has been identified. They present a compact radio morphology and in the plane  $\log \nu F(\nu)$  vs  $\log \nu$  the spectrum raises toward higher frequencies up to submillimeter-IR

region where most of the luminosity is observed (see Fig. 1.1), except in X-ray selected objects (*e.g.* Mkn 421, Makino *et al.* 1987; Ghisellini *et al.* 1986) (Fig. 1.3).

The strong evidences that the radio-optical emission is synchrotron radiation by a non-thermal distribution of electrons include: the high degree of linear polarization observed in the radio and optical bands, the smoothness of the radio-optical continuum, its variability and the inferred high brightness temperatures  $T_B$ . In the radio band  $T_B \simeq 10^{12}$  K (§5.3.2) but values up to  $T_B \simeq 10^{18}$  K (Quirrenbach *et al.* 1989) have been estimated. In fact the simultaneous intraday variations in the radio and optical bands recently detected, rule out an external cause for rapid radio variability (Rees 1992). In the IR and optical bands variability timescales imply values  $T_B > 10^6$  K (*e.g.* OJ 287, 3C345, Edelson & Malkan 1987, Moore *et al.* 1982).

Furthermore high brightness temperatures (or radiation densities) imply an high energy radiation flux by inverse Compton exceeding the observed one. If the emitting plasma is moving at relativistic speed, as first suggested by Rees (1966), the relativistic effects on flux, energy and variability timescales, can allow the predicted and observed values to be reconciled (§2.2.3; §5.3.1).

Also the IR flux is probably of non-thermal origin, as suggested by the continuity in the radio-IR emission and the lack of dust features in some radio loud objects. It has been suggested that a power-law component with spectral index  $\alpha \simeq 1$  (Edelson & Malkan 1986) probably of non-thermal origin extends over some decades in all AGN and emerges when thermal emission is weak.

### 1.1.2.b BL Lac objects

Their spectra do not present strong features. A high frequency turnover with a spectral index change  $\Delta\alpha \simeq 0.5$  ranges between IR and UV bands (Impey & Neugebauer 1988; Bregman *et al.* 1990); Landau *et al.* (1986) suggest that the smooth spectra from simultaneous observations can be best-fitted even with a quadratic form in the  $\log F/\log \nu$  plane. The spectrum of PKS 2155–304 has been recently best fitted with thermal emission from an accretion disc (Wandel & Urry 1989) (showing that the spectral shape alone can not constraint the emission mechanism). However optical polarization measures revealed that, on the contrary of HPQs, the linear polarization does not decrease with increasing frequency, as would be expected if the relative contribution of a thermal component would increase with energy (Smith & Sitko 1991).

A broad absorption feature at  $\sim 0.6$ – $0.7$  keV has been observed in the the soft X-ray spectrum of five BL Lac objects (Canizares & Kruper 1984; Madejski *et al.* 1991). High resolution spectra from BBXRT confirmed its presence for PKS 2155–304. The absence of features suggesting thermal emission in BL Lac objects has often be used as an indication

that they show the inner ‘naked’ emission region. However the BL Lac luminosity, if beamed, is not intrinsically intense, and instead most of the power is emitted in the form of kinetic energy of relativistic outflows (§5.4), as also suggested by the observation of this feature (§3.2.1.a).

Some objects show a diffuse emission, an optical excess and absorption lines (from which many redshifts have been estimated) probably due to the host galaxies. Most of them are elliptical, but recently a few host disc-type galaxies have been identified (Abraham, McHardy & Crawford 1991).

BL Lacs are strong X-ray emitters. No evidence of soft excess have been found (*e.g.* Madejski & Schwartz 1989), even if a very steep spectrum ( $\alpha \sim 5$ ) is observed between 300 and 600 eV in PKS 2155–304 (Sembay *et al.* 1992). Among blazars, they present a steeper X-ray spectral index, but the spectral shape is not yet uniquely determined. Urry (1986) suggests the presence, for five bright objects, of a steep ( $\alpha > 2$ ) component in the soft band flattening at higher energies ( $> 10$  keV). Below 8 keV, Barr *et al.* (1989) fit the spectrum with two power laws with increasing spectral indices ( $\Delta\alpha \simeq 0.5$ ) intersecting at 2–4 keV (see also Sembay *et al.* 1992). For three objects (PKS 2155–304, Mkn 421, H0323+022) a single power-law (with  $\alpha \simeq 1$ ) between 2–35 keV best fits the GINGA data (Ohashi 1989). A possible explanation of these different results is that the hard component is strongly variable.

Most BL Lacs were originally discovered in radio surveys, but X-rays satellites (HEAO-1, *Einstein*, EXOSAT) have discovered new objects (Schwartz *et al.* 1989; Giommi *et al.* 1989; Morris *et al.* 1991). The X-ray selected sources show a different spectral distribution (see Fig. 1.3), different peak emission frequency, lower polarization and variability (Stocke *et al.* 1985). They emit the same average X-ray, but less radio luminosity with respect to the radio selected ones. Their X-ray spectral index ( $\alpha \sim 1.5$ , Maraschi & Maccagni 1988) is both steeper than their UV one (*e.g.* Mkn 421, Makino *et al.* 1987; Bregman, Maraschi & Urry 1987) on the contrary of radio selected sources, and steeper than the X-ray slope of the radio selected ( $\alpha \sim 1$ ; Worrall & Wilkes 1990). This suggests that different components or emission processes produces X-rays (Maraschi 1991) (§4.1.2; §6.1).

An open question concerns the absence of broad emission lines in BL Lac spectra. In the assumption of isotropic emission this cannot be attributed to the lack of photoionizing continuum (Urry 1984). Alternative explanations include thermal instability of the BLR emitting clouds as the steep optical–UV continuum suggested (Guilbert, Fabian & McCray 1983; Worrall & Wilkes 1990), the absence of emitting gas, the possibility that it is hot or pair dominated, or that anisotropic ionizing radiation intercepts only a small fraction of it. Because the Doppler factor (in the radio band) is lower for BL Lac than for HPQ (§5.3.1), the hypothesis that relativistic amplification causes the BL Lac continuum to

overcome the thermal and line emission does not seem plausible. The difference between BL Lac objects and HPQs has been interpreted as due to a different strength of magnetic field, which would be responsible for the synchrotron emission and collimation of the jet. The alternative interpretation suggested by Ostriker & Vietri (1985), that Lac objects are OVV's the optical continuum of which is enhanced by microlensing in an intervening galaxy, predicts both the swamping of the lines and the low redshift distribution of BL Lac. This hypothesis presents however some serious difficulties (the rapid variability, the radio polarization structure; see also Padovani 1992).

#### 1.1.2.c $\gamma$ -ray emission

One of the most exciting recent discoveries is that an increasing number of blazars are intense  $\gamma$ -ray emitters above  $\sim 100$  MeV. The EGRET instrument ( $\sim 50$  MeV–50 GeV band) has detected up to now 16 sources. Based on a tentative identification (Kanbach *et al.* 1992; Fichtel *et al.* 1992a; Michelson *et al.* 1992; Hartman *et al.* 1992a,b,c; Hunter *et al.* 1992) 11 would be blazars. The bolometric luminosity of these sources can be dominated by the  $\gamma$ -ray emission. In Table 1.1 we report the estimated fluxes in the radio, optical, X-ray and  $\gamma$ -ray bands. Detailed results have been published for 3C279 (Hartmann *et al.* 1992a), the luminosity of which is  $L_\gamma \simeq 10^{48}$  erg s $^{-1}$ . Rapid variability in the  $\gamma$ -ray flux has been also reported for 3C 279 (Kanbach *et al.* 1992) (§4.2.1), while for other sources only long term variability has been observed. The spectrum of 3C 273 shows instead a break at about 1 MeV (Gehrels 1992). The weaker source appears to be Mkn 421, which has been recently observed at TeV energies (Punch *et al.* 1992) with luminosity output comparable to the X-ray emission.

All the sources are core-dominated (§1.2.1) and some show superluminal motion (§1.2.2). These observations and the apparent correlation between the radio and  $\gamma$ -ray fluxes suggest a link between the intense  $\gamma$ -ray emission and the presence of relativistic motion and jet structure (§4.2.4).

#### 1.1.3 Variability

Variability observations have become a powerful means to test models and understand the emission mechanism and the spatial distribution of the emitting material in AGN, particularly in the innermost regions (§2.1.4; §3.1.2; §4.1; §4.2). AGN vary in all bands and on all timescales, the shortest ones usually in the X-rays (*e.g.* Turner 1992). It is not clear if we observe an ‘equilibrium’ spectrum from a single source or the averaged spectral flux from many small regions (Guilbert, Fabian & Ross 1982). A high value

of  $\Delta L/\Delta t$  (or compactness) implies that we are dealing with compact objects, imposing strong constraints on the radiation mechanisms (§2.1.3, §2.1.4).

Generally strong variability (*i.e.* a large fraction of the observed flux varies on a short timescale) requires an unique source or a coherent mechanism able to induce simultaneous variations in different spatial regions.

We note that large and rapid variability of the hard X-ray continuum is one of the strongest evidences against models which explain the observed activity through bursts of star formation or supernovae (*e.g.* Terlevich 1990; Fabian 1992a).

Variability can constrain the dimensions of the emitting region through the causal connection argument  $R_0 \lesssim 2c\Delta t(1+z)^{-1}\delta$  cm, where  $\Delta t$  is the variability timescale and  $\delta$  is the Doppler factor (§2.2.3). In the case of optically thick sources the light crossing time is amplified by a factor  $\sim (1 + \tau_T)$  (which can be misleading in the case of non-spherical (*e.g.* sheet-like) geometries).

Simultaneous variability observations in different spectral bands put strong constraints on the spatial distribution of the emitting regions and indicate whether the same radiative process dominates at different frequencies.

Variability ‘parameters’ can be defined to quantify both timescales and amplitudes of variations, both of which depend on frequency and on the number of observations. Among the variety of variability behaviours some trends start to appear.

#### 1.1.3.a Timescales

The doubling variability timescale defined as  $\Delta t \equiv F/(dF/dt)$  (which corresponds to the time required for the sources to double its flux) is commonly used to estimate the source dimensions, even if the probability to observe this minimum timescale is low. Typically a timescale  $3-7 R_0/c$  would be observed (Done & Fabian 1989). Note that  $\Delta t$  does not refer to the true amplitude of variations and decreases with the interval between observations. Slower variability trends can be caused instead by long term changes in the structure of the source. Timescales for increasing and decreasing flux or ‘long’ timescales with constant flux (‘states’) are observed.

- One of the most striking result concerning radio quiet objects is that X-ray variability timescales as short as few hundreds seconds have been detected for few objects (Mkn 335, NGC 4051, NGC 5506, NGC 5548, MGC 6-30-15, Lawrence *et al.* 1987; Pounds & McHardy 1988; Nandra *et al.* 1989; Done *et al.* 1990; Kaastra & Barr 1989; Matsuoka *et al.* 1990). For the Seyfert 1 galaxy NGC 6814, the limit is  $< 50$  s (Kunieda *et al.* 1990). Therefore resolution on short timescales has allowed upper limits on the dimensions of

the X-ray emitting regions in some cases as small as  $10^{12}$ – $10^{13}$  cm (§3.1), which can be compared to the Schwarzschild radius  $R_s \simeq 3 \times 10^{11} M_6$  cm. X-ray variability timescales seem anticorrelated with the source luminosity  $\Delta t \propto L^{-1}$ , suggesting that sources emit at the same rate, with respect to the Eddington limit (Barr & Mushotzky 1986).

Optical microvariability on timescales of minutes has been reported for a Seyfert galaxy (Dultzin-Hacyan 1992).

- BL Lac objects show decreasing timescales with increasing photon frequency (Giommi *et al.* 1990; George, Warwick & Bromage 1988; Bregman 1990; Sembay *et al.* 1992). The timescales vary from months–years in the GHz band, several weeks in the far IR, days in the near IR, hours–day in the optical and similarly in the UV bands. Recently a variation in the UV flux of PKS 2155–304 corresponding to  $\Delta L/\Delta t \sim 2 \times 10^{40}$  erg s $^{-2}$  has been reported (Edelson *et al.* 1991). Variations on timescales 30 s has been found in X-rays (H0323–022, Feigelson *et al.* 1986), but usually the typical timescales are  $\sim$  hours, *e.g.* PKS 2155–304 (Morini *et al.* 1986; Treves *et al.* 1990). The only information on rapid variability at  $\gamma$ -rays frequencies is for the blazar 3C 279. The dependence on frequency of  $\Delta t$  can be roughly described as  $\Delta t \propto \nu^{-1/2}$  (Bregman 1990).

An interesting possibility is that the emission can be interpreted as due to a ‘quiescent’ component plus a variable contribution (flare). In the X-ray band Maraschi & Maccagni (1988) showed that 35 BL Lacs vary less than 50 % for more than 70% of the time.

### 1.1.3.b Amplitudes

An indicator of the amplitude of variability can be defined as  $\Phi(\nu) = F_{max}/F_{min}$  or  $v(\nu) = \sigma_v/\langle F \rangle$ , where  $F_{max}$ ,  $F_{min}$ , and  $\langle F \rangle$  are the maximum, the minimum and the average fluxes and  $\sigma_v$  is the standard deviation [eq. (4.1)]. The parameter  $v(\nu)$  can be independent of the number of observations (if many) and of the average flux (§4.1.1). Note however that the amplitude and the variability ‘duty cycle’ are not disentangled. Suppose, for simplicity, that the source can be observed only in two states (low and high) with an amplification factor  $A$  and let  $p$  be the probability to observe the high state.  $v(\nu)$  can be written as  $v(\nu) = (A - 1)\sqrt{p(1 - p)}/(1 - p + pA)$ . This function of  $p$  has a maximum (which increases for increasing  $A$ ) and therefore the same value of  $v(\nu)$  can be obtained for two values of  $p$ , for fixed  $A$ .

- Seyfert galaxies show a softening of the X-ray spectrum when the source brightens (NGC 4051, Lawrence *et al.* 1985; NGC 4151, Perola *et al.* 1986; NGC 5548 Branduardi-Raymont 1989; MR2251–178, Pan, Stewart & Pounds 1990; MGC 8–11–11, Treves *et al.* 1990). An anticorrelation between the spectral index and the flux can be



explained in the reflection model. For NGC 4151, Yaqoob & Warwick (1991) reported a variation  $\Delta\alpha \sim 0.3$  with an increase in flux of a factor of ten in the 2–10 keV flux, which is interpreted as due to the steepening of the spectrum (Perola *et al.* 1986; Yaqoob & Warwick 1991). The same behaviour is shown by 3C120 (Maraschi *et al.* 1991) with a delay of the ME band with respect to the LE flux. The amplitudes of variability are anticorrelated with the UV luminosities (Edelson 1992).

- Results on the dependence of the amplitude of variability on frequency have been reported for a large sample of blazars by Impey & Neugebauer (1988). The average amplitude (over all objects) increases regularly with frequency from the radio to the optical–UV band.

Giommi *et al.* (1990) systematically analyzed data on BL Lac objects in the EXOSAT archive and found that almost all the objects vary and the hardness ratio (ME over LE flux) increases with the ME flux. Correlations between spectral flattening and intensity are observed for PKS 2155–304 (Treves *et al.* 1989; Sembay *et al.* 1992) and quasi-simultaneous monitoring of Mkn 421 in the UV–X-ray bands (George, Warwick & Bromage 1988). These behaviours seem to consistently extend to high frequencies the findings of Impey & Neugebauer (1988) (§4.1.1).

This trend is present also in narrow bands, as variations in the spectral index, and generally increase with frequency (Impey & Neugebauer 1988). Single sources however show very different behaviours.

Another interesting result is the observation (with GINGA satellite) of an X-ray flare from an ‘ordinary’ quasar, PKS 0558–504 (Remillard *et al.* 1991). The flux increased of 67% in 3 minutes, implying a variation  $\Delta L/\Delta t \simeq 2.9 \times 10^{42} \text{ erg s}^{-2}$ . The authors suggest that it can be an indication of relativistic beaming (§2.1.3). A similar value of  $\Delta L/\Delta t$  was observed from the blazar 3C 279, with a variation of 20% in 45 min (Makino *et al.* 1989; §4.2.1).

#### 1.1.3.c Correlated variability

Unfortunately few and not systematic simultaneous observations in different spectral bands are available.

- An example of the power of this investigation is the results obtained for the Seyfert 1 galaxy NGC 4051 (Done *et al.* 1990). During a variation in X-rays (2.3–8.7 keV) greater than 50 %, the flux varied less than 1% in the optical and 4% in IR, ruling out the standard synchrotron self-Compton mechanism (§3.1.3). Similarly for 3C273 no correlations between mm and X-ray flux has been observed (Courvoisier *et al.* 1990).

Quasi-simultaneous optical-UV variability has been observed in NGC 4151, NGC 5548, Fairall 9 and 3C 273 (Courvoisier 1992) suggesting a common origin of the radiation (§3.3). Uncorrelated UV-X-ray (2–20 keV) variability has been observed for 3C 273 (Courvoisier *et al.* 1990), while strong correlations are reported for NGC 4151 (at least some observations, Perola *et al.* 1986) and NGC 5548 (Clavel *et al.* 1992). These variations are interpreted as due to instabilities in the inner part of the disc or irradiation of it from an X-ray source (*e.g.* Ulrich 1990; §3.3)

- Blazars show a good correlation between optical and near IR fluxes and optical and UV, while delays of weeks has been observed between optical and far IR fluxes (Marscher & Gear 1985). Bregman & Hufnagel (1980) found correlation of optical and radio variations, with delays of typically a year, while a delay of less than 2 months has been observed in OJ 287 (Valtaoja *et al.* 1989). A wide, intensive campaign on BL Lac itself has shown that optical and infrared variations are nearly simultaneous and precede radio flares by few years (Bregman *et al.* 1990).

In BL Lac objects radio and UV fluxes are strongly correlated (OJ 287, Pomphrey *et al.* 1976; 3C345, Balonek 1982) and similarly in 3C273, with the UV variations anticipating the radio ones. It is quite surprising if the emission mechanisms radiating at radio and UV energies are different.

In the radio bands generally high frequencies precede low frequencies flux variations by weeks–months at 20–100 GHz and months–years at 5–15 GHz (Balonek 1982; Aller *et al.* 1985) with decreasing amplitude toward lower frequencies, both in radio quiet objects and blazars (Valtaoja *et al.* 1985).

Very few observations suggest correlated variability between UV and X-ray bands (Maraschi 1991). X-rays appear to be correlated with optical flux when they are on the extrapolation of the IR–UV spectrum (*e.g.* Mkn 421, Makino *et al.* 1987; 0537-441, Tanzi *et al.* 1986), while uncorrelated X-rays and lower frequency emission is found for objects where the extrapolation of the UV flux underestimates the X-ray one (*e.g.* BL Lac, 3C446, 3C345, Makino 1989). 1156+285 showed an X-ray outburst between two optical flares, possibly correlated (McHardy 1989). Correlated variability was observed in X-rays for PKS 2155–304 (between LE and ME bands of EXOSAT), with no evidence of lags (Tagliaferri *et al.* 1991) (§4.1).

Interestingly it has been reported that radio and  $\gamma$ -ray variations were correlated during the EGRET observations of 3C279 (Impey 1992) (§4.2).

Finally a new VLBI component (§1.2) appeared in the map of 3C273 at the epoch of fast IR–optical variability (Krichbaum *et al.* 1990, Baath *et al.* 1991) suggesting that the continuum emission is related to the jet structure. Indeed the core and knot positions in VLBI radio maps coincide in coincidence with flares in the emitted flux (Marscher 1992).

### 1.1.3.d Power spectrum

In general X-ray variability shows an irregular behaviour, with outbursts and flickering on the shorter resolution timescales (Turner 1992). Power spectrum analysis has been performed for few objects, due to the lack of long trend observations. It shows a dependence on frequency  $f^{-1} - f^{-2}$  in the  $10^{-6} - 10^{-2}$  Hz band for Seyfert galaxies with a tendency to be steeper than  $f^{-1}$  at high frequencies (NGC 4051, Lawrence *et al.* 1987; MGC-6-30-15, McHardy 1988), and, recently for the BL Lac object PKS 2155-304 for which a dependence  $f^{-1.9}$  has been found (Tagliaferri *et al.* 1991). Note that the dependence  $f^{-1}$  implies that the same power is emitted at all frequencies, and this would suggest that there is no preferred timescale (and therefore dimensions) on which the source varies: the lack of a cut-off at high  $f$  shows that observations are not yet performed on sufficiently short timescale to evidence a minimum size of the emitting region.

Significant features have been found in the power spectra of two sources. An important feature to support the accretion disc picture would be the observation of the effects of a ‘spiraling’ perturbation. A strong indication of periodicity has been discovered for NGC 6814 in the EXOSAT data (Mittaz & Branduardi-Raymont 1989; Fiore, Massaro & Barone 1992) and recently confirmed by GINGA (Done *et al.* 1991). The fundamental frequency is at  $\sim 12200$  sec, with increasing period (Turner 1992). Marginal evidence of periodicity has been found for NGC 4151 (Fiore *et al.* 1989). The periodic behaviour on such short timescales is a strong evidence of a rotating structure close to a compact object, but it is not simply accounted for in the standard disc picture and different physical effects have been suggested (*e.g.* Abramowicz *et al.* 1989; Rees 1992; Blandford 1992; Fabian 1992).

In some objects periodic events are reported from light curves. OJ 287 showed possible periodicity with timescale of 20 min in the radio and optical bands (Visvanathan & Elliot 1976; Valtaoja *et al.* 1985), and Mkn 421 in the X-ray band with period of 4 hours (Brodie, Bowyer & Tennant 1986). Optical periodicity of 1540 days has been reported for 3C446 (Barbieri *et al.* 1990).

## 1.2 SPATIAL OBSERVATIONS

One of the most spectacular features associated with the activity of galactic nuclei is the presence of collimated structures, which are believed to be the signature of the power supply from the central sources to the extended (kpc-Mpc-scale) radio lobes. The energy involved with these phenomena can be a significant part of the AGN energy budget (§5.5). They can also be important orientation indicators, being observed in some detail (§6.1).

Here we briefly present the observational evidences for the presence of jets on large and small scales, mainly in the radio band, the discovery of sources moving with apparent

superluminal velocity and the relation with blazars. For a complete review see *e.g.* Begelman, Blandford & Rees (1984), Laing (1992), Marscher (1992).

### 1.2.1 Large and small scale jets

After the first interpretation of the observed double radio lobes as clouds of magnetized plasma ejected from the central galaxy, Rees (1971), Scheuer (1974) and with more details Blandford & Rees (1974), proposed that the lobes are instead continuously supplied of energy from the central galaxy through jets of plasma (solving the problem posed by the strong adiabatic losses). The energy would be transported in kinetic form and dissipated where the jet encounters the interstellar matter developing a shock wave, which accelerates the emitting particles (at the hot spots). In fact, due to the short cooling timescales, the electrons must be locally accelerated.

Later radio jets were observed. VLA maps with resolution of arcsec (corresponding to linear scale of kpc for typical distance of quasars) and sensibility of  $10^{-5}$  Jy, showed that jets are common in radio sources, and associated with objects of different luminosity and type (more than 300 jets have been observed).

Even if not surprising by itself, the discovery of collimated structures on m.a.s. scale revealed new features. High resolution VLBI maps (typically at  $\sim$  GHz frequencies) show that jets are in fact made of discrete emitting blobs (core-jet structure), sometimes moving with apparent superluminal speed (*e.g.* Porcas 1987). The m.a.s. size jets are sometimes aligned with the extended ones, sometimes appear blended (maybe due to projection effects), and one-sidedness is quite common.

The same kind of aligned structures is therefore observed on more than six orders of magnitudes in dimension. The flow can not be simply rescaled over different sizes, because the radiative cooling timescales increase faster than the dynamical ones with increasing size (see Table 1.2). Smaller jets should be more dissipative. Also the fact that large scale jets appear ‘aligned’ implies that the central source is stable at least over  $10^6$  years.

In Fig. 1.4 the jet of 3C 120 over many orders of magnitude in resolution is shown (Walker, Benson & Unwin 1987). On the smaller scales the jet appears more like unresolved bright blobs than a continuous flow. The blobs probably indicate regions of efficient particles acceleration or stronger magnetic field (as produced by a shock wave).

Note that the smallest observable radio dimension is about five order of magnitude larger than the supposed black hole dimension and is comparable with the BLR size. The only (indirect) information on smaller scales is therefore given from high energy variability.

A gross morphological division is between ‘extended radio sources’ with dimensions from kpc to Mpc and an optically thin ( $\alpha \simeq 0.5 - 1$ ) spectra at low frequencies, and the

‘compact radio sources’ close to the optical nucleus (sizes of  $\sim \text{pc}$ ) with an absorbed flat ( $\alpha \simeq 0 - 0.5$ ) spectra at  $\sim 5 \text{ GHz}$ , and generally associated with quasars or BL Lacs. Now this division has been substituted by the distinction between lobe dominated (LD) and core dominated (CD) sources, because of the discovery that at the proper sensitivity and spatial resolution luminous radio galaxies and quasars contain both a flat component from the core and a steep spectrum component from the jets and lobes. Extended and compact radio sources are substantially the same type of objects, probably observed at different angles.

Very schematically, large scale jets can be divided into two categories, depending on the luminosity. Fanaroff & Riley (1974) evidenced a correlation between morphology and the radio power in extended sources, suggesting that the transport and dissipation mechanisms depend on the radio luminosity (§5.5).

High power jets  $L_{178\text{MHz}} \gtrsim 2 \times 10^{33} \text{ erg s}^{-1}$  (FR type II sources or ‘edge brightened’) are often one-sided, with small spreading (opening angle  $< 4^\circ$ ), appear brighter on smaller size, the magnetic field is predominantly aligned with the jet (maybe stretched by the plasma flow). They are often associated with radio loud quasars, and radiate a significant fraction of the total power, but not when associated to radio galaxies (Bridle 1991). They have dimensions of about few hundred kpc and ‘terminate’ in bright, sometimes asymmetric, lobes, with hot spots.

The weak sources (FR I radio sources, or ‘edge darkened’) with lower luminosity, are two-sided (with a jet-counterjet ratio  $< 4 : 1$ ), opening angles  $> 8^\circ$ , and perpendicular magnetic fields (which is expected over large distances if magnetic flux is conserved). The brightness is almost constant, and they can emit more than 10 % of the total extended emission. They are more often associated with elliptical radio galaxies in clusters (Owen & Laing 1989) and end in ‘plume’ structures (extending up to 5 Mpc).

The radiative dissipation can be due to internal magnetic field; or to interaction with entrained matter at the jet boundaries or with obstacles, which causes dissipation of some kinetic energy; or to the variation of the ejection velocity which leads to the formation of shocks.

An estimate of typical physical parameters in synchrotron sources can be obtained, by assuming (for simplicity) the equipartition condition between the relativistic particles and the magnetic energy densities. If a source is resolved, it is possible to determine the volume emissivity. Denoting  $\nu_t$  the cut-off frequency which dominates the electron energy density,  $\gamma_t \propto (\nu_t/B)^{1/2}$ , for  $\alpha = 0.5$ , the synchrotron emissivity  $j_s(\nu_t) \propto p_e p_B^{3/4} \nu_t^{1/2}$  (§2.2), where  $p_e$  and  $p_B$  are the electron and magnetic pressures. Therefore the minimum pressure is given by  $p_{\min} \simeq 7.2 \times 10^9 j_s^{4/7}(\nu_p) \nu_p^{2/7} \text{ erg cm}^{-3}$ .

Typical values of parameters estimated from the synchrotron theory are reported in Table 1.2 (Blandford 1990).  $t_{syn}$  and  $t_{dyn}$  are the synchrotron cooling and dynamical

timescales,  $B$  is the magnetic field intensity,  $\gamma$  the Lorentz factor of the emitting electron and  $E_{min}$  is the (minimum) total energy in the source.

**Table 1.2. Physical parameters**

	$B$	$\nu$	$\gamma$	$t_{syn}$	$t_{dyn}$	$p_{min}$	$E_{min}$
	G	Hz		s	s	erg/cm <sup>3</sup>	erg
Extended source	$10^{-5}$	$10^9$	$10^4$	$10^{14}$	$10^{15}$	$10^{-11}$	$10^{59}$
Radio jet	$10^{-3}$	$10^9$	$10^3$	$10^{11}$	$10^{11}$	$10^{-7}$	$10^{57}$
Compact source	$10^{-1}$	$10^9$	$10^2$	10	$10^8$	$10^8$	$10^{54}$
Inner disc	$10^3$	$10^{16}$	$10^{3.5}$	$10^{-1}$	$10^7$	$10^5$	$10^{47}$
B.H. Magnetosph.	$10^4$	$10^{18}$	$10^4$	$10^{-3}$	$10^4$	$10^7$	$10^{47}$

#### 1.2.1.a Optical and X-ray jets

It is difficult to find jets at higher frequencies. The jet of the elliptical galaxy M87 has been observed in optical, UV and X-rays. The optical-UV observations show a remarkable ‘similarity’ with the radio filamentary structure and polarization; the optical spectral index is also similar along the jet (Boksenberg *et al.* 1992). High resolution X-ray observations show that the emission from the outer components is comparable to the emission of the core on arcsec scale (Biretta, Stern & Harris 1991). Optical jets have been observed also in 3C66 and PKS 0521–36, showing again similar optical-radio structure in the dissipative regions (Macchetto 1991). An X-ray jet has been observed in Cen A (Schreier *et al.* 1979) and 3C273 on the kpc scale, even if with low resolution.

#### 1.2.1.b Polarization

Linear polarization up to 64 % has been observed in radio knots (OJ287, Wardle & Roberts 1988) reaching almost the theoretical limits for synchrotron emission (from a power-law distribution of emitting electrons  $p = (\alpha + 1)/(\alpha + 5/3)$ , *e.g.* Rybicki & Lightman 1979). This requires an ordered magnetic field component and no Faraday depolarization (along the VLBI jet), while a disordered magnetic field in the core region could account for the observed increase of the linear polarization with the distance from the core (*e.g.* 3C273, Wardle *et al.* 1990; Roberts *et al.* 1990).

BL Lac objects show polarized radiation with magnetic field mostly perpendicular to the jet axis (but parallel to it in quiescent states), indicative of the presence of shocks.

For a planar shock wave a maximum degree of polarization is predicted at an angle with the jet axis similar to the critical angle for superluminal motion (*e.g.* Wardle & Roberts 1988, see §1.2.2). Quasars instead show a magnetic field generally parallel to the flow axis. Furthermore the polarization in the core of BL Lacs ( $\sim 1\text{--}5\%$ ) is greater than for quasars (where is sometimes  $< 1\%$ ) (Roberts *et al.* 1990). Both these facts strongly argue against the lensing model of Ostriker & Vietri (1985). Sometimes radio and optical polarization are correlated (*e.g.* 3C345, Sitko, Schmidt & Stein 1985). BL Lac showed flux and polarization variations simultaneous with the appearance of a new blob in VLBI map (Phillips & Mutel 1988), analogous to the IR–optical flux variations in 3C 273 and suggesting a correlation between flux variability and variations in the jet structure.

### 1.2.2 Superluminal sources

The upper limit on the angular dimension of compact sources estimated from rapid radio variability gives, in the assumption of synchrotron emission, a lower limit to the brightness temperature which exceeds the Compton limit (§2.2.5). The hypothesis suggested by Rees (1966) that the sources were expanding at relativistic velocities, reduced the Compton problem and predicted that they would have been observed to move with superluminal velocities. The observations of rapid variability in the dimensions of 3C279, implying velocities of  $\sim 2c$ , were interpreted by Moffet *et al.* (1972) as the first observational evidence of Rees' idea.

As already mentioned, high resolution VLBI maps have shown that the parsec-scale jets often consist of discrete emitting blobs, which sometimes move with apparent superluminal velocities (*e.g.* Zensus & Pearson 1987).

An example of a superluminal source is shown in Fig. 1.5, in which the compact component of 3C179 is assumed to be stationary and the other moves with apparent linear velocity  $\beta_a \sim 4.8h^{-1}$ . The emitting knots appear to be separated by about 1 pc.

The quantity measured is the proper motion  $\mu$ , (*i.e.* the apparent angular separation velocity). If the redshift is known, by transforming the time intervals (between the observer and source frames)  $\mu$  can be converted into the projected linear velocity  $\beta_a c$  (in a Robertson–Walker metric)

$$\beta_a = \mu \frac{d_\theta(1+z)}{c} = 47.4\mu \frac{q_0 z + (q_0 - 1)(\sqrt{1 + 2q_0 z} - 1)}{hq_0^2(1+z)} \quad (\text{m.a.s. yr}^{-1}) \quad (1.1)$$

where  $d_\theta = d_L/(1+z)^2$  is the angular distance and  $d_L$  the luminosity distance (Weinberg 1972).

The knots show different kinematical behaviours: linear or curved trajectories (CTA 102, Wehrle & Cohen 1989), sometimes accelerating (*e.g.* 3C345, Biretta & Cohen 1987) or decelerate, but no contracting components have been observed.

Most of superluminal sources are identified with quasars, however more and more superluminal BL Lacs have been found (§5.3.3). In fact to be observed as superluminal, a source must emit more than  $\sim 1$  Jy and its distance must be known.

All the superluminal show also an extended radio component ( $> \text{arcsec}$ , Browne 1987): the superluminal components, like the ‘subluminal’, often are not aligned with the larger scale jet (Mutel 1990). The compact objects associated with luminous extended radio lobes show lower superluminal velocities (§5.3.3). Quite interestingly, there is some evidence of superluminal velocity also on kpc scale (M87, with  $\beta_a \sim 0.6 - 1$ , Biretta & Owen 1990; 3C120,  $\beta_a \sim 3.7$ , Walker *et al.* 1988).

In the simplest interpretation of superluminal motion, the emitting plasma moves at relativistic speeds at a small angle to the line of sight. The emitted radiation is thus beamed along the direction of motion, giving rise to the high synchrotron brightness temperatures observed without the overproduction of inverse Compton X-rays (§5.3.4).

### 1.2.3 Blazars

There is increasing evidence that most compact radio sources show features characteristic of blazars: most, if not all, flat spectrum radio quasars are blazars (Fugmann 1988; Impey & Tapia 1990; Impey 1992). At least 70% of superluminal sources have IR, optical or X-ray properties typical of blazars and core-jet sources show a very flat ( $\alpha \sim 0$ ) spectral component. Vice versa, Cohen (1986) found that the 80 % of bright sources at 10 GHz showed superluminal motion and a correlation with flat spectrum and optical polarization has been shown (Moore & Stockmann 1984).

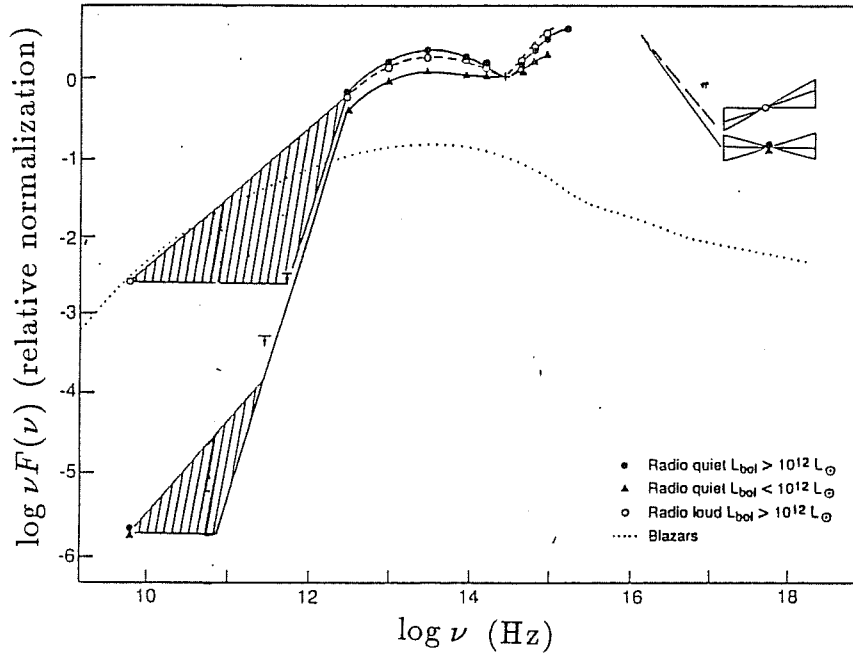
More specifically BL Lac objects always show core-jet radio structure. They present weak extended radio emission, with a ‘core-halo’ morphology, and deprojected linear dimensions consistent with double sources observed at small angles (Antunucci & Ulvestad 1985); the core radius parameter  $R_{CD} = \text{core/extended fluxes}$  (usually used as a beaming indicator, in the hypothesis that extended emission is not beamed) correlates with polarization, variability and one-sidedness.



Table 1.1.  $\gamma$ -ray blazars

Source	$\nu F(\nu)$ :	$\simeq 100$ MeV	1 keV	5500 Å	5 GHz
0208-512		$1.6 \times 10^{-10}$	$1.9 \times 10^{-13}$		$1.7 \times 10^{-13}$
0235+164		$2.4 \times 10^{-11}$	$4.1 \times 10^{-13}$	$3.6 \times 10^{-11}$	$8.8 \times 10^{-14}$
0420-014		$2.4 \times 10^{-11}$	$1.3 \times 10^{-12}$	$1.3 \times 10^{-12}$	$7.9 \times 10^{-14}$
0454-463		$2.4 \times 10^{-11}$	$1.2 \times 10^{-13}$	$1.3 \times 10^{-12}$	$6.5 \times 10^{-14}$
0528+134		$2.4 \times 10^{-11}$	$8.7 \times 10^{-13}$	$2.1 \times 10^{-13}$	$2.0 \times 10^{-13}$
0537-441		$5.4 \times 10^{-11}$	$4.9 \times 10^{-13}$	$1.3 \times 10^{-11}$	$9.7 \times 10^{-14}$
0716+714		$3.2 \times 10^{-11}$	$5.3 \times 10^{-13}$	$1.1 \times 10^{-10}$	$2.5 \times 10^{-14}$
0836+710		$2.4 \times 10^{-11}$	$< 2.4 \times 10^{-12}$	$5.3 \times 10^{-12}$	$5.3 \times 10^{-14}$
1101+384		$4.6 \times 10^{-10}$	$3.4 \times 10^{-11}$	$9.7 \times 10^{-11}$	$1.2 \times 10^{-14}$
1226+0.23		$2.4 \times 10^{-11}$	$5.1 \times 10^{-11}$	$5.5 \times 10^{-11}$	$5.2 \times 10^{-13}$
1253-055		$4.6 \times 10^{-10}$	$3.4 \times 10^{-12}$	$1.7 \times 10^{-12}$	$7.3 \times 10^{-13}$
1633+382		$1.5 \times 10^{-10}$	$< 4.9 \times 10^{-14}$	$1.3 \times 10^{-12}$	$2.2 \times 10^{-14}$
2230+114		$2.4 \times 10^{-11}$	$8.3 \times 10^{-13}$	$2.5 \times 10^{-12}$	$2.7 \times 10^{-14}$
2251+158		$2.4 \times 10^{-11}$	$1.4 \times 10^{-12}$	$7.6 \times 10^{-12}$	$4.5 \times 10^{-14}$

The  $\gamma$ -ray data are from Fichtel *et al.* (1992b), while for the other bands we refer to Table 5.1.



**Fig. 1.1.** Mean spectral energy distribution (in  $\nu F(\nu)$ ) of different classes of AGN. The blazars spectrum is smooth and does not show particular features. The spectra of radio-loud and radio-quiet quasars appear similar from the IR to the soft X-ray band. From Saunders *et al.* (1989).

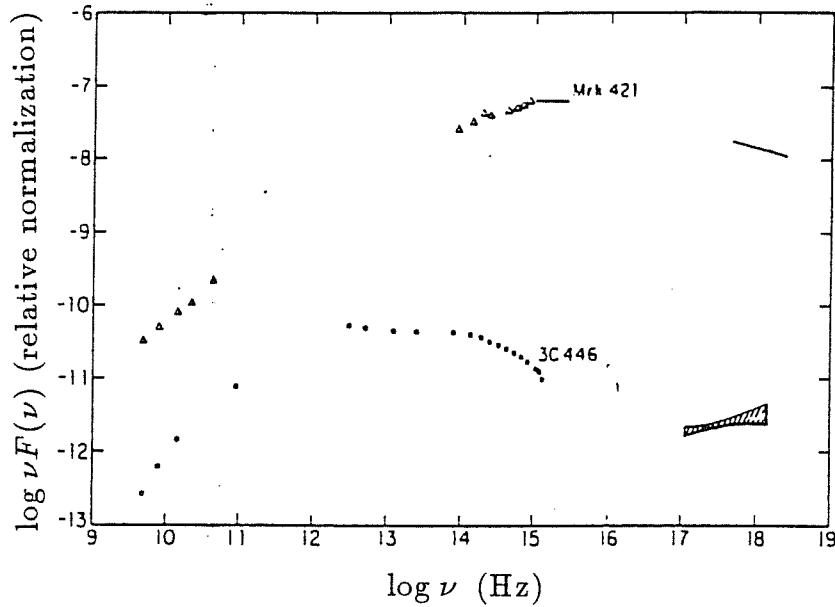


**Fig. 1.2.** Energy distributions of two BL Lacs: a X-ray selected (Mkn 421) and a radio-selected one (3C 446). (From Maraschi 1991 and references therein). They show different peak emission frequencies, X-ray slopes, connection with the UV spectra and relative X-ray to radio luminosities.

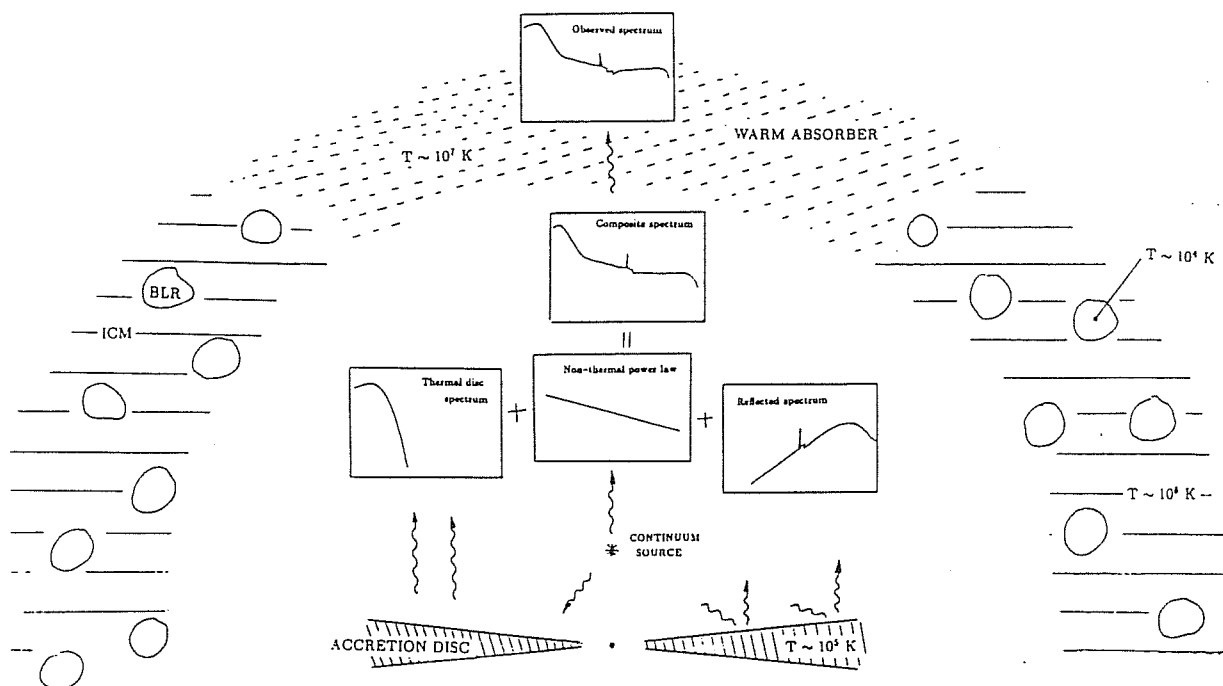


**Fig. 1.3..** A very schematic representation of the X-ray emission and absorption regions (from Nandra *et al.* 1989). The accretion disc is responsible for the EUV-soft X-ray emission and the cold iron line and edge. The warm absorber can produce a higher energy iron edge and the recently discovered O VIII edge. The BLR clouds could be also localized in the disc (*e.g.* Collin-Souffrin 1992).

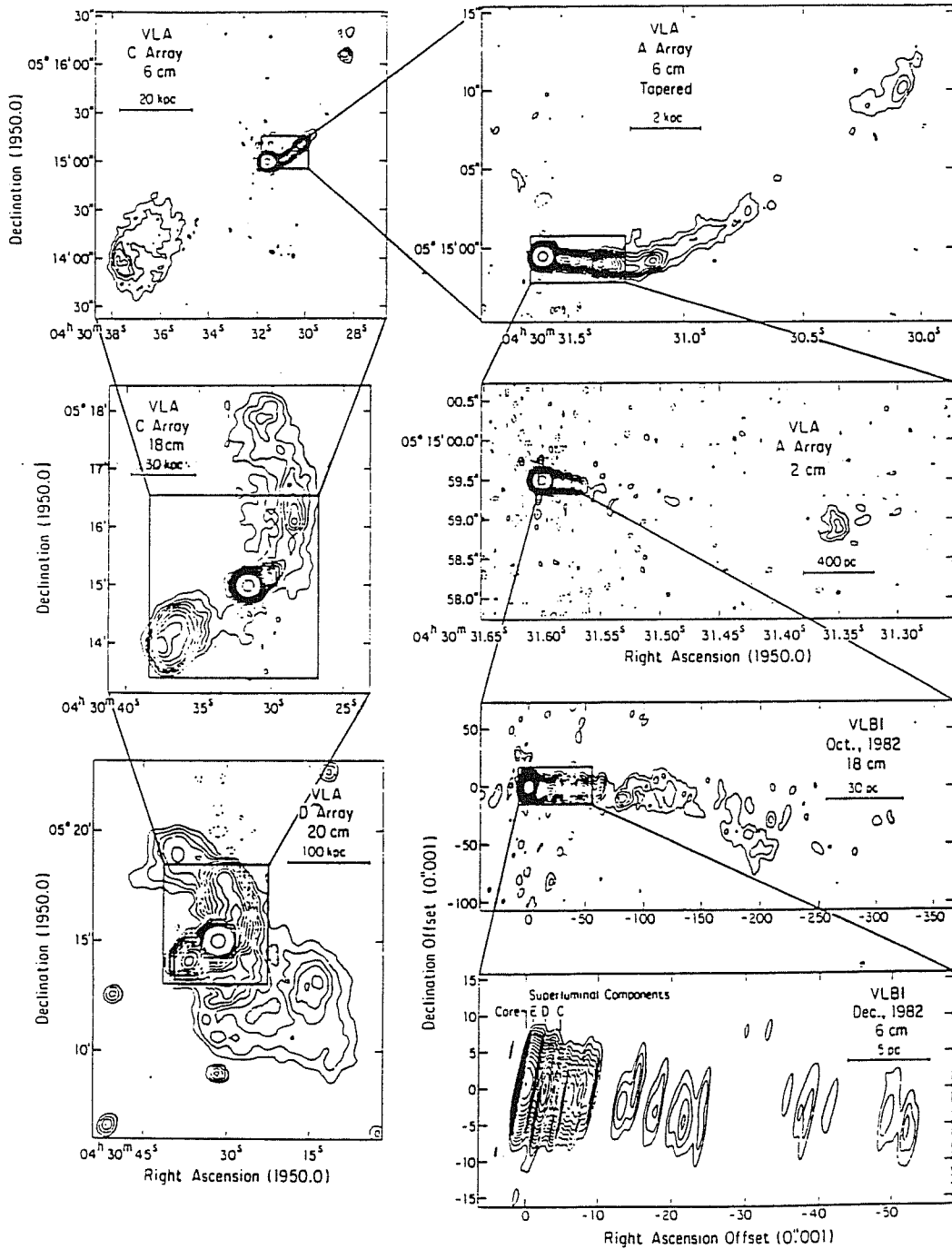


**Fig. 1.4.** The radio jet of 3C 120. The observations at different frequencies show the jet structure at different resolution, ranging between  $\sim$  pc to  $\sim$  100 kpc in linear size. (From Walker *et al.* 1987). At higher resolution the 'blobby' structure is evident. The jet presents a clear asymmetry and a strong bending between the small and the large scales.

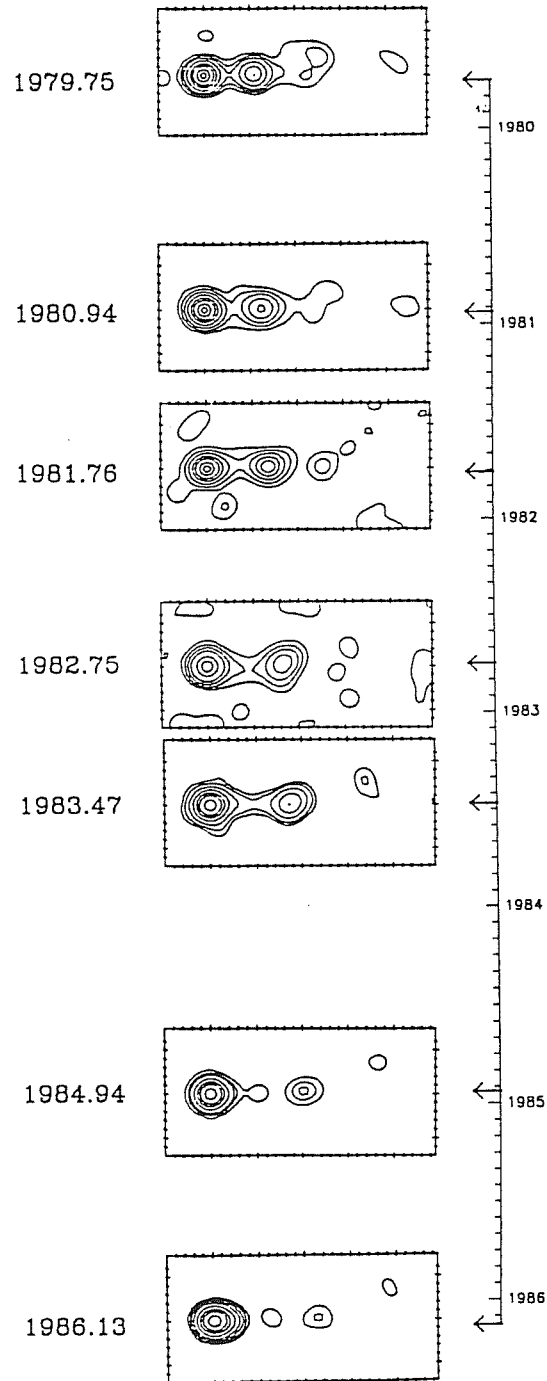


**Fig. 1.5.** Superluminal components of the source 3C 179. On the vertical scale the dates of the observations are reported. The left hand side component is assumed to be stationary, while other components appear to be subsequently ejected. The marks on the map axis correspond to 0.2 m.a.s. From Porcas (1987).

## Chapter 2. Non-thermal processes in compact sources

In this Chapter we briefly summarize the general constraints on radiative processes in compact sources. The main characteristic of the central emitting region is the high photon density, which implies that particle cooling is fast and copious pair production can occur.

Moreover there are strong indications that synchrotron and self-Compton radiation dominate the emission (at least on large scales, in the radio band). Therefore we describe in some details the standard synchrotron self-Compton theory, which is used in the following Chapters. The relativistic effects on the observed radiation, the evidence of which are presented in Chapter 4 and 5, are therefore examined.

For a description of the radiative processes see *e.g.* Tucker (1975), Rybicki & Lightman (1979), Svensson (1990) and references therein.

### 2.1 GENERAL CONSTRAINTS

#### 2.1.1 The compactness parameter

The general (and simplest) picture of the central region of AGN considers a spherical region with size  $R_0$  greater than  $\sim 3 R_s$ , where  $R_s$  is the Schwarzschild radius. It emits a total luminosity  $L$ , which is often compared to the Eddington limit  $L_E$ . Note that in a pure pair plasma this typical luminosity is a factor  $m_p/m_e$  smaller than that of an electron-proton plasma (Lightman, Zdziarski & Rees 1987).

The virial temperature is  $T_v \simeq 0.5(m_p c^2/k)(R_s/R)$  where  $R$  is the distance from the central core, which implies that electrons in virial equilibrium are relativistic at  $R \lesssim 1000 R_s$ .

The most important characteristic of AGN, concerning emission processes, is the high radiation density. This causes both electrons and photons to interact with the radiation field before escaping the source: high energy electron fast cool by inverse Compton scattering, while  $\gamma$ -ray photons, interacting with target photons can generate

electron–positron pairs. The photon density is roughly proportional to  $L/R_0^2$ , then the optical depth for interaction is proportional to  $L/R_0$ .

An (dimensionless) compactness parameter can be defined as (Cavaliere & Morrison 1980; Guilbert, Fabian & Rees 1983)

$$\ell = \frac{L}{R_0} \frac{\sigma_T}{m_e c^3} = \frac{2\pi}{3} \frac{m_p}{m_e} \frac{L}{L_E} \frac{3R_s}{R_0} = 2.7 \times 10^{-29} \frac{L}{R_0} \quad (2.1)$$

The Eddington value (at  $R \sim 3R_s$ ) corresponds to  $\ell \sim 3600$ , while for a pair dominated plasma the limit reduces to  $\ell \simeq 2$ : for higher  $\ell$  matter outflow is plausible.

In particular the value of  $\ell$  determines the cooling timescale for inverse Compton scattering of relativistic electrons,  $t_{IC} \simeq (R_0/c)(1/\gamma\ell)$ , where  $\gamma$  is the Lorentz factor of the electron. For all values  $\ell \gtrsim 1$  a particle releases its energy before escaping the source. Because of such short cooling timescale ( $t_{IC} \sim 10^{-4}R_0/c$  for typical values of  $\ell$  and  $\gamma$ ) it does not seem easy to interpret spectral breaks in compact sources as due to radiative losses.

In steady sources the high energy particles must be continuously heated or reaccelerated (on similar short timescales) in order that cooled electrons do not accumulate (Cavaliere & Morrison 1980; Done, Ghisellini & Fabian 1990). Among other suggestions (*e.g.* shock acceleration) there is the possibility (*e.g.* Biermann & Strittmatter 1985; Zdziarski 1991a) that ultrarelativistic electrons and positrons are produced as result of proton–photon or proton–proton interactions. Fast variability could pose problems for this hypothesis. In fact the proton–proton cross section is  $40\text{mbarn} \sim \sigma_T/20$  and therefore high proton densities are required (corresponding to  $\tau_T \sim 20$ ). If the particles density is lower (*e.g.* if protons are confined by a magnetic field) the typical collision timescales are  $\sim 20R_0/c$  for  $\tau_T \sim 1$ .

### 2.1.2 Pair production

The compactness also determines the optical depth  $\tau_{\gamma\gamma}$  for photon–photon interactions. If  $\gamma$ -rays are produced in the source they can create electron–positron pairs by interacting with low energy photons. The pair production threshold between two photons is given by  $x_1 x_2 > 2/(1 - \cos\theta)$ , where  $\theta$  is the interaction angle and  $x \equiv h\nu/m_e c^2$  is the photon energies.

On the other hand the pair production cross section peaks around  $x_1 x_2 \simeq 2$ , where it is about  $0.2\sigma_T$ , and decreases  $\propto x^{-1}$  (so that *e.g.* 100 MeV  $\gamma$ -rays react mainly with 5

keV photons). Therefore approximately

$$\tau_{\gamma\gamma}(x_1) = \eta(\alpha)\sigma_T R \frac{1}{x_1} n\left(\frac{1}{x_1}\right) \simeq \frac{\sigma_T}{5} R \frac{1}{x_1} n\left(\frac{1}{x_1}\right) \simeq \frac{9}{16\pi} \frac{0.2\sigma_T}{m_e c^3} \frac{L(1/x_1)}{R} \simeq \frac{\ell(1/x_1)}{30 x_1^{\alpha_x}} \quad (2.2)$$

where the photon density has been estimated as  $n(x) = L(x)/(4/3\pi R_0^3)(t_{esc}/x m_e c^2)$ , with the escape timescale  $t_{esc} \simeq 3R_0/4c$  for a spherical optically thin source, and  $\alpha_x$  is the spectral index of the target photons (Svensson 1984). We consider only pair production through photon–photon interactions, because the reaction rate is lower by one or two powers of the fine structure constant, with respect to photon–particle and particle–particle interactions.

In the case of a power-law spectrum with  $\alpha_x < 1$  (*i.e.* for  $\tau_{\gamma\gamma}$  increasing with energy), for  $\ell(1) \gtrsim 30$  the source is opaque to pair production at all  $\gamma$ -ray energies. The pairs produced cool and can modify substantially the primary spectrum, if they exceed the number of injected particles. Therefore the particle density and the emitted spectrum must be calculated self-consistently (see *e.g.* Svensson 1987; Ghisellini 1989; Svensson 1990 and references therein).

‘Standard’ pair production models (*e.g.* Fabian *et al.* 1986; Svensson 1987; Lightman & Zdziarski 1987; Zdziarski 1991b) assume the continuous injection of non-thermal relativistic particles and soft UV photons (‘blue bump’). Compton scattering of the UV photons produces  $\gamma$ -rays, which interact with X-ray photons and generate pairs, which contribute to the total emission, possibly also  $\gamma$ -rays. A pair cascade develops. At each generation the maximum photon energy emitted decreases, until no more pairs can be created (after few generations for typical parameters, Svensson 1987). The spectrum therefore tends to steepen, because of the depletion of  $\gamma$ -ray photons and the emission of radiation at lower energies due to the new pairs, and presents typically a maximum at high X-ray energies.

The cooled particles reach the Compton equilibrium temperature with the radiation field, comptonizing the spectrum, and eventually annihilate.

The assumption of a *stationary* source allows the computation of the equilibrium  $e^\pm$  pair density through the pair balance equation: pair production must equal pair annihilation and escape. In a steady, hot, thermal plasma, the pair yield  $\xi$ , defined as the fraction of the injected luminosity which is converted into pair rest mass, is always small ( $\xi < 10^{-3}$ ), and this results in low values of the predicted  $e^\pm$  pair optical depth  $\tau_{e^\pm}$  ( $\tau_{e^\pm} < 1$ ). Indeed the  $e^\pm$  pairs created in thermal models are assumed to have the same temperature as the particles responsible for the high energy emission. For high (transrelativistic) temperatures, the annihilation rate is small, and thus can balance pair production only for low production rates. For lower temperatures, on the other hand, the pair production rate is small, and hence the density of pairs remains relatively low.



In non-thermal plasmas, the  $e^\pm$  pairs (created through photon–photon collisions) join a thermal distribution at the Compton temperature, which is generally subrelativistic. (In fact the ‘Comptonization parameter’ increases for relativistic pairs as  $\tau_{e^\pm}^2 \gamma^2$ ).

The annihilation rate for cold pairs is given (assuming a pure pair plasma source) by

$$\dot{n}_+ = \frac{3}{8} \sigma_T c n_+^2 \quad (2.3)$$

where  $n_+$  is the positron density. (It is independent on temperature, being the decrease in the particles speed compensated by the increase in cross section as the particles cool). If radiative cooling is efficient annihilation of relativistic pairs is negligible.

Annihilation can balance a much higher  $e^\pm$  pair production rate than for a thermal plasma. Consequently, up to 10 per cent of the luminosity can be converted into pair rest mass. Guilbert, Fabian & Rees (1983) and Svensson (1987) have shown that  $\tau_{e^\pm}$  within a non-thermal source is given by

$$\tau_{e^\pm} \simeq \left( \frac{4}{\pi} \xi \ell \right)^{1/2} \quad (2.4a)$$

and independent of possible pair escape, as long as  $\tau_{e^\pm} > 1$ . The pair yield  $\xi$  is a linear function of  $\ell$  for  $\ell < 30$ , and saturates to a value  $\sim 0.1$  for higher  $\ell$  (Svensson 1987; Done, Ghisellini & Fabian 1990). Re-expressing in terms of the Eddington luminosity and the Schwarzschild radius, for  $\ell > 30$  (or equivalently, for  $L/L_E \gtrsim 0.01$ ) the  $e^\pm$  pair optical depth becomes:

$$\tau_{e^\pm} \sim 20 \left( \frac{L}{L_E} \frac{3R_s}{R_0} \right)^{1/2}, \quad (2.4b)$$

justifying a reference value  $\tau_{e^\pm} \sim 10$  (§5.4.2).

The thermalized pairs can Comptonize the soft blue bump photons, possibly producing the steep EUV–soft X-ray spectrum (Zdziarski & Coppi 1991). The cold pairs also downscatter hard X-rays and the line photons and therefore a break is expected at energies  $\sim m_e c^2 / \tau_T^2$ , with a spectral index change of  $\Delta\alpha \simeq 0.5$  (Svensson 1987) in highly compact sources. At energies above  $m_e c^2$  the spectrum flattens due to the reduction in the scattering cross section.

Note that the emitted annihilation line is downscattered and thermal broadened if pairs are not completely cooled and can result not detectable. It could be a more prominent feature if produced in a thin shell configuration.

From observations, a minimum compactness can be estimated deriving the source dimension from X-ray variability timescales. Done & Fabian (1989) compute the compactness of a sample of AGN (extrapolating the X-ray luminosities to 2 MeV). In Fig. 2.1 the distribution of their values of  $\ell$  is reported: for a large fraction of sources pair production plays an important role.

On the contrary if beaming effects are present (§2.2.3) the compactness is overestimated by a factor  $\ell = \ell_{obs}/\delta^5$  (using again the size inferred from variability), where  $\delta$  is the Doppler factor and  $\ell_{obs}$  the ‘observed’ compactness. Therefore the limit on pair production can be avoided if the source emission is anisotropic or beamed toward the observer. In fact the observation of strong and rapidly variable  $\gamma$ -ray emission in blazars can be a strong indication of relativistic beaming (§4.2). Also the observations in these sources of strong optical variability, polarization and high compactness suggest beaming effects or lack of high energy emission (*e.g.* a steep X-ray spectrum), because a high pair density would smear fast variability due to increased photon diffusion.

Until recently, the ‘standard’ pair model did not fit the typical spectrum observed, because in order to produce an X-ray spectral index  $\alpha \sim 0.7$  a compactness  $\ell \sim 30$  is required, which however predicts too many  $\gamma$ -rays photons to be consistent with the  $\gamma$ -ray background (§1.1.1.d). For higher  $\ell$  less  $\gamma$ -rays are produced but the spectrum steepens to  $\alpha \simeq 1$  after few pair generations. As already mentioned the contribution of the reflected component in the X-ray spectra of radio-quiet AGN, implies a primary spectrum with a typical slope  $\alpha \simeq 0.9$ , as predicted by saturate pair cascades for a large range of value of compactness. In Fig. 2.2 the spectrum computed by Zdziarski *et al.* (1990) with the pair-reflection model is reported. Different variability behaviours of the soft and hard X-ray spectra can be also accounted by the model, as discussed in detail by Zdziarski & Coppi (1991).

Few sources have been observed in the hard X-ray band, and the absence of any spectral signature of downscattering (below 50 keV) set an upper limit of  $\sim 3$  on the pair optical depth (Done, Ghisellini & Fabian 1991). Recent observations of NGC 4151 by *Sigma* (Jourdain *et al.* 1990) showed a spectral break with  $\Delta\alpha \sim 1.5$  at  $\sim 50$  keV. The spectrum has been fitted with the pair model by Coppi & Zdziarski (1992), assuming a compactness  $\ell \sim 100$ . However so marked a steepening can be reproduced only by the combined effect of downscattering and the intrinsic curvature of the spectrum.

In order to avoid the accumulation of cold matter (‘dead electron’ problem) a very efficient accelerator could operate. Done, Ghisellini & Fabian (1991) analyzed the possibility of a ‘reaccelerator’, in the frame of pair model, but the decrease in the predicted optical depth for a given compactness is not sufficient to solve the problem. The mechanism would continuously accelerate the cooled particles with a total fixed luminosity. For increasing number of produced pairs the mean particle energy must therefore decrease, in turn reducing the pair production rate (Cavaliere 1982). A typical maximum Lorentz factor for the reaccelerated particles produced by this feedback mechanism corresponds to  $\sim$  MeV energies.

### 2.1.3 Variability limits

Measures of persistent variability ( $\Delta L/\Delta t \propto \ell$ ) constraint radiative mechanisms (*e.g.* Fabian 1992).

Here the light crossing time is  $\Delta t \gtrsim 3R_0(1 + \tau_T)/4c$  for a spherical source, where the term  $(1 + \tau_T)$  accounts for the effects of diffusion.

- We can express the Eddington limit in term of variability limit, assuming a ‘minimum’ size  $R_0 = 3R_s$ , as a

$$L \lesssim \frac{8\pi}{9} \frac{m_p c^3}{\sigma_T} c \Delta t \sim 5 \times 10^{42} \Delta t \quad \text{erg s}^{-1} \quad (2.6)$$

- A limit on the compactness is derived from the efficiency limit (Fabian 1979). If the luminosity is stored in the form of matter (and not as magnetic or rotational energy), the electron are not reaccelerated and the process coupling the radiating electrons and the source of energy is rapid (electron-ion coupling in a thermal plasma requires  $kT_e \lesssim 35$  keV, Guilbert, Fabian & Stepney 1982), then the maximum rate of change in luminosity is obtained when all the rest mass energy is converted in the light escape timescale, *i.e.*  $\Delta L \Delta t = \eta M c^2$ , where  $\eta$  is the radiative efficiency.

The limit on  $\Delta L/\Delta t$  derives from the increase of both the diffusion timescale, due to the trapping of radiation, and the luminosity with increasing matter (Fabian 1979)

$$\Delta L \lesssim \frac{16\pi}{27} \eta \frac{m_p c^3}{\sigma_T} c \Delta t \simeq 4 \times 10^{41} \eta_{-1} \Delta t \quad \text{erg s}^{-1} \quad (2.7)$$

where the inequality maximizes  $\Delta L/\Delta t$  (for  $\tau_T \simeq 1$ ). In terms of the compactness parameter  $\ell \lesssim 250\eta_{-1}$ .

As already shown in Guilbert, Fabian & Rees (1983) this limit is increased by the factor  $\delta^5$  in case of relativistic motion, the effect of which is equivalent to have an efficiency  $\eta \gg 1$ .

- The pair production condition  $\ell \gtrsim 30$  [eq. (2.2)] can be expressed as a variability limit as

$$L \gtrsim 40 \frac{m_e c^3}{\sigma_T} c \Delta t \simeq 4 \times 10^{40} \Delta t \quad \text{erg s}^{-1} \quad (2.8)$$

- Fast variability constrains the X-ray emission mechanism. A maximum luminosity can be emitted by bremsstrahlung without Compton scattering on the radiation field starts

to dominate the particles cooling (Lightman *et al.* 1978). The bremsstrahlung cooling is more effective than the Compton cooling only if

$$L \lesssim 10^{39} T_9^{-3/2} \Delta t \quad \text{erg s}^{-1} \quad (2.9)$$

This inequality is not satisfied by many rapid varying AGN and we neglect in the following the possibility that bremsstrahlung radiation is responsible of X-ray emission.

Note that these limits assume a steady situation and they can be weaker in non-spherical geometries (*e.g.* sheet-like) which require a special observing direction (Guilbert, Fabian & Rees 1983).

In Fig. 2.3 (after Fabian 1992) we report the above limits, the X-ray data relative to the sample considered by Done & Fabian (1989) and data from Bregman (1990) and references therein, in a plot  $\Delta t$  versus  $L$ . In general, as already mentioned, variations with  $\Delta L/\Delta t$  exceeding the efficiency and Eddington limits [eqs. (2.5) and (2.6)] can be considered an indication of relativistic beaming (§1.1.3.b).

## 2.2 SSC RADIATION MECHANISM

As already mentioned (§1.1.2.a) at least in blazars the high polarization and the power-law spectrum suggest that radiation is synchrotron emission from a non-thermal distribution of relativistic electrons. If the source is compact the same electrons efficiently cool by inverse Compton on the synchrotron photons that they emit, producing high energy emission (Synchrotron self-Compton process, SSC).

### 2.2.1 Synchrotron and self-Compton emission

The standard model (Ginzburg & Syrovatskii 1965; Rees 1967; Jones O'Dell & Stein 1974a,b) considers an homogeneous spherical region, with a uniform and randomly oriented magnetic field  $B$  and a stationary isotropic electron distribution. Averaging over the pitch angles of the emitting electrons and the angles of incident photons and neglecting the effects of losses on the electron motion, the radiation energy losses of an ultrarelativistic electron of energy  $\gamma m_e c^2$ , due to synchrotron and inverse Compton are respectively

$$\dot{\gamma}_s = \frac{4}{3} \frac{\sigma_T c}{m_e c^2} U_B \gamma^2 \quad \text{and} \quad \dot{\gamma}_C = \frac{4}{3} \frac{\sigma_T c}{m_e c^2} U_r \gamma^2 \quad (2.11a)$$

Therefore, considering only first order scatterings in the Thomson regime, the ratio

$$\frac{\dot{\gamma}_s}{\dot{\gamma}_{1C}} = \frac{U_B}{U_{r,s}} = \frac{L_s}{L_{1C}} \quad (2.11b)$$

measures the relative importance of the two processes.  $U_B$  and  $U_r$  are the magnetic and radiation energy densities. For SSC emission the radiation energy density  $U_r$  is given approximately by the synchrotron radiation which scatters in the Thomson limit,  $U_{r,s} \equiv g(\nu)U_r$ , (*i.e.* photons with energy such that  $\gamma h\nu \lesssim m_e c^2$ ). This allow to use a constant Thomson cross section and neglect momentum transfer. For higher photon energies the exact Klein–Nishina cross section must be used. This reduces the power radiated at higher frequencies, and in turn implies a limit on the high energy radiation which can be emitted through multiple Compton scattering, solving the ‘Compton catastrophe’ problem. In Fig. 2.4 the the Klein–Nishina cross section is shown as a function of frequency, together with a step function approximation which is adopted in some of the following calculations.

The synchrotron power radiated by an ultrarelativistic electron can be approximated by a continuum spectrum:

$$P(\gamma, \nu) = \sqrt{3} \frac{e^3 \langle \sin \alpha \rangle}{m_e c^2} B \frac{\nu}{\nu_c} \int_{\nu/\nu_c}^{\infty} K_{5/3} \left( \frac{\nu}{\nu_c} \right) d \left( \frac{\nu}{\nu_c} \right) \sim \left( \frac{\nu}{\nu_c} \right)^{1/3} e^{-\nu/\nu_c} \quad (2.12)$$

with

$$\nu_c = \frac{3}{2} \sin \alpha \nu_B \gamma^2 \quad \text{Hz} \quad (2.13)$$

where  $\nu_B \equiv (eB/2\pi m_e c) \simeq 1.22 \times 10^6 B$  Hz is the cyclotron frequency,  $K_{5/3}$  the modified Bessel function of order 5/3 and  $\alpha$  the pitch angle.

Eq. (2.12) shows that the single electron emission peaks at  $\nu \simeq 0.29 \nu_c$ . The synchrotron emissivity  $j_s(\nu)$  [erg cm<sup>-2</sup> s<sup>-1</sup> Hz<sup>-1</sup> sr<sup>-1</sup>] from a fixed electron differential distribution of the form

$$N(\gamma) d\gamma = K \gamma^{-p} d\gamma \quad \text{for} \quad \gamma_{min} < \gamma < \gamma_{max} \quad (2.14)$$

(with  $p > 0$ ) and averaged for a random distribution of pitch angles is given by (Blumenthal & Gould 1970)

$$j_s(\nu) = \frac{1}{4\pi} \int N(\gamma) P(\gamma, \nu) d\gamma = c(\alpha) K B^{1+\alpha} \nu^{-\alpha} \quad (2.15)$$

where  $\alpha = (p - 1)/2$  and

$$c(\alpha) = \frac{\sqrt{\pi} e^2}{4c} \left( \frac{e}{2\pi m c} \right)^{1+\alpha} 3^{p/2} a(p)$$

$$a(p) = \frac{\Gamma((p+5)/4) \Gamma((3p-1)/12) \Gamma((3p+19)/12)}{(p+1) \Gamma((p+7)/4)}, \quad (2.15a)$$

$c(\alpha)$  is tabulated in Table 2.1 for some values of  $\alpha$ .

$j_s(\nu)$  can be also obtained with good approximation assuming  $P(\gamma, \nu) = P(\gamma)\delta(\nu - 0.29\nu_c)$  and integrating over the particles spectrum.

Note that the pressure and energy density of the relativistic electron distribution eq. (2.13) are dominated by the upper cut-off energy  $\gamma_{max}$  for  $p < 2$ . The synchrotron emissivity instead is dominated by the upper limit for  $p < 3$  and the number density depends on  $\gamma_{min}$ . The strong dependences can lead to significant errors in the determination of these quantities from observations (§5.4).

Eq. (2.15) is valid in the range  $3/2 \nu_B \gamma_{min}^2 \lesssim \nu \lesssim 3/2 \nu_B \gamma_{max}^2$ . At the extremes of the spectrum  $j_s(\nu)$  follows the behaviour of the single electron emission.

Low energy radiation can be reabsorbed. For the electron distribution (2.13) and  $\nu \gg (4/3)\nu_B \gamma_{min}^2$ , the absorption coefficient  $\kappa(\nu)$  [ $\text{cm}^{-1}$ ] is

$$\kappa(\nu) = \frac{3^{\alpha+1}\sqrt{\pi}}{8} g(p) \frac{e^2 K}{m_e c} \nu_B^{(3/2+\alpha)} \nu^{-(5/2+\alpha)} \quad (2.16)$$

where

$$g(p) = \frac{\Gamma((3p+22)/12) \Gamma((3p+2)/12) \Gamma((p+6)/4)}{\Gamma((p+8)/4)}. \quad (2.16a)$$

is tabulated in Table 2.1 for some values of  $\alpha$ .

Defining the self-absorption frequency  $\nu_t$  as the frequency of unit optical depth  $\tau_s = \kappa(\nu)R = 1$ , the Lorentz factor,  $\gamma_t$ , of the electrons emitting mainly at  $\nu_t$  is given by (see *e.g.* Ghisellini 1989b)

$$\gamma_t = \left[ \frac{9\pi\sqrt{3\pi}}{64} \left(\frac{3}{2}\right)^p g(p) \frac{eKR_0}{B} \right]^{1/(p+4)} \quad (2.17)$$

and  $\nu_t = (4/3)\nu_B \gamma_t^2$ . More precisely the low energy spectrum for a stationary electron distribution assumes a quasi-Maxwellian shape. This is suggested to be both an efficient thermalizing and heating mechanism (Ghisellini, Guilbert & Svensson 1988) (§5.4.1) and an acceleration mechanism for jets (Ghisellini *et al.* 1990) (§5.5). The effects of the absorbed radiation on the particle distribution are neglected in the following.

Typically  $\nu_t$  in compact sources is in the far IR band, implying that the observed radio luminosity cannot be emitted in the inner, compact region.

The inverse SSC emission can be approximately computed using the fact that the energy distribution of the scattered photons has as an average value  $\nu_C = (4/3)\nu_s \gamma^2$  where

$\nu_s$  is the frequency of the synchrotron photon. The first order Compton emissivity is obtained by integrating over the incident photon and electron distributions given by (2.13)

$$j_{1C}(\nu) = \frac{(4/3)^\alpha}{8\pi} \frac{m_e c^2 \tau_r}{R_0/c} \nu^{-\alpha} \int_{\nu_{min}}^{\nu_{max}} n(\nu') \nu'^\alpha d\nu' \quad (2.18)$$

for  $(4/3) \nu_{min} \gamma_{min}^2 \lesssim \nu \lesssim (4/3) \nu_{max} \gamma_{max}^2$ .  $\tau_r \equiv \sigma_T K R_0$  is the Thomson optical depth in relativistic electrons.

The extremes of integration depend on the photons and electrons distributions and in the spectral region where they do not depend on  $\nu$ , the Compton spectrum has the same frequency dependence as the synchrotron spectrum.

The self-Compton radiation is therefore the product of  $j_s$  with the scattering probability  $\tau_r$  and for  $\tau_r \ll 1$  the thin synchrotron emission or its extrapolation is a factor  $(4/3)^{\alpha-1} \tau_r \log \Lambda / 2$  above  $j_{1C}$  (at the same frequency). Similarly for higher Compton orders [see eq. (2.25)].  $\Lambda$  is approximately given, not at the extreme of the spectrum, by  $\simeq (\gamma_{max}/\gamma_{min})^2$  [see eqs. (2.29a)–(2.29c)].

We now explicitly report the expressions (which are used in §3.1) for the synchrotron, first and second order Compton monochromatic intensities  $I(\nu)$  [erg cm<sup>-2</sup> s<sup>-1</sup> Hz<sup>-1</sup> sr<sup>-1</sup>] in different frequency ranges. The observed flux is then estimated as  $F(\nu) = \pi (R_0/d_L)^2 I(\nu)$ .

The equation of energy transfer, in a slab geometry, reduces to

$$I(\nu) = \frac{j(\nu)}{\kappa(\nu)} (1 - e^{-\tau_s}) = j(\nu) \frac{1 - e^{-\tau_s}}{\tau_s} \quad (2.19)$$

We indicate with ‘thin’ and ‘thick’ the transparent or self-absorbed regime. In the case of Compton emission ‘thick’ refers to the fact that the scattered radiation energy density is calculated from self-absorbed synchrotron emission. It is assumed  $\gamma_{min} = 1$ .

For fixed  $R_0$ ,  $K$ ,  $B$ ,  $\gamma_{max}$  different emitting regime dominate in different frequency ranges. For  $\nu < \nu_t$

$$I_{s,thick}(\nu) = \frac{2m_e f(p)}{\sqrt{3}} \frac{\nu^{5/2}}{\nu_B^{1/2}}. \quad (2.20)$$

where  $f(p) = a(p)/g(p)$  is tabulated in Table 2.1 for some values of  $\alpha$ .

If  $\gamma_{max} < \gamma_t$  and for  $\nu_{s,max} < \nu < \nu_{1C,max}$ , the inverse Compton fluxes are calculated from the synchrotron self-absorbed photon density and are given by

$$I_{1C,thick}(\nu) = \frac{2m_e f(p)}{\sqrt{3}} \left[ \frac{\tau_r (4/3)^{\alpha-1}}{2} \right] \nu^{-\alpha} \frac{\nu_{s,max}^{5/2+\alpha}}{5/2+\alpha} \frac{1}{\nu_B^{1/2}}. \quad (2.21)$$

If  $\gamma_{max} < \gamma_t$  and for  $\nu_{1C,max} < \nu < \nu_{2C,max}$  we have

$$I_{2C,thick}(\nu) = \left[ \frac{\tau_r (4/3)^{\alpha-1}}{2} \right] I_{1C,thick}(\nu) \ln \Lambda_{2,thick}. \quad (2.22)$$

If  $\gamma_{max} > \gamma_t$  thin synchrotron emission is possible between  $\nu_t < \nu < \nu_{s,max}$ , with an intensity given by

$$I_{s,thin}(\nu) = c(\alpha) R_0 K B^{1+\alpha} \nu^{-\alpha}. \quad (2.23)$$

For  $\nu_t < \nu_{s,max} < \nu < \nu_{1C,max}$ ,

$$I_{1C,thin}(\nu) = \left[ \frac{\tau_r (4/3)^{\alpha-1}}{2} \right] I_{s,thin}(\nu) \ln \Lambda_{1,thin}. \quad (2.24)$$

If  $\gamma_t < \gamma_{max}$  and for  $\nu_{1C,max} < \nu < \nu_{2C,max}$ ,

$$I_{2C,thin}(\nu) = \left[ \frac{\tau_r (4/3)^{\alpha-1}}{2} \right] I_{1C,thin}(\nu) \ln \Lambda_{2,thin}. \quad (2.25)$$

The maximum frequency emitted by synchrotron radiation is  $\nu_{s,max} = (4/3) \nu_B \gamma_{max}^2$ . To calculate the  $\Lambda$  terms in the Compton expressions we use a step approximation to the exact Klein–Nishina cross section (Fabian *et al.* 1986; Lightman & Zdziarski 1987) (Fig. 2.4), setting the scattering cross-section equal to zero for

$$\gamma\nu/\nu_{KN} > 3/4, \quad (2.26)$$

where

$$\nu_{KN} \equiv m_e c^2 / h = 1.236 \times 10^{20} \text{ Hz}. \quad (2.26a)$$

With this approximation the maximum frequency of the first ( $\nu_{1C,max}$ ) and second order ( $\nu_{2C,max}$ ) Compton spectra are

$$\nu_{1C,max} = \min \left[ \frac{4}{3} \gamma_{max}^2 \nu_{s,max}; \frac{3}{4} \nu_{KN} \gamma_{max} \right], \quad (2.27)$$

$$\nu_{2C,max} = \min \left[ \frac{4}{3} \gamma_{max}^2 \nu_{1C,max}; \frac{3}{4} \nu_{KN} \gamma_{max} \right]. \quad (2.28)$$

The  $\Lambda$  terms are, at a given (scattered) frequency  $\nu$ ,

$$\Lambda_{1,thin} = \frac{\min [\nu_{s,max}; 3\nu_{KN}/4; 3\nu_{KN}^2/(4\nu)]}{\max [\nu_t; 3\nu/(4\gamma_{max}^2)]}, \quad (2.29a)$$

$$\Lambda_{2,thin} = \frac{\min [\nu_{1C,max}; 3\nu_{KN}/4; 3\nu_{KN}^2/(4\nu)]}{\max [\nu_t; 3\nu/(4\gamma_{max}^2)]}, \quad (2.29b)$$

$$\Lambda_{2,thick} = \frac{\min [\nu_{1C,max}; 3\nu_{KN}/4; 3\nu_{KN}^2/(4\nu)]}{\max [\nu_{s,max}; 3\nu/(4\gamma_{max}^2)]}. \quad (2.29c)$$



Neglecting the spectral curvature of the first-order spectrum produced by the logarithmic term when calculating the second-order Compton from thin synchrotron, we use

$$\ln \Lambda_{1,thin} \ln \Lambda_{2,thin} = 2 \ln(\gamma_{max}/\gamma_t) \ln \Lambda_{2,thin} \quad (2.29d)$$

with  $\Lambda_{2,thin}$  given as above.

**Table 2.1. SSC constants**

$\alpha$	$p$	$b(\alpha)$	$c(\alpha)$	$d(\alpha)$	$f(p)$	$g(p)$	$t(\alpha)$
0.25	1.5	1.8	$9.11 \cdot 10^{-22}$	0.16	0.72	1.42	1.33
0.5	2	3.2	$2.85 \cdot 10^{-20}$	0.18	0.49	1.21	0.56
0.75	2.5	3.6	$1.04 \cdot 10^{-18}$	0.2	0.37	1.10	0.29
1	3	3.8	$4.20 \cdot 10^{-17}$	0.22	0.29	1.05	0.16

### 2.2.2 Energy density estimates

Given a non-thermal distribution of relativistic electrons we describe a qualitative but simple way to estimate, in term of radiation and magnetic energy densities, the relative emission in the X-ray band due to SSC and Comptonization of blue bump photons.

A simple estimate of the synchrotron ( $U_s$ ) and first-order self-Compton ( $U_{1C}$ ) radiation energy densities is given by

$$U_{s(1C)} \simeq \frac{3R}{4c} \int N(\gamma) \dot{\gamma}_{s(1C)} m_e c^2 d\gamma \quad (2.30)$$

Let us define

$$y \equiv \tau_r \langle \gamma^2 \rangle \quad \text{with} \quad \langle \gamma^2 \rangle = \frac{\int N(\gamma) \gamma^2 d\gamma}{\int N(\gamma) d\gamma} \quad (2.31)$$

and  $\sigma_T R \int N(\gamma) d\gamma \sim \tau_r$ . Note that  $\langle \gamma^2 \rangle = \gamma_{max}^2$  if  $p = 2$  (corresponding to  $\alpha = 0.5$ ) and the minimum Lorentz factor of the electron distribution is  $\sim 1$ . With the above definitions and in the Thomson regime we have

$$U_s = y U_B \quad \text{and} \quad U_{1C} = y U_s. \quad (2.32)$$

The X-ray energy density  $U_x$  from the upscattering of soft ‘blue bump’ photons with energy density  $q U_{bump}$  is given by

$$U_x = q y U_{bump}. \quad (2.33)$$

$q \leq 1$  is a dilution factor, smaller than unity if the soft photons are produced in a region different to, or larger than, the X-ray one.

Let us now consider the case in which X-ray emission is mainly produced as Comptonization of soft photons (as assumed in §3.1 to determine upper limits on the intensity of  $B$ ). Therefore we require that the contribution from SSC emission to the X-ray flux to be negligible compared to the first-order Compton scattered ‘blue bump’ radiation.

Consider the X-ray flux up to a given frequency  $\nu_x$ . Synchrotron radiation contributes at  $\nu_x$  if  $\nu_{s,max} > \nu_x$ . In this case, the synchrotron emission does not exceed the observed X-ray flux if  $U_s < U_x$ , or, equivalently, if  $U_B < qU_{bump}$ . For frequencies  $\nu_{s,max} < \nu_x < \nu_{1C,max}$  the first-order Compton scattering contributes to the X-ray flux. In this case SSC radiation does not overproduce X-rays if  $U_s < qU_{bump}$ . If  $\nu_{1C,max} < \nu_x$ , it is the second-order Compton scattering that contributes in X-rays, and we require  $U_{1C} < qU_{bump}$ . These inequalities can be written, using eqs. (2.32) and (2.33), as

$$\begin{aligned} \frac{U_B}{U_{bump}} < q & \quad \text{or} \quad \frac{U_B}{U_x} < \frac{1}{y}, & \nu_x < \nu_{s,max} \\ \frac{U_B}{U_{bump}} < \frac{q}{y} & \quad \text{or} \quad \frac{U_B}{U_x} < \frac{1}{y^2}, & \nu_{s,max} < \nu_x < \nu_{1C,max} \\ \frac{U_B}{U_{bump}} < \frac{q}{y^2} & \quad \text{or} \quad \frac{U_B}{U_x} < \frac{1}{y^3}, & \nu_x > \nu_{1C,max} \end{aligned} \quad (2.34)$$

where the second relations give a direct comparison of  $U_B$  with the X-ray energy density.

A second limit can be imposed by requiring that the computed SSC flux does not exceed the observed one at a frequency  $\nu$ . For example, consider the limit imposed by synchrotron and the first-order Compton spectrum. The requirements  $U_s < U_{obs}$  and  $U_{1C} < U_{obs}$ , using again relations (2.32) and (2.33), imply

$$\frac{U_B}{U_x} < \frac{U_{obs}}{qy^2U_{bump}}, \quad \nu < \nu_{s,max} \quad (2.35a)$$

$$\frac{U_B}{U_x} < \frac{U_{obs}}{qy^3U_{bump}}, \quad \nu_{s,max} < \nu < \nu_{1C,max} \quad (2.35b)$$

### 2.2.3 Beaming

The discovery in radio sources of rapid variability (3C273, Dent 1965), and later the measures of VLBI dimensions imply a high radiation density and consequently, in the assumption that radio flux is produced as synchrotron in a spherical homogeneous source,

an inverse Compton flux at high frequencies exceeding the observed one. The hypothesis that the emitting plasma is moving at relativistic velocities (Rees 1966) predicts that the observed luminosities are overestimated and the dimensions (from variability measures) underestimated, solving the Compton problem for appropriate values of the Doppler factor. Nowadays several observations (§5.3) argue in favour of the presence of relativistic beaming effects in blazars.

The beaming toward the observer produces an increase in the observed flux, due to aberration, the shift in the observed frequency and the contraction in the observed timescales. All these effects can be quantified by the Doppler factor, defined as (see Fig. 2.5)

$$\delta = \frac{1}{\Gamma(1 - \beta_b \cos \theta)} \quad (2.36)$$

where  $\beta_b c$  and  $\Gamma$  are the bulk velocity of the plasma and the corresponding Lorentz factor and  $\theta$  the angle between the velocity vector and the line of sight. Therefore

$$\frac{1}{\Gamma} = \delta(90^\circ) \leq \delta \leq \delta(0^\circ) = \Gamma(1 + \beta_b) \rightarrow 2\Gamma \quad \Gamma \gg 1 \quad (2.36a)$$

$\delta > 1$  for  $\theta < \arcsin[2/(1 + \Gamma)]^{1/2}$ . Given a value of  $\delta$ , a lower limit on the Lorentz factor is given by the condition  $\delta \leq \delta_{max}$ , that is

$$\Gamma \geq \Gamma_{min}(\delta) = \frac{1}{2} \left( \delta + \frac{1}{\delta} \right) \quad (2.36b)$$

When  $\delta$  is a lower limit (§5.3.1) this expression is valid only for  $\delta > 1$ , since for  $\delta < 1$ ,  $\delta + 1/\delta$  decreases for increasing  $\delta$ . It can also be shown that for any value of  $\Gamma$

$$\sin \theta < \frac{1}{\delta} \quad (2.36c)$$

which gives a useful upper limit to  $\theta$  only if  $\delta > 1$ .

For a given monochromatic intensity in the source frame the corresponding intensity observed in the ‘lab’ frame is strongly amplified for small  $\theta$ . However, the degree of amplification is different if the source is a moving sphere or a continuous jet and if the source is optically thin or thick to the observed frequency (Lind & Blandford 1985; Phinney 1986).

We now examine the dependence of flux on  $\delta$  assuming that the reference frame comoving with the emitting plasma do not coincide with the frame of the observed emitting volume. Consider therefore a schematic situation with three reference frames: the frame comoving with the fluid, where emissivity is isotropic and can be easily computed (two apices), the frame of the emitting region (one apex) and the observer frame. The source is assumed homogeneous.

Let be  $j''(\nu'')$  and  $\kappa''(\nu'')$  the emissivity and the absorption coefficient in the fluid frame, which moves with constant velocity. If the emissivity depends on frequency as a power law  $j''(\nu'') \propto \nu''^{-\alpha}$

$$j'(\nu', \theta') = \delta'^2 j''(\nu'') = \delta'^{2+\alpha} j''(\nu') \quad (2.37)$$

and for synchrotron radiation

$$\kappa'(\nu', \theta') = \delta'^{-1} \kappa''(\nu'') = \delta'^{1.5+\alpha} \kappa''(\nu') \quad (2.38)$$

(Rybicki & Lightman 1979), where  $\delta'(\beta', \theta')$  is the Doppler factor of the moving fluid in the pattern frame and  $\nu'' = \nu'/\delta$ .

The optical depth strongly depends on the viewing angle

$$\tau_s(\nu, \theta) = \delta^{\alpha+2.5} \int_0^{R'_0} \delta'^{\alpha+1.5} \kappa''(\nu) dR' \quad (2.39)$$

Therefore in the optically thin case,  $\tau_s \ll 1$ , and using (2.37) the intensity is given by

$$I(\nu, \theta) = \delta^3 \int_0^{R'_0} j'(\nu', \theta') dR' = \delta^{3+\alpha} \int_0^{R'_0} \delta'^{2+\alpha} j''(\nu) dR' \quad (2.40)$$

while in the optically thick case,  $\tau_s \gg 1$ , the velocity dependence is weaker

$$I(\nu, \theta) = \delta^3 \frac{j(\nu', \theta')}{\kappa(\nu', \theta')} = \delta^{1/2} \delta'^{1/2} \frac{j''(\nu)}{\kappa''(\nu)} \quad (2.41)$$

The observed area projected orthogonally to the line of sight is invariant even if observed in a ‘rotated’ direction  $\theta'$ . There is no contraction of the observed area because it is compensated by the light travel time (Lind & Blandford 1985).

If there are only two rest frames the situation is simplified. In the case of a stationary jet, or different components which mimic a continuum, the emitting region and the observer frames coincide, and the exponent of the Doppler correction will be  $n = 2 + \alpha$ ; if instead the emission region coincides with the observed volume, the exponent will be  $n = 3 + \alpha$ , due to the volume transformation. In fact in the case of a rigidly moving sphere, a light ray travels, on average, a distance  $R_0$  inside the source, independently on the degree of aberration. Consider instead, for illustration, the plasma flowing in a cylindrical jet of radius  $R_0$ , whose walls are fixed in the observer frame, and whose axis makes an angle  $\theta$  with the line of sight. The path traveled by a light ray inside the cylinder has to be calculated in the comoving frame, and thus transforms  $\propto R_0/\sin \theta' = R_0/(\delta \sin \theta)$ , which reduces the dependence of the intensity on  $\delta$ . Furthermore the intensity integrated over a frequency band depends on  $\delta^n$  with  $n = 3, 4$  for the two cases, respectively.

In the particular case of a shock wave, three frames must be considered. The Doppler corrections reduce to the factor  $\delta^{2+\alpha}(\beta_2)\delta(\beta_s)$ , where  $c\beta_1, c\beta_2, c\beta_s$  are the pre, postshock and front velocities measured in the observer frame respectively, and for an ultrarelativistic fluid (*i.e.* adiabatic index of 4/3 for the upstream and downstream plasma)  $\beta_2 = (3\beta_s^2 - 2\beta_s\beta_1 - 1)/(\beta_1\beta_s^2 + 2\beta_s - 3\beta_1)$  (§4.1.4).

Hereafter primed quantities are measured in the frame comoving with the emitting plasma, unless otherwise indicated.

#### 2.2.4 Estimate of the source parameters

It is generally believed that the flat spectrum of the core of radio sources results from the superposition of different components, each with a different synchrotron self-absorption frequency  $\nu_m$ . The observed flux density at a given frequency is then dominated by the synchrotron-emitting component which becomes self-absorbed at that frequency, *i.e.*  $F(\nu_m) \equiv F_m$ .

In this case it is possible to infer the intensity of the magnetic field from the observed quantities  $\nu_m$ ,  $F(\nu_m)$  and  $\theta_d$  (angular diameter of the core) and set limits on the particle density and Doppler factor if the high energy flux (SSC) is measured.

In fact the synchrotron flux in the optically thick regime ( $\propto \theta_d^2 \nu^{5/2} B^{-1/2} \delta^{1/2}$ ) is independent of the particle density, and can therefore be used to derive the value of the magnetic field [from eq. (2.2.1)]

$$B = 10^{-5} b(\alpha) \theta_d^4 \nu_m^5 F_m^{-2} \frac{\delta}{(1+z)} \quad \text{G} \quad (2.42)$$

where  $\theta_d$  is in m.a.s.,  $F_m$  is in Jy,  $\nu_m$  in GHz, and  $z$  is the redshift. The dimensionless function  $b(\alpha)$  is given in Table 2.1.

Furthermore the synchrotron  $F_m$  and SSC  $F_x$  fluxes have the same functional dependence on  $B$  and  $\delta$ . Thus their ratio enables the particle density within the VLBI core to be derived *independently* of any effects due to relativistic beaming.

$$\tau_r = t(\alpha) \frac{F_x \nu_x^\alpha}{F_m \nu_m^\alpha} \frac{1}{\ln(\nu_b/\nu_m)} \quad (2.43)$$

where the function  $t(\alpha)$  is a dimensionless quantity given in Table 2.1 and  $\nu_b$  is the upper cut-off in the optically thin synchrotron spectrum (a value of  $\nu_b = 10^{14}$  Hz is assumed hereafter). In eq. (2.43), fluxes have the same units, as well as frequencies. Note that  $\tau_r$  does not depend on redshift, which is instead necessary to calculate the size  $R_0$ , and hence the particle density. The dimension must be deduced from VLBI measures. If estimated from variability timescale it must correspond to the frequency  $\nu_m$ .

The self Compton flux can be predicted knowing  $\theta_d$ ,  $F_m$  and  $\delta$ . By comparing the predicted and the observed self-Compton flux  $F_x$ , one can derive  $\delta$  in the case of a moving sphere. Substituting eqs. (2.42) and (2.43) into the expression for the optically thin SSC flux ( $\propto \theta_d^2 B^{1+\alpha} \tau_r \nu^{-\alpha} \delta^{3+\alpha}$ ), we can obtain the beaming factor  $\delta$

$$\delta = d(\alpha) F_m \left( \frac{\ln(\nu_b/\nu_m)}{F_x \theta_d^{6+4\alpha} \nu_x^\alpha \nu_m^{5+3\alpha}} \right)^{\frac{1}{2(2+\alpha)}} (1+z) \quad (2.44)$$

where  $F_x$  is in Jy,  $\nu_x$  is in keV and the function  $d(\alpha) \simeq 0.08\alpha + 0.14$  (Ghisellini 1987). Note that apart from the K-correction, the derived  $\delta$  is independent of distance. Note also the strong dependence on the observable quantities, especially  $\theta_d$ . For a detailed discussion on the observational aspect see Marscher (1987).

A few remarks are in order:

(i) Eqs. (2.43)–(2.44) can be applied to sources observed only in the *optical* band (rather than in the X-ray band) by substituting the relevant optical flux and frequency for  $\nu_x$  and  $F_x$ . We do this for those sources presented in §5.1 for which we lack X-ray data.

(ii) Eq. (2.43) actually provides the upper limit on  $\tau_r$  (and  $K$ ) such that the observed VLBI component of the radio core produces all the observed X-rays via the SSC process. Clearly if the VLBI component produced only a small fraction of the total observed X-ray emission, the particle density would be proportionally lower.

(iii) The smaller  $\tau_r$  the higher enhancement factor due to relativistic beaming is required in order to produce a given synchrotron flux.

If the source is a continuous jet, eq. (2.44) is not correct, because it assumes that the enhancement factor of the flux is  $\delta^{3+\alpha}$ . If  $n = 2 + \alpha$  we can derive the analog of eq. (2.44), by considering the following:

(i) The predicted SSC flux is  $F(\nu) \propto B^{1+\alpha} K^2 \delta^{2+\alpha}$  (where  $B$  and  $K$  are the values of the magnetic field and the electron density in the comoving frame).

(ii) Both the thin synchrotron and the self-Compton fluxes are proportional to  $\delta^n$ , and therefore their ratio is independent of which value of  $n$  is used. Consequently also the derived number density  $K$  of the emitting particles is independent on the enhancement factor.

(iii) The magnetic field  $B$  can be derived from the thick synchrotron flux (which does not depend on the source volume). Using eq. (2.20) we therefore arrive at the same formula for both the cases of a moving sphere and of a continuous jet, *i.e.*  $B \propto \delta$ .

(iv) The predicted self Compton flux is therefore proportional to  $\delta^{n+1+\alpha}$ . By comparing the predicted and the observed self Compton fluxes we have, in the case  $n = 2 + \alpha$

$$\delta_{2+\alpha} = [d(\alpha) F_m(1+z)]^{\frac{4+2\alpha}{3+2\alpha}} \left( \frac{\ln(\nu_b/\nu_m)}{F_x \theta_d^{6+4\alpha} \nu_x^\alpha \nu_m^{5+3\alpha}} \right)^{\frac{1}{3+2\alpha}} = \delta_{3+\alpha}^{(4+2\alpha)/(3+2\alpha)} \quad (2.45)$$

where the observable quantities have the same units as in eq. (2.44). For a continuous jet therefore, we would derive for the same observed quantities a higher  $\delta$  for those cases in which  $\delta > 1$ . In other words, a given enhancement requires a larger values of  $\delta$  if  $n = 2 + \alpha$ . Note however the weak correction with respect to the case  $n = 3 + \alpha$ , which does not allow to discriminate between the two physical situations from observations.

### 2.2.5 Brightness temperature

Historically, the brightness temperature  $T_B$  of a synchrotron source was the first indicator of beaming. In fact, for  $T_B \gtrsim 10^{12}$  K, the radiation energy density dominates over the magnetic one, and it is generally assumed that this condition leads to catastrophic inverse Compton losses, which rapidly cool the electrons so forcing the radiation to have a lower brightness temperature.

However, the above argument is strictly correct only when there is no continuous supply of energy in the source: in the case of continuous injection or reacceleration, instead, the radiation energy density can in fact be greater than the magnetic energy density, and this condition *does not* imply a catastrophic cooling because the higher order scatterings occur in the inefficient Klein Nishina regime (§4.2.2). On the other hand, as shown in the following, the maximum brightness temperature derived by the standard synchrotron theory depends very weakly on the physical parameters inside the source, and is therefore predicted to be distributed in a narrow range, independently of the ratio of the magnetic to radiation energy density.

To derive the predicted value of  $T'_B$  (in the comoving frame), we first note that its maximum corresponds to the peak of the synchrotron spectrum. Therefore it can be derived by equating the Rayleigh Jeans expression to the synchrotron flux at the self-absorption frequency:

$$2kT'_B \frac{\nu_m^2}{c^2} = \frac{2m_e}{\sqrt{3}} \frac{\nu_m^{5/2}}{\nu_B^{1/2}} f(\alpha) \left[ 1 - e^{-\tau(\nu_m)} \right] \quad (2.46)$$

The peak frequency  $\nu_m$  differs from  $\nu_t$  by a small factor, dependent on the spectral index (*e.g.* Pacholczyk 1970). Using eq. (2.46) and the relation between  $\nu_t$  and  $\nu_m$  for  $\alpha = 0.75$ , the brightness temperature is given by

$$T'_B = 1.64 \times 10^{11} \left( \frac{\tau_r}{B} \right)^{1/(2\alpha+5)} \text{ } ^\circ\text{K} \quad (2.47)$$

It is weakly dependent on the spectral index and on the parameters of the source, being related to the energy of the electrons emitting at the self-absorption frequency (thermodynamically it is expected it does not exceed the kinetic temperature  $\gamma_t m_e c^2/3$ ). Therefore the brightness temperature is roughly the same for all the objects (§5.3.2) and corresponds to  $\gamma_t \sim 100$ .

The observed brightness temperature is affected by beaming and a value of  $T_B$  exceeding the above limit is considered a possible indication of relativistic effects (§1.1.2.a; §5.3).

In the simpler case of a moving sphere ( $n = 3 + \alpha$ )

$$T'_B = \frac{T_B}{\delta} \quad (2.48)$$

where  $T_B$  is the observed value. If the dimensions are estimated from variability timescales,  $T'_B = T_B/\delta^3$ .

Let us derive the Doppler factor dependence in the case  $n = 2 + \alpha$ . To find the transformation rule for the self-absorption frequency  $\nu_m$ , we compare the frequency at which the optical depth  $\tau_s$  is unity in the comoving and in the observer frames. As explained above, aberration makes the paths in these two frames different, and therefore  $\nu_m$  is not simply  $\nu_m = \delta\nu'_m$  but the self-absorption frequency in the comoving frame is given by have

$$\nu_m = \nu'_m \delta^{1-[2/(5+2\alpha)]} \quad (2.49)$$

The corresponding intensities peaks at  $\nu_m$  and  $\nu'_m$ , respectively, and their transformation rule is

$$I(\nu_m) = \delta^{2+[2\alpha/(5+2\alpha)]} I'(\nu'_m) \quad (2.50)$$

Eq. (2.20) can be used to derive the value of the magnetic field  $B$ , since  $I(\nu_m) \propto B^{-1/2}$ , obtaining the same result as in the case of a moving sphere, eq. (2.42),  $B \propto \delta\nu_m^5/I^2(\nu_m)$ .

As a consequence of eqs. (2.49)–(2.50), the brightness temperature transforms as

$$T_B \propto \frac{I(\nu_m)}{\nu_m^2} = \frac{\delta^{2+[2\alpha/(5+2\alpha)]} I'(\nu'_m)}{\delta^{2-[4/(5+2\alpha)]} \nu'^2_m} = \delta^{(4+2\alpha)/(5+2\alpha)} T'_B \quad (2.51)$$



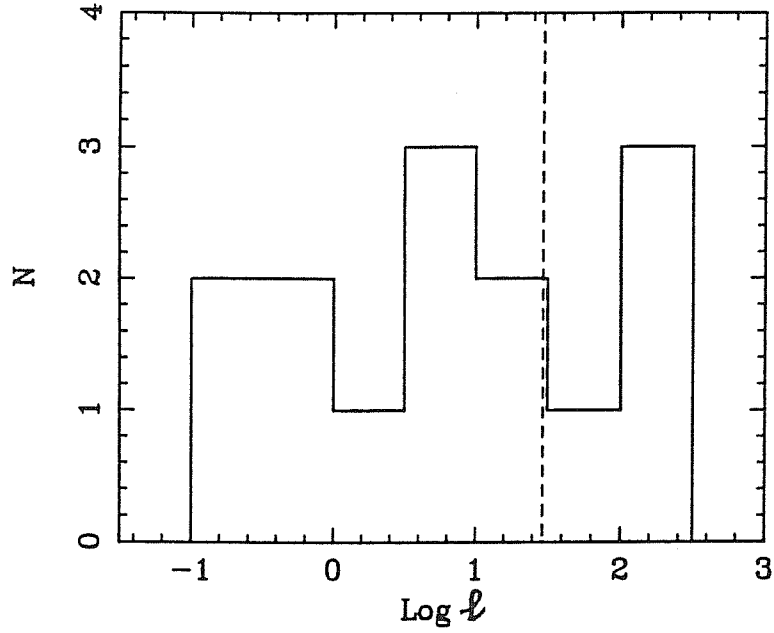


**Fig. 2.1.** The diagram reports the values of the compactness parameter estimated by Done & Fabian (1990). The vertical dashed line indicate the value of  $\ell$  for which the source is optically thick to pair production to all  $\gamma$ -ray photons above the energy threshold  $x = 1$  (§2.1.2), indicating that pair production is expected to be a rather common phenomenon in the compact region of AGN.

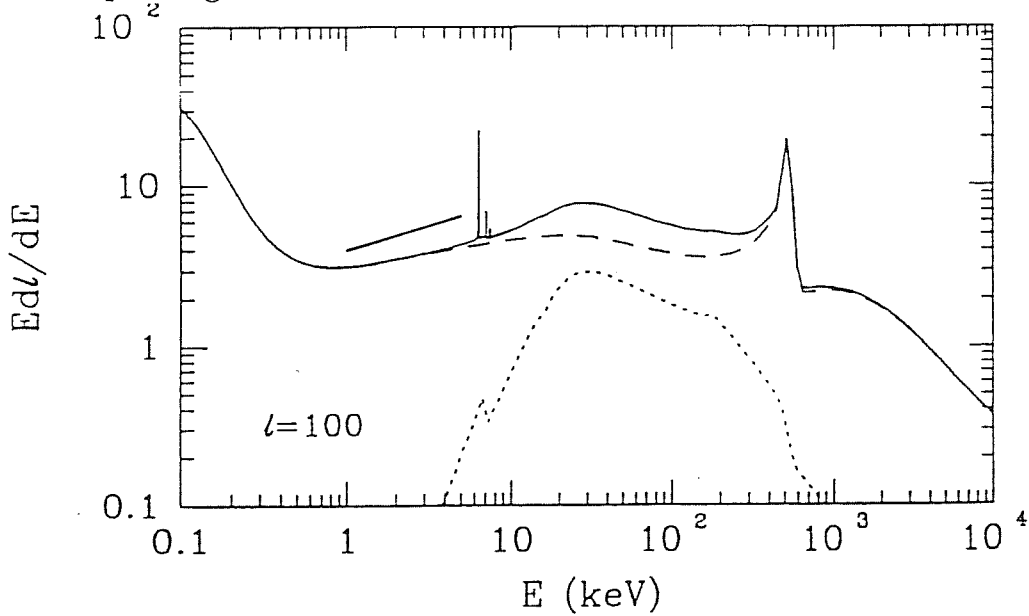


**Fig. 2.2.** Spectra from the non-thermal pair model and Compton reflection. The dashed curve represents the primary pair spectrum, the dashed curve is the reflected component and the solid curve is the sum observed. The compactness is  $\ell = 100$ . The luminosity which is not reflected is thermalized into the EUV blackbody. The solid line is a power-law with spectral index  $\alpha = 0.7$  as reference. The iron and nickel lines are also shown. From Zdziarski *et al.* (1990).

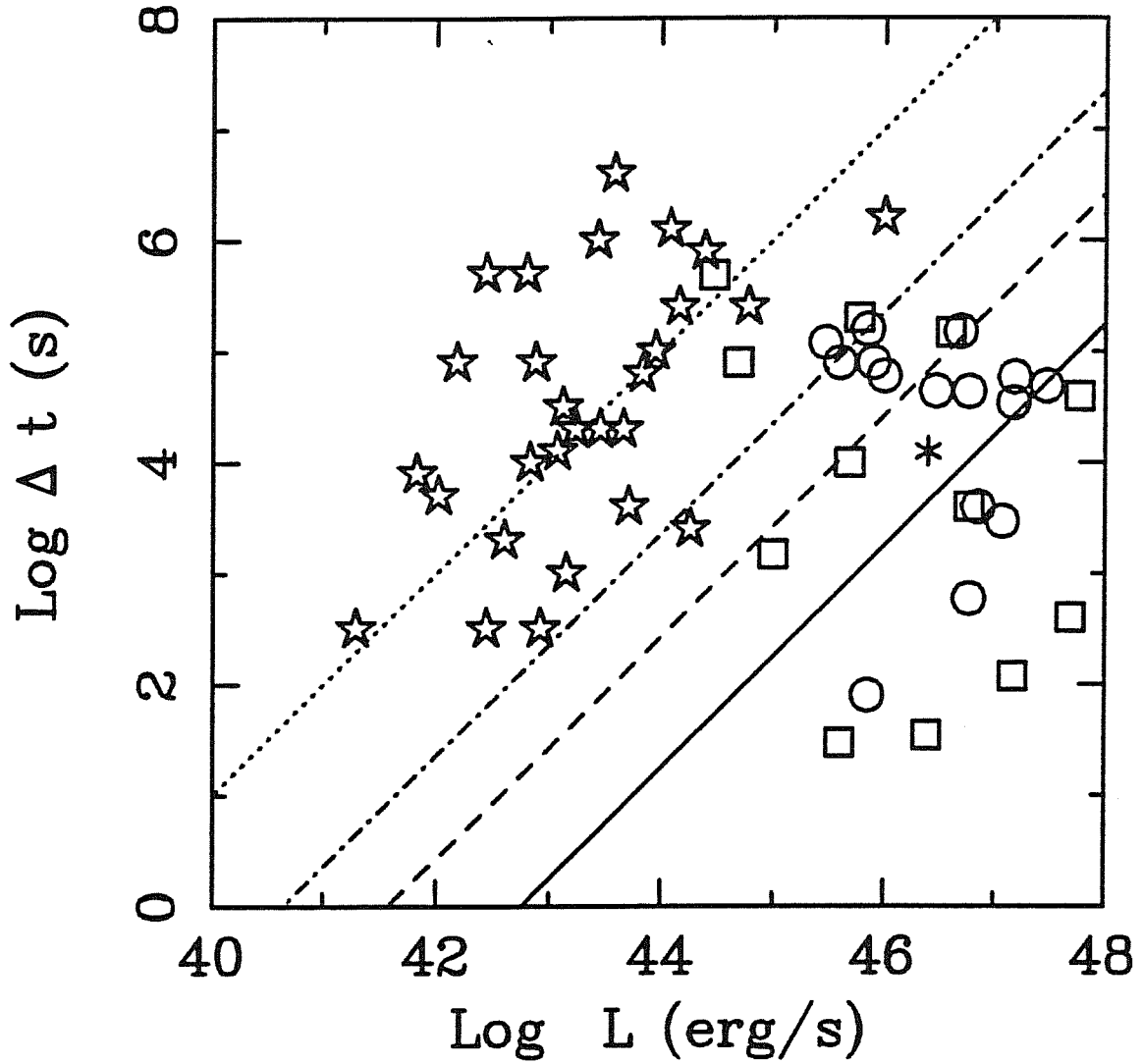


**Fig. 2.3.** The variability limits. The figure reports the minimum observed variability timescale  $\Delta t$  vs  $L$ . Stars are data from Done & Fabian (1989) and  $L$  is only the luminosity in the 2–10 keV X-ray band. The open circles are quasars and the squares are BL Lac objects. For them the bolometric luminosity is reported (data are from Bregman 1990 and references therein). The star symbol is 3C 279 (Makino *et al.* 1989). The lines indicate: the bremsstrahlung limit (dotted), the pair production limit (dash-dotted), the efficiency limit (dashed line) and the Eddington limit (continuous line) as described in §2.1.3.

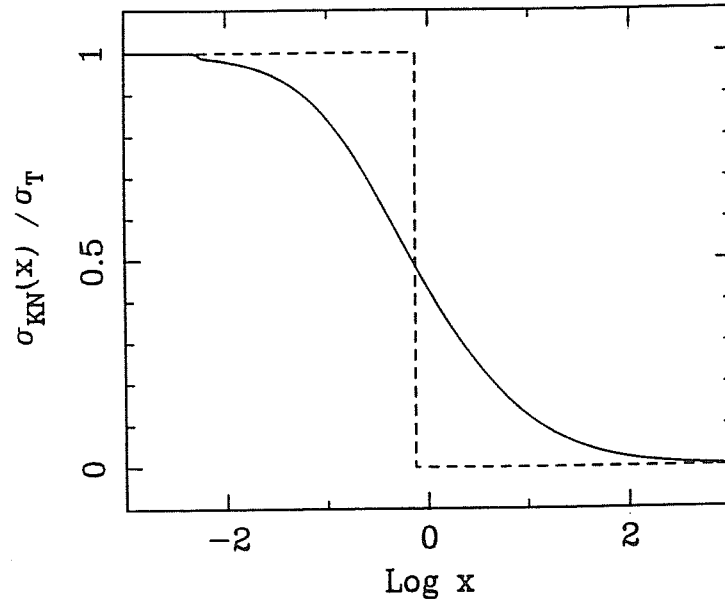


Fig. 2.4. The Klein-Nishina cross section, compared to the step function approximation.

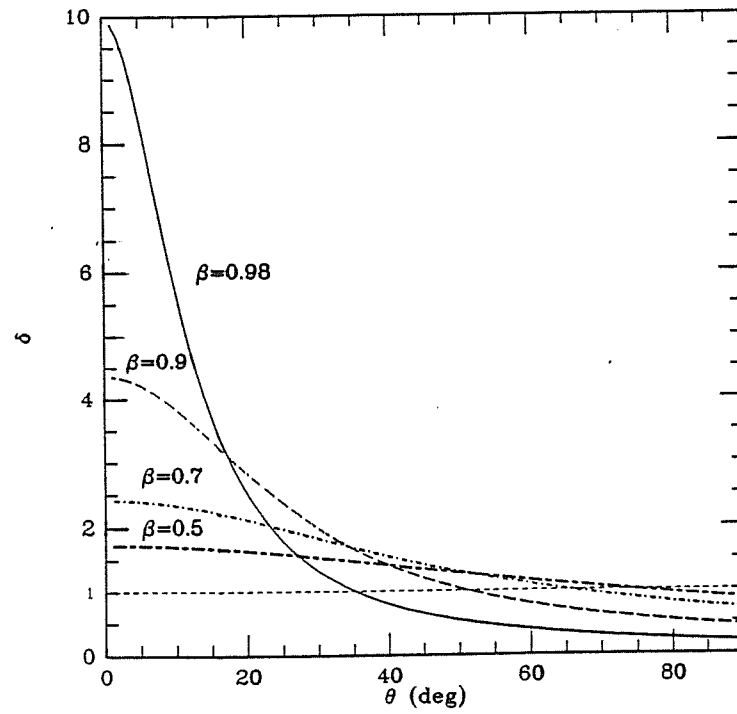
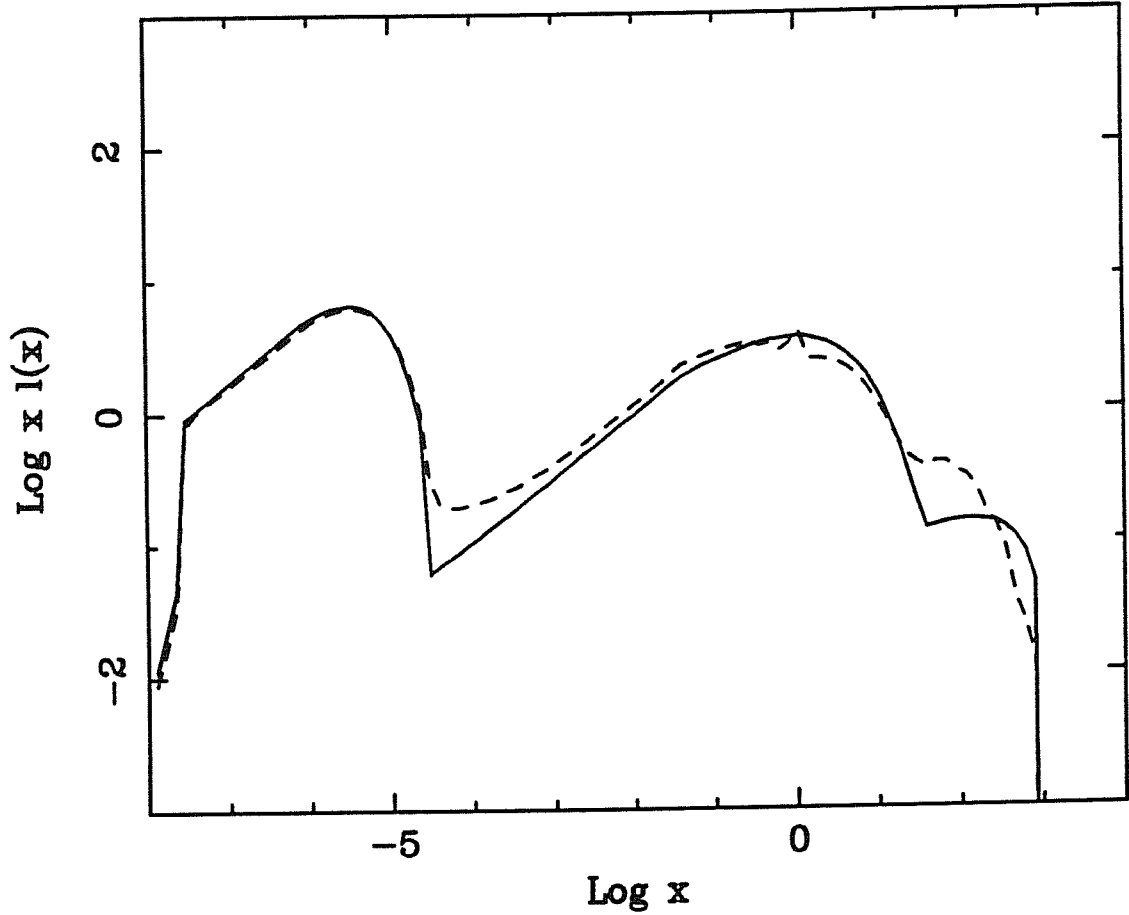


Fig. 2.5. The Doppler factor as a function of the viewing angle, for different velocities of the bulk flow. For any fixed  $\delta > 1$  there is a minimum value of  $\beta$  and a maximum angle consistent with it.



**Fig. 2.6.** SSC spectrum from a distribution of electrons calculated self-consistently with radiative losses, for a monoenergetic particle injection at  $\gamma_{max} = 10^3$ . The synchrotron emission is treated as scattering of ‘virtual’ photons (Blumenthal & Gould 1970) and the (approximated) intrinsic curvature of the spectrum at the higher frequencies has been considered [eq. (2.12)]. The magnetic field is in equipartition with the radiation field. As outlined in the Chapter pair reprocessing is probable to occur in compact sources. The dashed line show the effect of pairs, which must be derived considering the (non-linear) coupling of pairs and photons. We included pair production and annihilation, thermal and non-thermal Compton effect and radiative transfer, following the approach described *e.g.* in Done, Ghisellini & Fabian (1991), with the inclusion of synchrotron emission (some approximations have been modified, work in progress). The depletion of high energy  $\gamma$ -ray photons (first and second Compton order), the steepening of the X-ray spectrum and the appearance of an annihilation line can be clearly seen in the figure. We assumed  $\ell = \ell_B = 100$ .

## Chapter 3. The central region: reprocessed SSC radiation

We concentrate on the central compact region of AGN and in particular focus on two probable present ‘ingredients’: magnetic field and cold matter. Despite the increasingly detailed information about the X-ray spectra of AGN there is no consensus on the primary emission mechanism. However there are some indications that a strong magnetic field can play a dominant role in determining the observed spectrum. On one hand it makes electrons lose energy in synchrotron emission, on the other hand it can confine, in clouds or filamentary structures, some of the cold matter expected to be present in the central region. Even 0.1 per cent of this cold material can reprocess the radiation up to optical-UV frequencies and re-emit as quasi-thermal radiation in the UV band. Therefore a considerable fraction of the observed radiation in AGN (excluding at most BL Lac objects) can be due to reprocessing of radiation produced in the inner compact region, the emission of which is only directly observed in the X-ray band as synchrotron or SSC radiation.

The structure of the Chapter is the following. We first determine (§3.1) upper limits on the magnetic field strength in the X-ray emitting region of 5 AGN, on the assumption that the X-ray flux is Comptonized soft photon radiation. Such limits lie below the equipartition value with the radiation field. However a strong magnetic field (as requested by several theories) is allowed if the SSC radiation, which consequently would be an important energy loss mechanism, is partly reprocessed by cold matter. It is shown in some details (§3.2) that cold material is expected to be present in the central region of AGN and that the physical conditions required by the model are plausible. A discussion on the consistency of the model with the observations is presented in §3.3.

### 3.1 THE MAGNETIC ENERGY DENSITY

#### 3.1.1 Primary X-ray radiation

Recent observations of AGN, made at increased spectral resolution and in new wavebands indicate that several different emission processes contribute to the overall spectrum, including both primary and reprocessed radiation (§1.1). With the adjective ‘primary’, we refer (in contrast to reprocessed emission) to the radiative process operating in the ‘central’, compact region, which possibly transforms into radiation the gravitational or rotational energy converted into internal particle energy.

There is no certainty about the nature of the primary X-ray emission mechanism. Both non-thermal emission (*e.g.* SSC), and Comptonization of the soft X-ray or ‘blue bump’ photons from a thermal or non thermal distributions of electrons (*e.g.* in a corona above an accretion disc) can reproduce a power-law spectrum. Indeed it is not known what fraction of the power dissipated is thermalized and what is channeled into a small fraction of ultrarelativistic particles with a non-thermal distribution.

Thermal Comptonization however requires a fine tuning to produce a narrow range of observed X-ray spectral indexes and to maintain, during strong and fast variability, a slope which is a function of the temperature and optical depth of the electrons (Shapiro, Lightman & Eardley 1976; Fabian 1989). Moreover a rapid energy-exchange mechanism is needed in order to maintain a thermal distribution and to transfer energy from the ions to the electrons. In fact most of the energy of a thermal plasma is in the ions, and the electron-ion coupling timescales is  $\propto T_e^{3/2}$ , where  $T_e$  is the electron temperature. Consequently the timescale is longer when  $T_e$  is high, as required by the fast varying X-ray hard spectrum (Guilbert, Fabian & Stepney 1982), unless some plasma process effectively couples the two components.

Similarly, a ‘fine tuning’ of parameters is required if multiple Compton scattering dominates over synchrotron emission, as in the case of a steep electron injection spectrum or a low value of the maximum energy of the electrons ( $\gamma_{max} \lesssim 30$ , Ghisellini 1989a). Feedback processes could however select certain values of the spectral parameters.

Because the EUV region appears to carry much of the bolometric luminosity in many AGN, it is often assumed that the X-rays are Compton-scattered photons of the EUV-soft X bump from a non-thermal distribution of relativistic electrons. In particular, the lack of optical variability in the recent simultaneous optical and X-ray observations of NGC 4051 argued strongly for relativistic Comptonization as the radiation mechanism for the X-rays (Done *et al.* 1990). In this source, the steadiness of the infrared to UV flux, during rapid X-ray flux variations, means that any variable optical component lies

below an extrapolation of the X-ray continuum. This *apparently* rules out synchrotron and synchrotron self-Compton emission as candidates for the X-ray emission, since they predict a variable optical component on or above such an extrapolation.

The observations of spectral breaks (§1.1.1.d), line emission, variability and measures of polarization in the X-ray band can be critical tests to determine the origin of the X-ray spectrum.

### 3.1.2 Constraints on the magnetic field

Assuming that the X-rays are due to Comptonization of the EUV photons and using spectral and variability information, we show that the assumption that X-ray radiation is produced as Compton scattering from relativistic electrons implies that the X-ray emitting region is strongly dominated by radiation energy, while magnetic energy is well below the equipartition value. In fact the competition between synchrotron self-Compton emission and direct Comptonization enables us to estimate the relative importance of the radiation and magnetic fields (Celotti, Ghisellini & Fabian 1991a; Celotti, Ghisellini & Fabian 1991b).

We use variability timescales to estimate the dimension of the emission region and this allow us to derive the density of the relativistic electrons necessary to produce the observed X-ray flux. If a magnetic field is present, these electrons also produce infrared to X-ray radiation through SSC emission. By requiring that this radiation does not exceed the observed flux, we derive upper limits on the intensity of the magnetic field. The method parallels that used to estimate magnetic field strengths in extended radio sources. For the definition and formulae of the standard SSC model we refer to §2.2.

Consider a homogeneous spherical region with a size  $R_0$ , estimated from the X-ray variability timescale  $\Delta t$ , filled with electrons with a power-law energy distribution and soft photons with a blackbody spectrum. The photon density is calculated considering the maximum temperature blackbody, from the same volume, whose emission does not exceed the observed UV or soft X-ray (at 0.2 keV) fluxes. The assumption of a ‘maximum blackbody’ sets the highest possible limit on the derived magnetic field.

Note that the compact X-ray emitting region does not necessary coincide with the ‘central engine’, but it may occupy only a small fraction of its volume. One possibility is in fact that X-ray emission is a transient phenomenon produced in localized rapid events, which moves around in the central engine, due to impulsive release of energy (*e.g.* flares above the accretion disc). It is suggested by the fact that at increasing time resolution shorter variability timescales have been observed (§1.1.3.a).

Assuming that the X-ray emission is due to Compton scattering of the soft photons by the relativistic electrons, we can estimate  $\tau_r$  by dividing the extrapolated X-ray flux density

by the blackbody flux density, at the frequency where the blackbody peaks (Ghisellini 1987). Setting  $R_0 = c \Delta t / (1 + z)$  we then derive the normalization  $K$  of the electron distribution, whose slope  $p$  is fixed by the observed X-ray spectral index ( $p = 2\alpha_x + 1$ ).

If a magnetic field is present in the emission region, electrons emit synchrotron, first-order, second-order and higher order self-Compton radiation. The corresponding luminosities depend on the magnetic field intensity  $B$ , the density of the emitting electrons  $K$  and  $R_0$ .

Having derived  $R_0$  and  $K$ , the only remaining unknown physical quantity, which determines the synchrotron and self-Compton intensities, is the strength of the magnetic field. We can consequently impose a limit on it by requiring that the predicted SSC flux does not exceed the observed flux at any observed frequency. This limit depends on the assumed energy extent of the distribution of the emitting electrons, the maximum Lorentz factor  $\gamma_{max}$  of which determines which process (synchrotron or self-Compton) dominates at a given frequency. As shown in §2.2 synchrotron radiation dominates at a given frequency  $\nu$  if  $\nu < (4/3)\nu_B\gamma_{max}^2$ , so requiring  $B > 2.68 \times 10^{-7} \nu / \gamma_{max}^2$  G. If the  $B$ -field is lower, the flux at  $\nu$  is not due to synchrotron emission. It is mainly due to first-order Compton scattering if  $\nu < (16/9)\nu_B\gamma_{max}^4$ , or to higher-order Compton scattering otherwise.

For each pair of values of  $B$  and  $\gamma_{max}$ , the SSC spectrum is completely determined [eqs. (2.21)–(2.33)] and can be compared with the observed data: the values of the two parameters which predict a flux exceeding the observed one are not allowed. In this way we define a forbidden area in the  $B - \gamma_{max}$  plane.

Since the observed X-ray flux is produced by Compton scattering, we require that the electron population has a minimum  $\gamma_{max} \sim (\nu_x / \nu_{bb})^{1/2}$ , where  $\nu_x$  is the maximum observed X-ray frequency, and  $\nu_{bb}$  is the frequency where the assumed maximum blackbody peaks. We also considered third-order Compton emission, but, because it gives weaker limits on the magnetic field in the range of parameters considered, it is neglected in the following.

For low values of  $\gamma_{max}$  the synchrotron flux can be completely self absorbed. The relation between the magnetic field and the Lorentz factor  $\gamma_t$  of electrons emitting mainly at the synchrotron self-absorption frequency is given by eq. (2.18).

In the self-absorbed regime (*i.e.* for  $\gamma_{max} < \gamma_t$ ), the synchrotron flux  $\propto B^{-1/2}$ : for a fixed  $\gamma_{max}$  an increased magnetic field results in a decreased flux and a (linearly) increased maximum-emitted frequency  $\nu_{s,max}$ . Therefore in this regime we can derive a lower or upper limit on the magnetic field, depending on the value of the observed frequency used for the comparison between the predicted and the observed flux. Moreover if  $\gamma_{max} < \gamma_t$  the inverse Compton fluxes must be calculated using the self-absorbed synchrotron radiation energy density, as shown in §2.2.



### 3.1.3 The sample

We have applied the above method to five sources which sample the full range of active galaxies from low luminosity Seyfert galaxies to highly luminous quasars: two Seyfert galaxies, NGC 4051 and NGC 6814, the radio loud quasar 3C 273, the OVV quasar 3C 279 and the radio quiet quasar H1821+643. Basically, we selected sources with well-defined X-ray variability timescales and with ‘evidence’ for a blue bump component.

For each source, except NGC 4051 for which simultaneous optical and X-ray data are available, we use the lowest IR-UV fluxes obtained from different instruments. The maximum temperature EUV blackbodies consistent with the size of the X-ray region and the spectral data are computed; the soft X-ray flux is constrained by extrapolating the best-fitting power-law of the harder X-ray flux down to 0.2 keV. (Increasing this energy also increases the blackbody temperature, leading to stronger results). In Table 3.1 we list the redshifts, the blackbody temperatures  $T_{bb}$  and the dimension  $R_0$ , estimated from X-ray variability. We also give the minimum  $\gamma_{max}$  needed to emit the maximum X-ray frequency at which the source has been observed, by upscattering of the blackbody photons of frequency  $\nu_{bb}$ : it is indicated as  $\gamma_{max}^* \equiv (3\nu_x/4\nu_{bb})^{1/2}$ .

We assume  $H_0 = 100 \text{ km s}^{-1} \text{ Mpc}^{-1}$ ,  $q_0 = 0$ .

#### NGC 4051

Done *et al.* (1990) present results on correlated variability in the Seyfert galaxy NGC 4051. This source has previously shown rapid, large amplitude, variability in the X-ray down to time-scale of 100s (Lawrence *et al.* 1987; Matsuoka *et al.* 1990) and up to 20–30 per cent in the optical band (Lyutiy 1977; Penston *et al.* 1974). As a conservative value for estimating the X-ray dimension we use  $\Delta t = 300 \text{ s}$ .

NGC 4051 has been observed simultaneously in the X-ray band (2–20 keV) by the GINGA satellite, in the B band from a series of CCD images and in the IR band with the UKIRT. A spectrum in the UV band from IUE, even if not simultaneous, gives information on the overall spectral distribution and shows that the optical–UV spectrum is not badly contaminated by the thermal radiation of an accretion disc.

We show in Fig. 3.1a the overall energy distribution, after subtraction of the stellar contribution and the dereddening in the optical and IR band made by Done *et al.* (1990). The high luminosity state for the X-ray flux, corrected for galactic absorption, is best-fitted by the power law  $F(\nu) = 2.74 \times 10^{-15} \nu^{-0.79} \text{ erg s}^{-1} \text{ cm}^{-2} \text{ Hz}^{-1}$ . The source has been observed down to 0.2 keV by EXOSAT (Lawrence *et al.* 1985). The data between 10 and 83  $\mu\text{m}$  are IRAS data, taken from Ward *et al.* (1987): due to the lack of IR variability these can be considered as a good indication of the spectral distribution at low frequencies.

The analysis of Done *et al.* (1990) shows no short timescale correlation between the IR-optical and X-ray fluxes. A greater than 50 per cent increase in the X-ray flux ( $\simeq 2 - 9$

keV band) produced corresponding upper limits of 4 per cent and 1 per cent for the nuclear variability in the IR (K band) and optical (B band) over the same interval, after removing the effects of atmospheric variations in the optical light curve.

The lack of correlated variability allowed Done *et al.* (1990) to exclude the possibility that the optical and X-ray fluxes are produced as primary radiation by the same population of electrons, as is the case in the standard SSC model. This led to the conclusion that they should be produced in different spatial regions or that the optical emitting region is one order of magnitude bigger than the X-ray one. (The possibility of a varying inverse Compton flux with a stationary synchrotron emission proposed by Ghisellini, George & Done (1989) requires, unlike NGC 4051, a synchrotron-dominated source).

Our strongest limits on the magnetic field in this source are obtained by requiring that the variations produced at IR and optical frequencies during a 50 per cent variation in X-ray flux do not exceed the observed ones (4 per cent of the total flux in the IR and 1 per cent of the total flux in the optical).

### NGC 6814

The results on X-ray variability from GINGA observations (Kunieda *et al.* 1990) confirm earlier HEAO-1 results (Tennant *et al.* 1981) and indicate a maximum size smaller than  $R_0 \sim 1.5 \times 10^{12}$  cm.

We consider the overall spectrum shown in Fig. 3.1b. The IR-optical data are from McAlary *et al.* (1983) and McAlary *et al.* (1988), the J,H,K,L band fluxes are obtained by subtracting the stellar contribution. The UV data are averages of two short (SWP10680L and SWP10693L) and one long (LWR8961R) wavelength spectra from *IUE*. We use the X-ray state reported by Tennant *et al.* (1981) (best-fitting power-law spectrum  $F(\nu) = 5.9 \times 10^{-17} \nu^{-0.67}$  erg cm<sup>-2</sup> s<sup>-1</sup> Hz<sup>-1</sup>) from HEAO 1 observations.

The source has also been observed in the soft X-rays with EXOSAT (Mittaz & Branduardi-Raymont 1989) and up to 120 keV by HEAO 1 (Rothschild *et al.* 1983).

### 3C 273

A variation of the X-ray (2–10 keV) flux by a factor 2 in  $\Delta t = 0.5$  day for the quasar 3C 273 has been reported by Marshall *et al.* (1981). The overall spectrum for 3C 273, shown in Fig. 3.1c, has been obtained from the data of Courvoisier *et al.* (1987), Robson *et al.* (1986), Clegg *et al.* (1983), Landau *et al.* (1983) and Aller *et al.* (1985). The UV datum at  $\lambda_{obs} = 916\text{\AA}$  is from Reichert *et al.* (1988). The X-ray power law ( $F(\nu) = 5.2 \times 10^{-19} \nu^{-0.54}$  erg cm<sup>-2</sup> s<sup>-1</sup> Hz<sup>-1</sup>) refers to the EXOSAT observation reported by Turner *et al.* (1990).

The observed  $\gamma$ -ray flux reported by Bassani *et al.* (1985) and recently by EGRET (§1.1.2.c) are below the extrapolation of the X-ray spectrum. Therefore we conservatively assume that the X-ray spectrum extends to an energy of 1 MeV.

### 3C 279

We also consider the blazar 3C 279. The dimension of the X-ray region is deduced from the variability timescale of 45 min reported by Makino *et al.* (1989) for a 20 per cent X-ray flux variation. We therefore assume that  $\Delta t = 225$  min.

The spectrum, shown in Fig. 3.1d, has been constructed from the data of Makino *et al.* (1990), Brown *et al.* (1989), Landau *et al.* (1986). The X-ray data are from Makino *et al.* (1990), who report a best-fitting power-law spectrum,  $F(\nu) = 9.75 \times 10^{-19} \nu^{-0.58}$  erg cm<sup>-2</sup> s<sup>-1</sup> Hz<sup>-1</sup> from a GINGA observation.

The  $\gamma$ -ray fluxes recently detected by the EGRET and COMPTEL instruments are not simultaneous with the X-ray data (see Fig. 4.10). However they would indicate values for the minimum  $\gamma_{max}^*$  of the electron distribution much higher than the constraint from the GINGA data (§4.2.2.c).

### H1821+643

H1821+643 is a radio-quiet quasar for which an X-ray variation of a factor 2 in 10 days is reported by Snyder & Wood (1984).

The spectral data, in Fig. 3.1e, are from Kolman *et al.* (1990). The X-ray power law ( $F(\nu) = 6.18 \times 10^{-19} \nu^{-0.6}$  erg cm<sup>-2</sup> s<sup>-1</sup> Hz<sup>-1</sup>) is a fit of *Einstein Observatory* data (0.1–3.5 keV), and is consistent both with EXOSAT and GINGA results at higher energies (Warwick, Barstow & Yaqoob 1989, Kii *et al.* 1991).

## 3.1.4 Results

The  $B - \gamma_{max}$  constraints obtained for each object are shown in Figs. 3.2a,b,c,d,e. As explained the comparison of the predicted SSC flux with the flux observed at any given frequency defines a forbidden region (shaded) in the  $B - \gamma_{max}$  plane. Curved lines are defined by the synchrotron ( $\nu \propto B\gamma_{max}^2$ ), first- ( $\nu \propto B\gamma_{max}^4$ ), or second- ( $\nu \propto B\gamma_{max}^6$ ) order self-Compton relations between  $B$  and the minimum  $\gamma_{max}$  needed to emit a given frequency. In general, limits derived by the synchrotron flux refer to the largest values of  $\gamma_{max}$ . As an illustration in Fig. 3.1c, we show the computed SSC spectrum for  $B = 200$  G and  $\gamma_{max} = 120$ .

In Fig. 3.2b the (dash-dot) line defining the self absorption value  $\gamma_t$  is shown as a function of the magnetic field [eq. (2.18)]. On the left side of this line the synchrotron radiation is completely self absorbed, and the self-Compton flux is calculated using the energy density of the self-absorbed synchrotron radiation [eqs. (2.21)–(2.23)]. Continuous vertical lines refer to the minimum  $\gamma_{max}^*$ . Only the right-hand side (higher  $\gamma_{max}$ ) region of the parameter space is allowed. It is clear that stronger limits on the magnetic field can be obtained if hard X-ray or  $\gamma$ -ray observations *simultaneous* with the X-ray data

increase this minimum value of  $\gamma_{max}$ . The dashed vertical line (labelled  $\gamma_{1\text{ MeV}}$ ) refers to the value of  $\gamma_{max}$  needed to produce radiation at 1 MeV, which is the threshold energy for  $e^\pm$  pair production through photon–photon collisions. The lines labelled  $B_{eq}$  indicate the values of the magnetic field in equipartition with the radiation energy density. This is obtained by integrating the X-ray flux up to the frequency  $(4/3)\nu_{bb}\gamma_{max}^2$ . This value can strongly underestimate the radiation energy density since it neglects the contribution from the (unobserved) EUV radiation field. Observations in the UV from the HST can give tighter limits on the UV photon density.

For three of the sources we find that equipartition is not possible in the relevant range of  $\gamma_{max}$ . For 3C 279 and H1821+643 it is reached only if  $\gamma_{max}$  is within a factor two of the minimum value, on the assumption that the X-ray spectrum of these sources extends no more than 20 keV. Increasing  $\gamma_{max}$  increases both  $B_{eq}/B$  and the radiation energy density.

For a more detailed description of the results, consider the source NGC 6814, for which strong limits are found (see Figs. 3.1b and 3.2b). From the observed spectrum the strongest limits on  $B$  appear to be due to the long wavelength data of the UV spectrum. For high values of  $\gamma_{max}$  ( $> 700$ ) these frequencies can be emitted as optically–thin synchrotron and the implied upper limit on  $B$ , evident in Fig. 3.2b as a horizontal line, is  $B \simeq 600$  G. For lower values of  $\gamma_{max}$  the first–order Compton emission dominates at this frequency. The constraints derived on  $B$  depend on  $\gamma_{max}$ , due to the logarithmic term in the Compton emission. On the left–hand side of the line  $\gamma_t$  the flux is self–absorbed and the limits are imposed by the optically–thick synchrotron or Comptonized self–absorbed fluxes.

A simple estimate of these limits can be found using the approximate expression of §2.2.2, with a dilution factor  $q=1$ . For  $q < 1$ , the lower photon energy density in the X-ray region requires a larger electron density in order to produce the observed X-ray flux which in turn implies tighter limits on the magnetic field. For the case of NGC 6814, if  $\gamma_{max} \simeq 100$  then the UV emission can be produced by first–order Compton scattering of the synchrotron radiation. Rough estimates from eq. (2.33) give  $y \simeq 1.7$  and  $U_{obs}/U_{bump} \simeq 10^{-2}$  and using eq. (2.35b) we find  $U_B/U_x < 2 \times 10^{-3}$ , which corresponds to  $B_{eq}/B > 22$ . For  $\gamma_{max} \simeq 2000$ , UV radiation can be emitted by the synchrotron process. With  $y \simeq 10$  and using eq. (2.34), we have  $U_B/U_x < 10^{-4}$ , *i.e.*  $B_{eq}/B > 100$ . Both limits are in good agreement with the ones shown in Fig. 3.2b.

From the spectrum of 3C 273 reported in Fig. 3.1c is possible to see that the strongest limits on  $B$  are imposed by the X-ray flux. With  $\gamma_{max} \simeq \gamma_{1\text{ MeV}}$  it is possible to estimate  $y \simeq 8$ , and using eq. (2.35a), a limit of  $B_{eq}/B > 23$  is obtained, in agreement with the limits shown in Fig. 3.2c.

In Table 3.1 we also list the estimated radiation energy density  $U_x$ , computed for the minimum value of the Lorentz factor  $\gamma_{max}^*$ , the energy density of the relativistic electrons  $U_e$  and the value of the maximum allowed magnetic energy density implied by our limits,

again estimated at  $\gamma_{max}^*$ . It is shown that, except for NGC 4051, the particle energy density of the emitting electrons is a small fraction of the photon density, and can be comparable with the magnetic one.

### 3.1.5 Parameters

The calculated ratio of magnetic to radiation energy density depends on our assumptions. In the following, we discuss how our results change as some of the assumed parameters are varied.

(i) The first point concerns the determination of the soft photon energy density, which fixes the value of the electron density  $K$ . It is estimated by assuming a maximum temperature blackbody,  $T_{bb}$ , neglecting any dilution factor which is relevant if the blackbody and X-ray emission regions do not coincide. Both these assumptions tend to overestimate the photon density and, consequently, underestimate the electron density. Relaxing these assumptions therefore results in tighter limits on  $B$ .

(ii) A second critical parameter is the dimension  $R_0$  of the source. Since variability timescales yield only an upper limit on  $R_0$ , it may be smaller than our adopted value. To produce the same optically-thin synchrotron flux we must have  $R_0^2 \tau_r B^{1+\alpha} = \text{const}$ , while the X-ray energy density  $U_x \propto R_0^{-2}$ . In changing  $R_0$  we must also consider the possible changes in the temperature and flux of the assumed blackbody. In general, if  $R_0$  decreases, then higher values of  $T_{bb}$  are allowed, until eventually the observed flux becomes inconsistent with a further temperature change. To illustrate this, consider the simpler case of a constant  $T_{bb}$ . Here the scattering optical depth  $\tau_r$  is constant, and equipartition is possible for  $R_{eq}$  given by

$$R_{eq} = R_0 (U_B/U_x)^{(1+\alpha)/(2-2\alpha)} \quad (3.1)$$

where  $U_B$  and  $U_x$  are calculated with the initial  $R_0$ .

If  $T_{bb}$  increases so that the soft photon flux increases (corresponding to a more powerful blackbody), then we need fewer electrons to produce the X-ray flux, and so  $\tau_r$  decreases. In this case equipartition is reached for a dimension larger than that indicated by eq. (3.1). On the other hand, when the blackbody is limited by the low energy X-ray flux, a decrease in  $R_0$  corresponds to an higher  $T_{bb}$ , but also to a larger  $\tau_r$ . In this case equipartition is possible with a size smaller than that given by eq. (3.1).

To estimate the effects of decreasing  $R_0$ , we calculate for each new size the maximum temperature blackbody and the new limits on the magnetic field, until the minimum possible scattering optical depth,  $\tau_{min}$ , is reached. If equipartition is not allowed even using the size corresponding to  $\tau_{min}$ , we decrease  $R_0$  further, but now keeping  $\tau_r = \text{const} = \tau_{min}$ . We then use eq. (3.1) to estimate  $R_{eq}$ , where  $R_0$ ,  $U_B$  and  $U_x$  are the values found

for  $\tau_r = \tau_{min}$ . As a particular example of this, consider the source NGC 6814. In this case a decrease in  $R_0$  implies an increase of  $\tau_r$ , therefore we use eq. (3.1) to estimate the maximum size needed to reach equipartition. Assuming the minimum ratio  $B_{eq}/B \simeq 4$  from Fig. 3.2b (just for  $\gamma_{max}^*$ ), equipartition can be reached for dimensions of the emitting region at least  $10^3$  times smaller than that deduced from the variability timescale ( $R_0 \simeq 1.5 \times 10^{12}$  cm). For 3C 273, a minimum value of  $\tau_r$  is reached for  $R_0 \simeq 5 \times 10^{14}$  cm. Using this dimension we find  $B_{eq}/B \simeq 8$ . To obtain equipartition we again require a dimension a factor  $10^3$  smaller than that estimated from variability.

(iii) The results are also affected by the lack of simultaneous X-ray and optical-UV data. Therefore we have also calculated the limits imposed by lower flux X-ray states. For NGC 6814, from the EXOSAT observation (Mittaz & Branduardi-Raymont 1989) with a best-fitting power-law spectrum  $F(\nu) = 1.3 \times 10^{-20} \nu^{-0.51}$  erg cm $^{-2}$  s $^{-1}$  Hz $^{-1}$ , we find a minimum ratio of  $B_{eq}/B \simeq 2$ . Decreasing  $R_0$ , from eq. (3.1) we find that  $R_{eq}$  must still be at least a factor 8 smaller than that implied by the variability constraints. Weaker limits for the magnetic field in 3C 273 can be obtained by considering both the low X-ray state and assuming a dimension corresponding to the minimum possible  $\tau_r$ , for which  $B_{eq}/B \simeq 2.5$ . We have also considered the possibility that the size of the X-ray emission region in 3C 273 is much larger than the 0.5 light days assumed on the basis of the observation of Marshall *et al.* (1981). No later observation of 3C 273 shows such rapid variability, the observed two-folding timescale being 20 days or more (Turner *et al.* 1990). Taking  $\Delta t = 19$  days, we still find similar results.

(iv) Because of the increasing evidence that the typical observed 2–10 keV X-ray spectrum, at least for Seyfert galaxies, can be explained by a combination of a direct power-law spectrum with  $\alpha_x \simeq 0.9$  and its reflection from a cold disc, we have computed the limits on the magnetic field assuming an intrinsic X-ray spectral index  $\alpha_x = 0.9$ , keeping the total number of X-ray photons in the range 2–6 keV constant. We find no significant variations of the allowed region of the  $B - \gamma_{max}$  space.

For the other sources the results are similar, but less extreme. For each object we have considered the different observed X-ray states. For each state we calculate the limits on  $B$  for the value of  $R_0$  such that  $\tau_r$  is minimized. Equipartition can be reached in some cases, with an absolute maximum  $B/B_{eq} \simeq 7$ , but only over a restricted range of  $\gamma_{max}$ . For the quasars, it is not clear that the variability is persistent and involves the whole X-ray spectrum. For example, the variability of H1821+643 may be dominated by a soft component. Nevertheless, as we have seen for 3C 273, increasing the variability timescale by a factor of 10 does not qualitatively change our result.

We conclude that equipartition can be obtained in some sources only for very restricted values for  $\gamma_{max}$ . It requires a small (sometimes extreme) value of the radius.

### 3.1.6 Effects of beaming

For two of the sources considered here, namely 3C 273 and 3C 279, there is evidence that relativistic beaming (§5.3) can be important. Both are superluminal radio sources, and 3C 279 showed a very fast increase of the X-ray flux, corresponding to  $\Delta L/\Delta t > 2 \times 10^{42}$  erg s<sup>-2</sup>, from which Makino *et al.* (1989) estimate a minimum  $\delta \geq 1.6$  and an intense, variable  $\gamma$ -ray emission from which a minimum  $\delta \gtrsim 5.5$  can be inferred (§4.2).

We have therefore included the possibility that the X-ray flux is beamed, by taking into account the following: (i) the comoving size of the emitting region, larger than what variability indicates:  $R_0 = c \Delta t \delta/(1+z)$ ; (ii) the maximum temperature blackbody (assumed unbeamed) corresponding to this size; (iii) the optical depth  $\tau_r$  of the emitting plasma, as measured in the comoving frame; (iv) the predicted monochromatic fluxes, given by the formulae (2.20)–(2.29) are generalized to include the effect of beaming, using in the observer frame  $I(\nu) = I'(\nu) \delta^{3+\alpha}$  ( $\alpha = -5/2$  for self-absorbed synchrotron), where  $I(\nu)$  is given by those formulae. For a given observed frequency  $\nu$  we calculate  $\nu' = \nu (1+z)/\delta$  and select the radiation process dominant at  $\nu$ ; (v) the equipartition magnetic field, scaling as  $\delta^{-3}$ .

We then found, for 3C 279, the value of  $\delta$  for which the magnetic and the radiation energy densities are in equipartition, assuming the spectrum extends up to a (rest frame) energy of 1 MeV. We found  $\delta \simeq 3$ .

For 3C 273 the evidence of beamed X-ray emission is weaker than for 3C 279, even if beaming can be very important for the radio flux. Indeed, the presence of a fluorescent iron line argues against strong beaming effects. In the frame described in §1.1.1.c, if the source of X-rays moves away from a disc in a direction normal to its surface, the absorbed luminosity by photoelectric effect by cold matter in the disc scales approximately as  $\Gamma^{-3-\alpha}$ . On the other hand the observer sees an enhanced (by  $\delta^{3+\alpha}$ ) direct monochromatic flux. The equivalent width of the line therefore scales as  $(\delta\Gamma)^{-3-\alpha}$ . Comparing the typical equivalent width of the iron line observed in Seyfert galaxies ( $\sim 150$  eV) with the one observed in 3C 273 ( $\sim 50$  eV, Turner *et al.* 1990), and assuming  $\theta \sim 10^\circ$ , we derive  $\delta = 1.3$ . (A minimum beaming factor of about 1.7 for 3C 273 has been recently derived from the absence of a spectral break due to downscattering in the hard X-ray spectrum). The limits on the magnetic field, calculated assuming this value of  $\delta$ , remain unchanged.

### 3.1.7 Discussion

Equipartition magnetic fields are excluded from the X-ray emission regions of several AGN under the assumption that the X-rays are due to inverse-Compton scattering of EUV photons by relativistic electrons. This seems to imply three alternative conclusions:

- i) The assumptions about the emission model are too simplified (homogeneity, particle distribution or geometry)
- ii) Equipartition between magnetic and X-ray energy density is at best only marginally possible. (For 3C 279 beaming effects can allow an equipartition magnetic field, while for NGC 6814 it is strongly ruled out).

This hypothesis is surprising and would be possibly of great significance when it is considered that many models for the inner regions of AGN invoke strong magnetic fields. A low magnetic field (less than equipartition) poses problems for magnetic confinement of jets (§5.5). Furthermore most theories of accretion predict that magnetic fields are amplified in the flow. Finally a very plausible mechanism to accelerate electrons is through transient electric fields produced during magnetic reconnection (in fact it is not clear if shocks can accelerate rapidly electrons to high energies) (*e.g.* Christiansen 1989). If the magnetic energy density is not dominant then it is difficult to understand how magnetic fields can accelerate particles which emit radiation with a higher energy density. The magnetic energy cannot be replenished (or changed) faster than the radiation escapes from the emission region.

- iii) the X-ray radiation mechanism is not non-thermal Comptonization of blue bump photons, as instead often assumed.

Direct production of SSC radiation by a single population of electrons is apparently ruled out by the variability constraints in NGC 4051. There are no obvious reasons to suppose that the other sources, at least Seyfert galaxies and quasars which show uncoordinated variability behaviour, are different.

Our limits on synchrotron self-Compton emission rely on the X-ray emission region being directly visible in the optical and UV bands. This would not be the case if the X-ray emission region is blanketed in sufficient cold gas that free-free absorbs throughout the optical and UV wavebands. The main problem with a diffuse absorbing blanket is that it would have to be so dense and thick that the X-rays would also be absorbed (at the least by photoelectric absorption). An acceptable solution is obtained if the absorbing gas is distributed in small dense clouds with a large covering fraction and a total column density  $N_H \lesssim N_{21}$  in order that photoelectric absorption of soft X-rays is not observed. The pressure of the clouds is then so high that they would rapidly disperse at the internal sound speed if not confined. A scenario in which very dense cold clouds can survive close to the central engine in AGN has been suggested by Rees (1987). This mainly dealt with the BLR, at much larger radii than the X-ray emission region (§1.1.1.e). The intracloud



pressure is proposed there to be due to a strong magnetic field, maintained either by the accretion flow or by a relativistic wind. It was also suggested that much stronger magnetic fields may be present at smaller radii and that they support a population of very dense clouds. Free-free absorption can therefore allow the strong, equipartition magnetic field, apparently ruled out by our above results, to support a blanket of dense, cold clouds which hide its radiation signature.

## 3.2 COLD MATTER AND REPROCESSING

We first examine (§3.2.1) the observational evidences and theoretical inferences for the presence of cold material in the central engine of an AGN (excluding perhaps BL Lacs) and show that even small amounts of very dense matter can have an important effect on the emitted spectrum at ultraviolet and longer wavelengths. If only 0.1 per cent of the total matter expected there is in the form of small dense clouds then much of the infrared and optical spectrum is absorbed and reradiated in the ultraviolet. The magnetic field supports and confines the dense clouds in a manner analogous to prominences above the solar photosphere. We then show (§3.2.2) how such small dense clouds can arise and how this matter could be in the right conditions to absorb by free-free just up to UV frequencies (Celotti, Fabian & Rees 1992).

### 3.2.1 Cold matter

#### *3.2.1.a Observational evidences*

Recent detailed studies of the X-ray spectra of many AGN have revealed the presence of much cold (typically  $T \lesssim 10^6$  K) gas in the central engine, including the soft X-ray excess, the fluorescent iron emission line, the presence of a reflection component in the hard X-ray spectrum (§1.1.1.c). That the cold gas does lie in the central engine is shown by the variability of all the above spectral components (§1.1.3.a). Its geometry is uncertain, although a disc-like structure, with the X-rays emitted from above and below the disc, is plausible. As already mentioned an alternative to the disc geometry is given by high density cold clouds or filaments.

The lack of any obvious soft X-ray absorption in many typical variable AGN shows that our line of sight is obscured by a column density of less than about  $N_{21} \sim 1$  at solar abundances, with values of about 3 and 0.1 being measured by Turner & Pounds (1989) for NGC 6814 and NGC 4051, respectively (which are 2 of the objects studied in §3.1). The

presence of slightly thicker regions of partially-ionized gas (warm absorber) with typical  $N_{21} \sim 100$  and  $T_5 \sim 10 - 100$  is also suggested by observations.

Gas at still higher density than required by the X-ray spectra may also exist in the X-ray emission region. There are some indications of the presence of clumped material at temperatures and densities higher than the BLR clouds, close to the central engine.

It has been proposed (Krolik *et al.* 1985) that the broad absorption feature in the soft X-ray spectrum of some BL Lac objects (§1.1.2.b) could be due to O VIII, in a clumpy wind at  $R < 10^{16}$  cm, with outflow velocity up to  $2.5 - 5 \times 10^9$  cm s<sup>-1</sup>.

There are observational suggestions that the BLR is extended at distances smaller than those predicted by the ‘standard model’, possibly in a stratified configuration (§1.1.1.e). The high density of the inner clouds implies that the free-free is an important radiative mechanism.

The importance of free-free emission in this context has been envisaged in some recent papers. Barvainis (1990) has analyzed the IR-optical spectrum of 36 radio quiet quasars (see also Neugebauer *et al.* (1987) for high luminosity objects) and claims that the spectra can be best-fitted by including a flat  $\alpha \simeq 0.2$  component in the optical, extending from 1  $\mu$ m to the soft excess and interpreted as free-free emission.

Ferland, Korista & Peterson (1990) suggest that optically thin matter is present very close to the central region, on the basis of the observation in the Seyfert galaxy Mkn 590 of a variable continuum and core line emission while the broad wings of the hydrogen lines maintained constant luminosity. They propose that the wings are produced in a Very Broad Line Region, which reprocess 50–500 eV photons into the blue bump. This material should be partially ionized gas (possibly the warm absorber), as suggested by the lack of response to the central source variations, and emit in the radio band through free-free, with a very low filling factor and high covering factor  $\sim 1$ .

### 3.2.1.b Estimates of matter density

There are also strong ‘theoretical’ suggestions that cold matter is present and coexisting with hot and relativistic plasma, in the central region of AGN.

As discussed in §2.1, a high compactness implies that particles cannot escape a source before cooling.

- As outlined by Blandford & Rees (1978) the short cooling timescale of the emitting electrons require that power is continuously replenished. If new particles are supplied

(neglecting pair annihilation) they pile up or escape. The equilibrium optical depth is therefore given by

$$\tau_T \simeq \frac{\ell}{\langle \gamma \rangle \beta_{esc}} \quad (3.2)$$

where  $\langle \gamma \rangle$  is the average injected Lorentz factor and  $\beta_{esc}$  escape velocity of the electrons.

- If  $\langle \gamma \rangle$  is high enough pairs are produced and the equilibrium pair optical depth (neglecting dynamics) in a steady source can be obtained balancing pair production with the annihilation rate of cooled pairs. Assuming only photon–photon production and no escape of the pairs, it is given by  $\tau_{e\pm} \simeq (\xi \ell)^{1/2}$  [eq. (2.4a)].

- Any accretion powered source must contain some non-relativistic matter (not in form of pairs) with high opacity. Let us assume spherical accretion, with the matter accreting at the free fall velocity. Therefore  $\dot{M} = 4\pi R^2 m_p n v_{ff}$  and

$$\tau_T \simeq \frac{\dot{M} c \sigma_T}{20 G M m_p} \sim \frac{4}{\eta_{0.1}} \frac{L}{L_E} \quad (3.3)$$

for  $R = 3R_s$  and  $L = \eta \dot{M} c^2$ . This value must be multiplied by  $v_{ff}/v_{in}$  in a disc geometry, where the viscosity determines the infall velocity  $v_{in}$ .

Other opacities can be even more important. In any case the core of an Eddington accreting black hole is optically thick and feedback and trapping of radiation are effective. The gas is expected to be present unless the source is sub-Eddington and the efficiency is very high. (In fact the limit can be avoided if the power comes from electromagnetic extraction of the hole's spin energy in which case can be  $\eta \gg 1$ ).

As already mentioned optical depths  $\tau_T > 1$  cause the smoothing of rapid variations, because of the increasing diffusion timescale. Moreover if the optical depth in ordinary matter (not pairs) is  $\tau_T > 1$  depolarization of non-thermal emission occurs.

Note that the lack of the spectral break in the hard X-ray band due to downscattering suggests values of  $\tau_T \lesssim 3$  and  $\tau_T \sim \text{few}$  for the only possible break observed in NGC 4151 (§1.1.1.e; §2.1.2).

Sources the spectrum of which do not show thermal features require one of the following possibilities: the power is rotational energy extracted from the hole, without accreting matter; the observed luminosity is relativistically amplified in a beamed outflow; non-thermal heating or other acceleration mechanisms prevent the relativistic matter to cool.

### 3.2.1.c Radiative equilibrium

Thermal material immersed in the AGN environment comes into equilibrium with the radiation field. Ferland & Rees (1988) examine in detail the thermal and ionization

mechanisms which determine the equilibrium for clouds in an intense non-thermal radiation field, at distance  $\simeq 10^{15}$  from the central source.

At low densities the plasma is completely ionized and Compton cooling and heating tend to bring it to the Compton temperature determined by the spectrum of the ambient radiation. But at sufficiently high densities emission and absorption processes ( $\propto n^2$  per unit volume) dominate over scattering processes ( $\propto n$ ). At intermediate densities  $n \simeq 10^{10} \text{ cm}^{-3}$  three-fourth of the heating and cooling is due to Compton scattering and the remaining is due to free-free and free-bound processes. At  $n \simeq 10^{15} \text{ cm}^{-3}$  the temperature balance is between free-free (one-third) and free-bound processes. The lines (*e.g.* Ly $\alpha$ ) can be broadened by a strong Doppler effect and by Compton scattering, maybe producing large wings. At densities  $n \gtrsim 10^{16} \text{ cm}^{-3}$  the temperature of this matter reaches the equivalent blackbody temperature of the radiation field absorbed by the plasma, *i.e.*

$$T_{bb} = \left( \frac{L}{4R_0^2 c a} \right)^{1/4} \simeq 10^5 \left( \frac{L_{43}}{R_{13}^2} \right)^{1/4} \text{ K} \quad (3.4)$$

In Fig. 3.3 we report the dependence of the temperature as a function of density derived by Ferland & Rees (1988) assuming an incident spectrum which extends between 0.2 and 20 keV (and having ignored the cooling effects due to blue bump photons).

### 3.2.1.d Spectral effects

As already discussed in §1.1.1.d and §2.2.1, cold material can reprocess a fraction (depending *e.g.* on the beaming factor, geometry) of the primary non-thermal radiation, modifying the spectrum. The reprocessed radiation is reemitted as a quasi-thermal component. As a general condition [eq. (3.4)], the radiation emitted by thick material in a compact source of few Schwarzschild radii, is concentrated at UV frequencies (*e.g.* Rees 1984). In fact the blackbody temperature corresponding to the radiation energy density in a region of  $\sim 3R_s$  is given by  $T_{bb} \simeq 6 \times 10^5 (L/L_E)^{1/4} M_6^{-1/4} \text{ K}$ . Therefore the emission at UV frequencies indicates the presence of a thermalized component, independently on the physical distribution of the material.

The importance of pair reprocessing of rapidly varying (compact) sources has been outlined by Guilbert, Fabian & Rees (1983) and a more detailed analysis of the effects of cold matter is developed in Guilbert & Rees (1988) and Lightman & White (1988).

If optically thick to Thomson scattering, Comptonization produces features in the 10 keV–1 MeV region: a spectral steepening due to downscattering and possibly a soft X-ray component due to Comptonization of low energy photons. At energies lower than  $\sim$  few keV the effective cross section due to photoelectric absorption (mainly due to carbon and oxygen K shells opacities). attenuates the soft X-ray continuum.

The reprocessing cold matter could be either more distant from us than the central source (so that we see the primary and reflected radiation) or between the source and us, and the amount of reprocessing depends obviously on the covering factor. Brightness temperatures greater than  $T_{bb}$  in the optical would exclude thermal reprocessing.

Variability is predicted to be simultaneous at all frequencies (if the thermal response is fast) except at the energies which are Compton downscattered, which lag the primary source variations on timescale determined by the mean free path  $1/n\sigma_T$ .

Collin-Souffrin (1991) argues against the cold clouds reprocessing discussed in §3.3.2, but the arguments are based on the assumption that the cold material has to be very thick ( $N_H \sim 10^{23-25} \text{ cm}^{-2}$ ) to reprocess the UV flux, and its expected signatures on the spectrum (Lyman edge and X-ray absorption) have not been observed. But, as shown in §3.2.2., if the cloud density is sufficiently high the cold material can have a column density  $N_H \lesssim 10^{21} \text{ cm}^{-2}$ .

### 3.2.2 The properties of cold gas in the central engine

We now focus on the physical conditions of cold and very dense material ('cloud') and discuss the possibility suggested at the end of §3.1 that it absorbs the primary radiation up to optical-UV frequencies.

For simplicity in the following we refer to  $r$  as the radius of a (circular) area under which the central source sees each 'cloud', and to  $\Delta r$  as its thickness.

#### 3.2.2.a 'Macrophysics'

The dynamical and radiative equilibrium of clouds in a non-thermal radiation field from a compact object, have been carefully studied for the physical conditions in the BLR (§1.1.1.e). Overcoming the problems of the two phases model, Rees (1987) suggests that the clouds are confined by a strong magnetic field.

The densities we require exceed  $n \simeq 10^{17} \text{ cm}^{-3}$ , ten million times higher than the density of the broad line clouds; but we are now considering a region  $10^3$  times closer to the central engine.

Self-gravity is negligible. This implies that a external confining mechanism is required in order that the matter do not to disperse in the sound travel time. The clouds are assumed to be in pressure equilibrium with the magnetic field.

Let us estimate the radiation and magnetic energy densities. A simple upper limit to  $U_r$  is obtained by using the Eddington-limiting luminosity and  $R \sim 3R_s$ . Then

$$U_r \lesssim 9 \times 10^8 M_6^{-1} \text{ erg cm}^{-3}, \quad (3.5)$$

In practice,  $U_r$  could exceed this limit if radiation is trapped in the accretion flow or if the emission region (which may be transient) is smaller than the size of the central object. A less model-dependent limit is obtained from observations of X-ray variable AGN by using the observed luminosity and the variability timescale. Rewriting the luminosity in terms of the compactness parameter  $\ell$ , which is typically about 100 in the most rapidly X-ray variable AGN (see Fig. 2.1), we obtain

$$U_r = \frac{\ell}{\Delta t} \frac{m_e c}{4\pi\sigma_T} \approx 3 \times 10^6 \frac{\ell}{\Delta t} \text{ erg cm}^{-3}. \quad (3.6)$$

The ratio  $(\ell/\Delta t)$  ranges from 1 to about  $10^{-4} \text{ s}^{-1}$  in these sources. Of course there are several reasons (*e.g.* intrinsic variations do not occur at a speed  $c$ , or are smeared by scattering) why the observed values of  $\Delta t$  lead to overestimates of the size of the emission region, so the estimates of  $U_r$  obtained from eq. (3.6) are lower limits. Realistically we expect that  $U_r$  in the central engine of an AGN lies between estimates (3.5) and (3.6) above.

Therefore the intensity of an equipartition field can be written in term of the equivalent blackbody temperature as

$$B_{eq} \approx 9 \times 10^3 \left( \frac{\ell}{\Delta t} \right)^{1/2} = 4.4 \times 10^3 T_{bb,5}^2 \quad \text{G} \quad (3.7a)$$

In fact the magnetic energy density would be likely to exceed  $U_r$ : it could be in equipartition with the kinetic energy density (*i.e.*  $\simeq nkT_v$ ) of the gas which, in an object powered by accretion, would exceed  $U_r$  by  $(v_{in}/c)^{-1}$

$$B_{eq} \simeq 7 \times 10^5 \frac{1}{\eta_{-1}^{1/2}} \left( \frac{L}{L_E} \right)^{1/2} \left( \frac{R_s}{R} \right)^{5/4} \frac{1}{M_6^{1/2}} \left( \frac{v_{ff}}{v_{in}} \right)^{1/2} \quad \text{G} \quad (3.7b)$$

A reasonable approximation can be  $v_{ff} > v_{in}$ , because a strong magnetic field can itself provide viscosity.

In the case of a outflowing wind, carrying a luminosity  $L_{kin}$  (*e.g.* powered by extraction of spin energy of the black hole), the equipartition field is

$$B_{eq} \simeq 2 \times 10^4 \left( \frac{L}{L_E} \frac{L_{wind}}{L} \right)^{1/2} \left( \frac{R_s}{R_{13}} \right) \frac{1}{M_6^{1/2}} \left( \frac{c}{v_{out}} \right)^{1/2} \quad \text{G} \quad (3.7c)$$

A solid angle factor must be added in the case of non isotropic emission, as in a jet structure.

The field may pervade a corona above a thin disc, an ion torus, or a quasi-spherical inflow; what is important for our present discussion is that fields of  $10^4 - 10^5 \text{ G}$  are expected. The magnetic field is likely to have a complex structure, and to be flailing about with speeds of order the virial velocity  $v_v \sim c(R_s/R)^{1/2}$ .

The cold gas will not be uniform, but will be concentrated in a small fraction of the volume – one expects, in effect, a two-phase medium with an extreme contrast between conditions in the two phases.

The blackbody equivalent temperature in this region is  $T_{bb} \simeq 10^5 (U_{r,6})^{1/4}$  K. In this situation electron densities  $> 10^{16} \text{ cm}^{-3}$  are required for bremsstrahlung to dominate Compton heating and cooling (Ferland & Rees 1988).

Let us consider the properties of gas mixed up in this magnetosphere. In particular, we are interested in the scale of the clouds. A small volume filling factor is compatible with a large covering fraction if the clouds have a thickness very small compared to  $R$ . As we shall see, there are remarkably stringent limits on the cloud thickness – indeed this may be of ‘laboratory’ rather than cosmic scale, being measured only in metres.

The theoretically-simplest possibility is that the gas is confined to ‘pockets’ from which the magnetic field is excluded. The density would be such that thermal pressure fully balances the compressive magnetic stresses of the surroundings, so that  $3nkT = (B^2/8\pi)$ . For clouds with temperature  $T_5$  K this density is

$$n \simeq 10^{17} B_4^2 T_5^{-1} \text{ cm}^{-3} \quad (3.8)$$

In the absence of any other forces, there would be no constraint on the thickness or column density of cool material confined in this way. However, if this material is subject to a body-force such as gravity, then there is a scaleheight,  $\Delta r$ , given by  $\nabla p_B = \rho g$ , *i.e.*

$$\Delta r = kT/g m_p \quad (3.9)$$

where  $g$  is the effective acceleration. Taking  $g = GM/R^2$  yields a thickness or scaleheight of  $\Delta r_{grav}$  of order

$$\Delta r_{grav} \lesssim 10^4 M_6 T_5 \left( \frac{R}{R_s} \right)^2 \text{ cm} \quad (3.10)$$

in a static magnetosphere. This is the *maximum* thickness, in the direction of the effective gravity  $g$ , of a cool sheet or filament from which the field is excluded, whose maximum internal pressure equals the total external magnetic stress.

If dense cool plasma is not decoupled from the magnetic field, the lines of force threading it are distorted by the gravitational force acting on the dense plasma. This situation has been extensively studied in the context of solar prominences (Kippenhahn & Schluter, 1957; Priest, Hood & Anzer 1989, and references cited therein). A slab or ‘curtain’ geometry develops. The slab is compressed, and supported against gravity, by magnetic stresses due to a discontinuity in the tangential component of the field. When the field direction changes by a large angle ( $\sim \pi/2$ ) on passing through the slab, the confining pressure is  $B^2/8\pi$ , and the thickness of the slab that can be supported against gravity is of order  $\Delta r$  [eq. (3.10)].

There is thus a characteristic density – the density that yields a pressure  $B^2/8\pi$  for a kinetic temperature  $T_{bb}$ . Much thicker (or thinner) regions require much lower (or higher) densities, which are not compatible with the pressure of the magnetic field. There is then also, almost irrespective of how the dense plasma is linked to the field, a maximum thickness, inversely proportional to the effective gravity  $g$ .

But gravity is not the only (nor indeed the dominant) force acting on dense thermal plasma: there are two effects that could cause the effective  $g$  to be very much higher, and the thickness correspondingly less.

(i) If the plasma is coupled to the magnetic field, and the latter is in a dynamic state, with large-amplitude Alfvén waves being excited, then the instantaneous  $g$  may be higher, therefore reducing their scale height by a typical factor  $R/\lambda$ , where  $\lambda$  is the wavelength. This is hard to quantify precisely.

(ii) A more important (and, fortunately, more quantifiable) effect is radiation pressure. Let us examine the requirement that the blobs absorb through bremsstrahlung the radiation up to UV frequency. The optical depth is given by

$$\tau_{br} = 3.7 \times 10^8 \frac{n_e n_i}{T^{1/2} \nu^3} (1 - e^{-h\nu/kT}) \Delta r Z^2 g_{ff} \gtrsim 1 \quad (3.12)$$

where  $g_{ff}(\nu, T) \sim 1$  is the Gaunt factor (*e.g.* Rybicki & Lightman 1979), and we approximate  $Z \simeq 1$  and  $n_e \simeq n_i = n$ . For  $\nu_{br} \simeq \nu_{15}$  and  $N_H = n \Delta r \text{ cm}^{-2}$

$$n \gtrsim 2.3 \times 10^{18} \frac{T_5^{1/2} \nu_{15}^3}{N_{21}(1 - e^{-0.48\nu_{15}/T_5})} \text{ cm}^{-3} \quad (3.12)$$

This implies a gas pressure of about

$$p \gtrsim 3 \times 10^7 \frac{T_5^{3/2} \nu_{15}}{N_{21}(1 - e^{-0.48\nu_{15}/T_5})} \quad \text{and} \quad B \gtrsim 5 \times 10^4 \frac{T_5^{3/4} \nu_{15}^{3/2}}{N_{21}^{1/2}(1 - e^{-0.48\nu_{15}/T_5})^{1/2}} \quad (3.13)$$

where the last inequality follows from pressure equilibrium of eq. (3.8). The effect of the relativistic electrons pressure is negligible.

This means:

(i) That free-free absorption can be important in the optical and near UV band for a wide range of variable X-ray sources if  $B_4 \gtrsim 1$ .

(ii) At  $T_{bb} \simeq 10^5$  K, the gas is only partially ionized, therefore X-ray can be absorbed. The observational request of transparency to X-ray photons,  $N_{21} \sim 1$  (§3.2.1.a) in turn constraints the thickness of the cloud to be few meters in size,  $\Delta r < 450 N_{21} / T_5^{1/2} \nu_{15}^3 \text{ cm}$ .

Note that even if electron-positron pairs produced in the X-ray emission region could give free-free absorption in the IR-optical band without giving significant photoelectric absorption they cannot cool enough, due to heating by annihilation photons.



If the source is then operating near the Eddington limit, the radiation pressure due to free-free absorption causes the effective gravity on the clouds to be higher than the true gravity by a factor  $\gtrsim 1000$ . In fact the radiative acceleration is given by

$$g_{rad} \simeq \int_{\nu_{min}}^{\nu_{br}} \frac{L(\nu)}{4\pi R^2 c} d\nu \frac{1}{\Delta r m_p n} \quad \text{or} \quad \frac{g_{rad}}{g} \simeq \frac{L(< \nu_{br})}{L_E} \frac{1}{\tau_T} \quad (3.14)$$

where for simplicity, we assumed a step function for the dependence of the absorption coefficient on frequency. This is equivalent to saying that, at these high densities, the cross section for radiation peaking at around  $10^{15}$  Hz is larger than Thomson scattering by  $\sim 10^3$ . The radiation pressure on dense material therefore exceeds gravity by this same factor  $\times (L/L_E)$ .

So the effective gravity (now acting outward) is given by  $g \simeq g_{rad}$  and implies a maximum scaleheight, or prominence thickness, thousands of times smaller than would be implied by eq. (3.10). We reach the remarkable conclusion that the gas would be in sheets or filaments that are, at least in one dimension, only a few metres across. The absorption property of the clouds required to account for the presence of an equipartition magnetic field implies that they are squeezed by the radiation to have  $N_H \lesssim N_{21}$ .

Would the gas be expected to acquire this type of structure? Even if gas started off at  $T_v$ , and were uniformly spread, it would cool on a timescale much less than  $\Delta t$  to the Compton temperature. (Cyclotron/synchrotron cooling, which would otherwise be even more effective, can be impeded by reabsorption). The gas could then move along field lines under the action of gravity and radiation pressure, being compressed into a region whose filling factor would be only  $T_C/T_v$ . Once this degree of compression had been achieved, bremsstrahlung cooling could take over: as a consequence of the associated increase in opacity, the effective (negative) gravity  $g$  due to radiation pressure rises and the maximal density contrast is then achieved.

Since the clouds are so thin, a small volume filling factor is compatible with a large covering factor and indeed our picture requires a covering factor of these small clouds of about one. How large the covering factor actually is depends on the flow pattern and magnetic field configuration, but we can readily see that a large covering factor is generic in the case when gas is coupled to the field lines. The combined effect of radiation pressure and cooling drives the material outward along each magnetic flux tube to the place where the magnetic field is perpendicular to the direction of the radiation pressure. If the field geometry is complicated (as expected if the magnetic field is attached to an accretion disc) then the entire solid angle may be covered. In the special case of a dipole field and a radiation source symmetrical around the centre, the matter would be concentrated into a plane equatorial sheet. In the generic case the gas may still be in sheets, but these would

be non-planar. We can see this in the simple case of a dipole when the radiation source is displaced from the centre.

Radiation pressure also explains why there are not many clouds along each line of sight. Most of the radiation that supplies the pressure is absorbed in the first cloud along the line of sight and reradiated at the equilibrium temperature. Consequently it can not be reabsorbed by lower density material further out, which therefore is not compressed by radiation pressure to reach high density.

Realistically, the situation will not be static, and accretion and Alfvén waves will break up any large structures. Note that the overall dynamical timescale in the region,  $R/c$  is measured in hours, and individual sheets or filaments may persist for even shorter periods.

The sound (and Alfvén) timescales are in fact given by  $t_s \sim 3 \times 10^{-4} \Delta r_3 T_5^{-1/2}$  s, while the radiative ones (obviously  $t_C > t_{br}$ ) are of the order of  $t_{br} \simeq 6 \times 10^{-5} T_5^{1/2} / n_{18}$  s and  $t_C \sim 50 / T_5^4$  s.

### 3.2.2.b ‘Microphysics’

Note that due to the presence of the strong magnetic field and the very high density, the clouds can be treated as a plasma. In fact the Larmor radii for electron and protons are given by  $r_L^e \simeq 10^{-3} T_5^{1/2} B_4^{-1} \simeq r_L^p \sqrt{m_e/m_p}$  cm (where it is assumed that protons and electrons have the same temperature). The Debye length is given by  $\lambda_D \simeq 3 \times 10^{-6} (T_5/n_{18})^{1/2}$  cm, with an interparticle distance of about  $\sim 10^{-6} n_{18}^{-1/3}$  cm. All these lengthscales are typically are much smaller than the scaleheight of the cold matter.

The typical energy exchange timescale  $t_{e,p} \simeq 10^{-10} T_5^{3/2} n_{18}^{-1} \ll t_{br}$  and therefore the (longer) mean free path is approximately given by  $\lambda_{e,p} \simeq \beta_e c t_{e,p} \simeq 3 \times 10^{-5} T_5^2 n_{18}^{-1}$  cm  $\ll \Delta r$ . consistently with the assumption of one temperature plasma.

Finally, a general argument in order to estimate a lower limit on the dimension  $\Delta r$ , is imposed by the requirement that the diffusion timescale of the magnetic field in the plasma is longer than the radiative timescale, such that the cloud can be confined by the magnetic field for a time sufficient to absorb and reemit. (The argument is relevant if the mean free path due to collision is less or comparable to the Larmor radius and smaller than the size of the region). The plasma diffusion timescale can be defined from  $\partial B / \partial t = (c/4\pi\sigma) \nabla^2 B + \nabla \times (\beta_b c \times B)$ , where  $\sigma$  is the plasma conductivity and therefore the timescale is given by  $t_{diff} \sim \Delta r^2 4\pi\sigma/c \simeq 5 \times 10^{10} N_{21}^2 T_5^{3/2} / n_{18}^2$  s where we estimate  $\sigma \simeq ne^2/m_e t_{coll} \simeq 3.6 \times 10^6 T^{3/2}$  (Boyd & Sanderson 1969). Diffusion effects are negligible.

Note that the plasma frequency  $\nu_p \simeq 9 \times 10^{12} n_{18}^{1/2}$  Hz is below the emission frequency of the clouds.

The limits on parameters described above are reported in Fig. 3.4, in the  $n - T$  parameter space. It can be seen in fact that the allowed region is relatively constrained around the values of  $n$  and  $T$  for which reprocessing of the primary radiation is effective, *i.e.*  $T \simeq 10^5$  K and  $n \simeq 10^{18} \text{ cm}^{-3}$ . The line labelled 0.1 keV determines an indicative ‘maximum’ frequency which can be absorbed through bremsstrahlung without contradicting the observations.

The limits corresponding to each line are labelled on the figure. The constraints which are not shown are satisfied in all that parameter space.

### 3.3 DISCUSSION

We summarize the picture outlined in §3.1 and §3.2: a central compact X-ray emitting region consists of relativistic electrons, accelerated above an accretion disc, producing SSC radiation on an equipartition-strength magnetic field. It then pressure confines many small, dense, cold gas clouds which, like a blanket, reprocess most of the radiation, and reemit it in the UV band, causing the optical and UV photosphere to lie beyond the X-ray emission region. The opacity in the region is plausibly due to free-free absorption. There may, of course, be regions of lower density at larger radii which radiates as synchrotron the observed radio-optical continuum, required by the strong polarization observed at least in HPQs.

In fact since we cannot argue that the X-rays are also absorbed, we must fall back on SSC emission as the source of the non-thermal X-ray emission. In order that this can apply, the energy density of the EUV bump in the X-ray emission region must be less than the energy density of the synchrotron radiation. This can easily be achieved by using a small dilution factor, meaning that the quasi-blackbody component of the EUV bump is emitted by a much larger region than the X-ray emission.

The lack of correlated optical and X-ray variability in NGC 4051 is now explained as due to free-free absorption of the direct optical SSC radiation from the X-ray emission region.

If, as assumed above, the gas is mixed up with the plasma emitting the primary spectrum, on a scale comparable to that inferred from the X-ray variability timescale, not all of the primary spectrum is absorbed. The detailed shape of the optical/UV spectrum then depends on the precise distribution of the cold gas. Alternatively, if the clouds are external to the primary emission region, the equilibrium temperature will be lower than that estimated earlier and perhaps smaller amounts of cold gas could be effective in absorbing the primary optical/UV radiation.

This picture does not apply to BL Lacs, where beaming effects probably dominate (for example cold blobs could not form because a stronger radiation flux heat them). Note

that in the galactic source SS433 there are some evidences of the presence of very dense cold matter inside the jets, with  $T \simeq 10^4$  K.

We have shown that the plausible scale-height and column density of cold gas trapped by the equipartition magnetic field in the X-ray emission region of AGN are consistent with both a low X-ray opacity and the requirement that the optical/IR flux produced by the synchrotron self-Compton process is absorbed. Small quantities of cold gas thereby have an important influence on the observed spectrum. The absorbed primary flux is reemitted as quasi-blackbody radiation at the equilibrium temperature.

Obviously the amount of thermalized radiation at UV frequencies depends on the luminosity of the primary (not observed) emission and on the covering factor and it is not possible to estimate it from the observed X-ray radiation. If the X-ray emission is due to synchrotron extending to high energy, the reprocessed flux cannot exceed its extrapolation to lower frequencies, but if Compton emission contributes mainly to X-rays, the amount of the absorbed primary radiation depends on the density of relativistic electrons. It is not clear therefore if the whole blue bump emission can be accounted by the radiation reprocessed by the clouds or if the contribution from direct (or reprocessed) emission from *e.g.* an accretion disc is requested.

In the picture described no sharp Lyman edges (as predicted by many disc models) is expected to be observable. Any strong feature emitted by the clouds is broadened and smeared by both the strong Doppler effect due to the high velocities of the matter and also by the motion induced by Alfvén waves in the plasma.

Another advantage with respect to the standard disc model is that the time lag between optical/UV and X-ray variations will be very short. The upper limits on delays between variations in the optical and UV bands, recently measured (§1.1.1.a) cannot be accounted for in the standard disc model. Furthermore simultaneous variations in the optical-UV and X-ray bands (§1.1.3.c) have been reported, consistently with the possibility that the same primary process is responsible for the emission in both bands.

Variability predictions are not well determined from the model. Low energy flux could vary when clouds along the line of sight are destroyed and primary radiation is directly observed. The relative amplitude of variability at different frequencies and consequently the doubling timescale, depend on the fraction of reprocessed flux.

Quite interestingly it could be noted that the presence of a strong magnetic field in the central region could account for the lack of polarized radiation which is expected from an accretion disc (§1.1.1.a). In fact the Faraday depth is  $\Delta\phi \sim 350\tau_T B_4 \nu_{15}^{-2}$  rad.

The presence of cold dense clouds close or in the primary emitting region, and the clouds of BLR and NLR are probably a continuum distribution on different scales and physical parameters like temperature and density, which surround the core region, as

recent observations of the BLR suggest (§1.1.1.e). The gas is presumably continuously supplied by plasma outflows.

The dense cold gas has a high covering fraction and a very low filling factor. The situation may resemble that of solar prominences where small filaments of cool gas are supported above the surface by magnetic fields, except in this case the magnetic field is holding the clouds back against the radiation pressure (Fig. 5.14).

Slightly thicker regions of partially-ionized gas (warm absorber, §1.1.1.c) are also a possible source of free-free absorption. If the absorption is in the optical, then the required density of the warm material is comparable to, or exceeds, that considered above by about an order of magnitude so that it is difficult to see why the gas has not cooled to a low equilibrium temperature.

Further observations and analysis of existing data are required to determine stronger limits or measurements of the column density intrinsic to the quasi-power-law X-ray emission region. The free-free absorbing clouds do not necessarily cover all the region emitting the soft X-ray excess, which must be distinguished by its spectrum and variability. Future optical and UV studies of rapidly X-ray varying AGN, *e.g.* using the High Speed Photometer on HST, should be very important to determine the maximum free-free absorption frequency and improving the constraints on small dense clouds.

Table 3.1. Source parameters

Source	z	$R_o$ (cm)	$T_{bb}$ (K)	$\gamma_{max}^*$	$U_x$	$U_e$	$U_B$
NGC 4051	0.0023	$9.0 \times 10^{12}$	$3.6 \times 10^4$	42	$5.9 \times 10^4$	$1.1 \times 10^5$	$2.5 \times 10^4$
NGC 6814	0.0053	$1.5 \times 10^{12}$	$2.4 \times 10^4$	39	$6.4 \times 10^7$	$3.1 \times 10^5$	$4.8 \times 10^6$
3C273	0.158	$1.1 \times 10^{15}$	$8.5 \times 10^4$	205	$2.1 \times 10^6$	$2.2 \times 10^2$	$2.5 \times 10^3$
3C279	0.538	$2.6 \times 10^{14}$	$3.1 \times 10^5$	18	$2.8 \times 10^7$	$4.2 \times 10^2$	$> 4 \times 10^8$
H1821+64	0.297	$2.0 \times 10^{16}$	$1.6 \times 10^4$	71.7	$2.4 \times 10^5$	3.1	$1.8 \times 10^3$

Rest frame parameters for each source (assuming  $\delta = 1$ ).  $B_0$  is the dimension of the X-ray emitting region estimated from the variability timescale.  $T_{bb}$  (K) is the temperature of the maximum blackbody, emitted in a region of dimension  $R_0$  and consistent with the data.  $\gamma_{max}^* = (3\nu_x/4\nu_{bb})^{1/2}$  indicates the minimum value of the Lorentz factor needed to emit the highest observed frequency by scattering EUV photons.  $U_x$  (erg cm $^{-3}$ ) is the radiation energy density estimated integrating the X-ray spectrum up to the maximum observed frequency;  $U_e$  the energy density in the relativistic electrons and  $U_B$  is the estimated upper limit to the magnetic energy density, corresponding again to the minimum Lorentz factor  $\gamma_{max}^*$ .

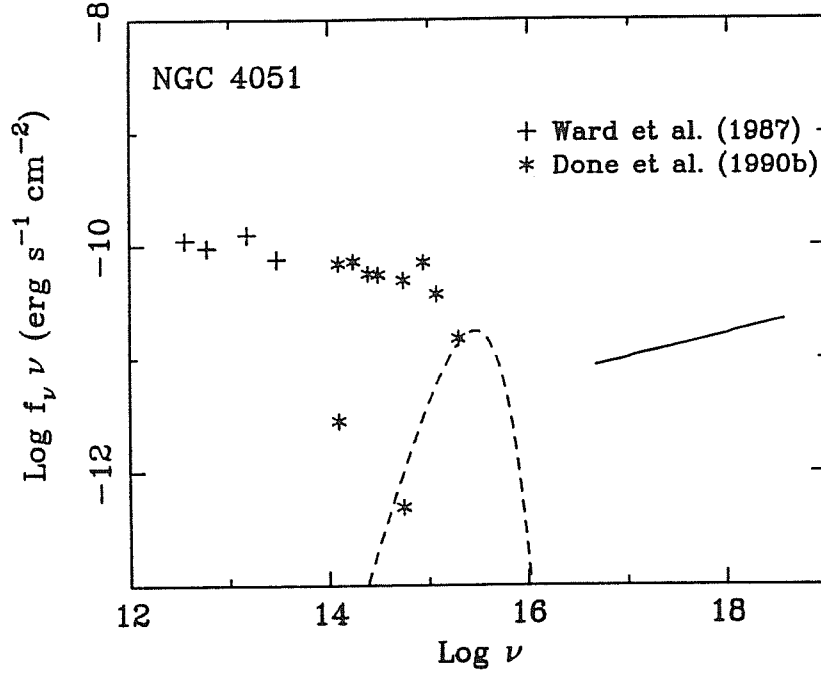


**Fig. 3.1a** Overall spectral distribution for the Seyfert galaxy NGC 4051. The composite spectrum is obtained from the simultaneous IR, optical (B band) and X-ray data reported in Done *et al.* (1990). The best-fitting GINGA X-ray power-law spectrum is  $F(\nu) = 2.74 \times 10^{-15} \nu^{-0.79} \text{ erg cm}^{-2} \text{ s}^{-1} \text{ Hz}^{-1}$  (extrapolated as described in §3.1.3), after correction for galactic absorption. The two low-flux points in the IR and optical bands correspond to the maximum nuclear contribution allowed to vary simultaneously with the X-rays (Done *et al.* 1990). The UV points are from IUE spectra (SWP33531 and LWP13231). The dashed line is the maximum temperature ( $T_{bb} \simeq 3.6 \times 10^4 \text{ K}$  in the observer frame) EUV blackbody consistent with the data. The emission region of the blackbody is assumed to be coincident with the X-ray one. The data between 10 and  $83 \mu\text{m}$  are IRAS data, taken from Ward *et al.* (1987).

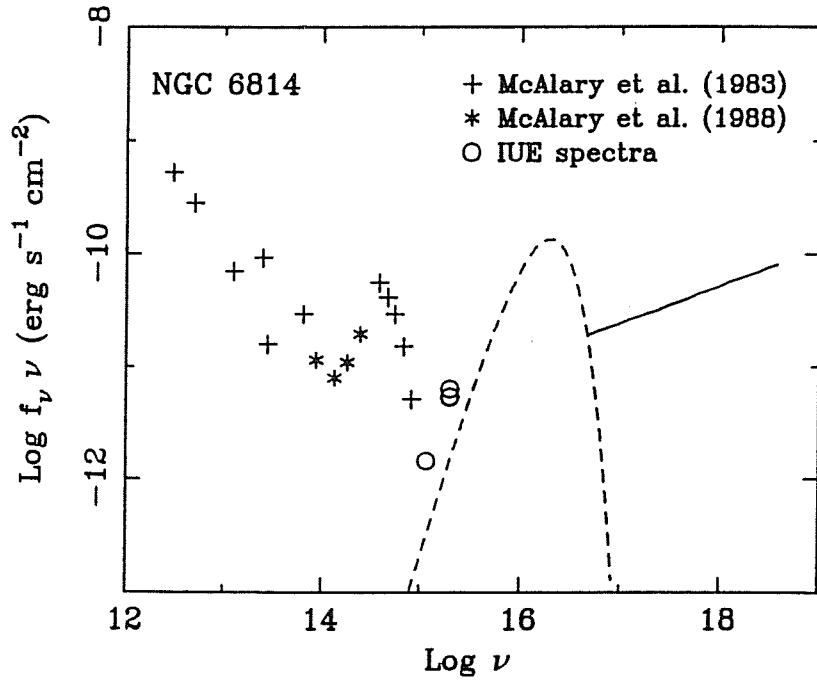


**Fig. 3.1b** Spectrum of the Seyfert galaxy NGC 6814. The IR-optical data are from McAlary *et al.* (1983) and McAlary *et al.* (1988): the J,H,K,L band fluxes are obtained after subtracting the stellar contribution. The UV data are averages of two short (SWP10680L and SWP10693L) and one long (LWR8961R) wavelength IUE spectra. We use the X-ray state reported by Tennant *et al.* (1981) (best-fitting power-law  $F(\nu) = 5.9 \times 10^{-17} \nu^{-0.67} \text{ erg cm}^{-2} \text{ s}^{-1} \text{ Hz}^{-1}$ ) from HEAO 1 observations. The maximum luminosity blackbody has a temperature  $T_{bb} \simeq 2.4 \times 10^4 \text{ K}$  (observer frame).

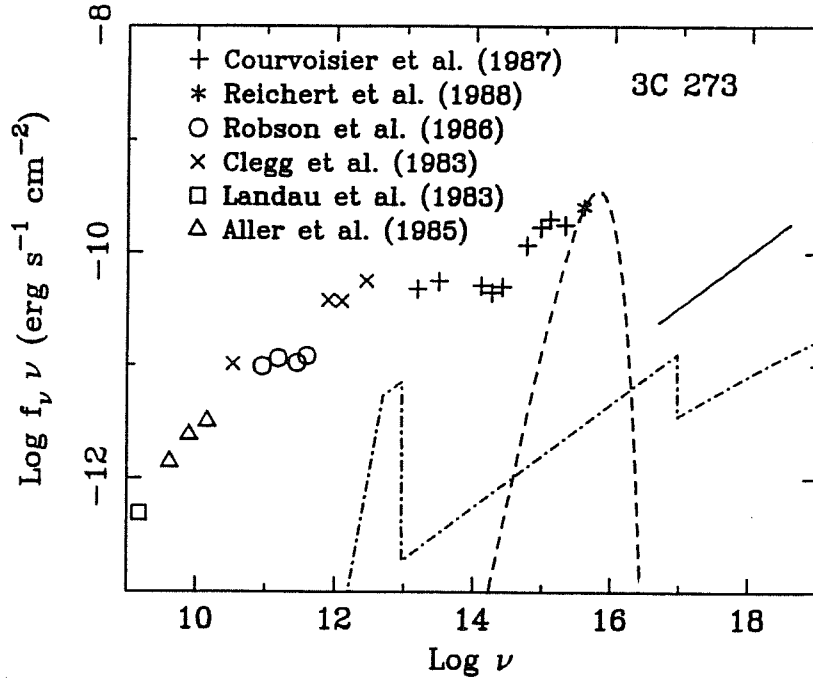


**Fig. 3.1c** The overall spectrum for 3C 273 is obtained with data from Courvoisier *et al.* (1987), Robson *et al.* (1986), Clegg *et al.* (1983), Landau *et al.* (1983), Aller *et al.* (1985). The UV datum at  $\lambda_{obs} = 916 \text{ \AA}$  is from Reichert *et al.* (1988). The reported blackbody has a temperature of  $T_{bb} \simeq 7.3 \times 10^4 \text{ K}$  (observer frame). The X-ray power-law ( $F(\nu) = 5.2 \times 10^{-19} \nu^{-0.54} \text{ erg cm}^{-2} \text{ s}^{-1} \text{ Hz}^{-1}$ ) refers to the EXOSAT observation reported by Turner *et al.* (1990). The dash-dot line shows an SSC spectrum, computed for  $B = 200 \text{ G}$  and  $\gamma_{max} = 120$ .



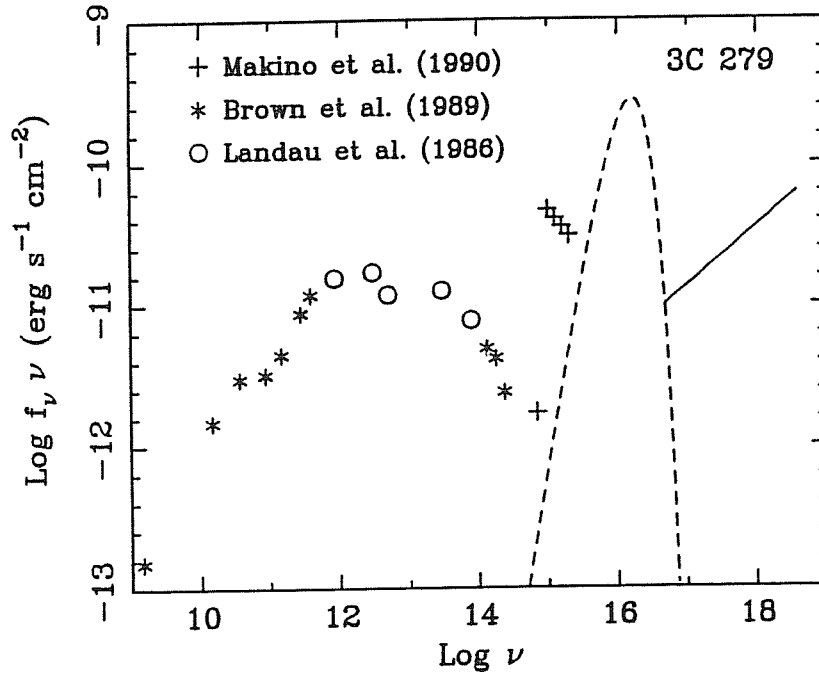


Fig. 3.1d The spectrum of 3C 279 constructed from the data of Makino *et al.* (1990), Brown *et al.* (1989), Landau *et al.* (1986). The maximum temperature of the reported blackbody is  $T_{bb} \simeq 2 \times 10^5$  K (observer's frame). The X-ray data are from Makino *et al.* (1990) who reports a best-fitting power-law  $F(\nu) = 9.75 \times 10^{-19} \nu^{-0.58} \text{ erg cm}^{-2} \text{ s}^{-1} \text{ Hz}^{-1}$  from a GINGA observation.

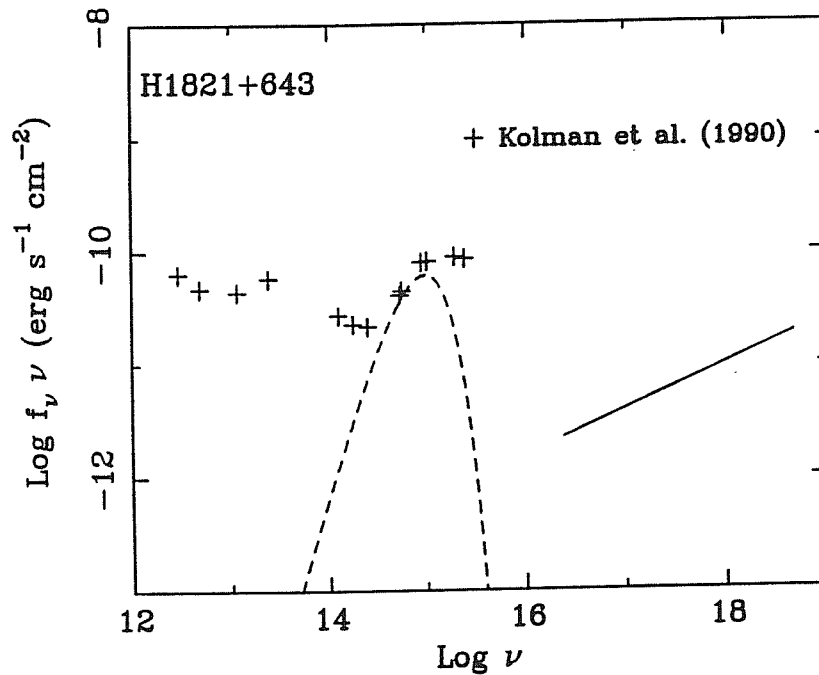
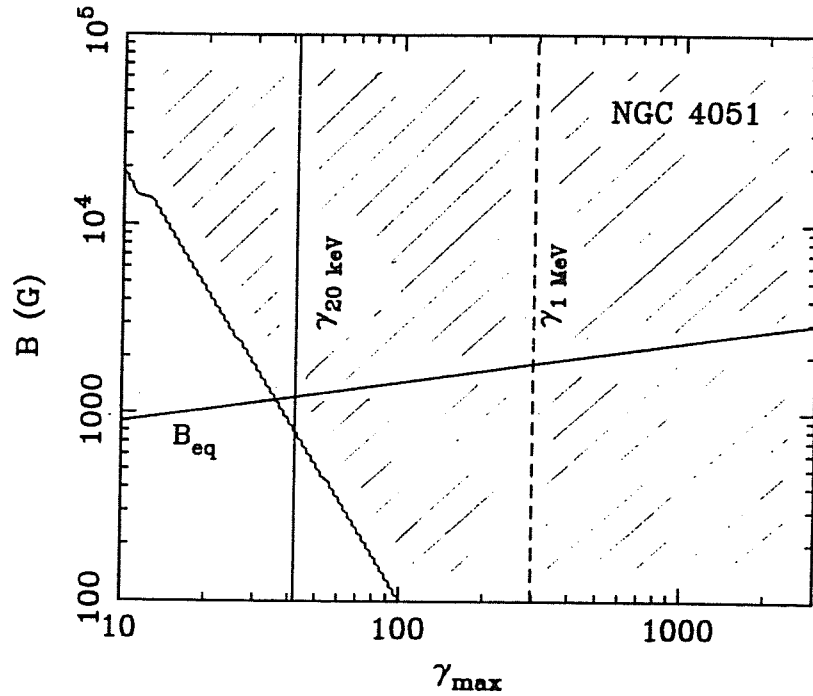
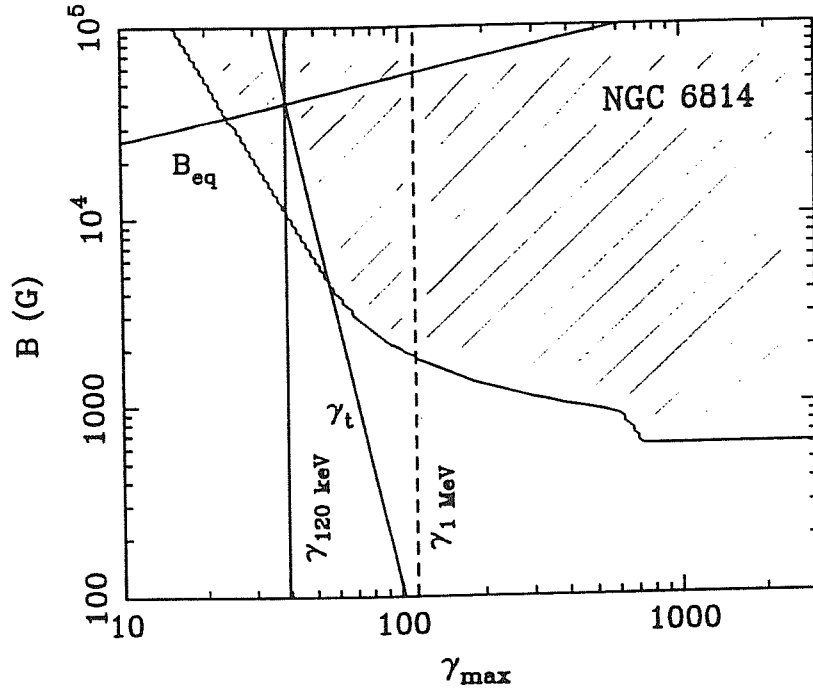


Fig. 3.1e The data for the source H1821+643 are from Kolman *et al.* (1990). The blackbody has a temperature of  $T_{bb} \simeq 1.2 \times 10^4$  K (observer's frame). The X-ray power-law ( $F(\nu) = 6.18 \times 10^{-19} \nu^{-0.6} \text{ erg cm}^{-2} \text{ s}^{-1} \text{ Hz}^{-1}$ ) is a fit to *Einstein Observatory* data (0.1–3.5 keV) and is consistent both with EXOSAT and GINGA results at higher energies.



**Fig. 3.2a** The figure shows the maximum allowed magnetic field versus the maximum Lorentz factor of the electron distribution for NGC 4051. The region on the right side of the oblique line (shaded area) is the region not allowed by the overall spectrum of the source. The vertical continuous line represents the minimum value of the Lorentz factor needed to produce the observed X-ray frequency by scattering the soft ‘blue bump’ photons; the permitted region therefore extends to the right of this line. The dashed vertical line represents the value of  $\gamma_{max}$  required to emit a reference frequency of 1 MeV. The line labelled  $B_{eq}$  shows the magnetic field in equipartition with the radiation energy density (which depends on the extension of the X-ray spectrum).



**Fig. 3.2b** As Fig. 3.2a but for the source NGC 6814. The dash-dot line shows the dependence of the Lorentz factor  $\gamma_t$  of the electrons, mainly emitting at the synchrotron self-absorption frequency, as a function of  $B$ . The limits on the magnetic field are imposed by the self-absorbed fluxes on the left-hand side of this line.

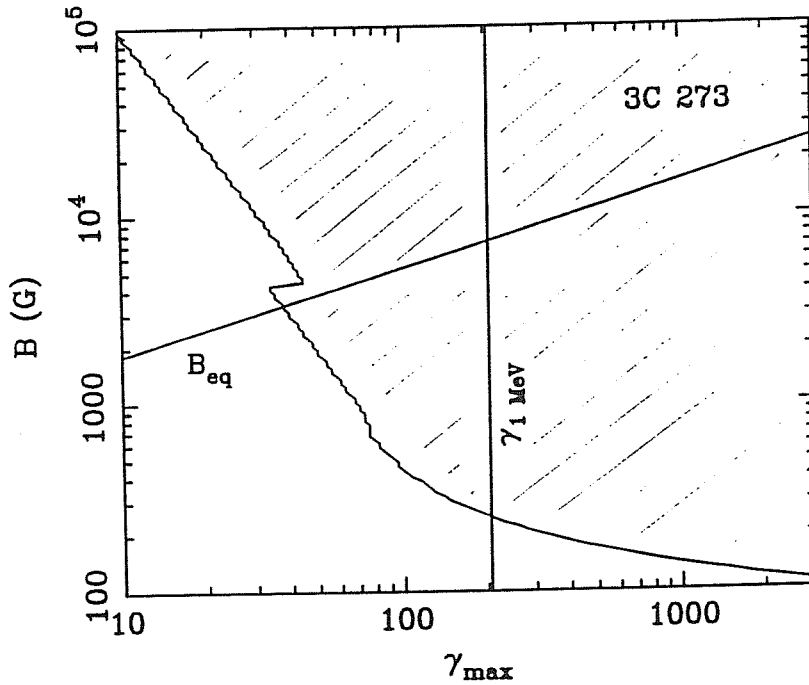


**Fig. 3.2c** As Fig. 3.2a but for 3C273. The source has been observed in  $\gamma$ -rays, but below the extrapolation of the X-ray spectrum; we assume that the X-ray power law extends up to 1 MeV.

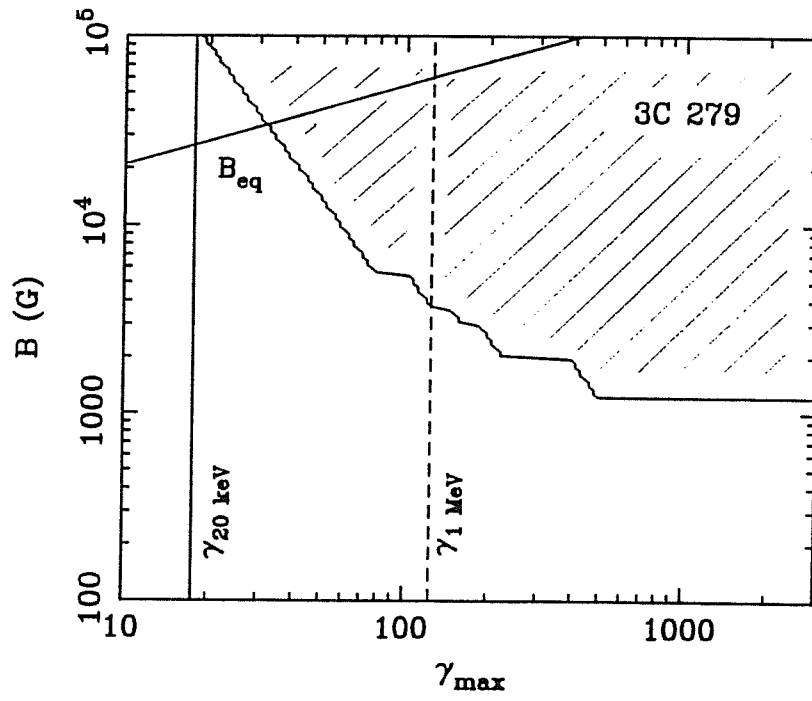


Fig. 3.2d As Fig. 3.2a but for the source 3C279.

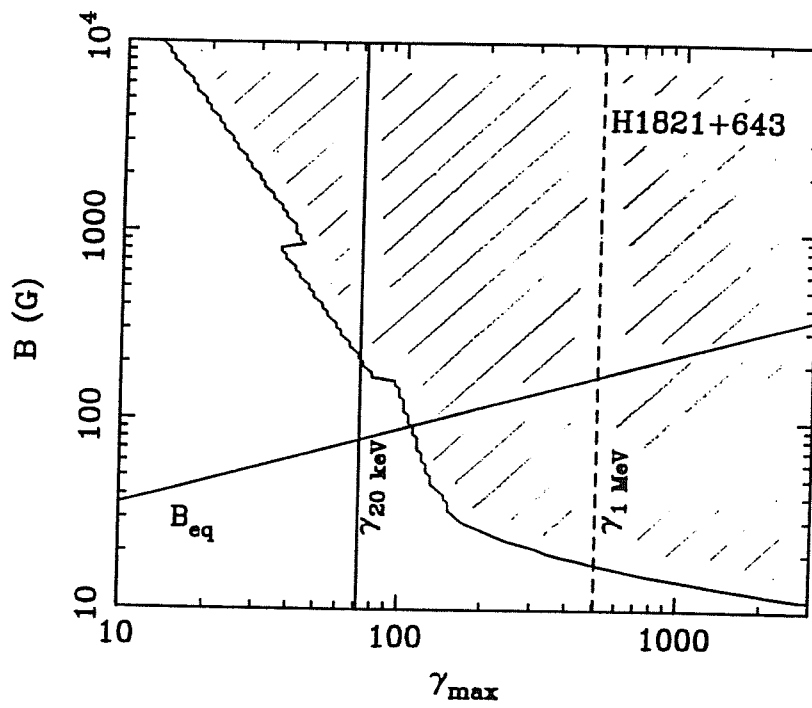
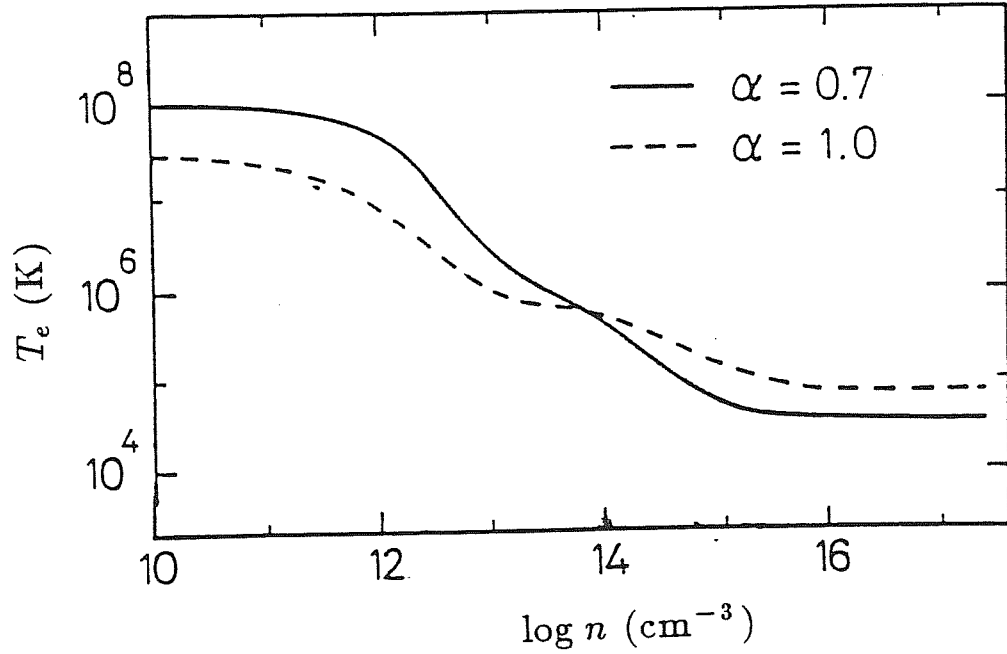
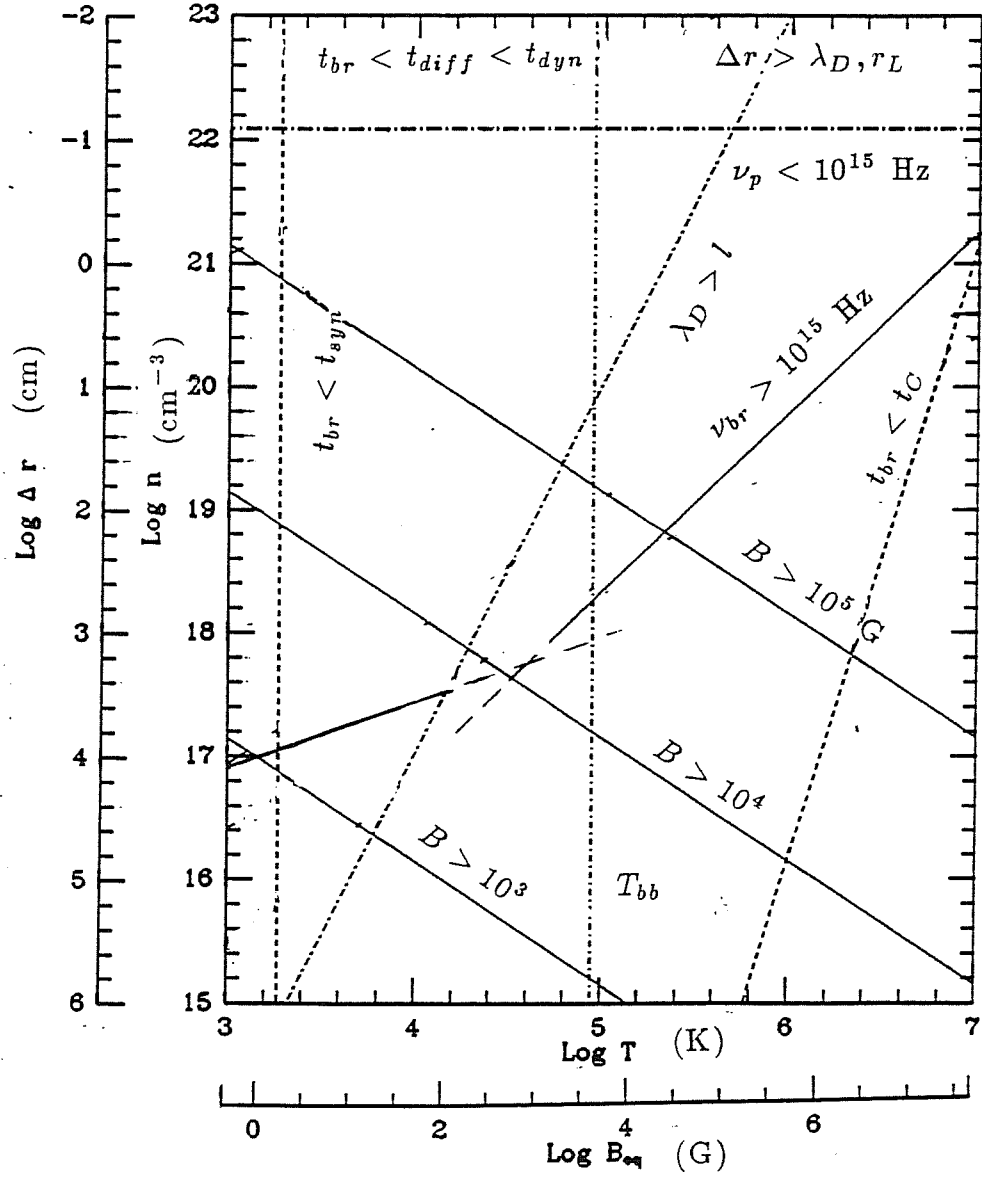


Fig. 3.2e As Fig. 3.2a but for the source H1821+643.



**Fig. 3.3** Equilibrium temperature of a cloud located at  $R_{15}$  cm from a non-thermal source (with  $L_{45}$ ) as a function of the gas density. The two curves refer to different spectral indices of the continuum radiation. (From Ferland & Rees 1988). At low density the radiation field dominates and the gas reaches the Compton temperature, while at very high densities ( $\gtrsim 10^{16} \text{ cm}^{-3}$ ) the system tends toward the thermodynamical equilibrium at an ‘equivalent’ blackbody temperature.



**Fig. 3.4** The figure illustrates the constraints on the temperature and the density of the cold matter, which would reprocess the primary SSC radiation. We assumed  $N_H = 10^{21} \text{ cm}^{-2}$  and  $p_{gas} = p_B$ . The condition on the column density imposes a maximum thickness  $\Delta r$  for each value of  $n$ .  $B_{eq}$  refers to the field in equipartition with the radiation energy density. All the lines are labelled (with the symbols defined in §3.2.2): the inequalities are satisfied in the semiplane where the label is located. The equivalent blackbody temperature  $T_{bb}$  is for  $L_{43}$  and  $R_{13}$ . The allowed region is quite small, around  $T_5$  and  $n_{18}$ .

## Chapter 4. The inner jet: high energy emission

Evidence has been accumulating that the strong non-thermal continuum responsible for the high polarization and rapid variability of blazars is produced as synchrotron and SSC emission by relativistic plasma within inhomogeneous collimated regions, the existence of which is manifest in the radio domain, on pc-scale (§1.2;§5). In fact a homogeneous source is inadequate to account for the broad band spectrum of blazars, in particular for its spectral curvature (§1.1.2.b). The possible parameterization of physical quantities varying along the axis of the flow, has been discussed by various authors after the seminal paper of Blandford & Rees (1978).

Models of emission from relativistic jets can naturally explain the observed overall spectra, but are only weakly constrained by the spectral shape alone (*e.g.* Königl 1989; Marscher 1992). However, stringent constraints are obtained when information on the spectral shape is combined with that on the variability timescales at different frequencies.

First (§4.1) we study in some detail the effects of a perturbation propagating along an inhomogeneous jet in order to compare the model predictions with observed high energy variability of blazars. The time evolution of synchrotron and first order SSC radiations are computed numerically and approximate analytic formulae are given. The evolution of the spectral shape with time and the light curves at fixed frequencies are presented and discussed in detail. The results are compared with observations. We estimate the expected amplitude of variability assuming that the perturbation is due to a planar relativistic shock wave. The dependence of the observed amplitude on the viewing angle and on the shock and fluid velocities is discussed.

We then concentrate on a specific source and consider (§4.2) the recent  $\gamma$ -ray observation of the blazar 3C 279. Independently of any model the general constraints that the variable  $\gamma$ -ray flux imposes on the degree of beaming and on the physical parameters of the  $\gamma$ -ray emitting region are derived. A highly variable  $\gamma$ -ray emission is a new, independent indication in support of the beaming hypothesis (§5.3). In particular we show that the  $\gamma$ -ray flux can be due to SSC emission from the same type of relativistic jet examined in §4.1. The results are particularly relevant because of the increasing number of  $\gamma$ -ray emitting sources which have been detected (§1.1.2.c).

#### 4.1 EMISSION FROM JETS

The earlier and simpler interpretation of the blazar spectra assumed that the radiation was SSC emission from spherical homogeneous regions (§2.2). Taking into account relativistic effects to ‘solve’ the ‘Compton catastrophe’ problem, Doppler factors  $> 25$  were estimated (PKS 2155–304, Urry & Mushotsky 1982; PKS 0537–441, Maraschi *et al.* 1983). Such high values of  $\delta$  and VLBI observations which show the presence of different emitting components at different frequencies, suggested that an inhomogeneous model is more probable. The flat radio spectra are interpreted as the superposition of synchrotron spectra from different regions self-absorbed at different frequencies. The overall spectrum of *e.g.* NRAO 140 has been reproduced from the superposition of the different components. Finally, the smoothness of the spectrum and the variability correlations at different energies suggest that these regions are connected and, together with the direct observations of collimated structures, lead to the development of emission models from inhomogeneous jets (Marscher 1977).

A physical description of the dynamic and emission properties of jets is still lacking. Therefore the simplest assumption is that physical quantities (magnetic field, emitting particle density and their maximum energies, bulk velocity) are functions of the distance along the jet and constant on its sections. These dependences are parameterised as power-laws and this in turn implies power-law dependences for the maximum and minimum emitted frequencies and emissivities. A power-law dependence of physical quantities on five orders of magnitude in size (from 1 pc to 100 kpc) describes the observations of the jet of 3C120 (Walker, Benson & Unwin 1987).

Different models have been developed on the basis of different shapes of the jet (parabolic or conical, *i.e.* hydrostatic confined or free expanding beam) and the behaviour of the maximum energy of emitting electrons with distance (Blandford & Königl 1979; Marscher 1977, 1980; Königl 1981; Reynolds 1982; Ghisellini, Maraschi & Treves 1985; Ghisellini & Maraschi 1989).

All the models describe the observed spectra, from radio to X-rays, as a superposition of locally emitted SSC spectra in an unresolved, relativistic and stationary jet (for a comparison of the models see also Königl 1989). However they predict different behaviour of variability. The models are characterized by the competition between the external and internal emitting regions of the jet in dominating the emission at a given frequency (*i.e.* the competition between increasing volume and decreasing emissivity along the jet). This in turn depends on the gradients of the physical quantities (typical values of which correspond to the conservation of the particles flux and the parallel or perpendicular magnetic field components).

The model developed by Ghisellini *et al.* (1985), which assumes a jet with an inner parabolic part and a conical outer part, implies naturally that high frequencies are



produced in the inner (and smaller) part of the paraboloid, as synchrotron radiation, and lower frequencies are emitted at increasing distance (and dimensions) along the jet. The predicted X-ray spectrum can be either steep, due to the superposition of locally emitted flux, and showing continuity with the UV spectrum or flat if produced as self-Compton emission, with an hardening with respect to the optical-UV slope. These two behaviours seem in agreement with the 'bimodal' X-ray spectra of blazars and in particular of the X-ray selected and radio-selected BL Lacs (§1.1.2.b; §4.2).

An opposite dependence (increasing dimensions of the emitting region for increasing frequency) is predicted by the model of Marscher (1980). The model of Königl (1981) predicts that very low and high frequencies are emitted in the same large region, while intermediate frequencies can be produced in the smaller part of the jet, implying correlated variability between low and high energies. Reynolds' (1982) approach substantially includes all the models, physically justifying the assumed gradients and the dynamical acceleration of the emitting fluid.

Therefore multifrequency monitoring programs, coupling spectral and time information, can impose strong constraints and help to discriminate among the various emission models. They have already yielded a large quantity of data in the radio frequency domain, allowing reconstruction of the spectral evolution of outbursts (and sometimes of polarization) from mm to cm wavelengths. This information has been used to model the physical evolution of the flaring components in terms of shock waves within the jet, as envisaged in the pioneering work of Blandford and Rees (1978). However detailed models based on the idea of adiabatically expanding shock waves which propagate along the jet has been developed quite recently. In this models a part or the whole time dependent evolution of the flux at low frequencies is due to the decrease in the optical depth of a 'perturbed' region during the expansion.

Hughes *et al.* (1985) have shown that a pure adiabatic expanding region (van der Laan 1966) cannot explain the observed radio variations of BL Lac and reproduced the light curve of the total and polarized radio fluxes by best-fitting the parameters of a time dependent model with three components. More recently Hughes, Aller & Aller (1989) have deduced the Lorentz factor required to obtain the observed variations ( $\Gamma \simeq 2.5$  with a compression factor  $k \simeq 2$ ) assuming a 'reverse' shock wave (see also Jones 1988) and compare it to the value derived from VLBI observations. A similar approach has been also considered by O'Dell *et al.* (1988) and O'Dell (1988) for the radio variability of AO 0235+164. Including delay effects due to the transverse dimension of the jet and different time profiles for injection, the dependence of luminosity on frequency and time is derived. A shock moving at constant velocity along a conical jet has been considered by Marscher & Gear (1985) in order to explain a 'flare' in the mm-IR region of 3C 273, assuming a stationary and a varying components: the different dependence on volume

of the self-absorption frequency and flux, is taken as an indication that the variations are due to the expansion of the shocked region. During its propagation, the emission is dominated progressively by Compton, synchrotron and adiabatic losses. The amplitude of the variations imposes limits on the strength of the shock.

Other kind of studies suggested the presence of shock waves. Cawthorne & Wardle (1988) derive two different velocities from the intense variable polarization of OJ 287 and the observed VLBI motion. Shocks are invoked to accelerate the particles emitting in the jet of M87 (Per  z-Fournon *et al.* 1988) and 3C273 (Meisenheimer & Heavens 1986). As already mentioned a shock wave compresses the perpendicular component of the magnetic field, increasing the degree of linear polarization, as often observed in radio superluminal knots (*e.g.* Gabuzda *et al.* 1989; §1.2.1.b).

Multifrequency programs have been performed also in the IR–optical–UV and X–ray ranges (§1.1.3.c), despite the obvious problems associated with using different observatories and techniques and despite the intrinsic difficulty, that a more frequent sampling is required at higher frequencies due to the decreasing variability timescales.

In the following we first quantify the amplitude of the observed high energy variability and then, after a summary of the features of the stationary jet model, we examine the effects of a perturbation propagating along the jet on the high energy emission (typically optical– $\gamma$ –rays). Finally we consider the relativistic corrections and in particular the dependence of the predicted amplitude of variability on the angle with the line of sight, in the assumption that the perturbation is a planar, relativistic shock wave.

#### 4.1.1 Observations

Interestingly, a group of recent results, referring to the X–ray and UV bands, though much less detailed than those at lower frequencies, seem to indicate a systematic behaviour of the spectral variability, *i.e.* an average amplitude increasing with frequency and a hardening of the X–ray spectral shape with increasing intensity, at least over sufficiently short time scales (§1.1.3.b).

Several BL Lac objects were repeatedly observed in X-rays with EXOSAT, with typical durations of few hours for each observation and irregular spacings, ranging from days to several months. For some of these sources, namely Mkn 421, Mkn 501, 1218+304 and PKS 2155–304, complete results have been published (George, Warwick & Bromage 1988; George, Warwick & McHardy 1989; Treves *et al.* 1989).

The cases of PKS 2155–304 and Mkn 421 are of particular interest, in that observations in the UV and optical bands, quasi-simultaneous to the X–ray ones, are also available.

From Giommi *et al.* (1990) (§1.1.3.b) we derive data on 3 other objects 1H 0414+009, Mkn 180 and PKS 2005–489, which show clear evidence of variability in both the LE and ME bands of EXOSAT.

For each source we use the count-rates in different bands, averaged over the entire observation, to compute the variability indicator defined as

$$v = \frac{\sigma_v}{\langle F \rangle} = \frac{\sqrt{\sum_i (F_i - \langle F \rangle)^2 / N - \sigma_{err}^2}}{\langle F \rangle} \quad (4.1)$$

where, for each target,  $F_i$  are the fluxes measured at different epochs,  $\langle F \rangle$  is their mean,  $N$  is the number of observations and  $\sigma_{err}$  is the measurement error. We assume in the following a fixed value of  $\sigma_{err}/\langle F \rangle = 5\%$  for the X-ray measurements and of  $\sigma_{err}/\langle F \rangle = 10\%$  for the ultraviolet ones (Giommi *et al.* 1987; Hackney, Hackney & Kondo 1982). The use of a normalized variability parameter allows to compare the average variability in different energy bands and in different sources.

For PKS 2155–304, 9 EXOSAT observations are available. Taking into account the spectral shape, the effective energies of the LE and ME bands are  $\sim 0.2$  keV and  $\sim 3$  keV respectively. UV fluxes at 1500 and 2500 Å, obtained from quasi simultaneous observations (delay or leads of few hours) with IUE, with integration times of  $\sim 1$  h are available for 8 of the 9 observations. Data in the optical range derive from the Fine Error Sensor on IUE and have integration times of minutes.

The resulting variability parameter at the various frequencies is reported in the top part of Table 4.1. It is apparent that  $v$  increases regularly with frequency. Roughly the dependence is of the type  $v \propto \log \nu$ .

The variability parameter can also be computed for the collection of all IUE spectra of PKS 2155–304 taken over a larger time span, from 1979 to 1984 (Maraschi *et al.* 1986). For this large set of observations we obtain  $v = 0.17$  and  $v = 0.23$  at 2500 and 1500 Å respectively. The dependence of  $v$  with frequency is similar to, but the values are significantly smaller than those obtained for the UV observations quasi simultaneous with the EXOSAT ones, indicating that at the latter epoch the object was more active.

For Mkn 421,  $v$  could be computed in the two ultraviolet and in the two X-ray bands from the data of George, Warwick & Bromage (1988) (11 and 14 observations respectively). Again a regular increase with frequency is apparent, which also in this case appears logarithmic.

For all the other objects the available data refer only to the two X-ray bands. Again an increase of specific variability with frequency is present.

The trend, found here, of increasing variability amplitude with increasing frequency in the UV to X-ray range, agrees with the results of Impey and Neugebauer (1988) (§1.1.3.b) for a much larger collection of data. A more quantitative comparison is impossible, since

those authors considered the ratio  $F_{max}/F_{min}$  for a large number of sources and averaged over the source population.

It is important to recall that the 7 objects listed above are X-ray bright and radio weak, X-ray selected BL Lac objects (§1.1.2.b; §6.1.1). It has been shown that the overall energy distribution of such objects differs significantly from that of the ‘classical’ radio selected members of the BL Lac population, in agreement with the model of Ghisellini, Maraschi & Treves (1985), which attributes the X-ray emission of the two types of objects to different radiation processes, that is inverse Compton for the radio selected and synchrotron for the X-ray selected BL Lac objects respectively.

#### 4.1.2 The stationary model

We will adopt the stationary inhomogeneous jet model described in Ghisellini *et al.* (1985), which naturally explains the variability trend described in §1.1.3.a of decreasing of variability time scales with increasing frequency.

The overall continuum is obtained as an appropriate superposition of locally produced SSC spectra, which have the same slope but different lower and upper frequency limits (due to synchrotron self absorption and the maximum electron energies).

The inner portion of the jet, emitting at high frequencies, is confined with parabolic shape (*e.g.* Marscher 1980)

$$r = r_0 (R/R_0)^\epsilon \quad (4.2)$$

where  $r$  and  $R$  are the transverse and axial coordinates and  $\epsilon$  is a geometrical parameter ( $\epsilon < 1$  corresponds to a parabolic jet).  $r_0$  and  $R_0$  are linear dimension scales and we assume  $r_0 = R_0$ . This region extends up to  $R_{max}$ . Here and in the following the subscript ‘0’ refers to quantities at the base of the jet.

In order to explain the observed (optically thick) flat radio spectra, the outer part of the jet should be freely expanding with conical shape,  $\epsilon = 1$ . Here we shall be concerned only with the high frequency emission, from optical to  $\gamma$ -rays; therefore, only the inner, parabolic portion of the jet will be considered.

The electron power-law distribution is assumed to have constant slope along the jet. The maximum Lorentz factor  $\gamma_{max}$ , the relativistic particle density and the magnetic field intensity are assumed to be decreasing functions of the distance from the central engine, according to the simple parametric laws ( $x = R/R_0$ ):

$$\gamma_{max} = \gamma_{0,max} x^{-\epsilon_e} \quad K = K_0 x^{-\epsilon_n} \quad B = B_0 x^{-\epsilon_m} \quad (4.3)$$

The local synchrotron emissivity as a function of the distance from the ‘core’ is therefore given by

$$j_s(\nu, x) = j_{0,s}(\nu) x^{-\epsilon[n+m(1+\alpha)]} \quad \nu_{min}(x) < \nu < \nu_{max}(x) \quad (4.4)$$

the self absorption frequency,  $\nu_{min}(x)$ , and the maximum emission frequency,  $\nu_{max}(x)$ , are given by

$$\nu_{min}(x) = \nu_{0,min} x^{-k_m} \quad \text{and} \quad \nu_{max}(x) = \nu_{0,max} x^{-\eta} \quad (4.4a)$$

where  $\eta = \epsilon(2e + m)$ ,  $k_m = \epsilon[m(1.5 + \alpha) + n - 1]/(2.5 + \alpha)$ . For the numerical values and expressions of  $j_s(\nu, 1)$ ,  $\nu_{0,min}$  and  $\nu_{0,max}$  see §2.2. The model assumes that  $\eta > 0$ , so that high frequencies are produced only at small  $x$ .

The monochromatic luminosity is obtained integrating  $j_s(\nu, x)$  over the volume emitting at the considered frequency

$$L_s(\nu) = 4\pi^2 c(\alpha) R_0^3 K_0 B_0^{1+\alpha} \nu^{-\alpha} \int_{x_1(\nu)}^{x_2(\nu)} x^{\zeta-1} dx \quad (4.5)$$

where  $\zeta = 1 + \epsilon[2 - n - m(1 + \alpha)]$  and the integration limits derive from inverting eqs.(4.4a). For the values of  $c(\alpha)$  see Table 2.1.

Note that the sign of  $\zeta$  determines whether the upper or lower integration limit is important. For  $\zeta > 0$  the dominant contribution to  $L_s(\nu)$  comes from  $x_2(\nu)$  (outer regions). It was shown in Ghisellini *et al.* (1985) that the model can reproduce the steepening of the continuum for positive values of  $\zeta$  and  $\eta$ . The positive values for the two parameters guarantee the essential feature of the model. Therefore we adopt this choice hereafter.

With these assumptions ( $\eta > 0$  and  $\zeta > 0$ ) the integrated synchrotron spectrum can be described by two power laws. At low frequencies (far infrared)  $\nu_{min}(x_{max}) < \nu < \nu_{max}(x_{max})$  the spectral index is the same as the local one,  $\alpha$ , since all the regions of the jet contribute to the spectrum, with a dominance of the external and larger regions  $x \simeq x_{max}$ . At higher frequencies (optical–UV), above  $\nu_{max}(x_{max}) \equiv \nu_b$ , the spectrum steepens to  $\alpha_1 = \alpha + \zeta/\eta$  due to the fact that the volume contributing above  $\nu_b$  decreases with increasing  $\nu$  and only the inner parts of the jet can contribute to the integrated spectrum. Being produced in the inner jet, the highest synchrotron frequencies can vary with the shortest timescales.

If the photon density is high, the inverse Compton emissivity must also be considered. The model assumes that the radiation energy density is due to photons produced locally. The monochromatic inverse Compton luminosity can then be derived analogously to the synchrotron one:

$$L_c(\nu) = 2\pi^2 \left(\frac{4}{3}\right)^{\alpha-1} c(\alpha) R_0^3 \tau_0 K_0 B_0^{1+\alpha} \nu^{-\alpha} \int_{x_1(\nu)}^{x_2(\nu)} x^{l-1} \ln \left[ \frac{\nu_2(R)}{\nu_1(R)} \right] dx \quad (4.6)$$

where  $l = \zeta - (n-1)\epsilon$  and  $\nu_1$  and  $\nu_2$  are the minimum and maximum synchrotron frequencies which contribute to the Compton emission at frequency  $\nu$ . The parameter  $l$  has a role analogous to  $\zeta$ : for  $l > 0$  the largest contribution to the luminosity at fixed frequency is produced in the outer regions. In the 2–10 keV band, all the regions of the jet contribute (with a dominance of the external ones), and the resulting spectrum is flat with constant spectral index equal to  $\alpha$ . In the hard X-ray and  $\gamma$ -ray band, only the inner portions of the jet contribute, the integrated spectrum is steeper than  $\alpha$ , and the variability timescales are shorter.

The decline of the scattering cross section at high energies is taken into account approximating it with a step function, as discussed in §2.2.1.

Also the energy densities involved are functions of the distance along the jet, and depend on the assumed parameters: in particular while the emitting particle energy density is always a small fraction of the total energy involved, the radiation energy density dominates in the inner regions, but can decrease faster than the magnetic one, suggesting that Compton emission can be dominant also in the inner regions. The dependence of luminosity is monotonic, generally decreasing with distance. As far as the relevant timescales are concerned, we note that for typical parameters, escape and adiabatic losses of the electrons can be relevant (for low energy particles) only in the external conical region (Celotti 1991). At high frequencies radiative losses are greater than adiabatic ones, requiring an accelerating mechanism.

#### 4.1.3 Time dependent emission in the presence of a perturbation

Motivated by the systematic pattern of the multifrequency variability we study the spectral evolution of perturbations propagating outwards along the relativistic jet presented in §4.1.2 (Celotti, Maraschi & Treves 1991; for preliminary results Celotti, Maraschi & Treves 1989; Maraschi, Celotti & Treves 1989).

We first adopt a schematic description of the perturbation showing how some general features naturally follow from this ‘elementary’ model: this simplification allows us to give approximate analytic expressions for the time dependence of the spectral flux, which are sufficient to understand the essential results.

The perturbation is modelled as an increase in the relativistic electron density and magnetic field strength by constant factors,  $(1 + k)$  and  $(1 + b)$  respectively, relative to the stationary values, the shape of the particle distribution being unchanged. The latter assumption is clearly a minimal one. In fact it is plausible that the average energy and also the spectral shape will be affected by the perturbation (§4.2.3).

The front of the perturbation is assumed to move at constant velocity  $\beta_p c$ , starting from  $R_0$  at  $t = 0$ . Here we do not introduce Doppler and relativistic corrections, which will

be discussed in §4.1.4. Thus the time used strictly refers to an observer at rest with the nozzle of the jet and with line of sight nearly perpendicular to the jet axis, for which the Doppler factor is 1. The velocity of the stationary fluid is assumed to be subrelativistic.

In the region affected by the perturbation the synchrotron emissivity is given by:

$$j_s^*(\nu, x^*) = (1+k)(1+b)^{1+\alpha} c(\alpha) K(x^*) B(x^*)^{1+\alpha} \nu^{-\alpha} = (1+a_s) j_s(\nu, x^*) \quad (4.7)$$

within the frequency range defined by

$$\nu_{min}^*(x^*) = \nu_{min}(x^*) [(1+b)^{1.5+\alpha} (1+k)]^{\frac{1}{2.5+\alpha}} \quad \text{and} \quad \nu_{max}^*(x^*) = \nu_{max}(x^*) (1+b) \quad (4.7a)$$

where the asterisk denotes quantities referring to the perturbation, whose location is given by  $x^* = 1 + \beta_p c t / R_0$  and  $(1+a_s) = (1+k)(1+b)^{1+\alpha}$ .

The inverse Compton emissivity has a stronger dependence on particle density and its perturbed value is

$$j_{1C}^*(\nu, x^*) = (1+a_c) j_{1C}(\nu, x^*) \quad (4.8)$$

where  $(1+a_c) = (1+k)^2 (1+b)^{1+\alpha}$ .

The perturbation is assumed to extend to the full cross section of the jet. As for the thickness we consider two cases: *i*) constant thickness  $\Delta x^* = h \leq 1$ , *i.e.* a slab geometry; *ii*) the perturbed region is self-similar with a conical shape determined by the sound velocity,  $c_s$ , in the stationary fluid. Thus the height of the cone is  $\Delta x^* = (\beta_p c / c_s) x^{*\epsilon}$  which increases as the jet width,  $x^\epsilon$ , when the perturbation moves outward. This geometry could represent the emission region after the transit of a planar shock wave as suggested by Lind and Blandford (1985).

The total monochromatic luminosity at frequency  $\nu$  can be thought of as the sum of contributions from two regions: 1) from the volume  $V^*$  affected by the the perturbation, 2) from the unperturbed portion,  $V - V^*$ , of the stationary jet. In both cases the volumes emitting at the given frequency,  $V^*(\nu)$  and  $V(\nu)$  may be smaller than  $V^*$  and  $V$  respectively. Moreover, due to the frequency shift of the emission from the perturbed region with respect to the unperturbed one,  $V^*(\nu)$  is not simply a portion of  $V(\nu)$ . In Appendix A we give the exact definitions of the two contributions, which are used in the numerical computations.

It is useful to derive analytic expressions: to this end we neglect the frequency shift due to the perturbation, which is small compared to the frequency range of the emission. With this approximation  $V^*(\nu) = V(\nu) \cap V^*$ , where the intersection symbol defines the volume emitting at  $\nu$  within the perturbed region. We can thus write:

$$L(\nu, t) = L^1(\nu, t) + L^2(\nu, t) \quad (4.9)$$

where

$$L^1(\nu, t) = 4\pi \int_{V^*(\nu)} j^*(\nu, x) dV \quad L^2(\nu, t) = 4\pi \int_{V(\nu) - V^*(\nu)} j(\nu, x) dV \quad (4.9a)$$

With  $V(\nu) - V^*(\nu)$  we indicate the unperturbed part of  $V(\nu)$ . Recalling (4.9) we have

$$\begin{aligned} L(\nu, t) &\simeq 4\pi \int_{V(\nu)} j(\nu, t) dV + 4\pi \int_{V^*(\nu)} (j^*(\nu, t) - j(\nu, t)) dV = \\ &= L^{st}(\nu) + 4\pi a \int_{V^*(\nu)} j(\nu, t) dV \end{aligned} \quad (4.9b)$$

where  $L^{st}$  is given by eqs. (4.5) or (4.6) and  $a$  coincides with  $a_s$  or  $a_c$  defined in eqs. (4.7), (4.8) depending on whether we consider synchrotron or Compton radiation.

We further define a normalized amplification factor  $A(\nu, t)$  as the ratio between the monochromatic, time dependent luminosity and the stationary one:  $A(\nu, t) \equiv L(\nu, t)/L^{st}(\nu)$ .

With the simplifying assumption mentioned above

$$A(\nu, t) = 1 + a \frac{\int_{V^*(\nu)} j(\nu, x) dV}{\int_{V(\nu)} j(\nu, x) dV} \quad (4.10)$$

Using for  $a$  and  $j$  the values appropriate for synchrotron or Compton emission, the approximate expressions (4.9b) and (4.10) or the corresponding exact eqs. (A.6) and (A.7) in Appendix A allow to derive the two dimensional behaviour of  $L(\nu, t)$ , which can be represented on one-dimensional plots either as frequency spectra at different times or as light curves at different frequencies. We neglect delays due to the light travel time across the jet and (to the same accuracy) across the perturbation. The results are presented below. All the figures derive from numerical computations of eqs. (A.6), (A.7).

#### 4.1.3.a Time dependent spectra

Let us first consider the synchrotron flux from a perturbation of fixed size,  $\Delta x^* = h$  (case *i*). Since  $h \leq 1$  we can approximate the perturbed region as homogeneous: in this case  $V^*(\nu)$  is either  $\simeq V^*$  or null. Furthermore let us treat  $V^*$  as a cylindrical slab. Then

$$A_s(\nu, t) \simeq 1 + a_s \zeta \frac{h x^{*(\zeta-1)}}{x_2^\zeta(\nu)} \quad (4.11)$$

This expression is valid for frequencies in the interval  $\nu_{min}^*(x^*) \leq \nu \leq \nu_{max}^*(x^*)$ . For  $\nu$  outside this range  $A_s(\nu, t) = 1$ .

$x_2(\nu)$  is the outer boundary of the region emitting at frequency  $\nu$  in the stationary jet, and is derived inverting the second equation (4.7a). For  $\nu > \nu_b$ , where  $\nu_b$  is the ‘break’



frequency for the stationary spectrum (§4.1.2),  $x_2 = (\nu_{max}^o/\nu)^{1/\eta}$ , while, for  $\nu < \nu_b$ ,  $x_2$  is constant  $x_2 = x_{max}$ . This behaviour of  $x_2$ , which is responsible for the occurrence of the break in the stationary spectrum, also determines the spectral evolution of the perturbation. In fact, for  $\nu > \nu_b$ ,  $A_s(\nu, t)$  increases with increasing  $\nu$ , whereas, for  $\nu < \nu_b$ , it is independent of frequency. We can thus write, introducing the explicit time dependence, for  $t_0 \leq t \leq t_{max}$ ,

$$A_s(t) \simeq 1 + a_s \zeta \frac{h(1+t/t_0)^{(\zeta-1)}}{x_{max}^\zeta} \quad \nu_{min}^*(x_{max}) \leq \nu \leq \nu_b \quad (4.11a)$$

$$A_s(\nu, t) = 1 + a_s \zeta \frac{h(1+t/t_0)^{(\zeta-1)}}{(\nu_{max}^o)^{\zeta/\eta}} \nu^{\alpha_1 - \alpha_0} \quad \nu \geq \nu_b \quad (4.11b)$$

where  $t_0 = R_0/\beta_p c$  and  $t_{max} = (R_{max} - R_0)/\beta_p c$ .

The perturbed spectrum is obtained multiplying  $A_s(\nu, t)$  by the stationary spectrum. For  $\nu < \nu_b$  the result is a power law with index  $\alpha$ , while for  $\nu > \nu_b$  the perturbed spectrum is given by the sum of two power laws with index  $\alpha_1$  and  $\alpha$ . Thus above  $\nu_b$  the effective spectral index will be intermediate between  $\alpha$  and  $\alpha_1$ , close to  $\alpha$ . Therefore the model predicts no spectral variability below  $\nu_b$  and a hardening of the spectrum above  $\nu_b$  when the flux increases, with a limiting value  $\alpha$ .

The calculation of the amplification factor for the first order Compton follows the same lines, yielding

$$A_c(\nu, t) = 1 + a_c l \frac{hx^{*(l-1)}}{x_{1(2)}^l} \quad (4.12)$$

where  $a_c$  is given by eq. (4.8) and  $x_1$  or  $x_2$  appear in the denominator depending on whether  $l < 0$ , or  $l > 0$  respectively. For  $\nu$  in the X-ray domain, which is relevant here, neither  $x_1$  nor  $x_2$  depend on frequency. Thus the amplification factor for the Compton spectrum is independent of frequency, implying no spectral change.

Figs. 4.1a,b show the evolution with time of the energy spectrum, due to the passage of a perturbation with constant thickness, for different sets of parameters describing the stationary jet structure (see Table 4.2) which we refer to as case *a*) ( $\zeta < 1$ ) and *b*) ( $\zeta > 1$ ). In both cases at high frequencies the spectrum flattens with increasing intensity, while for  $\nu < \nu_b$  the change in intensity is not associated with spectral changes. Variations of one order of magnitude in X-rays are reproduced for values of the enhancement parameters  $b$  and  $k \simeq 3$ , for  $h = 1$ , while, below  $\nu_b$ , the variation amplitude is much smaller.

The value of the parameter  $\zeta$  measures the importance of the outer regions in building up the stationary luminosity and plays a similar role in the perturbed luminosity. For larger  $\zeta$  the effect of the perturbation is comparatively stronger (with respect to smaller  $\zeta$ ) at low frequencies, which are emitted at larger distances. In particular, for  $\zeta > 1$ , the dependence

of the amplitude on  $x^*$  changes substantially, from decreasing to increasing with increasing  $x^*$  [see eq. (4.11)]. We come back to this point in discussing light curves.

Let us now consider the case of a perturbation of increasing thickness (case *ii*). The behaviour of the perturbed flux can be derived, computing again expressions (A.6) and (A.7) of Appendix A.

In order to derive simple analytic results, we assume again in the following that the perturbation region is homogeneous: due to the larger size of the perturbation the approximation is more severe here than in the previous case. We evaluate the perturbed emissivity at an intermediate position in the interval  $[x^* - \Delta x^*, x^*]$ , which divides the emitting region in two parts of equal volumes. We indicate this position with  $x^{**} \simeq (x^* - 0.2 \beta c/c_s x^{*\epsilon})$ . For  $x^* \gg 1$ ,  $x^{**} \rightarrow x^*$ .

We can thus write

$$L(\nu, t) \simeq L^{st}(\nu) + 4\pi a \int_{V^*} j(\nu, t) dV \simeq L^{st}(\nu) + 4\pi^2 R_0^3 a j(\nu, x^{**}) \frac{x^{*2\epsilon} \Delta x^*}{3} \quad (4.13)$$

where the fraction represents the volume of the emitting cone. Full expressions are given in Appendix A and are used in the numerical computations.

The amplification factor for synchrotron emission in case *ii*) is thus given by:

$$A_s(\nu, t) \simeq 1 + a_s \zeta \frac{\beta c x^{*\zeta-1+\epsilon}}{c_s x_2^\zeta} \quad \text{for } x^* \gg 1 \quad (4.14)$$

The amplification will be greater than 1 for frequencies in the interval  $\nu_{min}^*(x^{**}) \leq \nu \leq \nu_{max}^*(x^{**})$ .

An analogous procedure is followed to obtain the amplification of the Compton emission  $A_c$ .

Eq. (4.14) shows that the dependence of the amplification factor on frequency is qualitatively the same as for a perturbation of constant thickness, but the amplitude of the variation is larger at lower frequencies, because the emitting volume is larger. In this case the critical value of  $\zeta$ , above which the dependence of the amplitude on  $x^*$  changes trend, is  $\zeta \simeq 1 - \epsilon$ .

The time evolution of the energy spectra for case *ii*) is shown in Figs. 4.2a,b adopting for the stationary jet and for the initial perturbation the same parameters as for the perturbation of constant size. Comparing Figs. 4.1 and 4.2 one can see that, as argued above, at high frequencies the behaviour is similar but at low frequencies the effect is stronger due to the larger volume of the perturbation.

The Compton emission varies without spectral changes, in a similar way to the low frequency synchrotron emission. In each case the Compton spectra associated with the synchrotron ones are shown in the figures.

#### 4.1.3.b Light curves at different frequencies

Another way of examining the results is to plot the flux at a given frequency vs. time (light curve). This allows a better understanding of the timescales involved. In the following we discuss the general properties of the light curves and give formulae for interesting time intervals and time scales, adopting the same approximations introduced above in the description of the spectral evolution.

The light curves for the synchrotron flux are computed at three representative frequencies: in the X-ray ( $2 \cdot 10^{17}$  Hz), UV-optical ( $10^{15}$  Hz) and far-infrared ( $10^{13}$  Hz) bands, chosen to illustrate different behaviours in observationally relevant spectral regions. They are shown in Figs. 4.3 for a model *a* jet ( $\zeta < 1$ ), and in Figs. 4.4 for a case *b* jet ( $\zeta > 1$ ). Both, amplitude and timescales, are logarithmic in the figures.

The lowest frequency considered,  $\nu = 10^{13}$  Hz, is below the self-absorption frequency of the perturbation at its start. As the perturbation moves down the jet, the self-absorption frequency decreases, causing the delayed rise in the light curve when it falls below  $10^{13}$  Hz. At lower frequencies still the model becomes inadequate since it does not include the far regions of the jet which are important at low frequencies.

In all the high frequency light curves one can recognize a first time interval  $\tau_1$  corresponding to the time necessary for the perturbation, which has a finite thickness  $\Delta x^*$ , to fully enter the emission region for a given frequency

$$\tau_1 = \Delta x^* t_0 = \begin{cases} h t_0 & \text{case } i), \text{ fixed thickness} \\ (\beta c/c_s)(1 + t/t_0)^\epsilon t_0 & \text{case } ii), \text{ growing thickness} \end{cases} \quad (4.15)$$

For case *ii*)  $\tau_1$  is somewhat larger than for case *i*). In all cases the amplitude grows during  $\tau_1$ .

A second time interval  $\tau_2$  corresponds to the time it takes for the perturbation to cross the region of the jet which emits at the considered frequency. We have

$$\tau_2(\nu) = (x_2^*(\nu) - x_1^*(\nu))t_0 \simeq \begin{cases} x_{max} t_0 & \nu < \nu_b \\ (\nu_{max}^o(1 + b)/\nu)^{1/\eta} t_0 & \nu > \nu_b \end{cases} \quad (4.16)$$

where  $x_1^*, x_2^*$  are the boundaries of the region emitting at frequency  $\nu$  with the enhanced value of the magnetic field. The factor  $(1 + b)$  accounts for this frequency shift.

From eq. (4.16) one can see that at high frequencies, the crossing time decreases with increasing frequency, with a dependence assigned by the parameter  $\eta$ . This is shown, for example, in Figs. 4.3, where the duration of the  $10^{15}$  Hz light curves is much longer than that of the  $2 \cdot 10^{17}$  Hz light curves.

The value of  $\zeta$  is critical in determining the shape of the light curves during  $\tau_2$ . For  $\zeta < 1$  (or  $\zeta < 1 - \epsilon$  for case *ii*, eq. (4.14)) the flux decreases, while for  $\zeta > 1$  (or  $\zeta > 1 - \epsilon$ ) the flux continues to increase. Thus the structure of the jet, characterized by the parameter

$\zeta$ , introduces a fundamental difference between the light curves of Figs. 4.3 and 4.4. For  $\zeta < 1(-\epsilon)$  the maximum intensity is reached after the interval  $\tau_1$ , that is simultaneously for all frequencies above  $\nu_{min}^*(1)$  (Fig. 4.3a). For values of  $\zeta > 1(-\epsilon)$  (see Fig. 4.4a) the maximum intensity is reached after the crossing time  $\tau_2$ .

Since  $\tau_2$  depends on frequency, eq. (4.16), there is a time lag between the maxima at different frequencies given by the difference in the two crossing times. For  $\nu_1, \nu_2 > \nu_b^*$

$$\tau_{lag}(\nu_1, \nu_2) \simeq (\tau_2(\nu_1) - \tau_2(\nu_2)) = [(1+b)\nu_{max}^o]^{1/\eta} \left[ \frac{1}{\nu_1^{1/\eta}} - \frac{1}{\nu_2^{1/\eta}} \right] t_0 \quad (4.17)$$

We recall that the delay in the maximum intensity at frequencies below  $\nu_{min}^*(1)$  is due to a different effect, that is the variation in the optical depth of the perturbation.

While the time intervals discussed above do not involve the amplitude of variability it is possible to introduce the ‘e-folding time scale’  $\tau_e$ , defined as:  $\tau_e(\nu, t) \equiv L(\nu, t)/(dL(\nu, t)/dt)$ . For the sake of simplicity we consider here only case *i*) with the approximations discussed above and  $\nu > \nu_{min}(1)$ . In the two parts of the light curves,  $\tau_1$  and  $\tau_2$ ,  $\tau_e$  is given respectively by

$$\tau_e(\nu, t) = \begin{cases} 1/(1 + \zeta t/t_0) \left\{ (1 + t/t_0)t/t_0 + (1 + t/t_0)^{(2-\zeta)} x_2^\zeta / a_s \zeta \right\} t_0 & t < \tau_1 \\ |\zeta - 1|^{-1} \left\{ (1 + t/t_0) + (1 + t/t_0)^{(2-\zeta)} x_2^\zeta / h a_s \zeta \right\} t_0 & \tau_1 < t < \tau_2 \end{cases} \quad (4.18)$$

Since  $\zeta < 2$ , for  $\tau_1 < t < \tau_2$ , parameters  $\tau_e(\nu, t)$  is an increasing function of  $t$  (at fixed  $\nu$ ) and the shortest e-folding time scale is thus obtained at the beginning of this interval. For  $t < \tau_1$ , the same is true for  $\zeta < 1$  (for  $\zeta > 1$  the minimum of  $\tau_e$  depends on  $\zeta$  and  $\nu$ ).

In particular for  $\nu > \nu_b^*$  we have

$$\tau_{min}(\nu) = \begin{cases} \left\{ (\nu_{max}^o/\nu)^{\zeta/\eta} / a_s \zeta \right\} t_0 & t < \tau_1 \quad (\zeta < 1) \\ |\zeta - 1|^{-1} \left\{ (1 + h) + (1 + h)^{2-\zeta} (\nu_{max}^o/\nu)^{\zeta/\eta} / h a_s \zeta \right\} t_0 & \tau_1 < t < \tau_2 \end{cases} \quad (4.18a)$$

From eq. (4.18) we can see that also the e-folding time decreases with frequency,  $x_2^\zeta = (\nu_{max}^o/\nu)^{\zeta/\eta}$ . We recall that  $\zeta/\eta$  gives the steepening of the stationary spectrum,  $\Delta\alpha = \zeta/\eta$  (§4.12).

The contribution of the inverse Compton emission may be important in the X-ray band: its temporal behaviour is compared in Fig. 4.5 with that of the synchrotron emission in the same band. Only two of the four cases are shown in the figure, *i.e.* (*a, i*) (constant thickness) and (*b, ii*) (increasing thickness). The parameter  $l$  now has a role analogous to  $\zeta$  for the synchrotron emission. Again, for  $l < 1$ , the amplitude reaches its maximum after  $\tau_1$  and decreases thereafter, while, for  $l > 1$ , the Compton flux is increasing for a time  $\tau_2$ , after which the perturbation exits from the region of the jet considered here.

In the first case the Compton X-rays rise simultaneously with the synchrotron ones. In the second case, due to the fact that the region emitting X-rays through the Compton process is larger than that emitting X-rays through synchrotron, the maximum of the Compton flux is delayed with respect to the synchrotron one.

In §4.14 we introduce relativistic corrections for the observed amplitudes under various assumptions concerning the velocities of the stationary and perturbed fluid. Obviously the time scales should be corrected too. However the Doppler factor correction, apart from compressing or stretching the time scale, not alter the general features that we have discussed, at least within the approximations adopted, of neglecting time delays across the jet and across the perturbation.

#### 4.1.3.c Normalized variability parameter

In §4.1.1 we defined an observational parameter  $v(\nu)$  in order to quantify the ‘average’ amplitude of the observed variations. Given the sampling of the available data,  $v(\nu)$  refers to timescales from days to years.

The comparison with model predictions is not direct because of the necessity of choosing the instants of ‘observation’ and of specifying a duty cycle to calculate the mean. Moreover our model is appropriate to discuss variations on time scales related to the evolution of the perturbation (hours to weeks). Additional variability may result from long term changes in the jet structure and, on short time scales, from random inhomogeneities in the radiating region. Tentatively, we assume that the observed variability results uniquely from perturbations of the type described here and compute  $v(\nu)$  for  $N$  observations randomly chosen within a time interval comprising the duration of one full event  $t_{max}$  plus a number  $M-1$  of quiescent periods.

The results are reported in the bottom part of Table 4.1 for the 4 cases considered above and for values of  $b$  and  $k$  chosen so as to come close to the observed values. It can be seen from Table 4.1 that in all cases the model predicts too small amplitudes at low frequency for ‘single event’ averages. However, introducing a duty cycle tends to smear out the high frequency amplitude more than the low frequency one so that a better agreement with observations can be obtained (in Table 4.1 the case for  $M=6$  is reported). The necessary values of  $b$  and  $k$  are in the range 2-4, corresponding to values of  $a_s \simeq 15 - 56$ .

#### 4.1.4 The case of a relativistic shock wave

The most plausible physical model for a perturbation of the kind discussed in the previous section is that of a relativistic shock wave. Using jump conditions with simple equations of state, it is possible to estimate the compression ratio across the shock as a function of

the velocity of the upstream fluid in the frame of the shock  $u_1$  ( $u$  indicate velocities measured in the shock frame, while  $\beta c$  are measured in the observer frame).  $u_1$  is determined by the velocity of the front  $\beta_s$  and of the stationary fluid  $\beta_1$  in the frame of the observer. Furthermore, in the case of a shock wave, the fact that the velocity of the perturbed fluid,  $\beta_2$ , must be different from that of the stationary emitting fluid,  $\beta_1$ , introduces different relativistic corrections for the stationary (upstream, labelled with '1') and perturbed (downstream, labelled with '2') emission. Thus not only the observed flux but also the amplitude of variability depends on the stream velocities and on the viewing angle.

The relativistic jump conditions across a planar adiabatic shock are given *e.g.* by Königl (1980), Blandford & McKee (1976): by requiring that the energy flux  $4pu_1\gamma^2$  and the momentum flux  $(3u^2 + 1)p\gamma^2$  are conserved across the shock, in the particular case of upstream ultrarelativistic temperature ('adiabatic index' = 4/3), the solution of the jump equations is simply given by  $u_1u_2 = 1/3$ . Thus, using the conservation of particle number  $u_1\gamma_1n_1 = u_2\gamma_2n_2$ , the shock strength  $\Psi = n_2/n_1$  can be derived

$$\Psi = u_1\gamma_1\sqrt{9u_1^2 - 1} \quad (4.19)$$

Note that the compression ratio in the relativistic case can become arbitrarily large for increasing  $\gamma_1$ .

We will assume that the emitting relativistic electrons simply follow the compression of the fluid, so that the factor  $(1 + k)$  in §4.1.3 equals  $\Psi$ . This is clearly a crude approximation, which is motivated by the fact that the electron radiative lifetimes are rather short compared to the dynamical ones, making an adiabatic approximation for the electrons questionable. A direct estimate of the spectra produced by particle acceleration at the shock front would be extremely valuable (*e.g.* Peacock 1981; Schneider and Kirk 1989) but is not considered here.

As for the magnetic field, only the component parallel to the shock front is increased: so  $1 \leq (1 + b) \leq \Psi$ , and we assume an angle of  $45^\circ$  between the field and the shock.

With the above assumptions one can derive the enhancement of the synchrotron and Compton radiation in the frame of the shock as a function of  $u_1$ . The parameters  $a_s$ ,  $a_c$  defined in the previous section for the synchrotron and Compton emission read:

$$a_s = u_1\gamma_1(9u_1^2 - 1)^{1/2}[(1 + u_1^2\gamma_1^2(9u_1^2 - 1))/2]^{(1+\alpha)/2} \quad (4.20a)$$

or

$$a_c = u_1^2\gamma_1^2(9u_1^2 - 1)[(1 + u_1^2\gamma_1^2(9u_1^2 - 1))/2]^{(1+\alpha)/2} \quad (4.20b)$$

The observed amplitude must include the relativistic corrections associated with the velocities of the shock itself  $\beta_s$  and of the upstream and downstream fluid velocities  $\beta_1$  and

$\beta_2$ . Using the expression given in §2.2.3 for the spectral intensity observed from a shocked fluid in a thin source, with planar geometry, we obtain:

$$F_{obs}^* = \delta(\beta_s)\delta(\beta_2)^{2+\alpha}F^* \quad (4.21)$$

where  $\delta(\beta_s) = (1 - \beta_s^2)^{1/2} / (1 - \beta_s \cos \theta)$  is the Doppler factor computed with the shock front velocity and  $\delta(\beta_2)$  is the Doppler factor for the post-shock fluid velocity in the observer frame (the velocities are parallel to the jet axis). In formula (4.21) it is assumed that the volume of the perturbed emission region is measured in the frame of the shock front. The relativistic correction factor for the flux observed from the stationary jet is  $\delta_1^{2+\alpha}(\beta_1)$ . It follows that the variability amplitude derived in §4.1.3 transforms to

$$A_R(\nu, t) \simeq 1 + C_R a \frac{\int_{V^*(\nu)} j(\nu, x) dV}{\int_{V(\nu)} j(\nu, x) dV} \quad (4.22)$$

where

$$C_R = \frac{\delta(\beta_s)\delta(\beta_2)^{2+\alpha}}{\delta(\beta_1)^{2+\alpha}} \quad (4.22a)$$

The product of the intrinsic synchrotron enhancement  $a_s$  and the relativistic correction factor  $C_R$  characterizes the ‘strength’ of the variability. In fact, at fixed frequency and time,  $C_R a_s$  determines the amplitude. It has the same role as  $(1 + k)(1 + b)^{1+\alpha_0}$  in the preceding section. We compute this factor as a function of  $\beta_1$  and  $\theta$ , for various values of  $u_1$ .

Two cases must be distinguished. In the first one, the fluid enters the shock from the far side of the jet and exits on the nozzle side, in the second one the opposite situation occurs. Fig. 4.6 may serve as reference for the definition of the kinematics of the two cases.

The shock velocity in the observer frame  $\beta_s$  should be directed outwards in order to guarantee the properties discussed in §4.13. This agrees with observations of superluminal motions, though it should be recalled that the variability we are modelling originates in a different portion of the jet and may not be strictly related to the radio knots. In the first case  $\beta_s = (\beta_1 + u_1)/(1 + \beta_1 u_1)$ . Therefore  $\beta_s$  is always larger than  $u_1$  and a high value of  $\beta_s$  does not require a high value of  $\beta_1$ . In the second case  $\beta_s = (\beta_1 - u_1)/(1 - \beta_1 u_1)$  so that  $\beta_1 > u_1$  is required in order to advect the shock front outwards and a large value of  $\beta_s$  implies large  $\beta_1$ . Another important difference between the two configurations is that in the first case the velocity of the shocked fluid is larger than that of the stationary one ( $\beta_2 > \beta_1$ ). The opposite is true for the reverse shock (for which the Lorentz factor of the superluminal component is expected to be lower than that derived from the flux amplification).

The computed value of the product  $C_R a_s$  for the first configuration, is shown in Figs. 4.7a,b for two values of  $u_1$ . From the discussion in §4.13, values of  $C_R a_s$  consistent

with observations should be of the order of  $10 - 10^2$  for a thickness  $h \simeq 1$ , while larger values are required for thinner perturbations.

We can see that the amplitude is larger for small viewing angles. For a modest value of the upstream fluid velocity,  $u_1 = 0.7$  (Fig. 4.7a), the intrinsic strength of the shock is barely sufficient to produce the observed variability amplitude. For  $u_1 = 0.9$  the appropriate range is met for viewing angles less than  $50^\circ$  (Fig. 4.7b). The amplitude decreases for increasing  $\beta_1$  and the dependence on the viewing angle is stronger for high  $\beta_1$ . Recall that  $\beta_s > u_1$  and is larger for larger  $\beta_1$ .

The alternative kinematic situation, in which the shock propagates backward in the frame of the fluid, is illustrated in Figs. 4.8a,b, for the same values of the shock compression, determined by  $u_1$ , as in the previous case. Now, due to the fact that the shocked fluid has smaller velocity than the stationary one in the observer frame, relativistic corrections work against variability, reducing the computed amplitude parameter to insufficient levels, except for the most extreme values of  $\beta_1$ . Furthermore, except for the highest values of  $\beta_1$  the amplitude is larger for larger viewing angles. We consider this case rather implausible, at least for the high frequency emitting region, although it is a choice adopted in modelling intensity and polarization variability in the radio band (Hughes, Aller and Aller 1989; Jones 1988).

The models described in §4.1.2, which reproduce with surprising details the observations of low frequency variability, can be considered as perturbations propagating in the conical low-frequencies emitting region of the Ghisellini *et al.* (1985) model.

## 4.2 THE GAMMA-RAY EMITTING BLAZAR 3C 279

The physical conditions of one particular source, the  $\gamma$ -ray emitting blazar 3C 279 are now discussed (Maraschi, Ghisellini & Celotti 1991; Maraschi, Ghisellini & Celotti 1992). The requirement of transparency for  $\gamma$ -rays, together with the observation of rapid variability, imply that the high energy radiation is relativistically beamed. This an important indication, being *independent* of the low energy (radio) estimates (§5.3).

We then consider the relativistic jet model discussed in the previous section and show that the  $\gamma$ -ray spectrum can be explained as the high energy extension of the SSC radiation responsible for the X-ray emission. It is softer than the X-ray spectrum due to upper cutoffs in the electron energy spectra along the jet. The same electrons are responsible for the low frequency emission ( $10^{13}$ – $10^{16}$  Hz) via synchrotron radiation as shown in §4.1. The expected correlation of variability at different frequencies is discussed.



### 4.2.1 Observations

3C 279 is a ‘typical’ blazar with a compact, variable, flat spectrum radio core and a highly polarized and violently variable optical continuum. It was the first source discovered to show superluminal expansion ( $\beta_a \approx 18$ , Whitney *et al.* 1971). The X-ray emission is strong relative to the optical–UV flux, with  $\alpha_{ox} \simeq 0.9$ , and exhibited a large outburst in 1988, in correspondence with a similar flare in the IR, optical, and UV bands (Makino *et al.* 1989).

The discovery, by the EGRET instrument aboard GRO (Hartman *et al.* 1992a), of an extraordinary  $\gamma$ -ray flux from 3C 279 tightly constrains the physical conditions at the source, possibly shading light on the mechanisms operating in blazars at large (§1.1.2.c).

The  $\gamma$ -ray observations took place in 1991 June 15–28. No information is presently available on the intensity of the source at other wavelengths during the  $\gamma$ -ray observation period. However, in late 1990 early 1991, both the radio brightness and the X-ray emission increased (Makino, Fink & Clavel 1991) to levels comparable to the 1988 outburst (Makino *et al.* 1989). Since the source was not detected by the two previous  $\gamma$ -ray telescopes, SAS-2 and COS-B, flown in the seventies, with upper limits incompatible with the flux measured by EGRET, it seems likely that the intense  $\gamma$ -ray emission is associated with a brightening of the source at all wavelengths. Even so, comparing the observed  $\gamma$ -ray luminosity with the brightest states ever recorded at other wavelengths, *the  $\gamma$ -ray output dominates the bolometric luminosity*. At the redshift of 3C 279, and assuming that the radiation is emitted isotropically, the observed flux corresponds to a luminosity in excess of  $10^{48}$  erg/s in the 0.03–5 GeV band ( $H_0 = 50$ ,  $q_0 = 0.5$ ).

Moreover, Kanbach *et al.* (1992) have reported rapid variability of the  $\gamma$ -ray flux of 3C 279, with a timescale of about 2 days.

### 4.2.2 General constraints

Starting for simplicity with the hypothesis that the  $\gamma$ -ray and X-ray fluxes are produced in a homogeneous spherical source, we show that the high energy radiation must be strongly anisotropic and attributing the anisotropy to relativistic bulk motion of the emitting plasma we infer a lower limit for the Doppler factor. Furthermore general constraints on the physical parameters at the source are then derived assuming that  $\gamma$ -rays are produced by SSC.

The first and most general requirement is that the source be transparent to photon-photon interaction, as required by the fact that the  $\gamma$ -ray luminosity largely dominates the total power. This condition must hold for any model, irrespective of the emission processes considered. We assume here for simplicity that the source is

homogeneous and spherical, and that in the source frame photons are isotropically distributed. Similar constraints hold in more elaborate models (§4.2.3) with minor quantitative modifications.

#### 4.2.2.a Beaming factor and $\gamma$ -ray variability

As shown in §2.1.2, the optical depth for photon–photon collisions in a compact source is  $\tau_{\gamma\gamma} \simeq \ell/30$  at 511 keV and increases for photons of higher energies as  $\tau_{\gamma\gamma}(x) = (\ell/30)x^{\alpha_x}$ .

For 3C 279, assuming that X-rays and  $\gamma$ -rays are produced in the same region, and setting  $\alpha_x = 0.5$  (Makino *et al.* 1989), the condition of transparency for 5 GeV photons,  $\tau_{\gamma\gamma}(10^4) \leq 1$ , implies  $\ell \leq 1$ . This yields for the  $\gamma$ -ray emitting region a size  $R_0 \geq 6.5L_{48}$  pc, comparable to the scale over which relativistic expansion of the radio knots is measured by VLBI, but incompatible with the observed variability timescale of 2 days.

In view of the independent evidence of relativistic motion in this source it is natural to suppose that also the  $\gamma$ -ray emitting plasma moves with a bulk Lorentz factor  $\Gamma$ . If the radiation is beamed  $L' = \delta^{-n}L$  and the intrinsic size  $R'_0$  of the  $\gamma$ -ray emitting region  $R'_0 = c\Delta t\delta$ . The limit on the comoving optical depth (*i.e.* compactness) translates into a limit for the beaming factor  $\delta$ . For a moving sphere (§2.2.3),  $\tau'_{\gamma\gamma} \propto L'(\delta/x)/\delta^{(3+\alpha)}/(\Delta t\delta) \propto x^\alpha \delta^{(-4-2\alpha)}/\Delta t$ . Therefore if the target photons are produced in the  $\gamma$ -ray emitting region we have

$$\delta \geq 6.3(L_\gamma/\Delta t_d)^{1/5}(x/10^4)^{1/10} \quad (4.23)$$

where  $\Delta t_d$  is the variability timescale in days.

A timescale of 2 days therefore implies the *model independent* limits  $\delta \gtrsim 5.5$  and  $R_0 \gtrsim 3 \times 10^{16}$  cm for the  $\gamma$ -ray emitting region.

#### 4.2.2.b Magnetic and radiation energy densities

We now assume that the  $\gamma$ -rays are produced by relativistic electrons via SSC. The fact that the  $\gamma$ -ray luminosity, produced via Compton scattering, is higher than that emitted at lower frequencies ( $10^{14} - 10^{16}$  Hz), supposedly via the synchrotron process, implies a radiation energy density,  $U_r$ , higher than the magnetic energy density,  $U_B$ . From the observed power ratio we derive that  $U_r$  must be one order of magnitude greater than  $U_B$ , which may be a lower limit if Klein Nishina effects reduce the efficiency of the self Compton emission. This result is independent of the degree of beaming, which, for a homogeneous source, affects both the synchrotron and the self Compton fluxes in the same way. This source is therefore the first observed case of the result of a ‘Compton catastrophe’ (Hoyle, Burbidge & Sargent, 1966). The fact that the  $\gamma$ -ray sources observed by GRO are strongly variable implies that the ‘Compton catastrophe’ may just occur during flares.

By combining the limits on the compactness discussed above,  $\ell \leq 1$  and  $U_r/U_B \geq 10$ , we can derive a limit on the magnetic field:

$$B \lesssim 15/(\delta \Delta t_d)^{1/2} \text{ G} \quad (4.24)$$

This limit is shown in Fig. 4.9 as a vertical line (for  $\Delta t_d = 2$  and  $\delta = 5$ ) in the plane  $B$  vs.  $\gamma_{max}$ .

It is worth recalling that for anisotropic geometries, the limit on the compactness can be somewhat relaxed, and the magnetic field can be correspondingly larger, but not by a large factor.

#### 4.2.2.c Maximum electron energy

If the maximum energy of the synchrotron photons in the emitting plasma frame is  $x_{s,max}$ , the self Compton mechanism produces photons of energy exceeding 5 GeV if  $\gamma_{max}^2 x_{s,max} \geq 10^4/\delta$ , which yields

$$\gamma_{max} \geq 2.5 \times 10^4/(\delta B)^{1/4} \quad (4.25)$$

A lower limit to  $\gamma_{max}$  is imposed also by requiring that the synchrotron process produces the observed UV and soft X-ray photons. Hence  $\nu_{s,max} \geq 10^{16} \text{ Hz}$ , which corresponds to

$$\gamma_{max} > 6 \times 10^4 [\nu_{16}/(\delta B)]^{1/2} \quad (4.26)$$

Furthermore, requiring that the scattering process is in the Thomson regime, yields the upper limit:  $\gamma \leq 1/x_{s,max}$ , which corresponds to

$$\gamma_{max} \leq 3.5 \times 10^4/B^{1/3} \quad (4.27)$$

Electrons above this energy may be present, but they will contribute to the  $\gamma$ -ray emission by scattering only photons of energy  $x \leq 1/\gamma \leq x_{s,max}$ , thus using a small fraction of the radiation energy density.

Finally, the request that the energy of the emitted photons do not exceed the electron energy, requires  $\gamma_{max} \gtrsim 10^4$ .

The above limits are shown in Fig. 4.9 in the  $B$ - $\gamma_{max}$  plane. It is interesting to note that the available parameter space is rather restricted. The Klein-Nishina condition sets a strong limit to the energy range of the relativistic electrons effective in producing  $\gamma$ -rays especially for high values of the magnetic field. On the other hand, for intermediate values of  $B$ , the production of  $\gamma$ -rays is practically inevitable if a high frequency synchrotron component is observed. The ‘favoured’ region is the shaded triangle.

### 4.2.3 The jet model

Here we show how the relativistic jet models discussed in §4.1 naturally explains the entire IR to  $\gamma$ -ray spectrum and variability of 3C 279. Despite of the number of parameters, the IC emission accounting for the  $\gamma$ -rays can be tightly related and constrained by the observed energy distribution from the infrared to the X-ray band.

The treatment is extended to allow for an increasing (rather than constant) Lorentz factor of the bulk flow along the inner, parabolic part of the jet as proposed by Ghisellini & Maraschi (1989) where it increases with distance as  $\Gamma = \Gamma_0(R/R_0)^a$ . This latter assumption has the consequence that the shape of the energy distribution depends on the angle of view (§6.1). For reasonable choices of the parameters, the bulk of the inverse Compton flux in the X-ray range is produced in the outer regions of the jet, where the relativistic boosting is stronger. It follows that the ratio of the Compton to the synchrotron flux, in the X-ray band, will be larger for small viewing angles since the second is less beamed.

In Fig. 4.10 we compare our best models for 3C 279 with the multifrequency data for this object in enhanced (filled squares) and quiescent (open symbols) periods, as assembled by Makino *et al.* (1989) and Hartman *et al.* (1992a). The data points are reported schematically. The  $\gamma$ -ray observations are not simultaneous with those in other bands but it is plausible that they refer to the ‘high’ state.

The continuous curves represent the synchrotron and self-Compton emission from the jet in ‘high state’ as computed from the model. The slope of the synchrotron emission steepens gradually, from the infrared to the UV band and the shape of this component essentially determines the shape of the inverse Compton component from the hard X-ray to the  $\gamma$ -ray band. Thus the agreement between the model and the observations in the latter bands lends strong support to the model in general, even though the detailed parameter choice can be somewhat changed.

The model parameters are reported in Table 4.2. We have tried to minimize the necessary value of the beaming factor and have chosen  $\tau_{\gamma\gamma}(5 \text{ GeV}) = 1$  at the base of the jet, implying a minimum dimension of  $R_0 = 2 \times 10^{15} \text{ cm}$  with  $\Gamma_0 = 5.5$ . It is possible that the flow starts with smaller dimensions possibly thick to  $\gamma$ -rays. A treatment of this regime, which would not produce high energy  $\gamma$ -rays, is neglected here.

The observed ‘low state’ spectrum up to the UV band can be well reproduced by varying two parameters, that is reducing the density of relativistic particles (by a factor of 2) and their maximum energy (by a factor of 3.6) (dashed curve). The Compton component predicted for the low state falls above the lowest X-ray data, which may be due to the fact that the observations are not simultaneous. In this case the predicted  $\gamma$ -ray flux is strongly reduced, both in energy range and intensity and its spectrum is steeper. The predicted  $\gamma$ -ray flux, in fact, is extremely sensitive to the maximum electron energy  $\gamma_{max}$

( $\nu_{C,max} \propto \gamma_{max}^4$ ). Therefore the  $\gamma$ -ray variability is predicted to be of greater amplitude than that at lower frequencies.

The energy densities in relativistic particles,  $U_e$ , magnetic field and radiation are not too far from equipartition (factor 30) along the whole jet: as expected,  $U_r$  is dominant over  $U_B$  especially at the beginning,  $U_e$  starts out intermediate between the other two, but becomes dominant further out. In the ‘quiescent’ state  $U_B$  and  $U_r$  are much closer to equipartition (factor 3).

A well defined time structure is predicted for the variability at different frequencies. A quantitative treatment requires to assume the perturbation parameters (§4.1.4) but the general behaviour can be inferred by simply considering separately the contributions of different regions of the jet to the overall spectrum. As an illustration we report in Fig. 4.11 the synchrotron and IC spectra obtained integrating the emission from the jet up to different distances along the axis. Based on this ‘tomography’ we expect that the far UV flux should vary with the shortest timescale:  $\Delta t_{UV} \simeq R_0/(c\delta_0)$ , which is of the order of hours. This is also the timescale predicted for the most energetic  $\gamma$ -rays, produced at the base of the jet, whose variations should be correlated with those in the UV. At the other extreme, the far infrared flux and the bulk of the medium energy X-ray flux are expected to vary together, though with different amplitudes, with a minimum (doubling) timescale of  $\sim 10$  days. Faster variability can occur even in these bands, but only with small amplitude due to the small contributions of the inner regions in these bands.

#### 4.2.4 Other gamma-ray sources

If the jet model we propose is correct, it is likely that 3C 279 is not a unique source. Other quasars, with large bulk motion and seen at small viewing angles, may have their beamed and flat Compton component dominating the X-rays and extending into the  $\gamma$ -ray band. For these sources, it is likely that the  $\gamma$ -rays are not absorbed in photon-photon collisions, and freely escape. Therefore the most promising target candidates for GRO are superluminal quasars with a flat X-ray spectrum such as the majority of HPQs, and some flat spectrum radio source. Also, sources with the flattest  $\alpha_{ox}$  should be selected, both because of the implied large X-ray flux density, and because a flat  $\alpha_{ox}$  is indicative of a large ratio of  $U_B/U_r$ , and therefore of a large Compton luminosity. Since this is strictly true only for a pure non-thermal, synchrotron self Compton model, the absence or weakness of the UV bump should be considered as a further reason in favour of a possible copious  $\gamma$ -ray luminosity.

As mentioned in §1.1.2.c, the EGRET instrument on board of GRO, has observed, until now, 16 radio loud objects. This indicates that the physical conditions inferred for 3C 279 may be common in highly luminous flat spectrum radio sources. The weaker source

(see Table 1.1) appears to be Mkn 421, which can be considered as an ‘X-ray’ type BL Lac (§6.1.1). If its emission at TeV energies (§1.1.2.c) is produced as SSC, electrons with Lorentz factors  $\sim 10^6$  which scatter IR photons are required.

The estimate of the emission from these sources can set important constraints on the origin of the diffuse  $\gamma$ -ray background, and/or on the high energy variability in blazars (Fabian 1992).

### 4.3 DISCUSSION

We have considered SSC emission from inhomogeneous relativistic jets, which are invoked to explain the smooth high energy spectra of blazars.

First we have shown that a simple model for a perturbation of fixed amplitude, travelling at constant speed along a jet of the type envisaged by Ghisellini *et al.* (1985), produces X-ray and UV variability with well defined spectral properties, *i.e.* with amplitude increasing with increasing frequency. This property follows naturally from the structure of the underlying stationary jet and is in agreement with the observations presently available. The above statement is valid for frequencies above the ‘break’ in the stationary spectrum, which is usually observed to occur between the infrared and UV bands of BL Lacs (§1.1.2.a). In a frequency range of about one decade below the ‘break’ frequency, the variability amplitude is independent of frequency. At still lower frequencies the evolution is dominated by opacity effects in the outer regions of the jet and the model does not extend thus far.

Within these general properties the light curves may follow two different types of behaviour: if the emission of the stationary jet is weakly weighted towards the outer regions ( $\zeta < 1$ ) the light curve maxima at all frequencies are strictly simultaneous, while for a jet heavily dominated by the outer regions the maxima occur later at lower frequencies ( $\nu > \nu_b$ ). Data of sufficient quality to test these properties are not available yet. A cross correlation analysis of variability at different frequencies within the EXOSAT energy range (0.3-6 keV) for PKS 2155-304 (Tagliaferri *et al.* 1991) did not show evidence of delays larger than few hundreds of seconds, and is consistent with the cross correlation function of light curves computed from the model. However the analysis was limited to small amplitude variability and to a narrow frequency range.

A relativistic shock wave can easily produce compression ratios sufficient to explain the observed amplitudes. It is worth mentioning that the perturbations envisaged here should maintain individuality for a few decades in path length ( $10^{14} - 10^{16}$  cm). They may extend further out to generate the emission knots observed at radio wavelengths with VLBI, but the present model does not include these scales. Since we have assumed that the perturbation is adiabatic, with constant amplitude over a wide range of distances,

the associated energy appear to be substantial, but relativistic effects clearly alleviate the energy requirements. In §5 we discuss the relative amount of bulk and radiative powers in pc-scale jets.

If the shock velocity in the frame of the stationary fluid is in the same direction as the jet stream, relativistic corrections enhance the variability amplitude observed at small angles for a relatively wide parameter range, while, for oppositely directed shocks, relativistic corrections reduce the observed amplitude at small angles, except for extreme values of the bulk velocity. Thus the first alternative predicts that sources viewed at small angles not only appear brighter, but also more variable, a point raised by Lind and Blandford (1985) in connection with the radio emission. Here only moderate values of the bulk velocity are required. The second alternative allows a similar conclusion but only if  $\beta_1 > 0.98$ .

The model therefore offers an interesting framework to interpret the observed hardening of the the X-ray spectra of BL Lac. It predicts a definite correlation of X-ray and UV variability, which can be measured by future campaigns of coordinated observations. In this respect the joint operation of IUE and ROSAT offers a unique opportunity. Such a campaign has been already performed for the source PKS 2155–304 by a large international collaboration and will allow a detailed comparison of the model predictions.

The model also predicts that the X-ray variability and its correlation with variability at lower frequency should be different for BL Lac sources with steep and hard X-ray spectra, which are expected to emit respectively via the synchrotron and Compton mechanisms. For objects with flat X-ray spectra correlated variability should be observed between X-rays and low energy synchrotron photons, with a long X-ray variability timescale, as in the case of 0735+178, BL Lac and 3C345 (Bregman *et al.* 1984, 1986, 1990; Maraschi 1991). X-rays can instead precede optical–UV variations when the X-ray flux is produced as synchrotron emission (OJ 287, Pollock *et al.* 1985; 1156+295, McHardy, 1989).

Variability at even higher energies, in the  $\gamma$ -ray band, can be a powerful means to study the physical conditions in blazars. In particular we have shown that the requirement of transparency together with the observed  $\gamma$ -ray variability timescale of 2 days imply that the high energy radiation from 3C 279 is relativistically beamed. Assuming a homogeneous spherical source, the lower limit to the Doppler factor is  $\delta \gtrsim 5.5$ .

Adopting a relativistic jet model, the escape of high energy photons is favoured by the geometry of the source. In fact, due to relativistic aberration, in the comoving frame most of the photons escape at large angles from the jet axis. Nevertheless we found that beaming is necessary in order to meet the transparency condition for 0.1–5 GeV photons. In the model considered, these are produced in a region up to  $2 \times 10^{17}$  cm length,  $2 \times 10^{16}$  cm across with a beaming factor  $\delta$  between 10 and 18 (bulk Lorentz factor  $\Gamma$  between 5.5 and 14, for an angle of view of 3 degrees). It is interesting to compare these values of  $\delta$ ,

derived solely from the high frequency emission to those derived from arguments based on the radio emission, which would indicate a connection between the emitting regions.

Similar arguments were previously applied to 3C 273 (Mc Breen 1979), where however the requirement of transparency is less compelling. In fact the steep high energy  $\gamma$ -ray spectrum of 3C 273 ( $\alpha_\gamma \sim 1.5$ , Bignami *et al.* 1981; §1.1.2.c), suggests that photon-photon absorption is actually taking place. In addition the 2–10 keV X-rays presumably are not strongly beamed, since the fluorescent Fe emission at 6.4 keV is observed (§3.1.6).

If the  $\gamma$ -ray luminosity of 3C 279 is due to the self-Compton process the radiation energy density must dominate the magnetic one. Arguments against this condition (the ‘Compton catastrophe’) have been raised. However, as mentioned in §2.1, the arguments apply only if there is no continuous injection or reacceleration of electrons, which is instead needed in all the compact emission regions of AGN, where cooling times are short.

In the framework of SSC models, it is possible to avoid the requirement  $U_r \gg U_B$  if the  $\gamma$ -rays are produced directly by the synchrotron process (Ghisellini 1989). In this case, however, one has the problem of how to accelerate the electrons to the extremely high energies required ( $\gamma_{max} > 2.3 \times 10^8 / B^{1/2}$  for  $\nu_s > 1$  GeV). Energies so large could be achieved in processes involving proton-photon collisions (Sikora *et al.* 1987; Mannheim & Biermann 1992), but the energy budget becomes prohibitive unless the energy distribution of ultrarelativistic protons is flat.

Alternatives to SSC models can be considered, in which the production of  $\gamma$ -rays is due to processes involving protons (as discussed in Hartman *et al.* 1992a), or to the interaction of an ultrarelativistic ( $\Gamma > 10^4$ ) or relativistic ( $\Gamma = 10$ ) jet with soft photons produced in an accretion disk, as proposed by Melia & Königl (1989) and Dermer, Schlickheiser & Mastichiadis (1992). However, it is not clear yet whether these models can satisfy at the same time all the limits posed by the luminosity, the spectrum and the variability observed for 3C 279.

In conclusion, the model discussed here is a natural extension of models previously applied to explain the radio to X-ray emission of blazars. It makes definite predictions on the timescales and correlation of variability at different frequencies. If our scheme is close to reality, by studying multiwaveband correlated variability, we will be able to trace the structure of relativistic jets much closer to the ‘central engine’ than is possible through radio observations. The campaign for coordinated observations of 3C 279 in the UV, X-ray and  $\gamma$ -ray bands, proposed by a collaboration of several groups including us, should be an important step in this direction.



Table 4.1 Specific Variability  $v$ 

	N	5500 Å	2500Å	1500Å	0.2 keV	3 keV
1H 0414+009	4				0.05	0.26
Mrk 421	14		0.16	0.18	0.45	1.12
Mrk 180	3				0.37	0.73
1218+304	9				0.16	0.24
Mrk 501	9				0.05	0.26
PKS 2005-489	5				0.84	1.17
PKS 2155+304	9	0.26	0.27	0.37	0.43	0.65
<i>a) i)</i> M=1			0.016	0.017	0.12	0.95
<i>a) ii)</i>			0.011	0.012	0.22	1.14
<i>b) i)</i>			0.017	0.017	0.49	3.93
<i>b) ii)</i>			0.15	0.15	0.82	3.38
<i>b) ii)</i> M=6			0.20	0.20	0.70	1.54

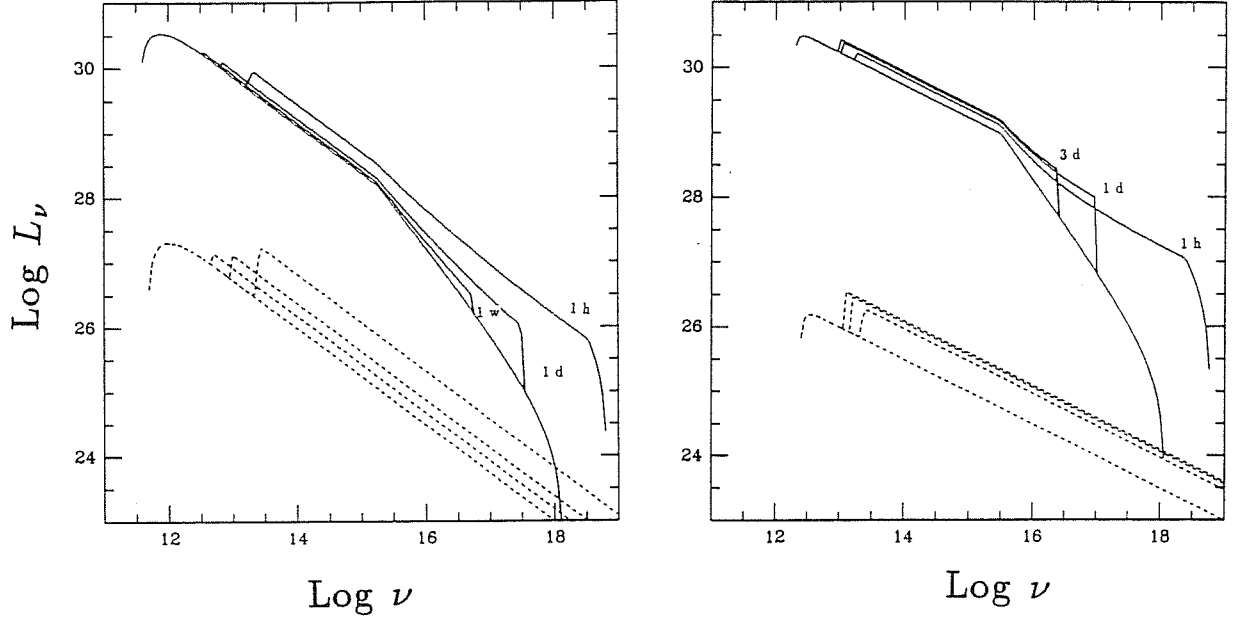
The table reports the values of the variability parameter  $v(\nu)$ . In the top part, the values obtained from observations (N is the number of X-ray observations). The bottom part reports the computed values for different jet parameters and characteristic of the perturbation (cases *a*, *b* and *i*, *ii*). In all these cases  $k=2$  and  $b=2$  were adopted for the intensity of the perturbation. The total number of ‘simulated observations’ is always  $N=500$ , while M indicates the number of crossing periods of the perturbation through the whole jet, during which the ‘observations’ are sampled.

**Table 4.2 Model parameters**

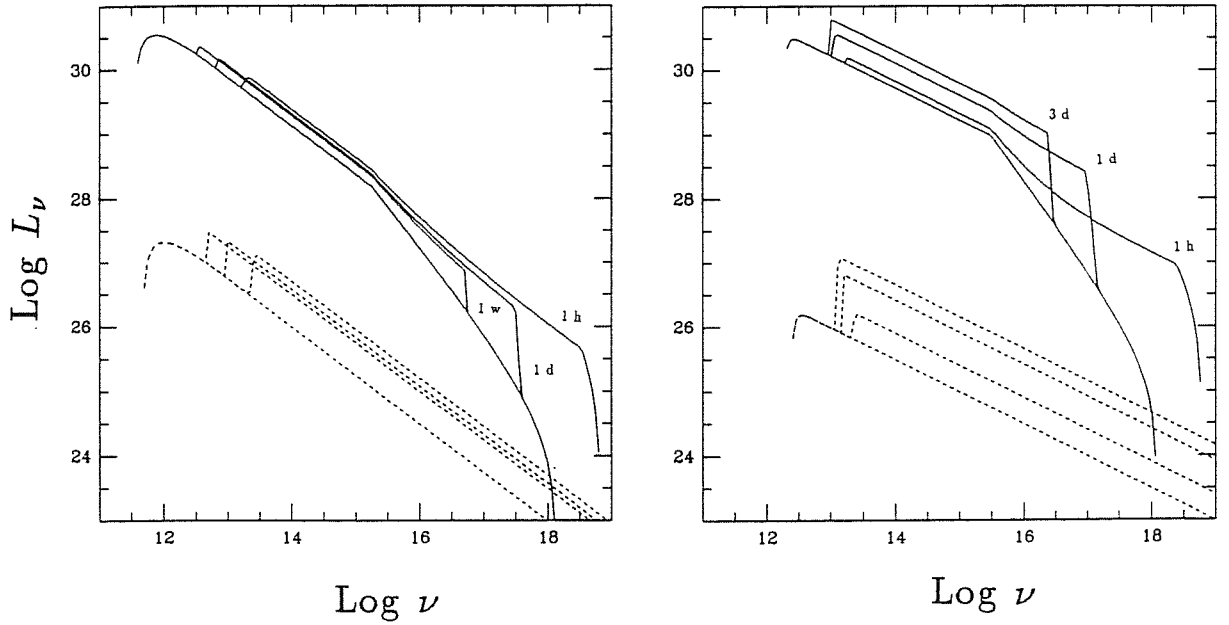
	$B_0$	$\tau_0$	$R_0$	$R_{max}$	$\gamma_{max}$	$\alpha_0$	$\Gamma_0$	$\zeta$	$\eta$
a)	$10^3$	$3 \cdot 10^{-1}$	$10^{14}$	$10^{17}$	$2.5 \cdot 10^4$	0.75	1	0.49	0.98
b)	900	$7 \cdot 10^{-5}$	$10^{14}$	$10^{16}$	$3.5 \cdot 10^4$	0.5	1	1.15	1.3
3C279 (high)	8	$2 \cdot 10^{-3}$	$2 \cdot 10^{15}$	$4 \cdot 10^{18}$	$2.0 \cdot 10^4$	0.5	5.5	0.5	1
(low)	8	$10^{-3}$	$2 \cdot 10^{15}$	$4 \cdot 10^{18}$	$5.5 \cdot 10^3$	0.5	5.5	0.5	1

Top part: model parameters for case a) and b). The model parameters are defined in the text, and are given in cgs units. For both cases  $\beta_p = 0.9$ ,  $b = k = 4$ .

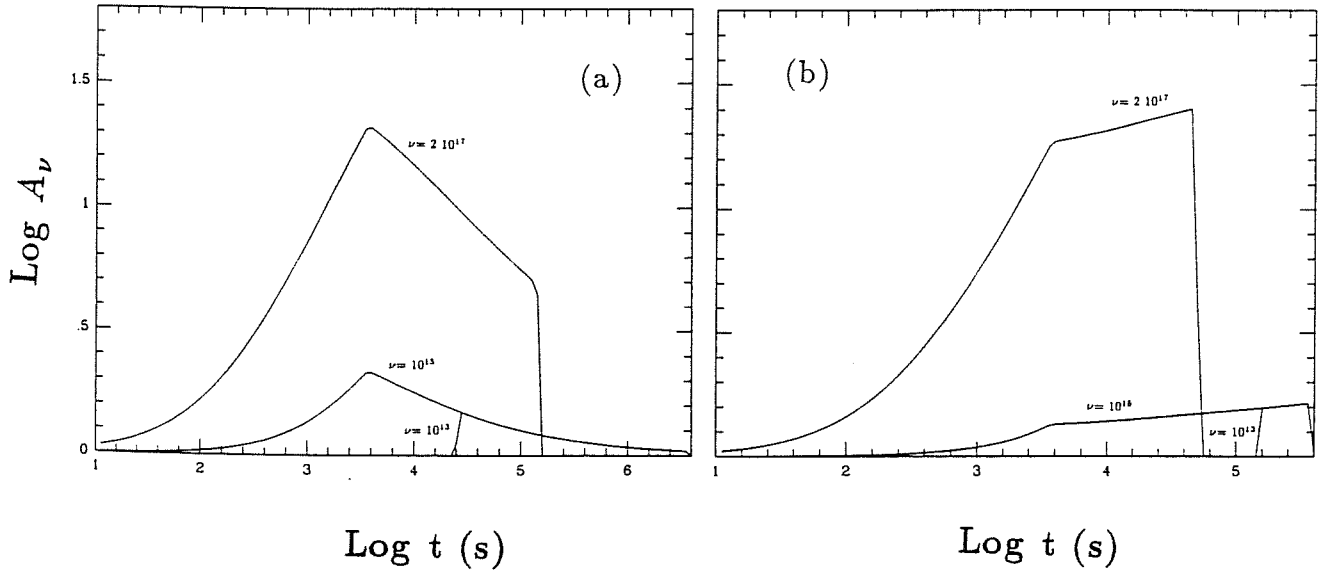
Bottom part: model parameter for 3C 279 (high state and low state).



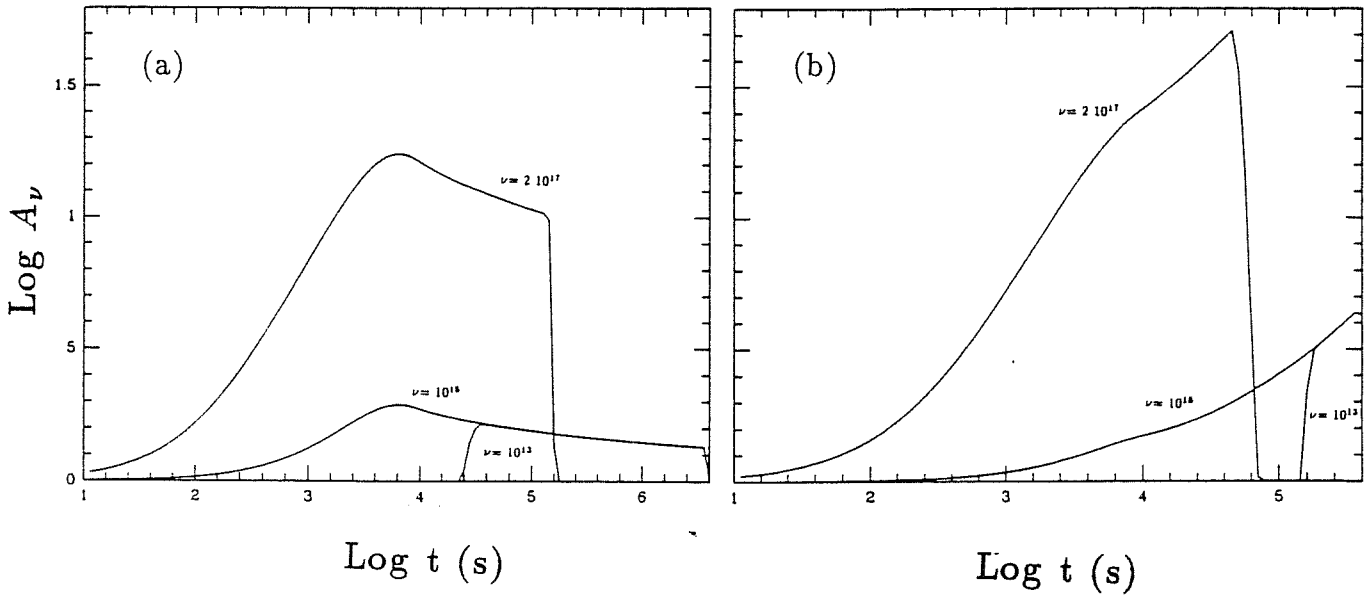
Figs. 4.1a,b. Synchrotron (solid lines) and inverse Compton (dashed lines) spectra emitted by jet models *a*) and *b*) respectively: The continuous line without label refers to the stationary spectrum. The spectra emitted 1 hour, 1 day and 1 week (or 3 days) after the start of the perturbation at the jet nozzle are labelled accordingly. The perturbation is assumed to have a constant thickness (case *i*).



Figs. 4.2a,b. The same as Figs. 4.1 for a perturbation with growing thickness (case *ii*).



Figs. 4.3a,b. Synchrotron light curves at different frequencies are shown for model *a*) and *b*) respectively, for a perturbation of constant thickness (case *i*). The monochromatic luminosities are normalized to the stationary ones at the same frequency. Both scales are logarithmic.



Figs. 4.4a,b. Light curves as in Figs. 4.3, but the thickness of the perturbed region increases with time (case *ii*).

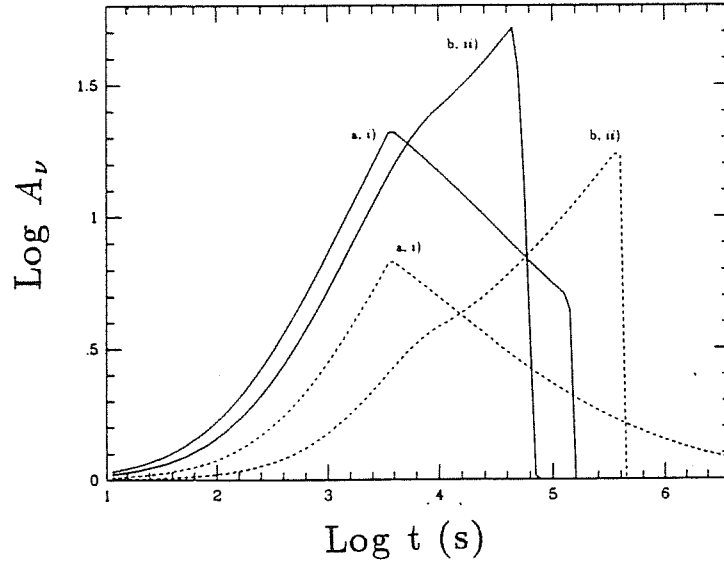


**Fig. 4.5.** Synchrotron (solid lines) and inverse Compton (dashed lines) light curves at the same frequency,  $\nu = 2 \cdot 10^{17} \text{ Hz}$ , are compared. Labels denote jet model *a*), case *i*) and jet model *b*) case *ii*). The monochromatic luminosities are normalized to their stationary values. Both scales are logarithmic.

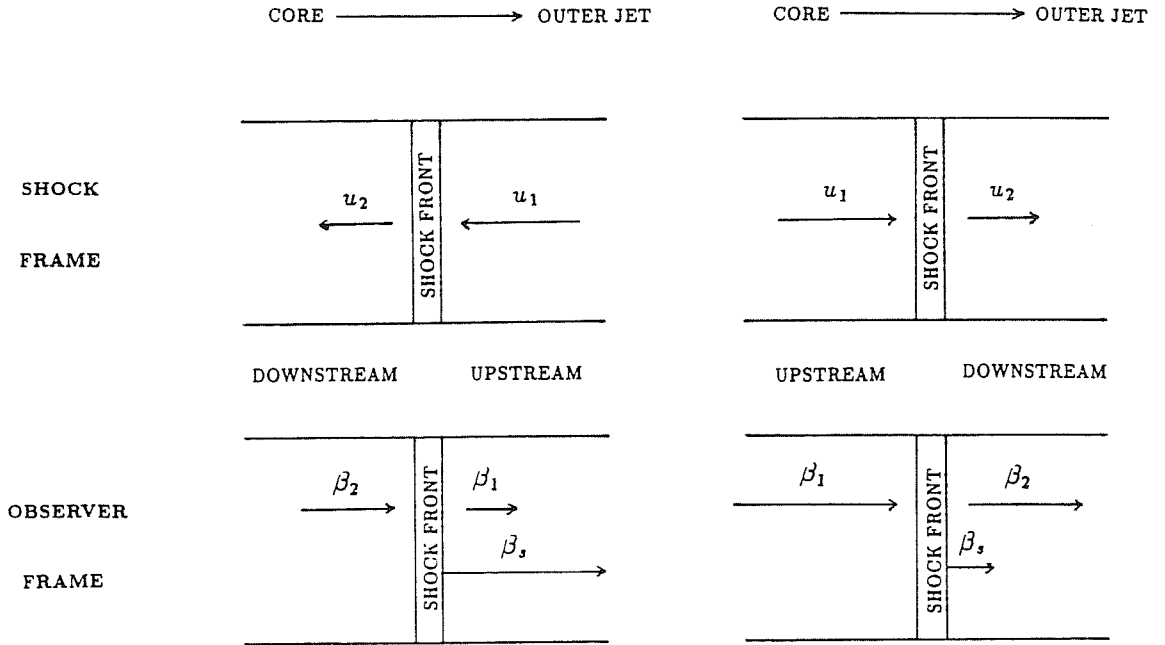
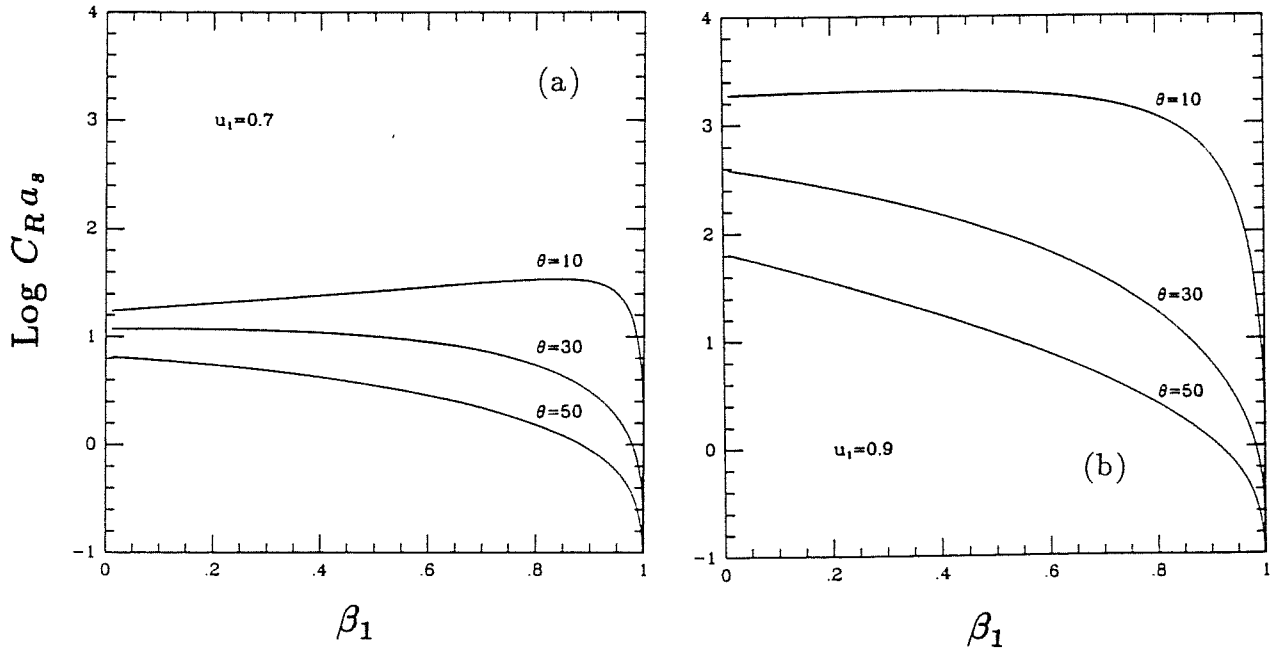
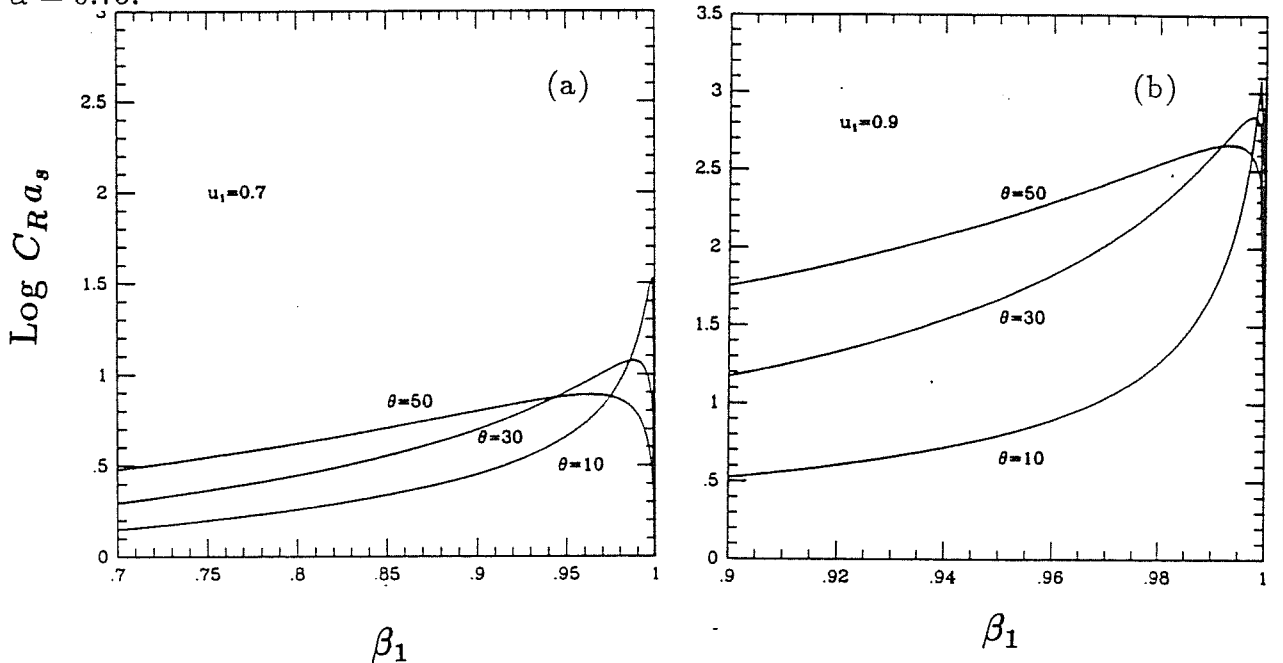


**Fig. 4.6.** Schematic representations of the kinematic of a planar shock: (left) upstream fluid on the outer side of the jet, (right) upstream fluid on the inner side of the jet. The upper panels show the kinematic in the shock frame, while the lower ones refer to the frame of the observer. Note the different relation between  $\beta_1, \beta_2$  and  $\beta_s$ .



**Figs. 4.7a,b.** The amplitude parameter  $C_R a_s$  computed with relativistic corrections for a planar shock (see §4.1.4 for precise definitions) is plotted as a function of the unperturbed fluid velocity  $\beta_1$  for different values of the angle of view  $\theta$ , for a case in which the upstream fluid enters the shock from the far side of the jet. The upstream velocities, determining the shock strength, are  $u_1 = 0.7$  (panel a) and  $u_1 = 0.9$  (panel b). The spectral index is  $\alpha = 0.75$ .



**Figs. 4.8a,b.** The same amplitude parameter as in Figs. 4.7 is computed for a 'reverse' shock, in which the unperturbed fluid enters the shock from the "nozzle" side for the same values of  $u_1$  and  $\beta_1$ .

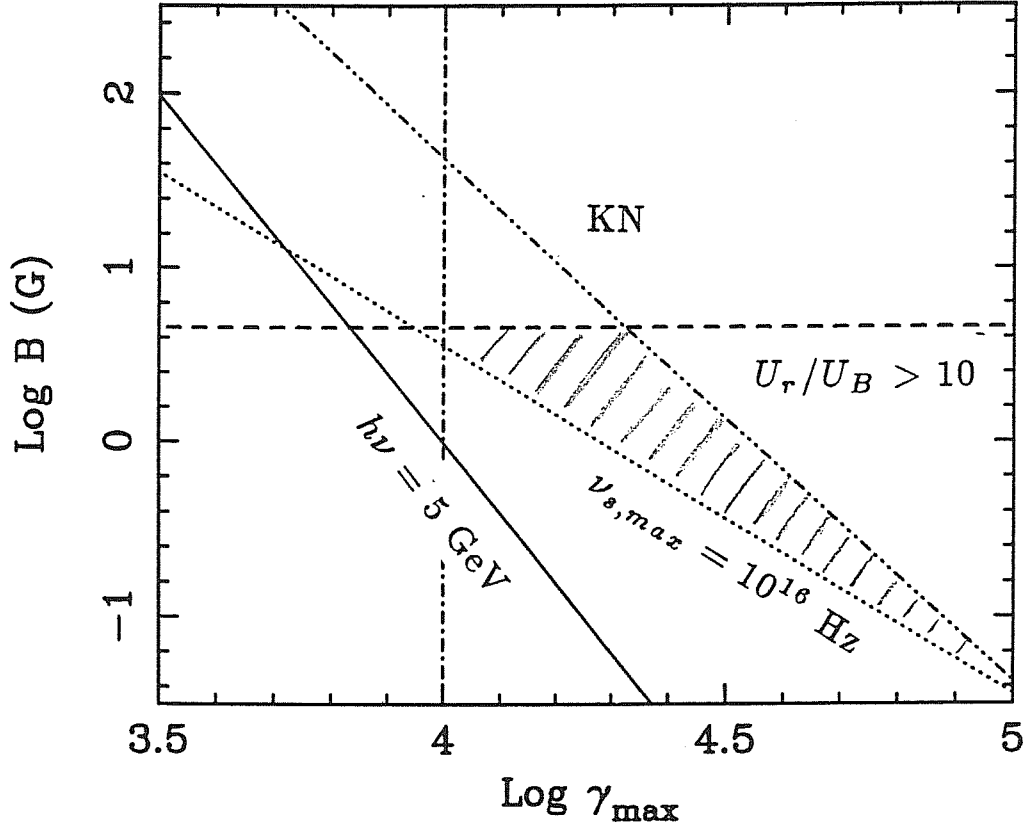


**Fig. 4.9.** The parameter space  $B$ - $\gamma_{\max}$ . Above the thick solid line (labelled  $h\nu = 5$  GeV) the self Compton process produces photons of observed energy greater than 5 GeV. Below the dot-dot-dot-dashed line (labelled KN) the scattering is completely in the Thomson regime. The dotted line (labelled  $\nu_{s,\max} = 10^{16}$  Hz) corresponds to an observed synchrotron frequency of  $10^{16}$  Hz. Below the horizontal line the magnetic field is sufficiently small to satisfy the limits  $U_r/U_B > 10$  with  $\ell = 1$ . For the latter limit we have assumed a spherical source with minimum observed variability timescale of 2 days. The vertical line indicates the minimum energy of electrons emitting 5 GeV photons. For all limits we considered a beamed model, with a value of  $\delta$  equal to 5.

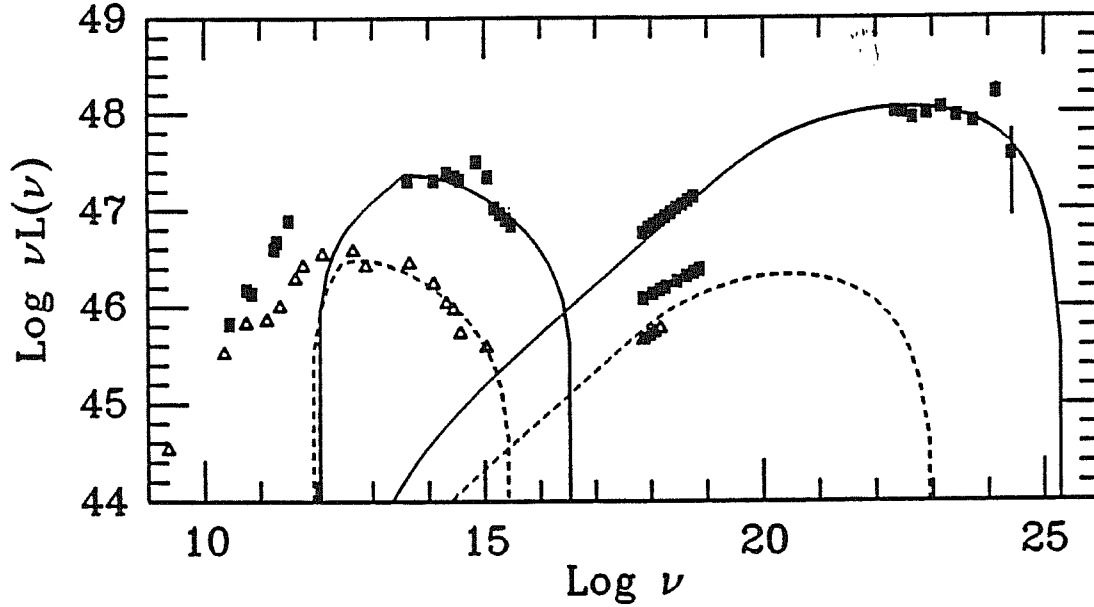


**Fig. 4.10.** The overall spectrum of 3C 279 from an inhomogeneous jet model is compared with observations. Data from Makino *et al.* (1989), Hartman *et al.* (1992a) and references therein. The overall synchrotron and self Compton spectra are shown separately. The parameters used for the high (solid line) and low (dashed line) states are as follows (see also Table 4.2).

*High state:* the jet extends from  $r_0 = R_0 = 2 \times 10^{15}$  cm, to a distance  $R_{max} = 4 \times 10^{18}$  cm. At the base of the jet we assumed:  $B_0 = 8$  G; the scattering optical depth of the relativistic electrons  $\tau_0 = 2 \times 10^{-3}$ ;  $\nu_{0,s,max} = 4 \times 10^{15}$  Hz;  $\Gamma_0 = 5.5$ . The jet axis forms with the line of sight an angle of 3 degrees. The bulk Lorentz factor increases, reaching the value  $\Gamma = 25$  at the end of the jet.

*Low state:* all parameters are the same as in the high state, except for  $\nu_{0,s,max} = 3 \times 10^{14}$  Hz, and the for the scattering optical depth,  $\tau_0 = 10^{-3}$ .



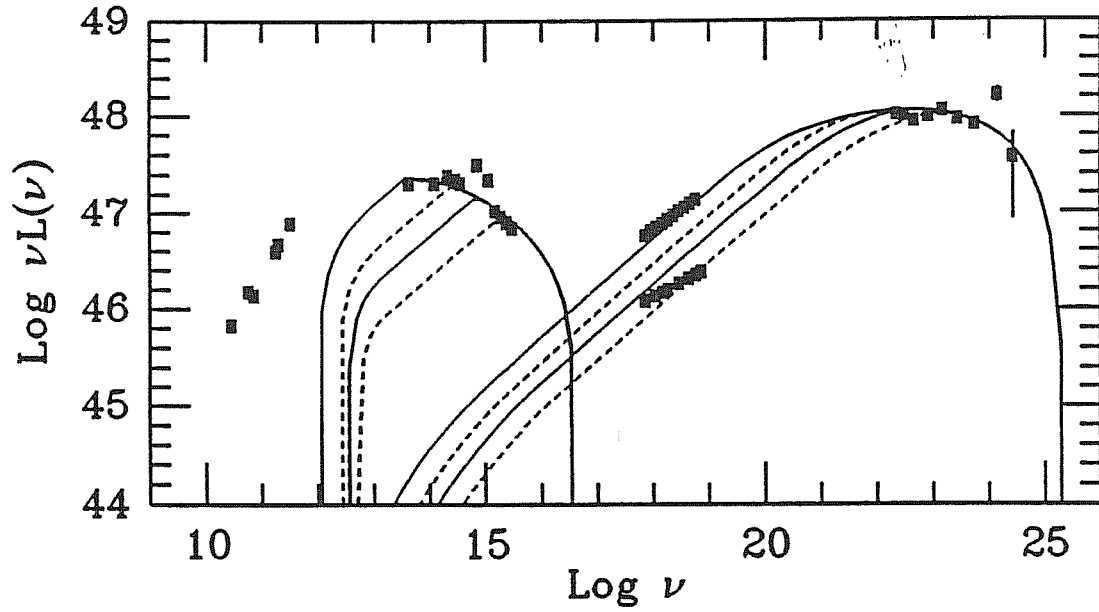


**Fig. 4.11.** Computed spectra for different portions of the jet, with the same parameters as for the high state shown in Fig. 4.10. The different spectra corresponds to the flux produced within  $R/R_0 = 30, 100, 300$ , and  $2000$  (from bottom to top). Note that the most energetic  $\gamma$ -rays are produced in the same small region as the UV photons, while the X-ray flux is mainly produced in the outer regions of the jet, together with the synchrotron infrared flux.

## Chapter 5. Pc-scale jets

Relativistic jets, the appearance of which have been assumed in §4, are commonly observed on pc-scale in the radio band (§1.2). Such jets are thought to be the result of the interaction of plasma outflowing from the ‘central engine’ with the ambient medium. Even if it is not clear how to disentangle the environmental effect from the ‘product’ of the engine, jets can certainly be used to infer more information of the central activity, *e.g.* that there is a (stable) symmetry axis.

Despite the increasing number of detailed observations, fundamental questions on the physics of jets remain unanswered (*e.g.* their matter content, velocities, initial collimation and acceleration mechanism). Numerical simulations seem to suggest that the two ‘flavors’ (FR I and FR II) of large scale structure may be reproduced by the supersonic motion of a collimated light fluid. Mildly relativistic flows affected by significant entrainment and deceleration can generate a type I objects, while at higher Mach numbers the jet interacts with the ambient through shocks and gives rise to type II morphology (Bridle 1991). The relative importance of ‘intrinsic’ physical differences and environmental effects is unclear, as is the relation with the central source (radio loud objects have host elliptical galaxies).

The numerical approach concerns the propagation of the jets but does not address the problem of their ‘origin’ and their relation with the central engine. It is therefore important to infer the physical parameters on smaller scales, in particular with respect to the power involved. In fact at least for blazars, the major power output can be in form of kinetic luminosity of a flow. It should be noted that there is also increasing evidence for the presence of relativistic outflows associated with the Broad Absorption Line phenomenon (which occur in about 10% of the quasars at high redshifts), which lead to the conjecture that the major difference with blazars could be ascribed to the degree of collimation (*e.g.* due to a different magnetic field or ambient medium).

Possible mechanism(s) responsible for the collimation and acceleration of jets can be constrained by the knowledge of the physical conditions of the flow. The physical parameters of the inner regions of many jets can now be estimated from detailed radio maps on milliarcsec scales and broadband spectral information. The use of standard SSC formalism allows the bulk Doppler factor, the emitting electron density and the magnetic field intensity to be estimated.

In the following we apply the standard SSC theory on a sample of sources with core sizes directly measured with VLBI. The sample consists of 105 sources obtained assembling from the literature the relevant data (Ghisellini *et al.* 1991; Ghisellini *et al.* 1992b).

The Chapter is structured as follow:

- In §5.1 we describe the sample of sources and in §5.2 we specify the quantities adopted to apply the SSC formalism.
- In §5.3 we concentrate on the *indicators of beaming*. In fact beaming is an ‘economic’ hypothesis to explain many observed phenomena: a quantitative, statistical comparison among the Doppler factors and velocities required to explain the different observations is crucial to verify the model. We therefore use the available data to estimate the Doppler factor (§5.3.1) for the various classes of sources of the sample and the brightness temperature distribution (§5.3.2). We then examine the correlation among various indicators of beaming effects (*i.e.* superluminal expansion velocity, core-dominance parameter, brightness temperature) (§5.3.3; §5.3.5; §5.3.6). And finally from both the apparent expansion velocities and Doppler factor, we estimate the bulk Lorentz factor and the viewing angle. The former is particularly important in connection with the unknown acceleration mechanism (§5.5), while the latter is an important test for the prediction of unification models (see also §6.1).
- §5.4 concerns the estimate of the emitting *particle density*, which constrains the matter content of jets (proton–electron or  $e^\pm$  plasma). We try to set limits on it by comparing information on different scales, from the compact region to the pc- and kpc-scales. In particular we compare the SSC particle flux with the expected maximum flux of  $e^\pm$  pairs which can escape the compact source (§5.4.2) and with the particle flux expected from an Eddington accreting source (§5.4.3); and finally we compare the predicted kinetic luminosity with the radiative luminosity and with the kinetic power estimated from large scale emission (§5.4.5).
- The amount of *dissipation* of jet kinetic energy is considered in §5.4.4, by both estimating the ratio of the kinetic and radiative luminosities on pc-scale and by comparing the kinetic power on small and large scale (§5.4.5).
- Some considerations on the dynamical role of the estimated *magnetic field* (in connection with the confining/accelerating mechanism) are mentioned in §5.5.

## 5.1 THE SAMPLE

The sample includes 105 extragalactic radio sources with VLBI core size data, derived mainly from Madau, Ghisellini, and Persic (1987), Pearson & Readhead (1988), and Linfield *et al.* (1989, 1990). It comprises 33 BL Lacs, 53 core-dominated quasars (CDQs), 11 lobe-dominated quasars (LDQs) and 8 radio galaxies. About 40% of our sources are

superluminal. The sample should represent, to the best of our knowledge, a ‘complete’ survey of the literature from 1986 onward, although it is not complete in any other sense. About 3/4 of the sources belong to the 1 Jy catalogue (Kühr *et al.* 1981), a complete sample of 518 radio sources with 5 GHz fluxes  $> 1$  Jy, covering 9.81 sr. For all these sources we then looked for additional optical flux, optical polarization, X-ray flux (available for all but 17 objects) and core dominance parameter  $R_{CD}$ . The sample was subdivided into the following classes: BL Lacs, quasars, and galaxies. The classification of the sources was based on the following criteria.

Following Stickel *et al.* (1991), a BL Lac has been defined as a radio source with a flat-spectrum at a few GHz having optical non-thermal emission with no or weak emission lines (rest-frame equivalent width  $< 5 \text{ \AA}$ ). Of the 33 objects so classified, 21 belonged to the 1 Jy sample (Stickel *et al.* 1991) and so were known to satisfy the equivalent width criterion. The remaining 12 objects were in the BL Lac lists of Burbidge & Hewitt (1989) and/or Véron-Cetty & Véron (1991). Of these, six sources had no redshift determination, and therefore extremely weak lines, while for the remaining six the published spectra showed only absorption features or very weak emission lines. Estimates of the ratio  $R_{CD}$  of core to extended flux on arc second (*i.e.* VLA) scales were found for all but two BL Lacs: all of them are core-dominated ( $R_{CD} > 1$ ). Moreover, all the 31 BL Lacs with optical polarization data are highly polarized ( $p_{max} > 3\%$ ). About 30% of the BL Lacs (*i.e.* basically all the ones mapped more than once with the VLBI) are superluminal. Note that about 85% of the objects have a redshift determination (a lower limit in six cases): for the remaining ones, a redshift of 0.4 was assumed in the derivation of the Doppler factor (see Ghisellini *et al.* 1986).

Sixty-four objects were classified as quasars, that is objects in which the optical spectrum is clearly dominated by non-stellar emission and shows broad lines. We have included under this denomination not only sources with stellar counterparts on sky survey plates, but also objects in which the underlying galaxy is detected (*i.e.* Seyfert 1’s). All quasars in our sample had published values (or lower limits) of the core dominance parameter, so we subdivided them in core-dominated (CDQs) and lobe-dominated (LDQs) quasars, (almost exactly equivalent to a division in flat- and steep-spectrum quasars §4.2). Due to obvious selection effects, the great majority (83%) of quasars in our sample are CDQs. For all but 10 sources optical polarization data were available so that the majority of the objects (both CDQs and LDQs) could be further classified as high-polarization quasars (HPQs;  $p_{max} > 3\%$ ) or low-polarization quasars (LPQs;  $p_{max} < 3\%$ ). About 45% of the quasars are superluminal, while one is subluminal.

Finally, 8 objects were classified as galaxies, that is radio sources in which the optical emission is mainly stellar. It is important to note that, due to the requirement that the sources had published VLBI core size data, the galaxies in our sample are either nearby, like M87 and NGC 6251, or more distant but with a strong, compact core. In

fact, 0108+388, 0710+439, 2021+614, and 2352+495 are classified as compact doubles by Pearson & Readhead (1988) and as candidate gigahertz peaked-spectrum (GPS) sources by O’Dea *et al.* (1991). Note also that these four sources are strongly core-dominated on arc second scales (Ulvestad *et al.* 1981; Baum *et al.* 1990), with  $R_{CD} \gtrsim 5$ , at variance with typical radio galaxies which are lobe-dominated. 3C 84 (NGC 1275) should be in a class by itself: it is the central galaxy of the Perseus cluster, it has FR type I morphology, a flat radio spectrum, and a Seyfert 2-like optical spectrum. It is also highly polarized, and probably in interaction. We have classified it as a galaxy but one should bear in mind that it is a very peculiar object. Five galaxies are subluminal while one is superluminal (but only an upper limit on  $\beta_a$  is available).

The observational data for the sample are presented in Table 5.1, which gives the source name; redshift; VLBI core size ( $\theta_d$ ) (when the major and minor axes  $a$  and  $b$  are given we assume  $\theta_d = \sqrt{ab}$ ); the radio flux ( $F_m$ ) at the frequency  $\nu_m$ ; X-ray (at 1 keV, if available) and optical fluxes (5500 Å); superluminal speed (the fastest one in the case of more than one component) and ratio  $R_{CD}$  of core to extended flux on arc second scales. All values were K-corrected to 5 GHz rest frequency taking  $\alpha_{extended} - \alpha_{compact} = 1$ . It is also noted if the object belongs to the 1 Jy (Kühr *et al.* 1981) or 2 Jy (Wall & Peacock 1985) catalogues (all 2 Jy sources also belong to the 1 Jy catalogue). When a source is not included in the 1 Jy sample, a reference to the Burbidge & Hewitt (1989) and/or Véron-Cetty & Véron (1991) list is given for BL Lacs, or to the Parkes (PKS) catalogue (1990) for other sources, if appropriate. In the last column the objects are classified as high- or low-polarization objects (HP and LP respectively), and a reference to polarization data is given. We indicate with an asterisk the sources which have been detected in the  $\gamma$ -ray band above 100 MeV by GRO, at the time of writing (§1.1.2.c; Table 1.1).

## 5.2 THE SSC FORMALISM

We estimate the Doppler factor, the particle density of the emitting electrons and magnetic field intensity from the ‘classical’ condition (§2.2.4) that the SSC flux should not exceed the observed flux at high frequencies. We considered only sources whose radio cores have been measured by VLBI because the core angular dimension is a crucial parameter for estimating the Doppler factor through the standard SSC model. We assume that the frequency of the VLBI observation is the self-absorption frequency,  $\nu_m$ , of the core component dominating at that frequency. This assumption, generally is believed to account for the observed flat radio spectra of the core emission, may not be verified for individual emission knots observed at some distance from the core, which may well be transparent at VLBI frequencies and since the self-absorption frequency is generally unknown for the emission knots, we limit our considerations to the cores.

We remind that because X-rays can be produced by mechanisms other than SSC or in regions different from the radio emitting one the particle densities are upper limits only and the Doppler factors are lower limits. Since the derived  $\delta$  is a lower limit in any case, we have assumed an amplification factor appropriate for a moving sphere ( $\delta_{3+\alpha}$ ), which minimize the Doppler factor (§2.2.3). The thin synchrotron emission has a spectral index  $\alpha = 0.75$  for all sources (or possibly ranging between  $0.5 \leq \alpha \leq 1$ ). These assumptions will be discussed.

For the fraction of sources with no X-ray data, we have applied the same formalism to derive the beaming factor  $\delta$ ,  $K$  and  $B$  but comparing the predicted and the observed optical fluxes. The derived Doppler factor should not critically depend on which flux is used, given the weak dependence of  $\delta$  on the X-ray or optical flux. And this confirms the suggestion that part of the radio sources have to be beamed, in order that the radio component does not overproduce the optical flux by self-Compton emission.

Values in brackets in the tables refer to objects with no measured redshift (for which we used  $z = 0.4$ ).

In the whole Chapter, the values  $H_0 = 50 \text{ km s}^{-1} \text{ Mpc}^{-1}$  and  $q_0 = 0.5$  will be used, unless otherwise indicated.

### 5.3 BEAMING INDICATORS

In the 20 years after the original suggestion of Rees (1966, 1971) that radio jets are the signature of energy transport in the form of bulk energy, from the central galaxy to the extended radio lobes, and that the plasma in the jet moves with relativistic velocity, this hypothesis has found increasing observational support. In the following the main evidences are summarized.

- *Superluminal motion*

Perhaps the most striking indication is the measurements of superluminal velocities in many of the sources which could be resolved by VLBI (§1.2).

The usual explanation of superluminal motion involves a blob of magnetized plasma ('ballistic model') or a perturbation in the jet, moving with the pattern velocity  $c\beta_p$  in a direction close to the line of sight (Blandford & Rees 1978; Blandford & Königl 1979) (even if the various behaviours described in §1.2 would require a more sophisticated model).

In this case due to Doppler and geometrical effects, the apparent (transverse) speed is

$$\beta_a = \frac{\beta \sin \theta}{1 - \beta \cos \theta} \quad (5.1)$$

$\beta_a > 1$  for  $\Gamma > \sqrt{3/2}$ .

Alternative explanations of the superluminal effect involve the motion of perturbations or waves which brighten the region through which are passing (*e.g.* accelerating locally the emitting particles) or screen models (which suffer from the fact that contraction of the VLBI components has never been seen). For a review of the possible interpretations see Blandford, McKee & Rees (1977), Zensus & Pearson (1987).

In particular the same argument leading to eq. (5.1) applies if the moving component is a shock wave, the front of which is identified with the superluminal feature (Blandford & Königl 1979). In the latter case the relativistic speed is not connected directly with the plasma motion, but with the velocity of the perturbation. Note also that in the case of a conical shock waves the opening angle of the beamed radiation ( $\sim 1/\Gamma$ ) can be different from the angle of the bulk velocity, as model for VLBI radio jets suggest (Mutel *et al.* 1990).

It is therefore important to determine whether the matter is really moving or not: the major difference is that in the case of plasma motion the emitted radiation is also beamed along the velocity direction (so giving rise to the high synchrotron brightness temperatures observed without the overproduction of inverse Compton X-rays). The observed superluminal motion strictly requires that some ‘phase’ or ‘pattern’ speed of a wave to be relativistic but there are strong arguments also for relativistic bulk velocity of the radiating plasma. The main ones follow.

- *Brightness temperatures in excess of  $10^{12}$  K and paucity of X-rays.*

The Compton flux becomes very large if the photon and electron densities are large. The photon density is measured by the brightness temperatures, and multiple Compton scattering (leading to efficient cooling) becomes important when  $T_B \gtrsim 10^{12}$  K (§2.2.5). Many sources seems to violate this limit predicting too many X-rays produced by the self Compton mechanism. When the dimension of the source is measured directly (VLBI) the brightness temperature  $T_B \propto 1/\delta$ . If instead the dimensions are estimated by time variability,  $T_B \propto \delta^{-3}$  and consequently Doppler factors of 10 could explain  $T_B \sim 10^{15}$  K. But note that the intraday radio variability observed in some QSO and BL Lacs implies  $T_B > 10^{18}$  K, hence requiring  $\delta \sim 100$ . These measures of rapid variability have received strong support by the observations of simultaneous optical variability, which indicates that the variations are intrinsic to the source. Note that Lorentz factors  $\gtrsim 100$  are also invoked in some jet emission models (Melia & Königl 1989; Coppi, Kartje & Königl 1992) and recently in order to explain the  $\gamma$ -ray bursts phenomenon (Brainerd 1992).

Furthermore for  $T_b \gtrsim 10^{11}$  K radiation is so intense that induced Compton scattering can be relevant, being the relative optical depth  $\tau_{ic} \simeq (kT/m_e c^2)\tau_T$ . It would affect the spectral shape near the brightness temperature peak but up to now no signs of its effects has been observed. For brightness temperatures as high as  $10^{18}$  K, this would imply an

external optical Thomson depth  $< 10^{-8}$  (while the typical optical depth in the BLR is  $\sim 10^{-2}$ ), suggesting that relativistic effects are present (Blandford 1990).

Analogously SSC theory often predicts an X-ray flux in excess to the one observed and, as discussed in §2.2.4, beaming can solve the problem. This in fact allow us to derive limits on the Doppler factor, electron density and magnetic field intensity for our sample.

- *Strong and rapid variability of blazars*

The violent activity of blazars can be explained if radiation is beamed towards the observer.

The Doppler boosting of the flux  $\propto \delta^n$  and time contraction  $\delta^{-1}$  makes possible to easily explain luminosity changes  $\Delta L/\Delta t \propto \delta^{n+1}$  in excess of  $10^{42}$  erg s $^{-2}$  (Blandford & Rees 1978). ( $n$  depends on the structure of the emitting plasma, §2.2.3).

- *One sidedness of jets*

In most of the core-jet sources only one jet is observed (Marscher 1992). The one sidedness can be accounted for by the so-called Doppler favoritism. In fact if the central engine produces two intrinsically equal but oppositely directed jets and beaming effects are present, the ratio,  $J$ , of the fluxes observed from the jet closer to the line of sight and the opposite one (counterjet) can reach very high values. Assuming no isotropic emission from the jet

$$J = \left( \frac{1 + \beta_b \cos \theta}{1 - \beta_b \cos \theta} \right)^n \sim \left( \frac{2}{\theta} \right)^{2n} \quad \text{for } \Gamma > \frac{1}{\theta} > 1 \quad (5.2)$$

Extreme values of the parameters are not required to account for a ratio in the fluxes greater than the dynamical range of VLBI. Observations of one-sidedness on kpc scale, with the same asymmetry of the small scale jet, argues for relativistic or mildly relativistic velocities also on large scales: typical values  $J \sim 4 - 10$ , imply  $\beta_b \gtrsim 0.5 - 0.8$ , even if for M87  $J \gtrsim 300$  (Marscher 1992).

It has been also proposed that the one-sidedness is intrinsic: it could be due to an alternation of the jet ejection angle, of about  $2\pi$  ('flip flop' behaviour, Rudnick & Edgar 1984) or asymmetric dissipation, *e.g.* due to different ambient conditions. However these suggestions seem ruled out by the so called 'Laing-Garrington' effect (Laing 1988; Garrington *et al.* 1988).

- *Asymmetric Faraday depolarization ('Laing-Garrington' effect)*

Measures of polarization tend to show that even when the oppositely directed beam is observable, the observed jet is always on the same side as the less depolarized lobe. It should be a signature of the fact that radiation from that jet should pass through more material along the line of sight (Laing 1988), *e.g.* for obscuration by a central disc/cloud.



For  $T = 10^4$  K radiation at  $< 5$  GHz would be free-free absorbed if  $n^2 l \gtrsim 10^{27}$ , where  $l$  is the thickness of the region.

Despite this effect strongly supports the beaming hypothesis, it now appears that there is a systematic difference in spectral indices between the two lobes.

- *$\gamma$ -ray emission*

The recent detection of strong and variable  $\gamma$ -ray emission in radio loud quasars, indicates that not only the radio, but also the high energy emission has to be beamed to avoid absorption due to photon-photon collisions (§1.1.2.c; §4.2)

- *The simultaneous optical-radio variability*

Even if it is produced in different parts of a jet, it can be explained if some perturbation travels along the jet at relativistic speeds  $\beta_p c$  at small viewing angles  $\theta$  (Salvati & Fanti 1983). If the base of the jet emits optical, while the radio is produced further out, the radio photons lag the optical ones only by a time contracted by the Doppler effect by a factor  $1/\Gamma_p^2$  (for  $\theta = 1/\Gamma_p$ ). If  $\Gamma_p = 10$ , and the radio region is one pc from the optical one the observed delay can be only 10 days.

- *Strong jet bending.*

The strong jet bending seen in some sources, can be explained if it is amplified by projection for small viewing angles. Furthermore if the bending is due to external ram pressure, the curvature results proportional to the beam velocity (Begelman, Rees & Blandford 1979) and non-relativistic flows would imply implausible high values for the external pressure.

- *Ionized matter*

The estimate of the incident continuum in highly ionized filaments radio galaxies, as in the FR I radio galaxy Cen A (Morganti *et al.* 1992). Beaming effects are also suggested in order to explain the observed conical patterns of ionized gas close to radio galaxies. (Tadhunter & Tsvetanov 1989).

- *Jet physics*

If the power which supplies the radio lobes has to be transported in the form of kinetic energy, very fast jets have also the advantage to minimize the mass flux required to produce the observed power. Moreover relativistic speeds are not unexpected, if relativistic potential wells are present. Fast speed on large scale is also suggested by the observation of superluminal motion on kpc scales (which would confirm the effective flowing of the emitting plasma), by the fact that plasma must flow faster than the separation velocity of lobes, which can be  $\sim 0.1c$  (Longair & Ryle 1979), by ram pressure arguments

( $\beta \sim 0.05 - 0.1$ , *e.g.* Alexander 1992) and by jet/lobe/emission line asymmetries which are consistent with mildly relativistic ( $\beta \gtrsim 0.5$ ) velocities (Bridle 1991).

- *Possibility of a unification picture*

‘Unified’ models of AGN, whereby different classes of sources such as radio galaxies, radio loud quasars, and blazars can be interpreted as a same basic phenomenon viewed from different angles. The recent results of surveys lead to the construction of complete samples of BL Lacs and HPQs and their luminosity functions. This has allowed, for a chosen parent population, the comparison of the predictions of beaming models with the observed luminosity functions for BL Lacs and for radio quasars, yielding quantitative estimates of the required bulk Lorentz factors (§5.3.6.c; §6.1).

There are also arguments against the beaming picture.

The observations of iron line emission at  $\sim 6.4$  keV, with large equivalent width, would argue against strong beaming effects in the X-ray band (§3.1.6). A line with  $EW \sim 50$  eV has been detected in 3C 273 (while only upper limits of about 60 eV, 120 eV and 200 eV have been detected in 3C 279 and the core-dominated quasars NRAO 140 and 4C34.47, Ohashi *et al.* 1992).

Furthermore there is not the expected correlation between core dominance and apparent superluminal speed (Gabuzda, Wardle & Roberts 1990; §5.3.5) and the deprojected linear sizes of some superluminal sources appear to be extreme.

Systematic differences in the two lobes of extended radio sources, like the asymmetry in the optical line emission on kpc scale, the distance of the hot spot and the spectral index (Liu & Pooley 1991) could be another indication against Doppler favoritism (or, at least, indicate the importance of environmental effects).

Despite this large body of information we are still lacking a quantitative assessment of the beaming parameters, *i.e.* the values of the bulk and/or phase velocities in the jets and of the viewing angles, which are important not only to understand the physics of jets, but also in view of understanding the vastly different behaviour and morphology of different classes of sources.

One can find direct limits on the bulk velocity by estimating the degree of relativistic beaming necessary to reconcile predictions and observations of the high frequency Compton flux, and by the distribution of the flux ratio  $R_{CD}$ , between the (beamed) core and the (unbeamed) extended radio emission. For the superluminal sources, we can infer the ‘pattern’ velocity by the observed superluminal speed.

Here we derive and discuss the ‘direct’ limits on the beaming parameters (Ghisellini *et al.* 1991; Ghisellini *et al.* 1992b). Although the sample is not complete nor homogeneous, it is the largest for which we can derive and compare the beaming parameters from different indicators.

### 5.3.1 The Doppler factors

From eq. (2.4.5) the Doppler factor  $\delta$  for all sources in the sample has been derived. For those without X-ray data (17 sources, *i.e.* about 16% of the sample),  $\delta$  has been estimated using the optical flux. To check that in this case  $\delta$  is not grossly underestimated, we compared the beaming factor derived with optical and with X-ray data for all sources having both fluxes, with the result that the optical limit on the inverse Compton flux yields on average values of  $\delta$  a factor 1.9 and 2.2 lower than those derived from the X-rays for  $n = 3 + \alpha$  and  $n = 2 + \alpha$  [eq. (2.46)] respectively.

In Fig. 5.1 the derived distributions of  $\delta$  for BL Lacs (5.1a), CDQs (subdivided in HPQs and LPQs) (5.1b), and LDQs and radio galaxies (5.1c), are shown; in Table 5.2 we report the values of  $\delta$  for each source and in Table 5.3 the mean and the median values for the different classes of sources. It is clear from Fig. 5.1 that the  $\delta$  distributions for BL Lacs and CDQs are significantly different (at the 98.7% level, according to a KS test), with BL Lacs having *lower* values of  $\delta$ . The difference between BL Lacs and high-polarization CDQs is even larger ( $> 99.9\%$  level). It may be noted that not only the averages, but also the shapes of the distributions are different, with BL Lacs spanning a wider range in  $\delta$ , with a significant tail towards low values. This confirms the results of Madau, Ghisellini & Persic (1987) (based on a much smaller sample), and is in conflict with the idea that BL Lacs are CDQs (or HPQs) whose continuum is so enhanced as to swamp the emission lines. Instead, this result suggests that the absence of lines in BL Lac objects is due to the isotropic emission components of BL Lacs (continuum and lines) being intrinsically weaker than in CDQs, and points to different parent populations for the two classes of objects.

Amongst CDQs, HPQs and LPQs have similar distributions of  $\delta$ .

The mean value of  $\delta$  is higher for HPQs than for LPQs, although the median values are equal. It is not clear, therefore, if the presence of polarization is related to a higher degree of beaming, or to an additional non polarized component in LPQ, diluting the non thermal polarized continuum.

To assess this problem, it will be very important to measure the degree of polarization of those quasars with no polarization measurements.

Lobe dominated quasars and radio galaxies are characterized by values of  $\delta$  much smaller than those of CDQs. As will be discussed in §5.3.4, this is in agreement with the lower values of superluminal velocities found for these sources and leads to the inference that the parsec scale jet in these sources is pointing at large angles to the observer.

We remark that if we consider the ensemble of core dominated, lobe dominated quasars plus radio galaxies, the overall  $\delta$  distribution is similar in shape to that of BL Lacs. This might be compatible with a scheme in which BL Lacs live in a very ‘clean’ ambient and are therefore recognized as such even when the beaming factor is small. On the other hand, in strong radio galaxies and quasars, the coexistence of different types of ‘activity’ makes only

the highly beamed objects be recognized by a separate classification. Thus from the point of view of the present considerations, LDQs and CDQs represent a sequence of increasing beaming factors in otherwise similar ‘host nuclei’.

### 5.3.2 Distributions of brightness temperature

As from eq. (2.48)  $T'_B \propto (\tau_r/B)^{1/6.5}$ . Typical values of  $\tau_r/B$  are between  $10^{-2}$  and 10, therefore  $T'_B$  is bound to have a narrow distribution around the numerical value indicated by eq. (2.48). Observationally, the brightness temperature is given by:

$$T_B = 1.77 \times 10^{12} \frac{F_m}{\theta_d^2 \nu_m^2} (1+z) \text{ } ^\circ\text{K} \quad (5.3)$$

where the observable quantities have the same units as in eq. (2.43).

For our sources we can derive the intrinsic brightness temperatures from the observed ones using  $T'_B = T_B/\delta$  (moving sphere) or eq. (2.52) (continuous jet).

In Fig. 5.2 we show the distribution of the observed brightness temperatures, together with that of the intrinsic ones, derived for a moving sphere. As can be seen, the distribution of  $T'_B$  has a very small dispersion with a mean value of  $(1.84 \pm 0.08) \times 10^{11} \text{ } ^\circ\text{K}$ , in good agreement with eq. (2.48). For  $n = 2 + \alpha$  and using eqs. (2.46) and (2.52) the distribution and the mean value of brightness temperatures do not significantly change.

Note that both  $T_B$  and  $\delta$  depend on the observables in a similar way, so that their ratio is rather insensitive to them. For  $\alpha = 0.75$  we have  $T'_B \propto F_x^{0.18} \theta_d^{-0.36} \nu_m^{0.68}$  (assuming  $n = 3 + \alpha$ ).

### 5.3.3 Superluminal motion

Of the 105 sources in our sample, 39 BL Lacs and quasars have shown superluminal motion, one quasar has a subluminal upper limit on the expansion velocity, while 5 radio galaxies have shown subluminal motion, and for another radio galaxy we have a superluminal upper limit on the expansion velocity.

It has been suggested (Lind & Blandford 1985; Cohen & Vermeulen 1991) that the velocity responsible for the boosting of the radiation may be smaller than the velocity of the pattern responsible for the superluminal motion as would be for a shock wave. Consider a source moving with a bulk Lorentz factor  $\Gamma < \Gamma_p$  at an angle  $1/\Gamma$ : for this source  $\delta = \Gamma$ , while  $\beta_a = \delta\beta_p(1 - \beta_b^2)/(1 - \beta_p\beta_b)$  [eq. (5.1)], which approaches  $2\delta$  as  $\beta_p \rightarrow 1$ . If  $\Gamma < \Gamma_p$ , therefore, the average Doppler factor of a reasonably large sample of sources should be significantly smaller than the average apparent velocity.

### Correlation of $\beta_a$ with $\delta$

The apparent velocities measured for the 46 sources within our sample having data of proper motion are compared with the values of  $\delta$  derived from the SSC argument for the same sources in Fig. 5.3.

There is a significant correlation (99.7% level) between the two quantities, independent of the choice of  $n$ , as derived by means of a survival analysis to take into account the upper/lower limits on  $\beta_a$ . When the sample is subdivided into different classes the correlation remains significant only for LDQs and it is only marginal for LDQs+CDQs, but in this case the statistics is quite poor.

It was noted before that the expansion velocities of BL Lacs are smaller than those of quasars, which was explained either assuming that they are extremely aligned sources, but with the same Lorentz factor as the other superluminals (*e.g.* Roberts, Gabuzda & Wardle 1987; Cohen 1989) or assuming that they have smaller Lorentz factors (*e.g.* Mutel 1990). We instead find that the mean apparent speeds of BL Lacs and quasars are equal, while LDQs, LPQs and HPQs appear to lie on a sequence of increasing  $\beta_a$  (Table 5.3b).

Fig. 5.3 shows that there is no systematic preference for  $\beta_a$  to be greater than  $\delta$ : the mean values for the whole sample are in fact  $\log \beta_a = 0.64 \pm 0.10$  and  $\log \delta = 0.50 \pm 0.08$ , consistent within  $\sim 1\sigma$ . Note that we have assumed  $H_0 = 50$  (which gives a larger value for  $\beta_a$ ), and  $n = 3 + \alpha$  (which results, on average, in slightly smaller values of  $\delta$ ), and that the estimated  $\delta$ 's are lower limits. For  $H_0 = 100$  and  $n = 2 + \alpha$ , one obtains  $\log \beta_a = 0.34 \pm 0.10$  and  $\log \delta = 0.61 \pm 0.10$ , with  $\delta$  being now, on average, larger than  $\beta_a$ .

We conclude that the pattern and the bulk velocities are not required to be different. If this result is confirmed with larger samples, not available at the moment, then the simplest picture of ballistic motion of a knot will receive considerable support.

### 5.3.4 Derivation of the bulk Lorentz factor and viewing angle

Assuming the simplest picture of ballistic motion of a knot ( $\Gamma_p = \Gamma$ ), we can calculate the Lorentz factor  $\Gamma$  and the viewing angle  $\theta$  from the values of  $\delta$  and  $\beta_a$ . In fact, in eqs (5.1) and (2.36) have four unknowns, so given two of them the other two can be determined. We can re-write eq. (5.1)

$$\beta_a = \delta \Gamma \beta_b \sin \theta = \sqrt{2\delta\Gamma - \delta^2 - 1} \quad (5.4)$$

which has a maximum for  $\beta_{a,max} = \delta \beta_b \sim \delta$  for  $\sin \theta = \Gamma^{-1}$  ( $\cos \theta = \beta_b$ ) *i.e.*  $\Gamma = \delta$ . For  $\delta \ll \Gamma$ ,  $\beta_a \approx \sqrt{2\delta\Gamma} \propto \delta^{1/2}$ .

In terms of  $\Gamma$

$$\Gamma = \frac{\beta_a^2 + \delta^2 + 1}{2\delta} \quad (5.5)$$

This implies that for a given  $\beta_a$  and  $\delta$  a minimum value  $\Gamma^* = \delta = \sqrt{1 + \beta_a^2}$  is predicted. If  $\delta$  is a lower limit, as in the SSC case, then the estimated  $\Gamma$  is an upper limit (of course always bound to be  $\geq \Gamma^*$ ) if  $\delta < \sqrt{\beta_a^2 + 1}$ , while  $\Gamma$  is a lower limit in the opposite case. For  $\delta \gg \sqrt{\beta_a^2 + 1}$ ,  $\Gamma \simeq \delta/2$ , while if  $\delta \ll \sqrt{\beta_a^2 + 1}$ ,  $\Gamma \simeq \Gamma^*/(2\delta)$ .

And finally the angle to the line of sight is

$$\tan \theta = \frac{2\beta_a}{\beta_a^2 + \delta^2 - 1} \quad (5.6)$$

which shows that, unlike the estimated value of  $\Gamma$ , when  $\delta$  is a lower limit the inferred  $\theta$  is always an upper limit.

The inferred values of  $\Gamma$  and  $\theta$  are reported in Table 5.2 and shown in Fig. 5.4. The relation between  $\beta_a$  and  $\delta$  for the minimum allowed value of  $\Gamma^*$  is shown in Fig. 5.4 as a dotted line: this line corresponds to sources seen at the angle  $\sin \theta = 1/\Gamma$ , yielding the maximum  $\beta_a$ . Sources to the left and right of this line would be observed at angles respectively larger and smaller than  $1/\Gamma$ . Fig. 5.3 shows then that a possible upward revision of  $\delta$  (recall that the derived  $\delta$  is a lower limit) for a source with given  $\beta_a$  would lead to lower (higher) values of  $\Gamma$  if the source is on the left (right) of the dotted line. This information is recorded in Table 5.2 where the value of  $\delta/(\beta_a^2 + 1)^{1/2}$  is reported: if this value is less than unity, then an increase in  $\delta$  corresponds to a lower value of the derived  $\Gamma$ . Note that the very large  $\Gamma$ 's in Table 5.2 are all upper limits to the real values, since they have  $\delta/(\beta_a^2 + 1)^{1/2} \simeq 0.1$ .

For reference, the two solid curves in Fig. 5.4 show the relation between  $\beta_a$  and  $\delta$  for fixed  $\Gamma = 5$  and 30. For this reasons, it turns out that if all  $\delta$ 's increase by a factor of 2, 4, and 8,  $\langle \Gamma \rangle$  decreases by  $\sim 13\%$ , does not change, and increases by  $\sim 40\%$  respectively, while the mean viewing angle is roughly inversely proportional to  $\delta$ . Similarly, a change from  $n = 3 + \alpha$  to  $n = 2 + \alpha$  does not affect, on average,  $\Gamma$  and  $\theta$ , while if  $H_0 = 100$  the mean Lorentz factor decreases by a factor of 2 and the mean viewing angle increases by  $\sim 25\%$ . The dashed lines in Fig. 5.4 are the lines of constant viewing angle (equal to  $5^\circ$  and  $30^\circ$ ). Note that the two pairs of dashed and solid lines embrace the majority of points.

As mentioned (§2.2.3), a lower limit to  $\Gamma_{min}$  and an upper limit to  $\theta_{max}$  can be derived, if  $\delta > 1$ , even when no information is available on  $\beta_a$ . These limits on  $\Gamma_{min}$  and  $\theta_{max}$  are reported in column 5 and 7 of Table 5.2, for those sources having  $\delta > 1$ .

Fig. 5.4 shows the derived values of  $\Gamma$  versus  $\theta$ , together with two curves, the first corresponding to the critical angle  $\sin \theta = 1/\Gamma$ , the second corresponding to  $\delta = 1$ . It is noticeable that a number of sources are close to the preferred angle  $\theta \sim 1/\Gamma$  and most of them fall between the two curves as expected from selection effects: for smaller angles the enhancement factor is larger, but the smallness of the proper motion makes observations difficult, while for larger angles the flux is dimmed, and the sources become too weak to be detected with VLBI.

Fig. 5.4 indicates that CDQs and LDQs have similar values of  $\Gamma$ , but LDQs are seen at larger angles, in agreement with the proposed unification of the two classes (Orr & Browne 1982; Padovani & Urry 1992). Among quasars, HPQs have the highest values of  $\Gamma$  and smallest viewing angles.

Superluminal BL Lacs (excluding the uncertain case of 0235+ 164) have larger viewing angles and smaller median values of the Lorentz factors than quasars, while the mean values of  $\Gamma$  are only marginally different. Mkn 421, which is the only X-ray selected BL Lac with superluminal data, has a  $\Gamma$  typical of the other BL Lacs but is seen at a larger angle of  $\sim 30^\circ$ , as compared to the average for the others,  $\sim 13^\circ$ . This is in agreement with the suggestion of Maraschi *et al.* (1986) that X-ray selected BL Lacs are sources whose radio axis makes a larger angle with the line of sight than the radio selected objects (§6.1).

As regards radio galaxies, it can be seen that the four compact doubles/GPS in our sample having superluminal data are characterized by  $\Gamma \approx 1$ , in agreement with other evidence suggesting that beaming effects are not very important in these sources (*e.g.* O’Dea *et al.* 1991).

### 5.3.5 The core dominance parameter

If the extended emission of radio sources is unbeamed, while the flux of the core is enhanced by beaming, the flux ratio  $R_{CD}$  of the core to the extended component should be a beaming indicator (Scheuer & Readhead 1979): a correlation would then be expected between  $R_{CD}$  and  $\delta$ . If, furthermore, the intrinsic (as observed in the comoving frame) power of the core component is a fixed fraction  $f$  of the power of the extended one, and there is no isotropic core component, we have  $R_{CD} = f\delta^n$ .

Published values of the core dominance parameter were available for all but two sources in our sample. Fig. 5.5 plots  $R_{CD}$  vs.  $\delta$  for the whole sample. A correlation between the two variables is apparent, although with a rather wide dispersion. A formal correlation analysis, including the lower/upper limits on  $R_{CD}$ , shows that the two variables are correlated at the 99.8% level. We can exclude the possibility that this correlation is due to the fact that both variables are linearly proportional to the core flux: a multiple correlation analysis shows in fact that  $R_{CD}$  is still correlated with  $\delta$  at the 99.0% level even when the effect of the core flux is subtracted. This is an important result, which gives confidence that the core dominance parameter is indeed a beaming indicator.

Dividing the sample in sub-classes, the correlation is significant only for BL Lacs and quasars, although for the former group it cannot be excluded that the correlation is due to the common core flux dependence of the two variables.

Quasars (both CDQs and LDQs) and BL Lacs tends to occupy different regions in the  $R_{CD}$ - $\delta$  plane, with BL Lacs having, on average, a larger value of  $R_{CD}$  for the same

estimated value of  $\delta$ . This can be interpreted, coherently with the results discussed in the previous sections, as a smaller flux in the extended components of BL Lacs at a given core flux, as compared with quasars, again suggesting that the two groups have different classes of radio galaxies as parent populations.

In principle, the observed  $R_{CD} - \delta$  relationship should allow to determine (or constrain) the values of both  $n$  and  $f$ . However, this is complicated by several factors:

(i) the  $\delta$  values are all lower limits, which makes it difficult to obtain any reliable estimate of  $n$ , *i.e.* of the slope of the relationship;

(ii) the value of  $f$ , that is the intercept of the relationship, is for the same reason going to be only an upper limit to the real one;

(iii) different classes of objects could have different values of  $f$ ;

(iv) finally, the core itself could have an isotropic component, and in this case the relationship between  $R_{CD}$  and  $\delta$  is not simply  $R_{CD} = f\delta^n$ .

The parameters  $f$  and  $n$  are important also for the luminosity functions predicted in the beaming model (§6.2). The luminosity function approach allows the determination of  $f$ , while  $n$  has to be taken as a free parameter. For simplicity,  $f$  is taken to be the same for a given class of objects. Following this approach Urry & Padovani (1991) and Padovani & Urry (1992) found the values of  $f$  for BL Lacs and for CDQs and LDQs which best fit the corresponding luminosity functions, assuming FR I and FR II as parent populations (also §6.2). They found values of  $f$  equal (within a factor of 2) for BL Lacs and quasars.

Using the values of  $f$  found with the luminosity function approach, and assuming, as usual,  $R_{CD} = f\delta^n$ , we can compare  $\delta_R = (R/f)^{1/n}$  with  $\delta_{SSC}$ . It turns out that  $\langle \delta_R / \delta_{SSC} \rangle$ , taking into account the lower/upper limits on  $R_{CD}$ , is  $\sim 8$ , while the median value of the ratio is  $\sim 4$ .

This discrepancy may be due to the points (i)–(iv) mentioned above, and also to the fact the  $R_{CD}$  is derived using the core flux at arc second scale, and does not refer to the flux of the VLBI jet which we use to derive  $\delta_{SSC}$ . Therefore the corresponding  $\delta_R$  are overestimates of the beaming factor of the VLBI core. It is interesting to note that using  $n = 2 + \alpha$  to derive  $\delta_R$  and to derive the best fit to the luminosity functions, one obtains the same discrepancy between  $\delta_R$  and  $\delta_{SSC}$ . This is due to the fact that, to give a good fit to the observed luminosity functions, the best fit value of  $f$  has to change, yielding  $\langle \delta_R / \delta_{SSC} \rangle$  roughly constant.

Concerning the  $\beta_a - R_{CD}$  relationship (Fig. 5.6), in this case the correlation is not significant (89% level). This could be due to the smaller number of objects having superluminal data, but this cannot be the only explanation since for the same sample a correlation is present between  $\beta_a$  and  $\delta$ .

Note that the incompleteness of our sample does not allow to derive statistical conclusions from the distribution of  $\beta_a$  (*e.g.* Cawthorne 1990).



### 5.3.6 Comparison of the derived beaming parameters with other estimates

In this section we compare the above results with the constraints obtained from other independent beaming measures.

#### 5.3.6.a The jet to counterjet intensity ratio

If the jet does not emit an isotropic component, and assuming that the pattern and the bulk velocities are equal we have

$$J = (\beta_a^2 + \delta^2)^n \quad (5.7)$$

For  $\beta_a \sim \delta \sim 10$ ,  $J = 4 \times 10^4$  for  $n = 2$  and  $J = 8 \times 10^6$  for  $n = 3$ , well above the current dynamic ranges. We have calculated  $J$  for all the superluminal sources in our sample, finding that the only sources with  $J < 3000$  (calculated with  $n = 2.75$ ) are radio galaxies, some lobe dominated quasars and the BL Lac Mkn 421 ( $J = 1.6 \times 10^3$ ). In particular the quasar 3C 273 is predicted to have  $J = 9 \times 10^6$ . Therefore it is not surprising that even in a recent observation with the unprecedented dynamic range of  $1.6 \times 10^4$  the counterjet for this source was not detected (Davis, Unwin & Muxlow 1991).

#### 5.3.6.b Beaming and $\gamma$ -ray emission

At the time of writing, EGRET has detected 16 AGNs in the  $\gamma$ -rays (§1.1.2.c; §4.2). These sources are radio loud core-dominated objects, nearly all belong to the 2 Jy sample, and 13 of them are in our list (see also Table 1.1). If  $\gamma$ -rays are produced in a source with a large compactness, they collide with softer radiation to produce  $e^\pm$  pairs. Indeed, in the case of 3C 279, the observed  $\gamma$ -ray variability timescale allows to derive a lower limit on the beaming factor ( $\delta \gtrsim 5.5$ ) of the X- and  $\gamma$ -ray emission (§4.2). This suggests that, for all the AGNs detected by GRO, beaming of the high energy emission is important. This is confirmed by our results on the  $\delta$  derived for the radio component, which for the  $\gamma$ -ray sources present in our list averages to a value  $\langle \delta \rangle = 7$ .

#### 5.3.6.c Parent Population Statistics

As discussed in §6.1 the hypothesis that FR type I and II radio galaxies are the parent population for BL Lacs and radio quasars respectively has been tested by computing the luminosity functions predicted for the beamed objects, given the luminosity function of the parents. In this way the parameters of the beaming model can be constrained (§6.1).

For BL Lacs, Urry *et al.* (1991) found that the radio data required a distribution of Lorentz factors, with  $\langle \Gamma \rangle \approx 7$  and an average viewing angle  $\theta \approx 7^\circ$ , while for radio quasars Padovani & Urry (1992) found that again a distribution of Lorentz factors was required, with  $\langle \Gamma \rangle \approx 11$  and an average  $\theta \approx 9^\circ$  for flat-spectrum quasars (*i.e.* CDQs) and  $\theta \approx 28^\circ$  for steep-spectrum quasars (*i.e.* LDQs). As can be seen from Table 5.3, there is very good agreement between the average Lorentz factors and viewing angles derived in §5.3.4 and those inferred by the entirely independent luminosity function approach for these classes of objects.

If this unification scenario is true, then we necessarily predict that most of FR I and FR II radio galaxies should be superluminal, but with modest values of the apparent speed. In fact, in the simple ballistic model, a blob moving with a Lorentz factor of 10 appear to expand at a speed of  $\beta_a = 2.4$  and 1 for a viewing angle equal to 45 and 90 degrees respectively. For the galaxies in our sample we do not derive high values of  $\Gamma$ , however they are very atypical and the relative dominance of their core (see Table 5.3) may be due to additional processes masking the effects of relativistic beaming.

As more detailed in §1.1.2.b and §6.2, BL Lac objects show different characteristics according to the band of discovery, *i.e.* radio or X-ray (and optical). Maraschi *et al.* (1986) proposed that the different behaviour of radio selected and X-ray selected BL Lacs could be understood on the basis of a different viewing angle, with X-ray selected objects having larger angles (and smaller  $\delta$ ). This is confirmed by Padovani & Urry (1990) who found, using the statistical approach on the X-ray data, that X-ray selected BL Lacs can have viewing angles as large as  $\theta \sim 30^\circ$ . The BL Lac in our sample are obviously mainly radio selected sources, with the exception of the optically selected objects Mkn 421, Mkn 501 and Zw 186, which also belong to X-ray selected BL Lac samples (Maraschi *et al.* 1986). We confirm that these 3 sources have amongst the lowest  $\delta$ -values within the BL Lac class.

### 5.3.7 Conclusions

In §5.3 we have discussed independent derivations of the parameters characterizing relativistic effects in compact sources. The results derived in the previous sections can be summarized as follows:

1) The Doppler factors derived from the SSC limit are largest for core dominated quasars, intermediate for BL Lacs and small ( $\simeq 1$ ) for lobe dominated quasars and radio galaxies.

2) The ‘Doppler corrected’ brightness temperatures of the VLBI core are distributed within a narrow interval around a mean value as inferred from theoretical expectation.

3) For the subsample of superluminal sources the expansion velocity  $\beta_a$  correlates with the Doppler factor and the mean values of the two quantities are close, especially for CDQs.

4) For the same subsample the derived values of the bulk Lorentz factors are  $\simeq 10$  with no significant differences (within the rather large errors) between CDQs, LDQs or BL Lacs, while radio galaxies have smaller values of  $\Gamma$ . However the average viewing angles are significantly different, with radio galaxies, LDQs, BL Lacs and CDQs representing increasingly aligned objects, with average angles of 41, 25, 14 and 8 degrees, respectively.

5) The core dominance parameter  $R_{CD}$  correlates with the Doppler factor but with a rather wide scatter. BL Lacs tend to have higher  $R_{CD}$  than CDQs.

Although the model applied to derive the above results is highly idealized, the comparison of the different beaming indicators suggests that the picture is consistent and gives us confidence that the derived values are a good approximation to reality. In particular the fact that the apparent expansion velocity is on average close to the derived Doppler factors indicates that the bulk motion which causes the beaming of the radiation can also account for the superluminal expansion and different pattern and bulk velocities are not required. By assuming that these two velocity are equal, we can then derive both the bulk Lorentz factor and the viewing angle.

Furthermore the consistency of the derived Doppler factors indicates that a significant fraction of the high energy flux in these objects must be due to the SSC mechanism.

Values of  $\Gamma \simeq 10$  are sufficient to explain the non detection of a counterjet in highly aligned objects (*e.g.* 3C 273, Davis, Unwin & Muxlow 1991). In radio galaxies, LDQs and in the BL Lac object Mkn 421 a counterjet should however be detectable with a dynamic range smaller than 3000.

These values of  $\Gamma$  can also account for the enormous apparent  $\gamma$ -ray luminosities detected from many blazars and radio loud quasars without violating the transparency condition for  $\gamma$ -rays.

We note that consistent trends appear in the mean values of the beaming and Lorentz factor, the core dominance parameter, and the viewing angle.

Our results directly support the idea that lobe dominated and core dominated quasars are the same phenomenon (same  $\Gamma$ ), but seen at different viewing angles. Within the class of core dominated quasars, the different level of polarization of HPQs and LPQs could be determined by a stronger beaming of the continuum in the first ones, or by the additional presence in the latter ones of a non polarized, probably thermal, emission. Although the available statistics is insufficient to make a firm statement, the present data slightly favour the first option in that both the Lorentz factor and the core dominance parameter are higher in HPQs and the viewing angle is smaller. Any information on the degree of polarization of those quasars in our sample with no measurements would be extremely useful to clarify this point.

BL Lacs have smaller values of the Doppler factor than core dominated quasars, even if they have, on average, similar values of the Lorentz factors and higher values of the core dominance parameter. This can be explained if the isotropic components (extended radio emission, isotropic optical continuum and line emission) in BL Lacs are dimmer than in quasars, and the beamed fraction  $f$  is larger. In this case, in fact, a BL Lac object can be recognized as such at viewing angles greater and at Doppler factors smaller than those typical for a quasar to become core dominated.

In conclusion, the values of the beaming parameters,  $\delta$ ,  $\Gamma$  and  $\theta$  derived from the direct approach agree well with those derived from space density arguments, *i.e.* from the comparison of luminosity functions, thus lending strong support to the following unification scheme, summarized in Fig. 5.7, in the form of ‘Barthel’s quadrant’ (Barthel 1989).

Relativistic jets are present in radio sources with low intrinsic power (FR I) and in powerful doubles (FR II). Objects drawn from the first population are classified as BL Lacs when viewed at small angles,  $\theta \lesssim 14^\circ$ . In these objects the broad lines and the UV bump are *intrinsically weak*. X-ray selected BL Lacs are not well represented in the sample studied here, but the few ones (3) which are included are amongst the least beamed, consistent with intermediate viewing angles  $15^\circ \leq \theta \leq 40^\circ$ .

Objects drawn from the FR II population, even when seen at low inclination, are usually classified as quasars rather than BL Lacs, meaning that despite the boosted non thermal continuum, the broad lines and the UV bump remain recognizable. Objects with viewing angles less than  $\sim 10$  degrees should be core dominated quasars, while objects observed at intermediate angles ( $10^\circ \lesssim \theta \lesssim 40^\circ$ ) become lobe dominated quasars, which can also be identified with the class of steep radio spectrum quasars.

From Fig. 5.7 a correspondence appear between X-ray selected BL Lacs and lobe dominated quasars. However, FR I radio galaxies lack a strong extended component, and their core can dominate the radio emission even at intermediate angles, yielding core dominated and flat radio spectra X-ray selected BL Lacs.

In this scheme, all sources should be superluminal: even FR I and II radio galaxies should have apparent velocities slightly exceeding  $c$ , while X-ray selected BL Lacs should have approximately the same apparent velocities than lobe dominated quasars. VLBI observations to establish the value of the apparent velocity in these sources are therefore crucial.

## 5.4 MATTER CONTENT

A major uncertainty in the physics of jets is their matter content. It is generally believed that jets are charge neutral: electrons and protons (e-p) and/or positrons ( $e^\pm$ ), which neutralize them, have the same density and move with the same velocity. Numerical

simulations of large scale jets can only suggest that jets are light compared to the ambient medium (*e.g.* Bridle 1991).

‘Light’ jets (*i.e.* made mainly by an  $e^\pm$  plasma) have some advantages:

- As shown in §5.4.3 the number flux of particles in the jet is larger or at most comparable with the number flux of accreting material. If the estimated bulk Lorentz factor has to be greater than, let’s say, 5–10 each proton must have an energy of 5–10 GeV, which is at least an order of magnitude greater than the energy it can get from accretion  $\sim kT_v \sim 0.5m_p c^2$ , while for an  $e^\pm$  plasma an energy per particle of  $\sim 5$  MeV is sufficient.

There is as yet no consensus on the mechanism responsible for the bulk acceleration of the emitting plasma. One possibility is that the bulk acceleration is provided by radiation pressure. In this case the contribution of the radiation energy density from accretion can be estimated by the ratio  $(U_r/nm_p c^2) \simeq 0.1(v_{in}/v_{ff})$ , implying that the radiation energy density  $U_r$  corresponds to  $\lesssim 100$  MeV per particle (see also §5.5).

Acceleration of ‘normal’ (electron–proton) matter via electron scattering clearly requires super–Eddington luminosities (but *e.g.* Cen A presumably contains a massive black hole, but radiates far below the Eddington limit), while for a pair plasma the effective Eddington limit is about 2000 times smaller, and the jet can be accelerated also in a thin disc structure, without invoking anisotropic radiation: the acceleration (but also the Compton drag) is more effective for a ‘light’ jet with lower inertia.

- Limits on the amount of thermal particles imposed from the absence of Faraday depolarization can not be applied to pair plasma, which do not depolarize radiation (§5.4.1).
- As mentioned in §2.2.1, copious pair production should occur in compact objects. It is therefore necessary to determine if these pairs can be a large fraction of the total mass flowing in the jet.

Further evidence of the importance of pair plasma in connection with jets, is from the recently discovered two–sided radio jet associated with the source of  $e^\pm$  annihilation line, 1E1740.7–2942, close to the Galactic Centre, which extends for  $\sim 2$  pc (Mirabel *et al.* 1992). The association is based on the correlated variability between  $\gamma$ –ray and radio flux. The radio structure and spectrum closely resemble the ones of extragalactic jets. The suggested interpretation is that  $e^\pm$  pairs formed in the central region partly annihilate in the inner part of an accretion disc, producing the large line component, and partly outflow and annihilate after interacting with molecular material surrounding the region, producing the variable narrow line. However no assessment on the jet matter content is possible.

Finally in Cygnus A an excess of momentum with respect to the external ram pressure is estimated for an heavy jet.

The density could be derived assuming that the outer lobes are powered by the kinetic energy flux transported by the jet, but this assumption may be wrong, the transport possibly being in the form of a Poynting flux, the power of which is reconverted to internal energy only in the outer regions (Rees 1981) (but see §5.4.5). However a lower limit on the density can be derived by calculating the number of particles required to produce the synchrotron radiation that is observed. We derive this limit for the sample of 105 sources through the SSC model (§5.4.1). Obviously other cold and non-emitting matter can be present, apart from the relativistic radiating particles.

From the derived particle density and Doppler factor for the sample of sources, we investigate the hypothesis that the parsec-scale jets consist of an  $e^\pm$  pair plasma using various constraints, obtained by joining informations on different scales, from the ‘central engine’ to the extended radio lobes (Ghisellini *et al.* 1992a; Celotti & Fabian 1992a,b):

- (i) We assume that an  $e^\pm$  pairs jet is filled by pairs which outflow from the compact source: due to annihilation in the innermost regions, there is an *upper limit* on the number of  $e^\pm$  pairs that can reach the parsec-scale jet, as derived in §5.4.2.a, §5.4.2.b. We compare this limit with the *lower limit* on the density of particles needed to emit the synchrotron radiation we observe and we find that the constituents of parsec-scale jets may be  $e^\pm$  pairs produced in the innermost regions only if their energy distribution has a low energy cut-off at  $\sim 50$  MeV. Remarkably, the same limit on the minimum particle energy is found in the case of jets consisting of electrons and protons in order that Faraday depolarization is avoided. Taken together these two limits would suggest that the particle spectrum has a low energy cut-off below which particles are unable to cool (§5.4.1).
- (ii) We estimate the minimum particle number flux in the jet with the particle flux (of protons) expected from an Eddington-accreting source (§5.4.3).
- (iii) In the assumption that most of the energy supplied to the radio lobes is transported in the form of kinetic power, we estimate the kinetic luminosity in the pc-scale flow and require both that it is not radiatively dissipated on the pc-scale and that it is larger than the minimum kinetic power estimated for the extended jets (§5.4.4 and §5.4.5).

We find that the most plausible hypothesis, which ‘satisfies’ all these three limits, is that jets are composed of an e-p plasma and that the distribution of the emitting electrons has a minimum Lorentz factor of  $\sim 100$ .

### 5.4.1 Particle density

Let us at first compute from the SSC model the particle density.

Having derived the particle optical depth  $\tau_V$  ('V' refers to quantities evaluated in the regions observed by the VLBI) by eq. (2.44), we compute the particle density as

$$n'_{SSC} = \int_{\gamma_{min}}^{\gamma_{max}} N(\gamma) d\gamma = \frac{\tau_V}{2\alpha\sigma_T r_V \gamma_{min}^{2\alpha}} \quad (5.8)$$

where  $r_V = (\theta_d/2) d_L / (1+z)^2$  is the linear cross sectional radius of the jet, derived from the VLBI angular dimension.

A first major uncertainty in this estimate is that, due to the steepness of the electron distribution, the number density critically depends on the minimum Lorentz factor  $\gamma_{min}$ .

If the emitting particles are not allowed (more by 'depletion' than by some heating mechanisms) to completely cool down to  $\gamma_{min} \simeq 1$ , the number density required can be drastically reduced. Since  $n'_{SSC} \propto \gamma_{min}^{-2\alpha}$ , a value of  $\gamma_{min} \sim 100$  implies decrease of a factor  $10^3$  in  $n'_{SSC}$ . Note that a value of  $\sim 100$  for  $\gamma_{min}$  is consistent with the values of  $\gamma$  one derives from  $\gamma_m = [\nu_m / (\delta\nu'_B)]^{1/2}$  which averages to 200-300 for these sources. That such a value of  $\gamma_{min}$  would not greatly change the predicted self Compton X-ray flux, which (at 1 keV) is mainly produced by particles of larger energies and therefore, apart from a small logarithmic correction, the derivation of  $\tau_V$  through eq. (2.44) remains valid.

Some possible reasons for the presence of this low energy cut-off are the following.

*Incomplete cooling.*

Suppose that the emitting particles are accelerated and injected at the base of the VLBI jet, and that thereafter they stream along the jet with a bulk velocity close to  $c$ . The particles reach the component we are observing after a time  $\sim R/c$ , with a spectrum different from the initial one, due to radiative cooling. However, low energy particles cool slower, and a low energy cut-off in the initial spectrum may have not moved down in energy. With  $R$  approximately 3 pc and a value of the magnetic field of about 0.1 G, the cooling time is equal to the dynamical timescale for  $\gamma = 100$ . In this case the thin synchrotron spectrum should steepen from the inner to the outer part of the jet.

*In situ reacceleration.*

Once they reach  $\gamma_{min}$ , particles can be reaccelerated to high energies, the value of  $\gamma_{min}$  being the result of the relative efficiency of the acceleration process with respect to cooling. This accelerator must be stochastic in the sense that low energy particles are reaccelerated more than the high energy ones, because of their great number. The entire particle spectrum is in this case the result of the balance between injection and cooling, and

can remain stationary (in a frame comoving with the component), allowing high frequency synchrotron radiation to be emitted also at large distances from the base of the jet.

#### *Self absorption.*

Synchrotron self absorption inhibits the cooling of the particles below the energy  $\gamma_t$ . Below  $\gamma_t$ , particles efficiently exchange energy by the exchange of photons, and their distribution becomes thermal (Ghisellini, Guilbert & Svensson 1988). The temperature depends on the details of the particle injection mechanism and on the amount of other cooling mechanisms, besides synchrotron, such as the inverse Compton process.

In the hypothesis that the radio spectrum in compact sources is due to synchrotron emission and from linear polarization measures, it is possible to deduce upper limits on the amount of cold or thermal electrons and their maximum energy (Jones & O'Dell 1977; Wardle & Roberts 1988). In fact Faraday rotation implies depolarization by the material distributed in the source, which can be measured (for an homogeneous source) by the 'Faraday depth'  $\Delta\phi \simeq 2.2 \times 10^{41} \nu^{-2} \int (n_e / \gamma_{min}) B_{\parallel} dl$  rad where  $B_{\parallel}$  is the magnetic field component parallel to the line of sight and  $dl$  the length element along the line of sight.

Limits on the amount of Faraday rotation and depolarization imply that both the number and energy densities  $U_e$  of cold electrons must be less than the relativistic ones [ $n_e(\gamma < 100) \ll n_e(\gamma > 100)$  and  $U_e(\gamma < 100) \ll U_e(\gamma > 100)$ ].

The observation that many jets are highly polarized then gives a strong upper limit on the particle density. For example in the case of the jet of 3C120 the deduced limit on thermal electrons density is  $n_e \lesssim 10^{-3} \text{ cm}^{-3}$  (Walker, Benson & Unwin 1987), or alternatively electrons must have a minimum Lorentz factor  $\gamma_{min} \sim 100$  (Wardle 1977; Jones & O'Dell 1977).

On the contrary depolarization can be due to the external inhomogeneous 'screen' and not refer to the internal matter content. Some evidences of internal Faraday depolarization has been found by Jägers (1987).

To avoid absorption by free-free imposes upper limits on the particle density: for  $T \sim 10^4 \text{ K}$ , the source is optically thin at  $\nu = 5 \text{ GHz}$  if  $n \lesssim \times 10^4 T_4^{3/2} l_{pc}^{-1/2} \text{ cm}^{-3}$ .

#### 5.4.2 Pair plasma jets

We now consider the hypothesis that jets are light. The natural site for the production of  $e^{\pm}$  pairs is the compact X- and  $\gamma$ -ray emitting region, which presumably lies in a few Schwarzschild radii. In this region both the expected high temperature of the emitting plasma and the possible presence of non-thermal particles make pair production



an inescapable process. The  $e^\pm$  pairs, once created, and if not confined or coupled (*e.g.* by a magnetic field) with the protons of the primary plasma, can form an outflowing wind driven by radiation pressure (the limiting luminosity in this case being a factor  $m_p/m_e$  lower than the Eddington value for an electron–proton plasma).

Here following previous work by Phinney (1983), Guilbert & Stepney (1985) and Svensson (1986) we calculate the maximum number density of pairs able to escape from the inner regions of the outflow, assuming a stationary pair-dominated source. We assume that the  $e^\pm$  outflow in the innermost region occurs in an isotropic manner for a few source radii. Beyond this isotropic outflow region, we assume that *all* the surviving pairs are channelled into two oppositely-directed jets by some unspecified mechanism. This is a conservative assumption, since not all the pairs may be collimated into the jets.

#### 5.4.2.a The dynamics of $e^\pm$ pairs

It has been increasingly realized that the  $e^\pm$  pairs are important in the formation of the high energy spectrum of AGN (§2.1.2), but the aspects concerning the dynamics of an outflow of  $e^\pm$  pairs from a compact source have received comparatively less attention.

A basic result is nevertheless apparent: there is an *upper limit* to the number of pairs that can escape to the outer regions of an outflow and reach the pc-scale jet which is model independent: the faster pairs are created in the inner region, the faster they annihilate. The pair density at several times the source radius is then only a very weak function of the  $e^\pm$  density at the base of the outflow, and the upper limit on the number flux of surviving pairs is independent of the details of the pair production mechanism. This limit can be evaded if the pairs are relativistic since the annihilation cross section (similar to the Klein Nishina cross section), is a decreasing function of energy. However a large density of hot pairs undergoes catastrophic Compton cooling, immediately lowering the temperature (or the mean energy) to subrelativistic values.

Note that even if a strong acceleration mechanism were operating which prevented the  $e^\pm$  pairs from cooling (such as synchrotron reabsorption, or heating by dissipation of Alfvén waves, as proposed by Henri & Pelletier (1991), in the context of the two fluid model), the resulting Comptonization would completely reprocess the emitted spectrum, driving it to a Wien shape, contrary to observations.

In the following, we therefore assume that the outflowing pair plasma is cold (*i.e.* subrelativistic).

We assume that the  $e^\pm$  pairs are uniformly created within a spherical source of radius  $R_0$  and luminosity  $L \gg (m_e/m_p)L_E$ . We assume that the source is pair dominated, and that no pairs are created outside  $R_0$ . We neglect the creation of pairs due to collisions of the annihilation photons, both for simplicity and because the cold pairs produce  $\gamma$ -rays just above threshold for pair production, where the cross section is small. The density

of electrons and positrons at  $R_0$  is  $2n'_+(R_0)$ , corresponding to a scattering optical depth  $\tau_{0,e\pm} \equiv 2\sigma_T R_0 n'_+(R_0) \gg 1$  where  $n'_+$  is the positron density in the comoving (primed) frame.

With these assumptions, the pairs are driven by the radiation, whose energy density exceeds that of the pairs, and can be treated as a relativistic fluid. In fact using eq. (2.4a), the ratio between the energy density in cold  $e^\pm$  pairs to the radiation energy density can be expressed as  $U_{e\pm}/U_r \simeq 4\pi\tau_{0,e\pm}/\ell = 8(\pi\xi/\ell)^{1/2} < 1$ .

For radial distances  $R \lesssim \text{few} \times R_0$ , we assume that the pair wind is spherically symmetric, and that only at larger radii is the wind channeled into two oppositely-directed jets.

The pair density will not decrease simply as  $R^{-2}$ , because of the annihilation and the acceleration of the plasma. As long as the particles and photons are able to interact they can be treated as an adiabatic fluid (photons cannot escape) whose dynamics is regulated by the conservation of the energy-momentum tensor, which gives the dependence of the bulk velocity  $\beta_b c$  on  $R$ . For  $\beta_b \simeq 1$ ,  $\Gamma \simeq \Gamma_0 R/R_0$ . Here we assume that  $\Gamma_0 = (3/2)^{1/2}$ , corresponding to the relativistic sound speed. The plasma ceases to accelerate at the ‘trapping radius’  $R_{tr}$ , beyond which radiation does not interact efficiently with the particles.

Beyond the ‘annihilation radius’  $R_a$ , the  $e^\pm$  density has decreased such that annihilation is unimportant. The values of  $R_a$  and  $R_{tr}$  will be explicitly calculated in §5.4.2.b, but note that, since the cross section for annihilation of cold pairs is slightly smaller than the Thomson cross section (by a factor 3/8), we always have  $R_a < R_{tr}$ . Beyond  $R_{tr}$ , only expansion is important, and assuming a constant bulk Lorentz factor, the pair density decreases as  $R^{-2}$ .

Our task is to derive the number flux of pairs able to reach the regions of the VLBI observations. To do this, in §5.4.2.b we follow this procedure:

- (i) we calculate  $n'_+(R)$  in the ‘annihilation’ region, ( $R < R_a$ ), where expansion, annihilation and acceleration are important, and in the ‘trapping’ region ( $R_a < R < R_{tr}$ );
- (ii) knowing  $n'_+(R)$ , we can explicitly calculate the characteristic radii  $R_a$  and  $R_{tr}$  as a function of the initial radius  $R_0$  and the initial optical depth  $\tau_{0,e\pm}$ . The bulk Lorentz factor at  $R_{tr}$  is calculated as  $\Gamma_{tr} = \Gamma_0(R_{tr}/R_0)$ ;
- (iii) we calculate the number flux,  $\mathcal{F}$ , at the trapping radius:

$$\mathcal{F}_{tr} = 8\pi R_{tr}^2 c \beta_{tr} \Gamma_{tr} n'_+(R_{tr}); \quad (5.9)$$

- (iv) we assume that the number flux  $\mathcal{F}_{tr}$  is conserved up to the VLBI regions of the jet. With this hypothesis we can calculate the expected density of pairs in the region observed by the VLBI.

The main points derived in §5.4.2.b are:

(i) since the annihilation rate is proportional to the square of the pair density, we have the situation that the larger the initial density, the more efficient the annihilation process. As a consequence, the density of pairs surviving at  $R_{tr}$  and the value of  $R_{tr}$  are very weakly dependent on the pair density at the base of the outflow. Furthermore, for any reasonable value of  $\tau_{0,e\pm}$ , the annihilation and the trapping radii are of the order of  $2R_0$ . This is again due to the fact that annihilation is a very efficient process.

(ii) the number flux of surviving pairs corresponds to unit electron scattering depth at around  $2R_0$ .

#### 5.4.2.b Number density of surviving pairs

We follow here the work of Phinney (1983), Guilbert & Stepney (1985) and Svensson (1986) on the dynamics of a stationary outflow of pairs.

In the comoving frame, the annihilation rate of cold positrons,  $\dot{n}'_+$ , is given by eq. (2.3)

$$\dot{n}'_+ = \frac{3}{8} c \sigma_T n'^2_+ \quad (2.3)$$

The positron density,  $n'_+$ , assumed to be equal to the electron density, can be found from the solution to the particle conservation equation

$$\frac{d}{dR} (R^2 \beta_b c \Gamma n'_+) = -R^2 \dot{n}'_+ \quad (5.10)$$

As long as radiation efficiently interacts with pairs,  $\Gamma \propto R$ , and eq. (5.10) gives (Guilbert & Stepney 1985)

$$n'_+ = \frac{n'_+(R_0)}{x^3 + (x^3 - 1)\tau_{0,e\pm}/(16\Gamma_0)}, \quad R < R_{tr} \quad (5.11)$$

where  $x = R/R_0$ . The quantity  $\tau_{0,e\pm}/(16\Gamma_0)$  is the ratio of the annihilation to the expansion terms as measured at  $R_0$ . For  $\tau_{0,e\pm} \leq 10$ , annihilation is relatively unimportant with respect to expansion and  $n'_+(R)$  falls approximately as  $R^{-3}$ .

For  $R > R_{tr}$ , only expansion is important, and the radial dependence of  $n'_+(R)$  is

$$n'_+(R) = n'_+(R_{tr}) \left( \frac{R_{tr}}{R} \right)^2, \quad R > R_{tr} \quad (5.12)$$

When  $n'_+$  becomes sufficiently small that photons and particles cease to interact via Compton scattering, the photons are free to escape, and the outflow can no longer be considered as a single fluid. As mentioned above, this occurs at the trapping radius  $R_{tr}$

(as measured in the observer's frame) defined such that the number of scatterings *in the comoving frame* from that distance to infinity is one, *i.e.*

$$N_{scatt} \equiv \int_{R'_{tr}}^{\infty} 2 n'_+(R') \sigma_T dR' = \int_{R_{tr}}^{\infty} \frac{2 n_+(R)}{\Gamma^2} \sigma_T dR = 1 \quad (5.13)$$

The maximum radius at which annihilation is important,  $R_a$ , is defined (analogously with  $R_{tr}$ ), as the distance at which the optical depth for  $e^\pm$  annihilation (from  $R_a$  to infinity) is equal to one. Since the annihilation cross section of cold pairs is a factor  $(3/8)$  smaller than the Thomson cross section, we can simply derive  $R_a$  by setting  $N_{scatt} = 8/3$  in eq. (5.13)

$$\int_{R_a}^{\infty} \frac{2 n_+(R)}{\Gamma^2} \sigma_T dR = \frac{8}{3} \quad (5.14)$$

Note that to find  $R_a$ , one must use eq. (5.11) for  $R_a < R < R_{tr}$ . Solving eqs. (5.13) and (5.14) we obtain

$$x_{tr} \equiv \frac{R_{tr}}{R_0} = \left[ \frac{17}{1 + 16\Gamma_0/\tau_{0,e^\pm}} \right]^{1/3} \quad (5.15a)$$

and

$$x_a \equiv \frac{R_a}{R_0} = \left[ \frac{7}{1 + 16\Gamma_0/\tau_{0,e^\pm}} \right]^{1/3} = \left( \frac{7}{17} \right)^{1/3} x_{tr} \quad (5.15b)$$

We see that  $x_{tr}$  and  $x_a$  are weak functions of  $\tau_{0,e^\pm}$  [and hence of  $n'_+(R_0)$ ], as illustrated in Fig. 5.8. This is a consequence of the higher initial  $e^\pm$  pair density within sources with high  $\tau_{0,e^\pm}$  resulting in a higher rate of  $e^\pm$  annihilation at the base of the outflow (at radii just beyond  $R_0$ , see Fig. 5.9).

In Fig. 5.9 we show the number of scatterings (eq. 5.13) as a function of  $R$  for various values of  $\tau_{0,e^\pm}$  between 1 and  $10^3$ .

The density of positrons at  $R_{tr}$  can now be calculated by means of equations (5.11) and (5.15a) yielding

$$n'_+(R_{tr}) = \frac{\Gamma_0}{2\sigma_T R_0} \quad (5.16)$$

*i.e.* by setting the optical depth at the trapping radius equal to unity in the comoving frame,  $2\sigma_T R'_{tr} n'_+(R'_{tr}) = 1$ .

It should be stressed that the extremely weak dependence of  $x_{tr}$  and  $x_a$  on  $\tau_{0,e^\pm}$  implies that the density of the  $e^\pm$  pairs able to survive to the outer regions of the outflow (which we compare with the density of emitting particles within the observed radio jet as deduced from SSC theory) is almost independent of the specific  $e^\pm$  pair production model one assumes. It should also be noted that since the particle density decreases so rapidly with  $R$ , the fluid is able to convert only a small fraction of the internal energy contained

in photons into bulk motion. For  $\tau_{0,e\pm} = 10$ ,  $R_a \simeq 1.33R_0$  and  $R_{tr} \simeq 1.78R_0$ , assuming no other acceleration mechanisms are operating, the maximum bulk Lorentz factor of the wind is  $\Gamma \simeq 2.2$ .

The number flux  $\mathcal{F}_{tr}$  of surviving particles can now be evaluated using equations (5.16) and (5.15a), and setting  $\Gamma_{tr} = \Gamma_0 x_{tr}$ . Thus

$$\mathcal{F}_{tr} = \frac{4\pi c}{\sigma_T} \Gamma_0^2 R_0 x_{tr}^3 \quad (5.17)$$

The number flux  $\mathcal{F}_{\square\nabla}$  depends upon  $\tau_{0,e\pm}$  only via  $R_{tr}$ , changing by only an order of magnitude for  $1 < \tau_{0,e\pm} < 1000$ . This result is already contained (in a qualitative way) in Svensson (1986) in the form of the luminosity in rest mass of outflowing pairs.

All the formulae derived so far assumed a spherical symmetric wind. We now assume that *all* the electrons and positrons able to escape within the inner portion of the  $e^\pm$  pair wind are conserved and channeled along two jets at a radius  $R \gtrsim \text{few} \times R_0$ . We impose, conservatively, that the jet formation mechanism is maximally efficient in channeling the pairs and impose conservation of the number flux (eq. 5.17), but allow for a further bulk acceleration of the plasma (perhaps associated with the collimation mechanism), as indicated by the required beaming of the radiation we observe and by the apparent velocities of superluminal sources (§5.1).

We call  $n'_{e\pm} = 2n'_+(r_V)$  the pair density at  $r_V$ . With this notation the particle number flux at  $r_V$  is

$$\mathcal{F}_V = \pi r_V^2 c \beta_V \Gamma_V n'_{e\pm} \quad (5.18)$$

By setting  $\mathcal{F}_{tr} = \mathcal{F}_V$  we derive the pair density  $n'_{e\pm}$  expected in the radio emitting component

$$n'_{pair} = \frac{2\Gamma_0}{\sigma_T R_0} \frac{\beta_{tr} \Gamma_{tr}}{\beta_V \Gamma_V} \left[ \frac{17}{1 + 16\Gamma_0/\tau_{0,e\pm}} \right]^{2/3} \left( \frac{R_0}{r_V} \right)^2 \quad (5.19)$$

#### 5.4.2.c $n'_{SSC}$ vs $n'_{e\pm}$

The density  $n'_{SSC}$  has to be compared with the expected pair density,  $n'_{e\pm}$  (eq. 5.19). We require that the pairs coming from the innermost regions have been accelerated, because, as mentioned before, they are cold on escaping the nucleus. In addition to this acceleration of individual particles, bulk acceleration of the plasma has also occurred to account for the inferred high Lorentz factor, in excess of  $\Gamma_{tr}$ . Therefore we set, for the VLBI component,  $\Gamma_V = \delta$  for those sources with  $\delta > 1$ , and  $\Gamma_V = \Gamma_{tr}$  for the remaining sources.

We take the derived upper limits on  $\tau_V$  as true values, and discuss the possibility of smaller values.

In Figs. 5.10 we plot the values of  $n'_{e\pm}$  versus  $n'_{SSC}$  assuming  $\alpha = 0.75$ ,  $\tau_{0,e\pm} = 10$ ,  $\gamma_{min} = 1$ , and  $R_0 = 10^{14}$  cm for the sources not known to be superluminal (Fig. 5.10a), and those known to be superluminal (Fig. 5.10b). For the latter sources it seems more reasonable to assume that the plasma in the jet is flowing with a velocity close to  $c$ . Different symbols distinguish resolved (filled points) and unresolved (open points) sources. It is interesting to note that there seems to be no difference between BL Lac objects, CDQs, LDQs and radio galaxies. As can be seen from the Figures there also seems to be no obvious difference between the resolved and unresolved sources, or between sources known to be superluminal and the remaining ones.

The main result from Figs. 5.10 is that all objects lie in the region of the plane such that  $n'_{SSC} > n'_{e\pm}$ , typically by two orders of magnitude in  $n'_{SSC}$  or in  $n'_{e\pm}$ . This can be seen more clearly in Fig. 5.11, which is the histogram of the ratio  $n'_{SSC}/n'_{e\pm}$ . Even though the density of the outflowing  $e^\pm$  pairs is only weakly dependent on the initial density, we recall (§2.1.2) that the values of  $\tau_{0,e\pm}$  predicted by pair production models for a stationary source is  $\tau_{0,e\pm} \sim 20 (L/L_E)(3R_s/R_0)^{1/2}$ , justifying the reference value  $\tau_{0,e\pm} = 10$ .

#### 5.4.2.c The effect of the assumptions

In order to check that our result is not an artifact of the assumed parameters, we have investigated its dependence on each of the following parameters:

(i)  $R_0$ : for a fixed  $\tau_{0,e\pm}$ , it is clear from eq. (5.19) that  $n'_{e\pm}$  depends linearly on  $R_0$ . To have  $n'_{e\pm}$  consistent with  $n'_{SSC}$  for all sources a size  $R_0 \sim 10^{17}$  cm is then required. Such a source size is completely ruled out by the short variability time-scales observed for the X-ray flux. In addition, if one applies a simple steady pair model, requiring  $\tau_{0,e\pm} = 10$  and  $R_0 = 10^{17}$  cm implies an X-ray luminosity in excess of  $3 \times 10^{48}$  erg s $^{-1}$  [eq. (2.4.b)].

(ii)  $\tau_{0,e\pm}$ : for fixed  $R_0$ ,  $n'_{e\pm}$  depends on  $\tau_{0,e\pm}$  (eq. 5.19) only through  $R_{tr}$ , but as discussed,  $R_{tr}$  varies only by a factor of  $\simeq 2.5$  for  $1 < \tau_{0,e\pm} < 1000$ . Thus an increase of only a factor of six in  $n'_{e\pm}$  is expected even for extreme values of  $\tau_{0,e\pm}$ .

(iii)  $\alpha$ : the derived SSC particle density is dependent upon the assumed value of the spectral index  $\alpha$ . For flatter spectral indices, less (low energy) electrons are required in order to emit the observed spectrum, and hence  $n'_{SSC}$  is decreased. However, for  $\alpha = 0.5$ , only 22 sources have  $n'_{SSC}/n'_{e\pm} < 1$ . Note that, if  $\alpha$  is estimated from the IR spectral index, Ghisellini *et al.* (1986) report an average value  $\alpha_{IR} = 0.94$  for a sample of blazars, and  $\alpha_{IR} = 1.25$  for a subsample of sources with strong emission lines.

(iv)  $F_x$ ,  $F_V$ : as discussed,  $n'_{SSC}$  is proportional to the used X-ray or optical flux [eq. (2.44)]. The derived density  $n'_{SSC}$  become consistent with  $n'_{e\pm}$  for the sources with the largest ratio  $n'_{SSC}/n'_{e\pm}$  if their VLBI component contributes only a factor  $10^{-3}$ – $10^{-4}$  of the total observed X-ray or optical fluxes. We think this is unlikely because:

a) We can calculate the beaming factor needed to lower the predicted X-ray or optical flux to the level required to have  $n'_{SSC}/n'_{e\pm} = 1$ . Taking into account that  $n'_{e\pm} \propto 1/\Gamma_V \sim 1/\delta$  (see eq. 5.19), we find that for some sources  $\delta > 30-50$  is needed (examples are 1749+096, 0106+013, 0711+356, 0804+499, 0906+430). This exacerbates the acceleration problem. In addition, such high values of  $\delta$  would contrast with the apparent velocities  $\beta_a c$  measured in superluminal sources.

b) Detailed observation of the (arcsecond scale) jet in M87 (Biretta, Stern & Harris 1991) from the radio through X-rays band have revealed that the knots in the jet have an overall spectrum similar to the one of the core, and are only a factor of a few dimmer.

(v) As already discussed  $\gamma_{min}$  is the most critical parameter. If the emitting particles are not allowed (by some heating mechanisms) to completely cool down to  $\gamma_{min} \simeq 1$ , the number density of required particles can be drastically reduced and a value of  $\gamma_{min} \sim 100$  could make  $n'_{SSC}$  small enough to be consistent with  $n'_{e\pm}$  for all sources.

Some escapes to the above conclusion are possible:

- (i) Pairs do not annihilate and therefore survive, because their initial velocity is only in the radial direction, without random component (Rees 1981). The pairs can then be re-heated on VLBI radio scale. However a high initial densities, *i.e.* optical depth, in the compact source in order to account for the simple volume expansion is required;
- (ii) We have neglected the possibility that pairs are created outside the central source. The interaction of ultrarelativistic protons with the ambient medium can lead to the formation of  $e^\pm$  pairs. This mechanism has been recently proposed by Giovanoni & Kazanas (1990) to explain the flatness of the radio spectrum of compact radio sources. We note that it requires a density of cold, target protons which is in excess of the limits derived by the polarization arguments (and therefore cannot be applied to sources having a polarized jet).
- (iii) Otherwise  $\gamma$ -rays can transport energy outside the central source (even if it is magnetized) and convert it into pairs locally, when interact with lower energy ambient photons (Rees 1981).

#### 5.4.2.d Results

In §5.4.2 we found that the density of  $e^\pm$  pairs able to reach the VLBI emission region is consistent with the densities deduced from SSC theory only for extreme choices of the parameters, and only if the  $e^\pm$  pairs are not allowed to cool down to Lorentz factors  $\gamma_{min} < 100$ .

This result is strengthened by our assumption that all the  $e^\pm$  pairs escaping from the central source emit the observed SSC radiation. A significant fraction of the escaping pairs may not reach the radio emission region, either as a result of isotropic escape (rather than being channeled into the jets), or as a result of interaction with the ambient medium.

Our result does not depend on the details of the pair production models for the compact source, even if we indeed assume that the  $e^\pm$  pairs are produced in a compact region, and therefore that they undergo annihilation while escaping. In the framework of the best-studied pair production models, the density of the  $e^\pm$  pairs we have assumed at the base of the outflow corresponds to extreme values of the compactness of the source. Therefore, if the X-ray source is less compact than we have implicitly assumed, our result is strengthened.

Combining our findings with the limits for the presence of thermal ‘normal’ matter from Faraday depolarization, we can reach a firm conclusion. In fact our results indicate that a jet can be supplied by pairs from the central source only if all pairs have energies greater than 50 MeV at the VLBI scale, and do not cool below  $\gamma_{min} \sim 100$ . Remarkably, this value of  $\gamma_{min}$  is very similar to the one derived for an electron–proton plasma, from the depolarization argument (§5.4.1).

### 5.4.3 Particle number flux

A further constraint on the matter content can be derived by comparing the number flux of particles flowing in the jet, with the number flux expected if the jet is fueled by material accreting onto the black hole.

An average value of the particle flux for our sample can be obtained using the average source size and particle density, given by  $\langle \log r_V \rangle = 18.56 \pm 0.44$  and  $\langle \log n'_{SSC} \rangle = 3.14 \pm 0.86$ , respectively (only sources with  $\delta > 1$  have been considered). The particle flux results  $\mathcal{F}_V = \pi r_V^2 \Gamma \beta_b c n'_{SSC} \simeq 1.7 \times 10^{51} \Gamma \beta_b \text{ s}^{-1}$ . (Here  $\Gamma$  and  $\beta_b$  refer always to the VLBI region).

If the matter associated with a stationary outflow in steady state is transported to the collimation region and fueled into the jet through the accretion flow then we can compare  $\mathcal{F}_V$  with the flux of baryons corresponding to the Eddington rate,  $L_E = \eta \dot{M}_E c^2$ , given by  $\mathcal{F}_E \sim 9 \times 10^{49} / \eta_{-1} M_8 \text{ s}^{-1}$ .

Obviously for an  $e^\pm$  jet this limit would not apply because copious particles production in the compact region can occur. If instead the jet is heavy this would imply that a super-Eddington accretion flow  $\gtrsim 10 \dot{M}_E$  is required, most of which should ‘evaporate’ and collimated into the jet. This does not simply agree with the predictions of magnetically driven wind models (§5.5), which require that only a fraction of the accreting flow can be ‘launched’ along the field lines to supply the jet (Blandford & Payne 1972).

A contribution to  $\mathcal{F}$  other than accretion could be due to entrainment of matter along the flow. This would imply a fast deceleration of the jet and indeed this effect has been claimed to allow a deceleration of the jet (which on larger scale is thought to be at most mildly relativistic) without loss of momentum. In the process however (also



for small fraction of mixing) the jet dramatically slows, becomes subsonic and decreases its collimation (Icke 1991). Moreover our particle flux estimates would imply that, for an Eddington source, copious entrainment (more than a factor of 10) occurs at most on pc scales where the jet velocity *is* extremely relativistic, requiring an even more efficient acceleration mechanism.

Therefore a more plausible explanation to reconcile the values of the two particle fluxes is that the density of protons,  $n'_{SSC}$ , is overestimated because  $\gamma_{min} \gg 1$ .

#### 5.4.4 Kinetic and radiative powers in parsec-scale jets

Another interesting piece of information comes from the estimate of the kinetic energy flux of the bulk flow,  $L_{kin}$ . In particular a *minimum ratio* of the kinetic over the *comoving* radiative powers for the sample of sources can be calculated.

We find that the amount of radiative dissipation in pc-scale jets is a negligible fraction of the kinetic power, as expected *if* the bulk luminosity has to supply the energy to the large-scale structures. On the contrary this assumption sets a lower limit on the amount of kinetic luminosity  $L_{kin}$  and in turn imposes other constraints on the matter content and particle density, on which the estimate of  $L_{kin}$  depends.

##### 5.4.4.a Kinetic luminosity

The kinetic luminosity is given by

$$L_{kin} = \pi r_V^2 n'_{SSC} m_e c^3 \Gamma^2 \beta_b \quad \text{erg s}^{-1} \quad (5.20)$$

For sources with  $\delta > 1$  we minimize  $L_{kin}$  assuming that the jets are observed at zero angle with the velocity direction, *i.e.*  $\Gamma = \delta/2$  (§2.3.6.b). If  $\delta < 1$  we use  $\Gamma^2 \beta_b = 1$  as a reference value. In the Figures the sources with  $\delta < 1$  are distinguished from the others.

The major uncertainties in the estimate of the kinetic power are:

- (i) If the jet is heavy (and charge neutral)  $L_{kin}$  from eq. (5.20) is underestimated by a factor  $\sim m_p/m_e$ . We also neglect the contribution of thermal, non-emitting matter on the basis of the limits from Faraday depolarization.
- (ii) Associated with the mass flux, there is an energy flux, which, for a relativistic fluid is given by the space-time components of the energy-momentum tensor, *i.e.*  $L_{tot} = \pi r_V^2 4p \Gamma^2 \beta_b c$ . For a fluid of relativistic electrons this would imply a multiplicative factor in eq. (5.20)  $\simeq 4(\langle \gamma - 1 \rangle)/3 \sim \gamma_{min}$ , for  $\gamma_{min} \gg 1$ .

In the case of an  $e^\pm$  pair plasma, particles most probably dissipate all their internal energy locally, adiabatically cool, loss energy radiatively (by synchrotron or Compton scattering) or annihilate (§5.4.2) on timescales shorter than the flow dynamical timescale.

Therefore the energy must be transported in the form of bulk kinetic energy or Poynting flux (*e.g.* Rees 1984). (The results of §5.4.2 are consistent with the fact that an  $e^\pm$  flow does not carries internal energy: in that section we estimate the number density of surviving particles independently of the form of the energy transport).

However, even if the particles could avoid cooling, for  $\gamma_{min} \gg 1$  their number density decreases  $\propto \gamma_{min}^{-2\alpha}$ . Therefore the total effect of increasing the internal energy but decreasing the density leads to a decrease in the bulk luminosity of a factor  $\sim 3$  (for  $\gamma_{min} \simeq 100$ ). Note that the electron internal energy contribution is negligible if protons are present.

(iii) Given the Doppler factor, the bulk Lorentz factor depends on the angle of view. We minimize it assuming that  $\Gamma = \delta/2$ . If information on the apparent superluminal speed are taken into account, the average Lorentz factor is expected to be at most a factor  $\lesssim 4$  greater than the average  $\delta$  for BL Lacs and CDQs (Table 5.3b). An independent constraint on the bulk Lorentz factor (§5.4.5) is that presumably Compton drag effect limits the amount of bulk kinetic luminosity if a radiation field is present (Phinney 1987).

#### 5.4.4.b Kinetic vs radiative luminosity

We can now calculate the ratio  $L_{kin}/L_{rad}$  of the kinetic luminosity to the *comoving* radiative luminosity. The latter is estimated as the maximum among the X-ray, optical and radio luminosities, computed from the observed fluxes, at the rest frame frequencies of 2 keV, 5500 Å and 5 GHz, respectively. The Doppler correction on the monochromatic luminosity is assumed to be  $L = \delta^{3+\alpha} L_{rad}$ . We verified that the assumption on  $n$  does not affect significantly the results. For sources with  $\delta < 1$  we do not apply the Doppler correction, and use the observed luminosity.

The ratio  $L_{kin}/L_{rad} \propto F_x^{-(1-\alpha)/(2+\alpha)} \theta_d^{-(16+11\alpha)/(2+\alpha)} / F$  where  $F$  refers to the radio, optical or X-ray flux. This implies that for  $\alpha < 1$  (and  $n = 3+\alpha$ ) our results are strengthened if the measured angular dimension  $\theta_d$  or SSC X-ray flux are overestimated.

If  $n = 2 + \alpha$ ,  $L_{kin}/L_{rad}$  increases with decreasing the size of the emitting region, but decreases with decreasing the SSC flux. However in order to decrease the ratio of a factor 1000, the X-ray flux should be 18 orders of magnitude smaller (for  $\alpha = 1$ ).

In Fig. 5.12a we show the histogram of the derived ratio  $L_{kin}/L_{rad}$ . The solid line is the sum of all sources with  $\delta > 1$ , while the dashed line refers to sources with  $\delta < 1$ . The distribution (for the sources with  $\delta > 1$ ) is centered around  $\log(L_{kin}/L_{rad}) = 4.4 \pm 2.5$ . This would indicate that radiative dissipation is not efficient. The values reported are for  $L_{kin}$  as given in eq. (5.20). The uncertain assumptions about the estimate of  $L_{kin}$  mentioned above (*i-iii*) would further increase the effective kinetic power.

In Fig. 5.12b we show the same histogram only for BL Lac (continuous line) and core-dominated sources (dashed line). It appears that there is no statistical difference

between the two populations, which, in the unified scheme (§6.1) are thought to be associated with FR I and FR II radio galaxies, respectively. The morphology and radio power in these two classes of radio sources do not seem correlated with the degree of radiative dissipation on small scale. Such conclusions can be however strongly biased, due to the incompleteness of the sample.

With respect to the interesting association of copious  $\gamma$ -ray emission with the blazars activity (§1.1.2.c) it should be mentioned that the estimated kinetic luminosity can be comparable with  $L_\gamma$  for all the sources only if the high energy emission is less beamed than the radio.

No correlation between the pc-scale kinetic power and  $R_{CD}$ , which could indicate a relation in the amount of dissipation on small and large scale, has been found.

The results suggest that for most sources the major part of the total power is in the form of bulk luminosity of a jet/outflow. A quite interesting ‘coincidence’ is the fact that the *beamed* luminosity is instead roughly comparable both to the kinetic power and to the typical power of the ‘blue bump’ emission in highly luminous sources.

Furthermore it appears that the kinetic power is not dissipated through radiation on small scales. Dynamical models show that jets rapidly decelerate if significant radiative dissipation occurs.

The last argument can be reversed. In fact, if we assume that jets carry power to large scales, they cannot radiatively dissipate their kinetic energy. This constraints  $L_{kin}/L_{rad}$  to be greater than, say,  $\sim 1-10$ .

From the previous discussion it appears that the only way to decrease  $L_{kin}$  is to assume that  $\gamma_{min} \gg 1$ . Therefore if  $\gamma_{min} \sim 100$ , as suggested from other arguments, the only alternative which would maintain  $L_{kin} > L_{rad}$  is to assume that the jet contains protons. In fact an increase in  $L_{kin}$  due to the electron internal energy or the bulk Lorentz factor does not account for the required factor ( $\sim 1000$ ).

Consequently, adopting an ‘economic’ point of view, the above argument would suggest that jets can be made either of  $e^\pm$  pairs (with  $\gamma_{min} \sim 1$ ) or of electrons and protons with  $\gamma_{min} \sim 10^2$ .

#### 5.4.5 Kinetic power on pc and Mpc scales

The fact that VLBI jets appear often well aligned and with the same sidedness of the large scale ones, strongly suggests that the same collimated structure is observed on very different scales. Several methods have been adopted to estimate the kinetic power of

the flow, the internal pressure and the magnetic field intensity of jets which extend over kpc-Mpc scales (*e.g.* Begelman, Blandford & Rees 1984; Leahy 1991; Saunders 1991).

As already mentioned, it is not possible to determine the conditions in the inner part of the jet from the estimates on large scale, assuming particle and energy conservation, because entrainment of ambient material, turbulence, transport of energy in the form of Poynting flux and other processes may all occur. However the detailed VLBI maps allow an independent estimates on the pc-scale jets, and therefore we can compare the kinetic powers of pc-scale and kpc-, or larger, scale jets.

Recently Rawling & Saunders (1991) reported an interesting correlation between the luminosity in narrow emission lines and the kinetic power of extended radio jets of a sample of FR I, FR II radio galaxies and quasars.

We have found in the literature the narrow line flux for 18 sources of our sample and for them we compute the pc-scale kinetic luminosity. We follow the Rawlings & Saunders' prescription for the estimate of the narrow line luminosity, *i.e.*  $L_{NLR} = 3 \times (3 \times L_{[OII]3727} + 1.5 \times L_{[OIII]5007})$ . If the  $[OII]3727$  luminosity is not available we adopt  $L_{[OII]3727} = L_{[OIII]5007}/4$  or estimate the  $[OII]3727$  luminosity from the relation derived by Saunders *et al.* (1989), for sources with  $z > 0.5$  and  $z < 0.5$ , respectively.

Data on the narrow emission-line luminosities (for 0430+052, 0906+430, 0923+392, 1101+384, 1222+216, 1226+023, 1253-055, 1510-029, 1548+114, 1618+177, 1641+398, 1721+343, 1845+797, 1921-293, 1928+738, 2234+282, 2254+158, 2345-167) are taken from Steiner (1981), Yee (1980), Rudy (1984), Stockton & MacKenty (1987), Jackson & Browne (1991). In order to compare with the results of Rawling & Saunders (1991) we use their same values of  $H_0 = 100 \text{ km s}^{-1} \text{ Mpc}^{-1}$  and  $q_0 = 0$ .

The results are shown in Fig. 5.13, which is a reproduction of Rawlings and Saunders' diagram representing the kinetic power vs the line luminosity, with our data superposed (big) stars and open circles. The open circles represents objects with  $\delta < 1$ . The kinetic power for our sample refers to the pc-scale radio jets.

A linear fit to distribution of the 18 objects of the pc-scale sample gives  $\log L_{kin} = (0.71 \pm 0.29) \log L_{NLR} + (14.55 \pm 13.04)$  with a probability that it derives from a random distribution  $p = 0.03$ . No significant trend has been found for objects belonging to different classes (probably due to the poor statistic). The 4 sources with  $\delta < 1$  tend to be in the lower part of the distribution. We checked that the results are not significantly affected by the assumptions on the spectral index and Doppler amplification exponent  $n$ .

The large and small scale kinetic powers, estimated in a completely independent way, appear to satisfy the same correlation and are remarkably in agreement, despite the uncertainties related to eq. (5.20) already mentioned. Note that, as discussed by Saunders (1991) also the power they estimate is a lower limit.

The comparison of the pc-scale with the large scale parameters could constrain the amount of energy dissipation. On the other hand *if* the bulk of the energy is transported to the radio lobes in the form of kinetic luminosity, and the process is stationary over timescale of  $\sim 10^3 - 10^6$  ys, then the power on small scale should be comparable or exceed the large scale one.

The power can be also extracted from the black hole spin energy and transported in the outer lobes in the form of Poynting flux. The luminosity which can be extracted in this process is approximately given by  $L_{em} \sim 10^{45} (a/R_s)^2 B_4^2 M_8^2 \text{ erg s}^{-1}$ , where  $a$  is the specific angular momentum. For typical magnetic field  $L_{em}$  can be comparable and in some cases smaller than the kinetic power on extended scale. This suggests that the contribution to the extended luminosity in the form of kinetic power can be significant.

If so, the constraints on the matter content and particles density discussed in the previous sections, can be applied again, with the same conclusions. Moreover on the larger scales we can further constraint on large scales the possibility that part of the energy is transported as internal energy in an  $e^\pm$  jet (point *iii* of §5.4.4.b). In fact the synchrotron cooling timescale for an electron with  $\gamma \sim 100$  in a typical magnetic field of  $10^{-2} B_2$  G (§5.5.1) is  $\sim 7 \times 10^{10} \gamma_2^{-1} B_2^{-2}$  s, implying that (if synchrotron reabsorption is not effective) in order to transport this internal energy to 10-100 kpc,  $\gamma_{min} < \text{few}$ . Even more dramatic are adiabatic losses, which cause  $\gamma \propto R^{-1}$  (depending on the geometry of the expansion). These losses in fact limit the possibility of an efficient increase of bulk kinetic energy through adiabatic acceleration.

The large and small scale kinetic powers estimated are surprisingly in agreement, despite the possible large differences in bulk velocity and age. This would suggest that all the energy required to supply radio-lobes can be supplied as bulk luminosity and the transport of energy from pc-scale is extremely efficient. As noted by Rawlings & Saunders (1991), the correlation with narrow-line luminosity means (if the narrow lines are powered by the central engine radiation and not by the jet) that  $L_{kin}$  is remarkably proportional to the ionizing luminosity of the central engine.

#### 5.4.6 Conclusion

We used joint constraints from different regions of the source, ranging from the supposedly central accreting object to the extended radio lobes, in order to determine the most plausible matter content of jets (Fig. 5.14).

If the bulk of the energy is in fact in the form of ordered motion, an  $e^\pm$  pair plasma cannot carry enough kinetic power to emit the pc-scale radiation and supply the radio lobes, unless the particle distribution extends to  $\gamma_{min} \sim 1$ . In this case however the pairs



cannot avoid annihilation in a central compact region and escape along the jet. On the other hand if the jet plasma is composed of electron and protons, the particle number flux cannot easily be provided through (Eddington) accretion.

None of the above estimates is definitive by itself, because of the possible uncertainties. However taken together a consistent solution, which simply satisfies all the requirements is that the emitting particles cannot cool below  $\gamma_{min}$  typically of 100 (as suggested by other argument) reducing the number estimated from SSC theory, but that the jet dynamic is dominated by an electron-proton fluid. In this case the estimate of  $L_{kin}$  from eq. (5.20) is correct in a factor  $\lesssim 2$ .

Obviously our results do not exclude the possibility that jets are composed by two fluids (Henri & Pelletier 1991), or that  $e^\pm$  pairs can dominate only in the very inner relativistic region of the flow (Blandford 1992).

## 5.5 CONFINEMENT AND ACCELERATION

The physics of the formation, collimation and acceleration of jets is highly uncertain (*e.g.* Begelman, Blandford & Rees 1984; Wiita 1991; Blandford 1992). Collimated structures and outflows are observed in Young Stellar Objects (suggesting that the jet phenomenon does not require a relativistic potential), even if the surprising similarity with extragalactic jets is probably only morphological, being different the relevant physical quantities and radiative processes (Blandford 1992; Phinney 1992). The two well collimated jets on Galactic scale, SS433 and the recently discovered jet associated with 1E1740.7-2942 (§5.4.2), suggest a more deep relationship with the extragalactic structures.

Jets appear to be collimated on scales smaller than the pc and, assuming that the observed jets trace the matter flow, on large scale they seem to be confined, as indicated by both the small aperture angles (sometimes  $<$  few degrees) and the excess of thrust implied by the assumption of a free expanding jet (Bridle 1991; Begelman 1992).

Hydrodynamical fluid models, which assume gas confinement with the formation of nozzles (*e.g.* ‘twin jet model’ Blandford & Rees 1974, Reynolds 1982), suffer from a major problem, especially on the small scales: the required high density external gas should be at unusual high temperatures in order not to emit as free-free radiation an X-ray flux exceeding the observed one. On large scales there are few examples of jets overpressured with respect to the ambient gas pressure, according to estimates from X-ray emission measurements (*e.g.* M87, by a factor 5-10, Cyg A, Potash & Wardle 1980; Perley *et al.* 1984; Arnaud *et al.* 1987).

Probably the most plausible confining mechanism is given by an intense magnetic field with a toroidal component (which has to increase toward the jet axis). However the

polarization due to the presence of a toroidal field is not observed (Blandford 1990, but see Laing 1992).

A magnetic field can also accelerate the plasma. In the best studied model the field is anchored on an accretion disc (suggestive of the symmetry axis) and wound by its differential rotation. Part of the accreting plasma is centrifugally accelerated and ‘launched’ along the field lines if enough inclined with respect to the axis of symmetry (Blandford & Payne 1982) (Fig. 5.15). This model however predicts that the outflow kinetic luminosity can be at most comparable with the radiative luminosity associated with the accretion disc (Königl & Ruden 1992).

Radiative acceleration through Compton scattering, maybe in a thick disc structure, requires super-Eddington luminosities (see §5.4), and suffers of the major problem of Compton drag (Phinney 1987) which limit the maximum speed obtainable: for an  $e^\pm$  flow the final Lorentz factor  $\Gamma \sim \ell^{1/7}$ . The more efficient mechanism of synchrotron absorption requires both the presence of a magnetic field and a significant fraction of the luminosity emitted at low (radio-infrared) frequencies (Ghisellini *et al.* 1990). Other opacities, like free-free absorption could be relevant to accelerate (or decelerate) high density and cold material. Indeed we are studying its effect on the kinematic of the jet in SS433 (where the presence of cold material has been inferred) (Celotti, in preparation).

### 5.5.1 Magnetic field estimates

Estimates on the intensity of the magnetic field can be obtained by the SSC model (eq. 2.43). In the last column of Table 5.2 we report the values derived. The average values for the subsample of sources with  $\delta > 1$  results  $\langle \log B \rangle = -2.19 \pm 0.73$ .

For a randomly oriented magnetic field this value corresponds to a magnetic pressure  $p_B \simeq 10^{-6}$  erg cm $^{-3}$ . On the other hand the internal pressure of the emitting electrons (assuming a relativistic fluid) is  $U_e \simeq 3 \times 10^{-4}$  erg cm $^{-3} \sim 10^2 p_B$ . Furthermore  $B$  refers to the synchrotron emitting region, where presumably the magnetic field (and the particle density) are enhanced with respect to the average flow. That would imply that the field cannot be dynamically important to accelerate and confine the jet on pc-scale.

However the result strictly concerns a region which is possibly orders of magnitude bigger than the initial collimation region. The derived values obviously depend on the strong assumption that the magnetic field is tangled, not accounting for possible large scale ordered field components.

More generally all the results presented in the Chapter are based on the applicability of the standard SSC model. For example the hypothesis of isotropy for both the emitting



particle distribution and the magnetic field, could be too simplified. Observations of filamentary structures, inhomogeneities and peaks in the emitting regions (similar to those observed on large scale), would make this assumption rather critical.

Table 5.1a: BL Lacs

Source	Name	$z$	$\theta_d$	$\nu_m$	$F_m$	Ref.	$F_X$	Ref.	$F_V$	Ref.	$\beta_a$	Ref.	$\text{Log} R_{CD}$	Ref.	Notes
			m.a.s.	GHz	Jy		$\mu\text{Jy}$		mJy						
0048-097	PKS	$>0.2^1$	0.34	2.3	0.62	L89	0.066	M87	0.88	M86	...	1.3	AU	1 Jy, HP (KS)	
0219+428	3C 66A	0.444	1.50	5.0	0.20	M87	0.16	M87	3.6	G86	...	0.3	AU	BH & VV, HP (AS)	
0235+164*	AO	0.940	0.50	5.0	1.75	M87	0.17	M87	6.6	G86	91 <sup>2</sup>	M90	AU	1 Jy, HP (KS)	
0300+471	4C 47.08	...	0.11	22.3	1.1	L	0.17	G90	0.38	LO	...	1.9	AU	BH & VV, HP (AS)	
0306+102	PKS	...	0.50	5.0	0.73	M87	0.11	M87	0.1	LO	...	...		BH & VV, no polarization data	
0454+844	S5	$>0.3^3$	0.55	5.0	1.30	M87	0.05	M87	0.24	M86	$>3.2$	S92	M90	1 Jy, HP (KS)	
0537-441*	PKS	0.896	1.1	2.3	4.2	P89	0.2	WW	2.46	HB	...	2.3	BMU	1 Jy, HP (IT)	
0716+714*	S5	$>0.3^3$	0.35	5.0	0.50	M87	0.22	M87	20.5	S91	4.6	S92	BP	1 Jy, HP (KS)	
0735+178	PKS	$>0.424$	$<0.30$	5.0	1.29	M87	0.32	M87	6.9	G86	$>14.4$	M90	AU	1 Jy, HP (KS)	
0754+100	OJ 090.4	...	0.60	5.0	0.53	M87	0.17	M87	4.0	G86	...	1.5	AU	BH & VV, HP (AS)	
0818-128	OJ-131	...	0.80	5.0	0.47	M87	0.07	M87	1.52	M86	...	0.6	AU	BH & VV, HP (AS)	
0823+033	OJ 038	0.506	$<0.10$	15.0	0.66	L90	...	...	0.25	S91	...	$>0.8$	U81	1 Jy, HP (KS)	
0829+046	OJ 049	0.18	0.90	5.0	0.26	M87	0.19	M87	1.4	G86	...	1.4	AU	BH & VV, HP (AS)	
0851+202	OJ 287	0.306	0.30	5.0	2.30	M87	1.7	M87	4.0	G86	6.4	M90	AU	1 Jy, HP (KS)	
0954+658	S4	0.368	0.19	5.0	0.48	G	0.5	D	0.82	PR	...	1.1	BP	1 Jy, HP (KS)	
1101+384*	Mkn 421	0.031	$<0.30$	5.0	0.24	M87	14.0	M87	17.8	G86	3.8	ZB	AU	BH & VV, HP (AS)	
1147+245	OM 280	$>0.2^1$	0.90	5.0	0.39	M87	0.08	M87	0.96	M86	...	1.8	AU	1 Jy, HP (KS)	
1215+303	ON 325	...	0.70	5.0	0.33	M87	0.85	M87	3.4	G86	...	0.7	AU	BH & VV, HP (AS)	
1219+285	ON 231	0.102	0.50	5.0	0.13	M87	0.42	M87	2.9	G86	...	$>3.5$	AU	BH & VV, HP (AS)	
1308+326	B2	0.996	0.50	5.0	1.97	M87	0.3	M87	1.7	G86	...	1.7	AU	1 Jy, HP (KS)	
1400+162	4C 16.39	0.244	1.40	5.0	0.08	M87	0.1	M87	0.51	M86	...	0.1	AU	BH & VV, HP (AS)	
1519-273	PKS	$>0.2^1$	0.36	2.3	1.59	L89	...	...	0.16	S91	...	$>0.9$	U81	1 Jy, HP (IT)	
1538+149	4C 14.60	0.605	0.60	5.0	0.56	M87	0.15	M87	0.48	M86	...	1.3	AU	1 Jy, HP (KS)	
1652+398	Mkn 501	0.034	0.23	5.0	0.45	M87	13.4	WW	3.3	G86	...	1.8	AU	1 Jy, HP (KS)	
1727+502	I Zw 186	0.055	1.20	5.0	0.04	M87	2.1	M87	1.22	G86	...	$<1.0$	AU	BH & VV, HP (AS)	
1749+096	4C 09.57	0.322	0.20	5.0	1.43	M87	0.35	M87	0.73	M86	...	$>3.2$	AU	1 Jy, HP (KS)	
1749+701	S5	0.770	0.39	5.0	0.22	G	0.22	E	0.98	IT	4.7	M90	O'D	1 Jy, HP (KS)	
1803+784	S5	0.684	0.40	5.0	1.80	M87	0.16	M87	0.61	M86	7.8 <sup>4</sup>	S92	M90	1 Jy, HP (KS)	
1807+698	3C 371	0.051	0.79	5.0	0.95	PR	0.6	M87	5.6	G86	12.1 <sup>5</sup>	M90	AU	1 Jy, HP (KS)	
2007+776	S5	0.342	0.40	5.0	1.17	M87	0.11	M87	0.61	M86	4.7	M90	BP	1 Jy, HP (KS)	
2200+420	BL Lac	0.069	0.35	5.0	1.60	M87	0.82	M87	5.9	G86	7.5	M90	AU	1 Jy, HP (KS)	
2254+074	OY 091	0.190	1.00	5.0	0.14	M87	0.1	M87	1.05	M86	...	1.9	AU	1 Jy, HP (KS)	
2335+031	4C 03.59	0.31 <sup>6</sup>	1.70	5.0	0.03	M87	$<0.023$	M87	0.19	LO	...	...		BH, no polarization data	

Table 5.1b: Core-dominated HPQs

Source	Name	$z$	$\theta_d$	$\nu_m$	$F_m$	Ref.	$F_X$	Ref.	$F_V$	Ref.	$\beta_a$	Ref.	$\log R_{CD}$	Ref.	Notes
			m.a.s.	GHz	Jy		$\mu\text{Jy}$		mJy						
0106+013	4C 01.02	2.107	<0.40	5.0	2.30	M87	0.22	M87	0.169	M86	16.4	W90	0.9	BMU	1 Jy, HPQ (IT)
0133+476	OC 457	0.859	0.08	22.3	2.4	L	...		0.1	IT	...		>0.7	U81	2 Jy, HPQ (IT)
0212+735	S5	2.370	0.47	5.0	1.36	PR	0.23	M87	0.1	M86	7.8	Z89	>3.5	A	2 Jy, HPQ (IT)
0234+285	CTD 20	1.213	0.09	22.3	1.7	L	0.15	O	0.107	C	...		2.0	BMU	1 Jy, HPQ (IT)
0336-019	CTA 26	0.852	0.57	2.3	1.52	L89	0.047	M87	0.17	M86	...		1.5	BMU	2 Jy, HPQ (IT)
0420-014*	PKS	0.915	0.70	2.3	3.43	L89	0.52	M87	0.242	M86	...		2.4	BMU	2 Jy, HPQ (IT)
0521-365	PKS	0.055	1.4	2.3	1.2	P89	0.68	M87	1.	G86	...		0.0	AU	1 Jy, HPQ (AS)
0804+499	OJ 508	1.430	0.23	5.0	1.34	PR	<0.24	B87	0.39	IT	...		>0.6	U81	1 Jy, HPQ (IT)
1034-293	OL-259	0.312	0.44	2.3	0.58	L89	0.13	LO	0.98	IT	...		>0.8	U81	1 Jy, HPQ (IT)
1156+295	4C 29.45	0.729	<0.123	22.2	1.4	H90	0.15	G86	5.1	G86	52.3	H90	0.9	AU	HPQ (S)
1253-055*	3C 279	0.538	0.14	15.0	4.84	L90	1.4	M87	0.319	M86	18.4	Z89	1.1	BMU	2 Jy, HPQ (IT)
1335-127	PKS	0.541	0.63	2.3	2.21	L89	0.24	IN	0.155	IT	...		1.1	BP	1 Jy, HPQ (IT)
1510-089	PKS	0.361	0.12	15.0	2.76	L90	0.44	LO	0.62	LO	...		1.5	BMU	2 Jy, HPQ (IT)
1548+056	4C 05.64	1.422	0.88	8.4	1.46	C	...		0.155	C	...		1.5	BP	1 Jy, HPQ (IT)
1641+399	3C 345	0.595	0.30	22.0	6.90	M87	0.66	M87	2.3	G86	18.9	Z89	1.5	BMU	2 Jy, HPQ (IT)
1739+522	4C 51.37	1.375	0.37	5.0	0.89	PR	0.10	BM	0.155	IT	...		1.7	BMU	1 Jy, HPQ (IT)
1741-038	OT-68	1.054	1.10	2.3	2.11	L89	...		0.155	IT	...		>0.6	U81	2 Jy, HPQ (IT)
1921-293	OV 236	0.352	0.54	2.3	3.49	L89	0.56	M86	0.39	M86	...		>0.8	BMU	PKS, HPQ (M)
1958-179	PKS	0.65	0.52	2.3	1.65	L89	...		0.155	S	...		>0.7	U81	1 Jy, HPQ (S)
2223-052	3C 446	1.404	0.10	15.0	1.98	L90	1.1	M87	2.9	G86	6.7 <sup>5</sup>	M90	1.5	BMU	2 Jy, HPQ (IT)
2230+114*	CTA 102	1.037	<0.50	5.0	0.54	M87	0.34	M87	0.46	M86	<28.4	W90	1.4	BMU	2 Jy, HPQ (IT)
2234+282	B2	0.795	<0.50	5.0	1.21	M87	0.05	M87	0.01	M86	...		2.4	BMU	1 Jy, HPQ (MS)
2251+158*	3C 454.4	0.859	<0.30	5.0	0.90	M87	0.56	M87	1.39	M86	17.7	Z89	1.2	BMU	2 Jy, HPQ (IT)
2345-167	PKS	0.576	<0.40	5.0	2.50	M87	0.18	M87	0.242	M86	...		1.4	AU	2 Jy, HPQ (IT)

Table 5.1c: Core-dominated LPQs

Source	Name	$z$	$\theta_d$ m.a.s.	$\nu_m$ GHz	$F_m$ Jy	Ref.	$F_X$ $\mu Jy$	Ref.	$F_V$ mJy	Ref.	$\beta_a$	Ref.	$\log R_{CD}$	Ref.	Notes
0016+731	S5	1.781	0.46	5.0	1.58	PR	0.12	E	0.246	BM	16.6	S92	>0.5	U81	1 Jy, LPQ (IT)
0153+744	S5	2.34	<0.59	5.0	0.64	E87	<1.0	E87	1.554	K	<2	S92	>0.4	U81	1 Jy, LPQ (IT)
0229+131	4C 13.14	2.065	0.85	8.4	2.76	C	0.1	O	0.1	C	...	...	1.1	BP	1 Jy, LPQ (IT)
0333+321	NRAO 140	1.258	0.33	3.2	1.60	MB	1.6	MB	0.515	MB	9.5	MB	1.5	BMU	LPQ (MS)
0430+052 <sup>7</sup>	3C 120	0.033	<0.4	5.0	3.9	P81	10	BM	3.905	K	8.1	Z89	1.4	WB	1 Jy, LPQ (A84)
0528+134*	OG 147	2.06	0.85	8.4	2.39	C	0.36	B85	0.039	IT	...	...	1.6	BP	2 Jy, LPQ (IT)
0552+398	DA 193	2.365	0.73	8.4	2.62	C	...	E87	0.246	C	3.5 <sup>5</sup>	C	>0.4	U81	no polarization data
0615+820	S5	0.71	<0.5	5.0	0.61	E87	<0.2	E87	0.39	K	<4.4 <sup>5</sup>	S92	>0.7	U81	1 Jy, no polarization data
0711+356	OI 318	1.620	0.11	5.0	0.27	PR	...	H	0.619	PR	...	...	>0.5	U81	1 Jy, LPQ (IT)
0723+008	OI-039	0.128	1.07	2.3	1.07	L89	0.35	E	0.246	VV	...	...	>0.9	U81	PKS, no polarization data
0836+710*	4C 71.07	2.170	0.34	5.0	1.05	PR	<1	E	0.981	PR	20.8	Z89	1.5	BP	2 Jy, LPQ (IT)
0859+470	4C 47.29	1.462	1.40	5.0	1.15	PR	<0.31	B87	0.129	B87	...	...	1.0	BP	1 Jy, LPQ (IT)
0923+392	4C 39.25	0.699	0.69	5.0	6.9	P81	0.37	WW	0.27	PR	7.1	Z89	1.2	BMU	2 Jy, LPQ (IT)
1039+811	S5	1.26	<0.5	5.0	0.29	E87	<0.1	E87	0.981	K	<4.4 <sup>5</sup>	S92	1.6	BP	1 Jy, no polarization data
1055+201	4C 20.24	1.110	0.2	5.0	0.516	P3	...	E87	0.155	K	...	...	0.6	P4	1 Jy, LPQ (MS)
1150+812	S5	1.25	<0.5	5.0	0.46	E87	<0.2	E87	0.155	K	<8.2	Z89	1.4	BP	1 Jy, no polarization data
1226+023*	3C 273	0.158	0.14	15.0	3.49	U85	21	U85	10.	U85	16.1	Z89	0.7	BMU	2 Jy, LPQ (IT)
1404+286	Mkn 668	0.077	0.77	8.4	1.05	C	<0.36	B87	2.7	C	...	...	>0.9	U81	1 Jy, LPQ (A84)
1548+114	4C 11.50	0.436	0.3	5.0	0.310	P3	0.32	WW	0.501	HB	...	...	0.3	P4	PKS, LPQ (S84)
1624+416	4C 41.32	2.550	0.33	5.0	0.43	PR	<0.85	B87	0.006	PR	...	...	1.0	O'D	1 Jy, no polarization data
1633+382*	4C 38.41	1.814	0.57	5.0	0.43	PR	<0.02	B87	0.246	PR	...	...	1.8	BP	2 Jy, LPQ (IT)
1730+130	NRAO 530	0.902	0.15	15.0	1.88	L90	0.2	MB	0.155	RS	...	...	1.8	BMU	PKS, no polarization data
1928+738	4C 73.18	0.302	0.49	5.0	2.11	PR	0.55	E	0.981	PR	14.1	Z89	0.7	HR	2 Jy, LPQ (IT)
1954+513	OV 591	1.220	1.06	5.0	0.85	PR	...	...	0.155	PR	...	...	0.6	BP	1 Jy, LPQ (MS)
2134+004	PHL 61	1.936	0.62	5.0	6.7	P81	0.04	BM	0.246	K	<0.8	Z89	1.9	BP	2 Jy, LPQ (MS)
2145+067	4C 06.69	0.990	0.16	15.0	5.43	L90	0.36	J	0.39	K	...	...	2.0	BP	2 Jy, LPQ (IT)
2216+038	4C-03.79	0.901	0.50	2.3	1.27	L89	0.15	KU	0.62	K	...	...	0.7	BP	1 Jy, LPQ (IT)
2245+328	OY-376	2.268	1.0	2.3	1.7	P89	...	...	0.142	HB	...	...	>0.4	U81	2 Jy, LPQ (IT)
2351+456	4C 45.51	2.000	0.69	5.0	0.32	PR	<0.31	B87	0.023	PR	...	...	>0.5	U81	1 Jy, no polarization data

Table 5.1d: Lobe dominated quasars

Source	Name	$z$	$\theta_d$	$\nu_m$	$F_m$	Ref.	$F_X$	Ref.	$F_V$	Ref.	$\beta_a$	Ref.	$\text{Log} R_{CD}$	Ref.	Notes
			m.a.s.	GHz	Jy		$\mu\text{Jy}$		mJy						
0850+581	4C 58.17	1.322	0.48	5.0	0.94	PR	0.97	B87	0.246	B87	7.8	Z89	-0.4	B86	1 Jy, LPQ (IT)
0906+430	3C 216	0.670	0.10	5.0	0.88	PR	0.1	M86	0.156	M86	17.2	BPR	-0.1	BMU	2 Jy, HPQ (IT)
1040+123	3C 245	1.029	0.33	10.7	0.59	HR	0.121	WW	0.474	HB	6.2	HR	-0.5	P4	2 Jy, LPQ (MS)
1222+216	4C 21.35	0.435	0.45	5.0	0.691	P1	...		0.39	HB	2.8	P1	0.0	P4	PKS, no polarization data
1317+520	4C 52.27	1.060	0.8	5.0	0.108	P3	...		0.619	HB	...		-0.2	P4	LPQ (S84)
1618+177	3C 334	0.555	<0.2	10.7	0.086	P5	0.3	BM	1.066	HB	1.6 <sup>5</sup>	P5	-0.7	P4	PKS, LPQ (S84)
1721+343	4C 34.47	0.2055	0.24	10.7	0.109	P2	1.9	WW	0.981	B	4.7	B	-0.1	P4	LPQ (S84)
1830+285	4C 28.45	0.594	0.5	5.0	0.303	P1	...		0.534	HB	5.1	P1	-0.3	P4	1 Jy, LPQ (S84)
1845+797	3C 390.3	0.057	0.50	5.0	0.31	PR	1.1	LO	2.7	G86	3.8	P87	-1.0	WB	2 Jy, HPQ (ILT)
2209+080	4C 08.64	0.484	3.	5.0	0.290	P4	...		0.155	HB	...		-0.8	P4	1 Jy, LPQ (MS)
2251+134	4C 13.85	0.677	0.5	5.0	0.370	P3	...		0.078	HB	...		-0.8	P4	PKS, no polarization data

Table 5.1e: Radio Galaxies

Source	Name	$z$	$\theta_d$	$\nu_m$	$F_m$	Ref.	$F_X$	Ref.	$F_V$	Ref.	$\beta_a$	Ref.	$\text{Log} R_{CD}$	Ref.	Notes
			m.a.s.	GHz	Jy		$\mu\text{Jy}$		mJy						
0108+388	OC 314	0.669 <sup>8</sup>	0.85	5.0	0.56	PR	<0.06	BM	0.006	PR	1.0	RPU	2.2	B90	1 Jy, no polarization data
0316+413	3C 84	0.018	0.30	22.2	6	R83	18	M87	16.2	G86	0.4	Z89	<1.0	AU	NGC 1275, 1 Jy, HP (ILT)
0710+439	S4	0.518	0.96	5.0	0.63	PR	<0.55	B87	0.02	PR	<2.5	Z89	>0.8	U81	1 Jy, no polarization data
1228+127	M 87	0.004	0.7	5.0	1.0	P81	0.68	F	564	K	<0.12	Z89	-1.0	J82	1 Jy, no polarization data
1637+826	NGC 6251	0.023	<0.2	10.7	0.67	J86	0.3	BM	24.6	WP	0.64	Z89	0.2	WWB	LP (A84)
2021+614	OW 637	0.227	0.60	5.0	1.01	PR	...		0.062	PR	<0.7	Z89	>0.9	U81	1 Jy, LP (ILT)
2201+044	PKS	0.028	0.70	5.0	0.16	M87	0.21	M87	3.19	M86	...		0.5	WJ	PKS, LP (K76)
2352+495	OZ 488	0.237	0.82	5.0	0.73	PR	<0.31	B87	0.098	PR	...		>0.9	U81	1 Jy, LP (ILT)

NOTES.—(1) Stickel *et al.* (1991). (2) Probably affected by gravitational lensing. (3) Schalinski *et al.* (1992). (4) Subluminal at m.a.s. scale, superluminal at submas scale. (5) Uncertain value. (6) Imaging estimate from Romanishin (1987). (7) FR I radio structure. (8) O’Dea *et al.* (1991).

Table 5.2a: BL Lacs

Source	$\delta$	$T_B$	$\Gamma$	$\Gamma^*$	$\theta$	$\theta_{max}$	$\delta/\Gamma^*$	$n'_{SSC}$	$n'_{e\pm}$	B
		$10^{11} \text{ }^\circ\text{K}$						$\text{cm}^{-3}$	$\text{cm}^{-3}$	G
0048-097	(10.5)	25.1	...	5.3	...	5.5	...	(890)	(23)	$(6.1 \times 10^{-4})$
0219+428	0.1	0.09	...	1.	...	90.	...	870	5.1	$9.2 \times 10^{-1}$
0235+164	6.5	9.6	637	3.3	1.3	8.8	0.1	250	9.8	$7.7 \times 10^{-3}$
0300+471	(4.8)	4.5	...	2.5	...	12.1	...	(920)	(480)	$(8.1 \times 10^{-2})$
0306+102	(2.1)	2.9	...	1.3	...	28.	...	(520)	(5.2)	$(2.0 \times 10^{-2})$
0454+844	(3.7)	4.3	3.4	2.	15.4	15.5	1.1	(120)	(24)	$(1.6 \times 10^{-2})$
0537-441	11.6	22.2	...	5.9	...	4.9	...	95	1.2	$1.2 \times 10^{-3}$
0716+714	(2.1)	3.8	6.3	1.3	20.4	27.9	0.5	(2500)	(140)	$(1.1 \times 10^{-2})$
0735+178	(7.3)	14.5	18.	3.7	6.3	7.9	0.5	(1400)	(40)	$(2.8 \times 10^{-3})$
0754+100	(1.1)	1.5	...	1.	...	70.8	...	(920)	(73)	$(3.9 \times 10^{-2})$
0818-128	(0.7)	0.7	...	1.	...	90.	...	(320)	(20)	$(1.0 \times 10^{-1})$
0823+033	3.7	7.8	...	2.	...	15.5	...	$4.6 \times 10^4$	650	$1.6 \times 10^{-2}$
0829+046	0.2	0.3	...	1.	...	90.	...	2300	42	$2.0 \times 10^{-1}$
0851+202	8.8	23.6	6.8	4.4	6.3	6.6	1.4	4900	47	$1.2 \times 10^{-3}$
0954+658	5.0	12.8	...	2.6	...	11.5	...	9860	170	$2.4 \times 10^{-3}$
1101+384	0.5	1.9	15.9	1.	29.	90.	0.1	$2.5 \times 10^6$	8000	$7.6 \times 10^{-3}$
1147+245	(0.5)	0.5	...	1.	...	90.	...	(390)	(16)	$(1.6 \times 10^{-1})$
1215+303	(0.4)	0.7	...	1.	...	90.	...	(6300)	(26)	$(6.8 \times 10^{-2})$
1219+285	0.2	0.4	...	1.	...	90.	...	$2.8 \times 10^4$	330	$8.8 \times 10^{-2}$
1308+326	6.8	11.1	...	3.5	...	8.4	...	390	9.3	$6.2 \times 10^{-3}$
1400+162	0.04	0.04	...	1.	...	90.	...	2000	11	2.1
1519-273	(13.7)	57.5	...	6.9	...	4.2	...	$(2.4 \times 10^4)$	(19)	$(1.5 \times 10^{-4})$
1538+149	1.3	1.8	...	1.	...	49.6	...	640	42	$3.8 \times 10^{-2}$
1652+398	1.5	6.4	...	1.1	...	42.9	...	$1.6 \times 10^6$	$1.7 \times 10^4$	$2.1 \times 10^{-3}$
1727+502	0.01	0.02	...	1.	...	90.	...	$3.3 \times 10^5$	170	1.7
1749+096	14.3	33.5	...	7.2	...	4.	...	2400	61	$9.5 \times 10^{-4}$
1749+701	1.1	1.8	11.4	1.	23.	70.1	0.2	3500	100	$3.3 \times 10^{-2}$
1803+784	8.5	13.4	7.9	4.3	6.7	6.7	1.1	310	13	$4.5 \times 10^{-3}$
1807+698	0.7	1.4	102.	1.	9.4	90.	0.1	6500	450	$3.3 \times 10^{-2}$
2007+776	4.7	6.9	4.8	2.5	12.3	12.3	1.0	440	43	$7.4 \times 10^{-3}$
2200+420	4.4	9.9	8.7	2.3	11.3	13.	0.6	9000	660	$2.7 \times 10^{-3}$
2254+074	0.1	0.1	...	1.	...	90.	...	1900	32	$5.5 \times 10^{-1}$
2335+031	0.02	0.01	...	1.	...	90.	...	(770)	(4.4)	$1.2 \times 10$

Table 5.2b: Core-dominated HPQs

Source	$\delta$	$T_B$	$\Gamma$	$\Gamma^*$	$\theta$	$\theta_{max}$	$\delta/\Gamma^*$	$n'_{SSC}$	$n'_{e\pm}$	B
		$10^{11} \text{ }^\circ\text{K}$						$\text{cm}^{-3}$	$\text{cm}^{-3}$	G
0106+013	18.9	31.6	16.6	9.5	3.0	3.0	1.2	330	5.8	$3.3 \times 10^{-3}$
0133+476	16.8	24.8	...	8.5	...	3.4	...	2700	150	$1.3 \times 10^{-2}$
0212+735	9.2	14.7	8.0	4.7	6.2	6.2	1.2	510	9.1	$8.1 \times 10^{-3}$
0234+285	16.6	16.5	...	8.3	...	3.5	...	480	120	$3.4 \times 10^{-2}$
0336-019	15.6	29.0	...	7.8	...	3.7	...	120	3.3	$8.9 \times 10^{-4}$
0420-014	16.8	44.9	...	8.4	...	3.4	...	470	2.0	$4.1 \times 10^{-4}$
0521-365	1.0	2.2	...	1.	...	90.	...	5100	130	$5.7 \times 10^{-3}$
0804+499	21.0	43.7	...	10.5	...	2.7	...	1000	14	$1.5 \times 10^{-3}$
1034-293	5.4	13.2	...	2.8	...	10.8	...	1700	35	$1.1 \times 10^{-3}$
1156+295	6.4	5.8	213.5	3.3	2.2	8.9	0.1	460	180	$8.4 \times 10^{-2}$
1253-055	18.0	29.9	18.4	9.0	3.2	3.2	1.0	1500	60	$5.3 \times 10^{-3}$
1335-127	11.9	28.7	...	6.0	...	4.8	...	430	4.5	$5.8 \times 10^{-4}$
1510-089	14.5	20.5	...	7.3	...	4.0	...	1300	150	$7.9 \times 10^{-3}$
1548+056	0.9	1.2	...	1.	...	390.	...	1150	9.2	$1.6 \times 10^{-1}$
1641+399	5.3	4.5	36.7	2.7	5.6	11.	0.3	180	42	$1.0 \times 10^{-1}$
1739+522	7.3	10.9	...	3.7	...	7.8	...	390	15	$8.2 \times 10^{-3}$
1741-038	4.3	12.0	...	2.3	...	13.4	...	1500	3.0	$1.6 \times 10^{-3}$
1921-293	18.2	54.1	...	9.1	...	3.2	...	900	6.0	$2.2 \times 10^{-4}$
1958-179	9.2	33.7	...	4.7	...	6.2	...	4400	7.5	$3.5 \times 10^{-4}$
2223-052	20.9	37.5	11.5	10.5	1.6	2.7	3.1	3500	74	$6.1 \times 10^{-3}$
2230+114	1.9	3.1	217	1.2	4.0	32.4	0.1	1600	34	$2.2 \times 10^{-2}$
2234+282	5.2	6.2	...	2.7	...	11.1	...	110	13	$1.4 \times 10^{-2}$
2251+158	6.0	13.2	29.3	3.1	5.8	9.6	0.3	2700	31	$3.6 \times 10^{-3}$
2345-167	10.8	17.4	...	5.5	...	5.3	...	260	12	$3.2 \times 10^{-3}$

Table 5.2c: Core-dominated LPQs

Source	$\delta$	$T_B$	$\Gamma$	$\Gamma^*$	$\theta$	$\theta_{max}$	$\delta/\Gamma^*$	$n'_{SSC}$	$n'_{e\pm}$	B
		$10^{11} \text{ }^\circ\text{K}$						$\text{cm}^{-3}$	$\text{cm}^{-3}$	G
0016+731	10.3	14.7	18.6	5.2	5.0	5.5	0.6	220	7.5	$7.5 \times 10^{-3}$
0153+744	2.3	4.4	2.2	1.4	26.1	26.1	1.0	3700	20	$2.3 \times 10^{-2}$
0229+131	3.8	2.9	...	2.0	...	15.4	...	40	6.4	$1.3 \times 10^{-1}$
0333+321	16.6	57.3	11.0	8.3	3.0	3.5	1.7	5200	8.6	$4.1 \times 10^{-4}$
0430+052	5.3	17.8	8.9	2.8	9.9	10.8	0.7	$7.8 \times 10^4$	1640	$9.8 \times 10^{-4}$
0528+134	2.6	2.5	...	1.5	...	22.9	...	170	9.3	$1.2 \times 10^{-1}$
0552+398	2.8	4.2	3.8	1.6	20.2	21.0	0.8	1340	12.5	$5.2 \times 10^{-2}$
0615+820	2.0	3.0	6.2	1.2	21.7	30.9	0.4	900	37	$2.2 \times 10^{-2}$
0711+356	8.3	41.1	...	4.2	...	6.9	...	$2.8 \times 10^5$	160	$7.3 \times 10^{-4}$
0723-008	1.7	3.5	...	1.1	...	37.2	...	1900	67	$3.9 \times 10^{-3}$
0836+710	8.7	20.8	29.2	4.4	4.7	6.6	0.4	3800	18	$3.8 \times 10^{-3}$
0859+470	0.9	1.0	...	1.	...	90.	...	250	3.6	$1.2 \times 10^{-1}$
0923+392	11.6	17.4	8.0	5.8	4.4	5.0	1.6	91	4.0	$3.6 \times 10^{-3}$
1039+811	1.4	1.9	8.0	1.1	23.5	46.1	0.3	880	45	$5.1 \times 10^{-2}$
1055+201	6.2	19.3	...	3.2	...	9.2	...	$1.9 \times 10^4$	62	$2.0 \times 10^{-3}$
1150+812	1.9	2.9	18.6	1.2	13.2	31.2	0.2	1100	32	$2.9 \times 10^{-2}$
1226+023	6.0	16.2	24.8	3.1	6.3	9.6	0.4	$6.6 \times 10^4$	780	$4.4 \times 10^{-3}$
1404+286	0.5	0.5	...	1.	...	90.	...	1800	230	$2.1 \times 10^{-1}$
1548+114	1.8	3.5	...	1.2	...	34.6	...	5600	160	$1.2 \times 10^{-2}$
1624+416	4.3	9.9	...	2.3	...	13.4	...	8600	41	$8.8 \times 10^{-3}$
1633+382	2.8	2.6	...	1.6	...	21.2	...	110	18	$6.3 \times 10^{-2}$
1730-130	11.0	12.5	...	5.6	...	5.2	...	460	65	$2.3 \times 10^{-2}$
1928+738	4.4	8.1	24.9	2.3	7.4	13.1	0.3	1100	35	$4.9 \times 10^{-3}$
1954+513	0.7	1.2	...	1.	...	90.	...	2300	6.3	$6.2 \times 10^{-2}$
2134+004	34.6	36.2	17.3	17.3	0.1	1.7	27	13	1.3	$4.4 \times 10^{-3}$
2145+067	26.9	33.2	...	13.5	...	2.1	...	260	23	$8.2 \times 10^{-3}$
2216-038	13.4	32.3	...	6.7	...	4.3	...	510	4.8	$6.3 \times 10^{-4}$
2245-328	6.6	18.8	...	3.4	...	8.7	...	1990	2.7	$1.6 \times 10^{-3}$
2351+456	1.0	1.4	...	1.	...	90.	...	1900	16	$8.0 \times 10^{-2}$



Table 5.2d: Lobe dominated quasars

Source	$\delta$	$T_B$	$\Gamma$	$\Gamma^*$	$\theta$	$\theta_{max}$	$\delta/\Gamma^*$	$n'_{SSC}$	$n'_{e\pm}$	B
		$10^{11} \text{ }^\circ\text{K}$						$\text{cm}^{-3}$	$\text{cm}^{-3}$	G
0850+581	3.3	6.7	11.1	1.8	12.5	17.9	0.4	2800	21	$9.6 \times 10^{-3}$
0906+430	43.4	104.	25.1	21.7	0.9	1.3	2.5	1600	43	$3.8 \times 10^{-4}$
1040+123	1.8	1.7	12.2	1.2	17.0	34.9	0.3	490	83	$1.5 \times 10^{-1}$
1222+216	1.3	3.5	4.1	1.	33.5	51.7	0.4	$2.1 \times 10^4$	99	$8.6 \times 10^{-3}$
1317+520	0.1	0.3	...	1.	...	90.	...	$9.5 \times 10^4$	11	$1.9 \times 10^{-1}$
1618+177	0.4	0.5	4.9	1.	62.0	90.	0.2	$1.6 \times 10^4$	240	$2.6 \times 10^{-1}$
1721+343	0.2	0.4	59.1	1.	24.0	90.	0.04	$1.1 \times 10^5$	490	$2.3 \times 10^{-1}$
1830+285	0.5	1.4	27.6	1.	22.0	90.	0.1	$5.3 \times 10^4$	36	$2.4 \times 10^{-2}$
1845+797	0.5	0.9	17.3	1.	29.1	90.	0.1	$5.1 \times 10^4$	930	$3.1 \times 10^{-2}$
2209+080	0.03	0.03	...	1.	...	90.	...	2890	1.2	$2.1 \times 10$
2251+134	0.9	2.8	...	1.	...	90.	...	6080	35	$5.3 \times 10^{-2}$

Table 5.2e: Radio Galaxies

Source	$\delta$	$T_B$	$\Gamma$	$\Gamma^*$	$\theta$	$\theta_{max}$	$\delta/\Gamma^*$	$n'_{SSC}$	$n'_{e\pm}$	B
		$10^{11} \text{ }^\circ\text{K}$						$\text{cm}^{-3}$	$\text{cm}^{-3}$	G
0108+388	0.9	0.9	1.6	1.	67.6	90.	0.6	240	22	$1.0 \times 10^{-1}$
0316+413	1.6	2.4	1.2	1.1	25.8	39.3	1.5	$8.4 \times 10^4$	$3.1 \times 10^4$	$6.8 \times 10^{-2}$
0710+439	0.5	0.7	7.4	1.	42.2	90.	0.2	1400	11	$8.2 \times 10^{-2}$
1228+127	1.0	1.5	...	1.	...	90.	...	$9.3 \times 10^4$	$8.0 \times 10^4$	$2.3 \times 10^{-2}$
1637+826	1.3	2.7	1.3	1.2	22.3	31.3	1.6	$2.3 \times 10^4$	$3.6 \times 10^4$	$3.4 \times 10^{-2}$
2021+614	1.4	2.4	1.2	1.1	44.5	45.9	1.1	2500	110	$1.6 \times 10^{-2}$
2201+044	0.2	0.2	...	1.	...	90.	...	$2.7 \times 10^4$	1800	$1.8 \times 10^{-1}$
2352+495	0.7	1.0	...	1.	...	90.	...	1200	35	$5.3 \times 10^{-2}$

**Table 5.3a. Average Values: all sources**

	N	$\log R_{CD}$ (mean)	$\log \delta$ (mean)	$\log \delta$ (median)
BL Lacs	33	$1.80 \pm 0.20$	$0.12 \pm 0.15$	0.33
CDQs	53	$1.46 \pm 0.12$	$0.75 \pm 0.06$	1.01
HPQs	24	$1.62 \pm 0.21$	$0.92 \pm 0.08$	1.00
LPQs	21	$1.20 \pm 0.13$	$0.69 \pm 0.11$	1.06
nPQs	8	$1.46 \pm 0.14$	$0.38 \pm 0.12$	0.46
LDQs	11	$-0.44 \pm 0.10$	$-0.17 \pm 0.25$	-0.31
Gal	8	$0.96 \pm 0.43$	$-0.09 \pm 0.12$	-0.05

NOTE: nPQs are core dominated quasars with no polarization measurements.

**Table 5.3b. Superluminal sources: mean values**

	N	$\log R_{CD}$	$\log \beta_a$	$\log \delta$	$\log \Gamma$	$\theta$
BL Lacs	11	$2.12 \pm 0.36$	$0.84 \pm 0.07^1$	$0.49 \pm 0.13$	$1.02 \pm 0.13^1$	$14.0 \pm 2.5^1$
CDQs	21	$1.43 \pm 0.15$	$0.85 \pm 0.12$	$0.80 \pm 0.09$	$1.22 \pm 0.10$	$8.4 \pm 1.7$
HPQs	8	$1.75 \pm 0.51$	$1.20 \pm 0.10$	$0.92 \pm 0.13$	$1.52 \pm 0.20$	$3.9 \pm 0.6$
LPQs	9	$1.34 \pm 0.17$	$0.83 \pm 0.17$	$0.92 \pm 0.12$	$1.11 \pm 0.11$	$7.4 \pm 2.5$
nPQs	4	$1.50 \pm 0.10$	$< 0.69 \pm 0.08$	$0.29 \pm 0.06$	$0.89 \pm 0.14$	$19.6 \pm 2.2$
LDQs	8	$-0.38 \pm 0.24$	$0.69 \pm 0.11$	$0.09 \pm 0.26$	$1.16 \pm 0.14$	$25.1 \pm 6.4$
Gal	6	$0.93 \pm 0.51$	$-0.40 \pm 0.17$	$0.04 \pm 0.09$	$0.22 \pm 0.13$	$41.3 \pm 6.6$

1: excluding 0235+164

**Table 5.3c. Superluminal sources: median values**

	N	$\log \delta$	$\log \Gamma$	$\theta$
BL Lacs	11	0.57	$0.92^1$	$11.8^1$
CDQs	21	0.78	1.27	5.6
HPQs	8	0.89	1.37	3.6
LPQs	9	0.94	1.24	5.0
nPQs	4	0.29	0.85	20.9
LDQs	8	-0.10	1.16	23.0
Gal	6	0.05	0.11	43.3

1: excluding PKS 0235+164

A: Antonucci *et al.* (1986); AS: Angel & Stockman (1980); AU: Antonucci & Ulvestad (1985); A84: Antonucci (1984); B85: Bregman *et al.* (1985); B86: Barthel *et al.* (1986); B87: Biermann *et al.* (1987); B90: Baum *et al.* (1990); B: Barthel *et al.* (1989); BH: Burbidge & Hewitt (1989); BM: Bloom & Marscher (1991); BMU: Browne & Murphy (1987); BP: Browne & Perley (1986); BPR: Barthel, Pearson & Readhead (1988); C: Charlot (1990); D: Della Ceca *et al.* (1990); E: Eckart *et al.* (1987); F: Fabbiano *et al.* (1984); G: Gabudza *et al.* (1992); G86: Ghisellini *et al.* (1986); G90: Giommi *et al.* (1990); H90: McHardy *et al.* (1990); H: Henricksen *et al.* (1984); HB: Hewitt & Burbidge (1987); HR: Hough & Readhead (1987); H1: Hooimeyer *et al.* (1992a); H2: Hooimeyer *et al.* (1992b); H3: Hooimeyer *et al.* (1992c); H4: Hooimeyer *et al.* (1992d); H5: Hough *et al.* (1992); J: Junkkarinen *et al.* (1982); J82: Jenkins (1982); J86: Jones *et al.* (1986); K76: Kinman (1976); K: Kühr *et al.* (1981); KS: Kühr & Schmidt (1990); KU: Ku, Helfand & Lucy (1980); IN: Impey & Neugebauer (1988); ILT: Impey, Lawrence, & Tapia (1990); IT: Impey & Tapia (1990); L89: Linfield *et al.* (1989); L90: Linfield *et al.* (1990); L: Lawrence *et al.* (1985); LO: Ledden & O'Dell (1985); M86: Maraschi *et al.* (1986); M87: Madau, Ghisellini & Persic (1987); M90: Mutel (1990); M: Mead *et al.* (1990); MB: Marscher & Broderick (1985); MS: Moore & Stockman (1984); O: Owen, Helfand & Spangler (1981); O'D: O'Dea *et al.* (1988); P81: Pauliny-Toth *et al.* (1981); P87: Porcas (1987); P89: Preston *et al.* (1989); PR: Pearson & Readhead (1988); R83: Readhead *et al.* (1983); RPU: Readhead, Pearson & Unwin (1984); RS: Rusk & Seaquist (1985); S: Smith *et al.* (1988); S84: Stockman, Moore, & Angel (1984); S91: Stickel *et al.* (1991); S92: Schalinski *et al.* (1992); U81: Ulvestad *et al.* (1981); U85: Unwin *et al.* (1985); W90: Wehrle *et al.* (1990); WB: Wills & Browne (1986); WJ: Weiler & Johnston (1980); WP: Wall & Peacock (1985); WW: Worrall & Wilkes (1990); WWB: Waggett *et al.* (1977); VV: Véron -Cetty & Veron (1991); Z89: Zensus (1989); ZB: Zhang & Baath (1990).

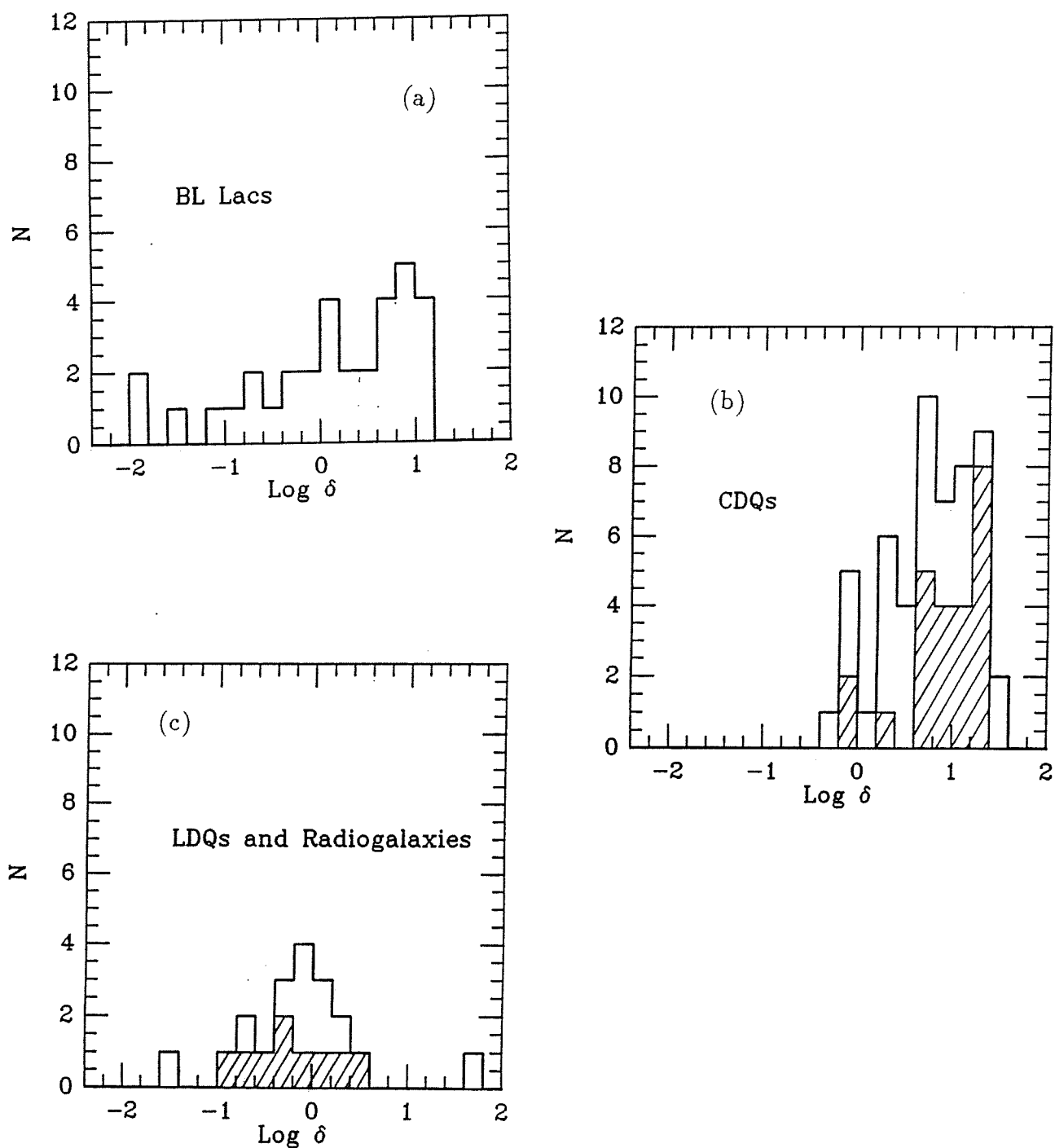
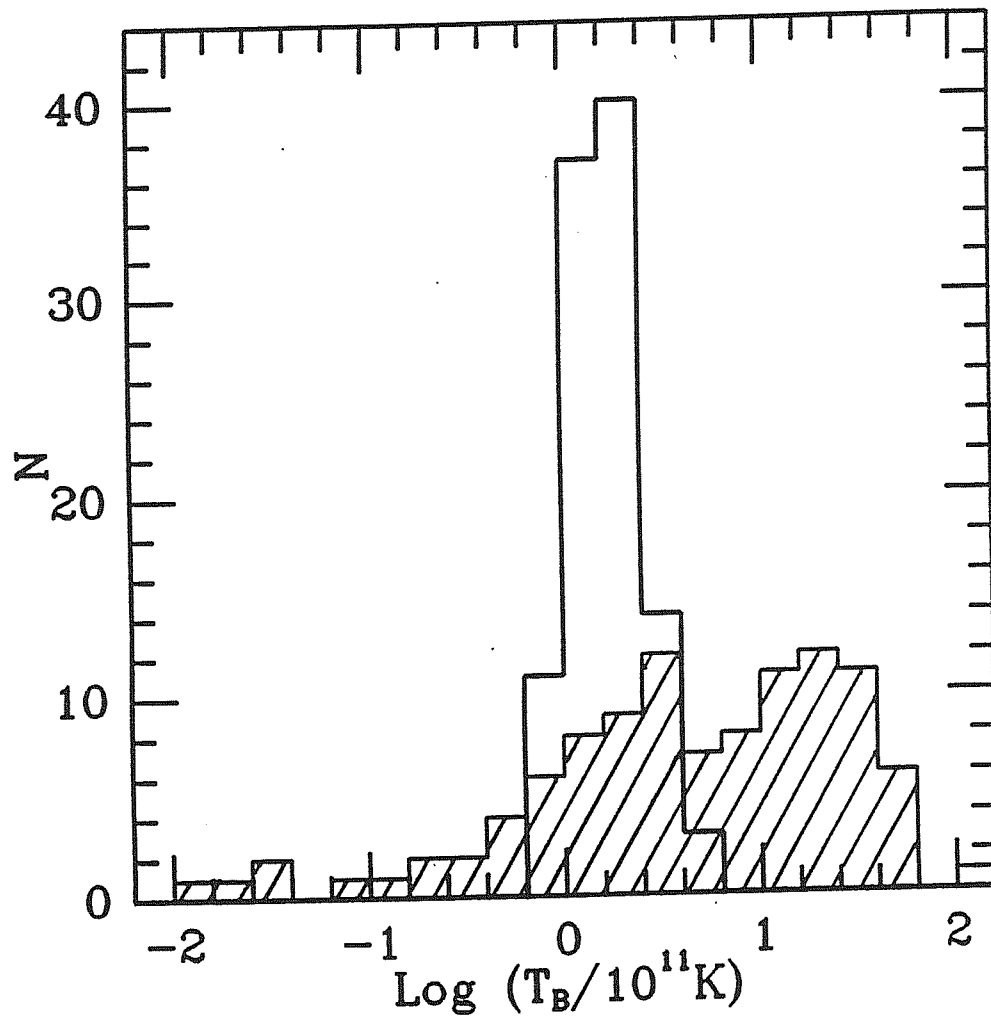
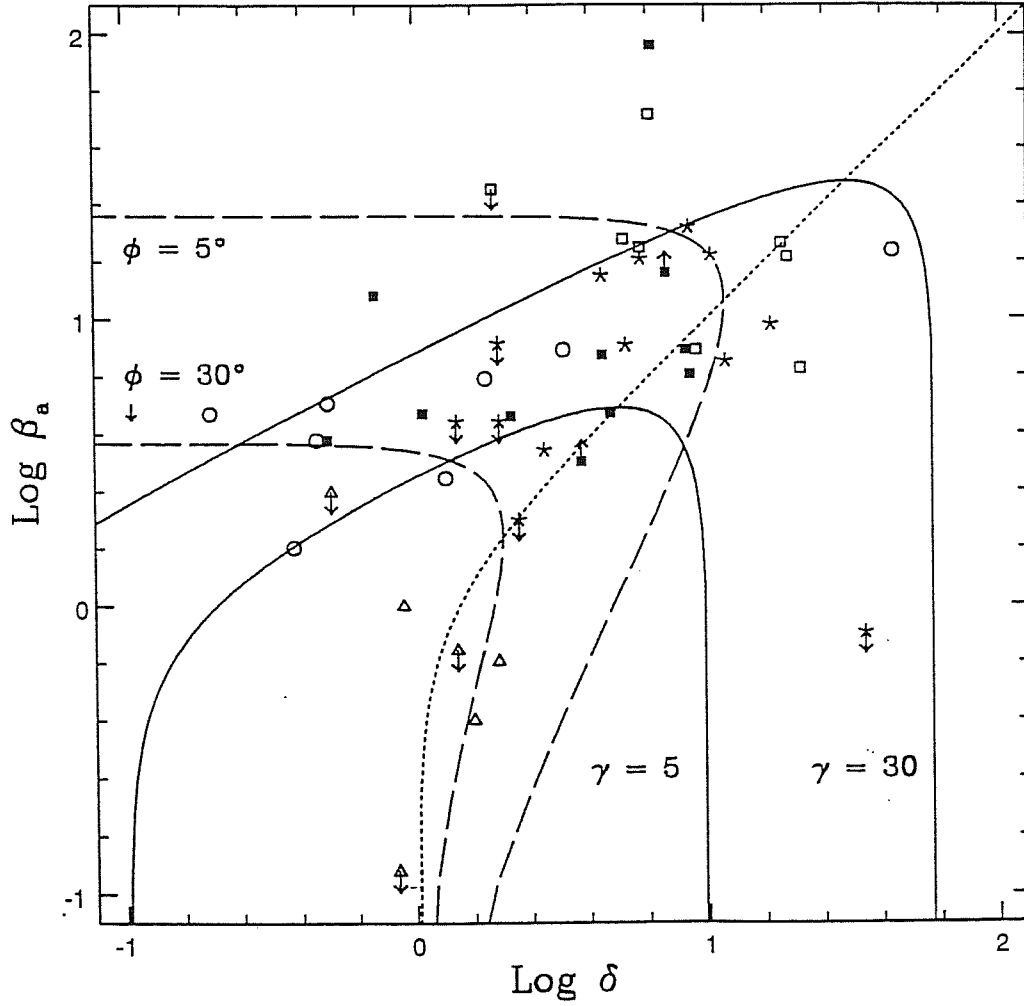


Fig. 5.1. The distribution of the Doppler factor  $\delta$  for BL Lacs (a), for core-dominated quasars (b) (dashed area referring to HPQs), and for radio galaxies and lobe-dominated quasars (c) (the latter indicated by the dashed area).



**Fig. 5.2.** The distribution of the observed (thin line) and intrinsic (solid line) brightness temperature  $T_B$  for the whole sample. The mean value for the intrinsic  $T_B$  is  $1.8 \times 10^{11} \text{ }^\circ\text{K}$ .



**Fig. 5.3.** The apparent expansion velocity versus the Doppler factor  $\delta$  for the superluminal sources in our sample ( $H_0 = 50$ ,  $n = 3 + \alpha$ ). Filled squares: BL Lacs; open squares: HPQ-CDQs; stars: LPQ-CDQs; circles: LDQs; triangles: radio galaxies. Solid lines correspond to the loci of constant  $\Gamma = 5$  and  $30$  as labelled. Dashed lines represent constant viewing angle  $\theta = 5^\circ$  and  $30^\circ$  as labelled. The dotted line,  $\beta_a = \sqrt{\delta^2 - 1}$ , indicates the relationship between the two variables for  $\sin \theta = 1/\Gamma$ . For sources on the left of this line an increase in  $\delta$  results in a decrease of the derived Lorentz factor. The opposite is true for sources on its right.

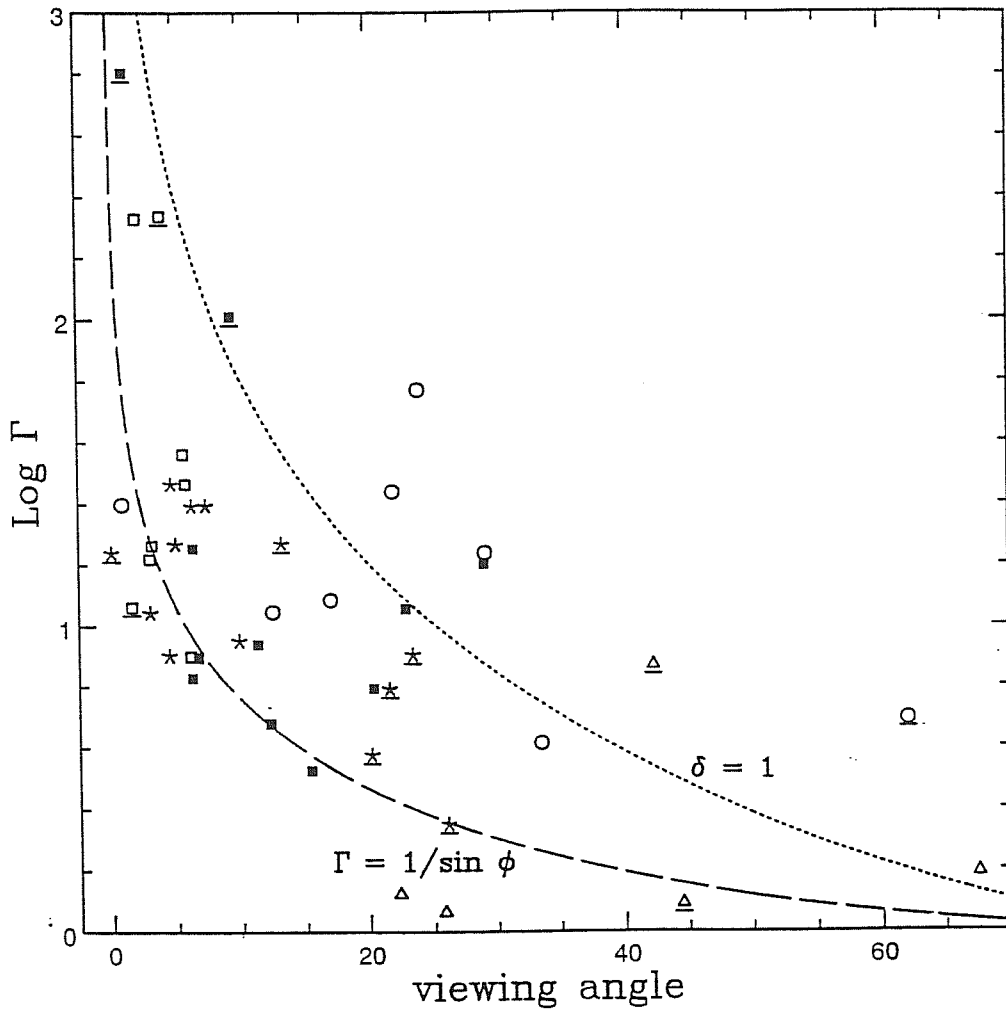


**Fig. 5.4.** The Lorentz factor  $\Gamma$  versus the viewing angle  $\theta$  for the superluminal sources in our sample. Filled squares: BL Lacs; open squares: HPQ-CDQs; stars: LPQ-CDQs; circles: LDQs; triangles: radio galaxies. Underlined symbols denote objects with uncertain or upper limits on  $\beta_a$ . The dashed line corresponds to  $\Gamma = 1/\sin \theta$ . Sources above the dotted line have  $\delta < 1$ .

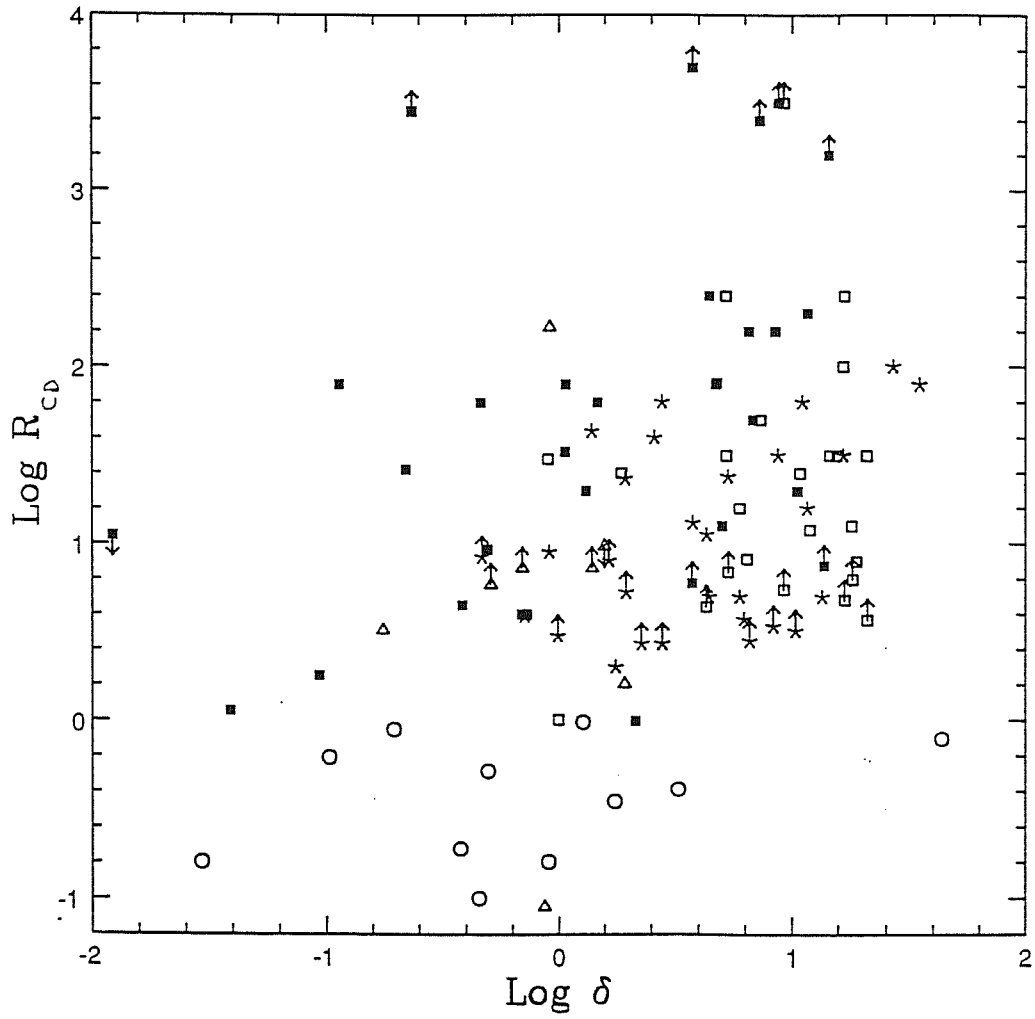


**Fig. 5.5.** The core dominance parameter  $R_{CD}$  versus the Doppler factor  $\delta$  for all but two sources in our sample. Filled squares: BL Lacs; open squares: HPQ-CDQs; stars: LPQ-CDQs; circles: LDQs; triangles: radio galaxies.



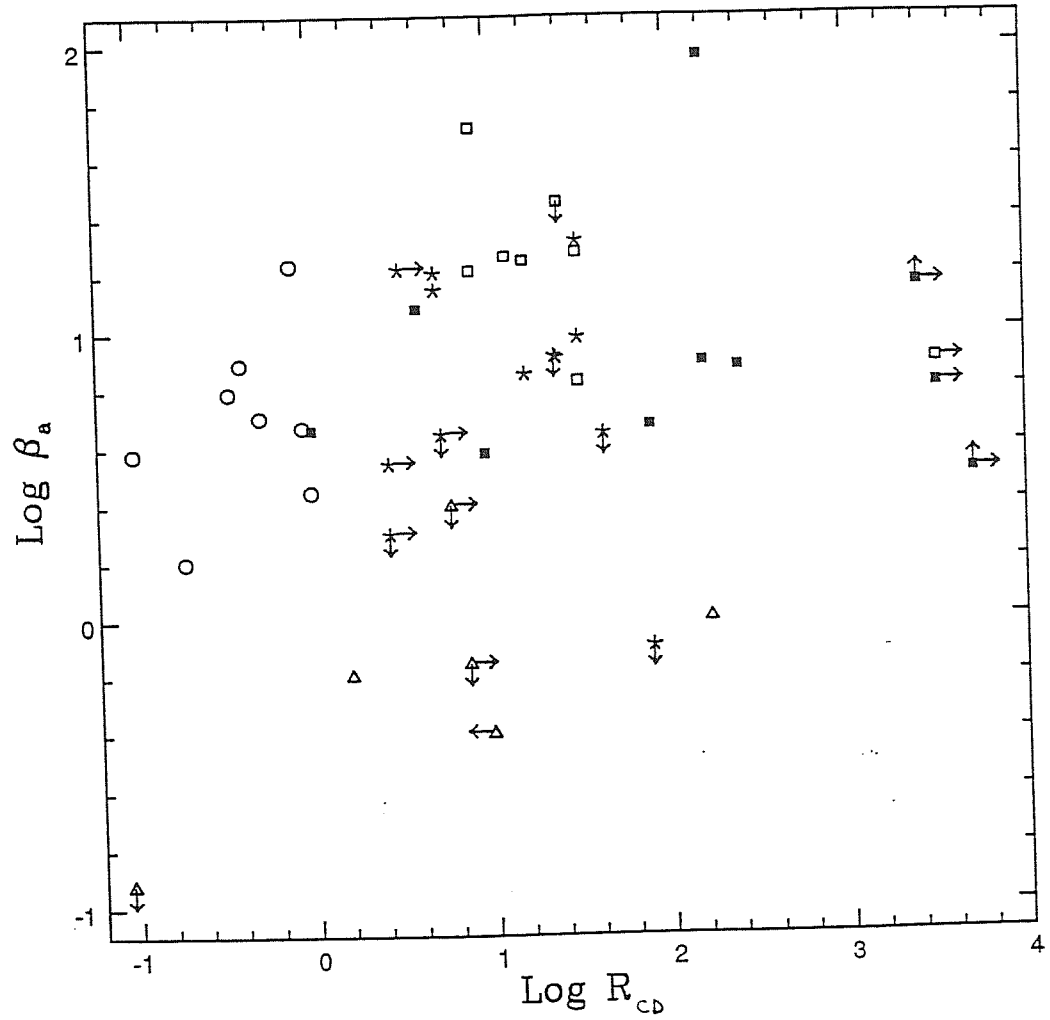


**Fig. 5.6.** The apparent expansion velocity  $\beta_a$  versus the Doppler versus the core dominance parameter  $R_{CD}$  for the superluminal sources in our sample. Filled squares: BL Lacs; open squares: HPQ-CDQs; stars: LPQ-CDQs; circles: LDQs; triangles: radio galaxies.

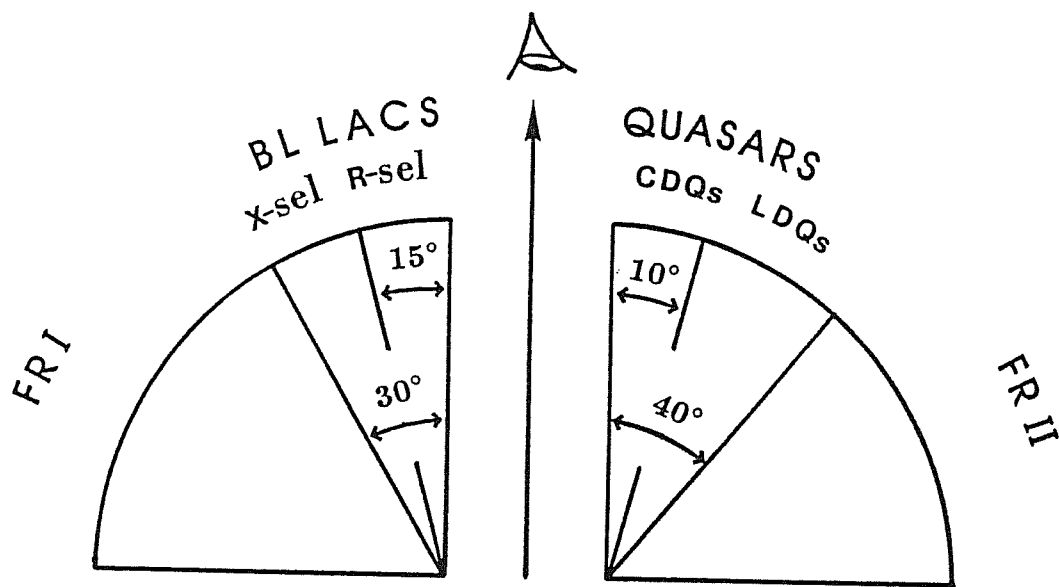


**Fig. 5.7.** Unifying picture, suggesting that FR I radio galaxies originate X-ray selected and radio-selected BL Lacs. The distinction between the three classes of sources corresponds to different viewing angles of a jet of Lorentz factor  $\Gamma \sim 10$ . Analogously, FR II radio galaxies originate steep radio spectrum, lobe dominated quasars (LDQs), and flat radio spectrum, core dominated quasars (CDQs).

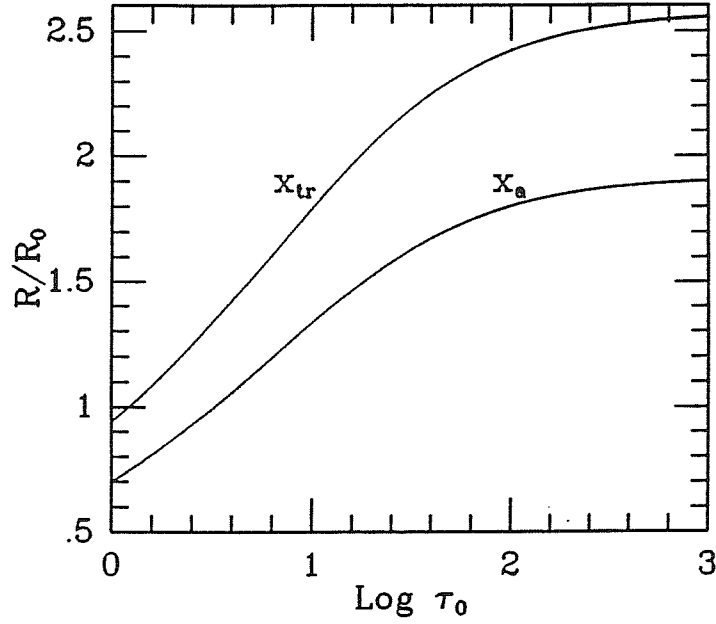


**Fig. 5.8.** The 'trapping' ( $x_{tr} = R_{tr}/R_0$ ) and 'annihilation' ( $x_a = R_a/R_0$ ) radii as a function of  $\tau_0$ . Note the slight dependence of both radii on  $\tau_0$ , although the ratio  $R_{tr}/R_a \simeq 1.34$  is independent of  $\tau_0$ .  $R_0 = 10^{14}$  cm. Note the linear scale of the  $y$ -axis.

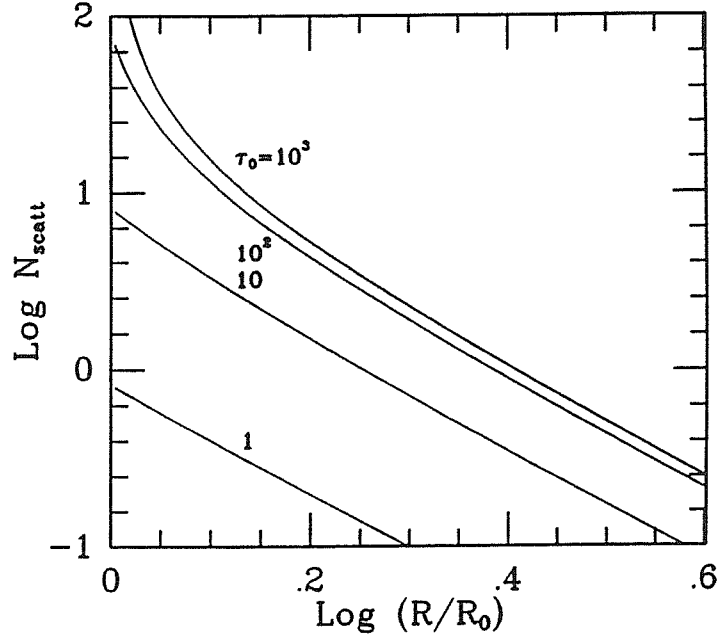
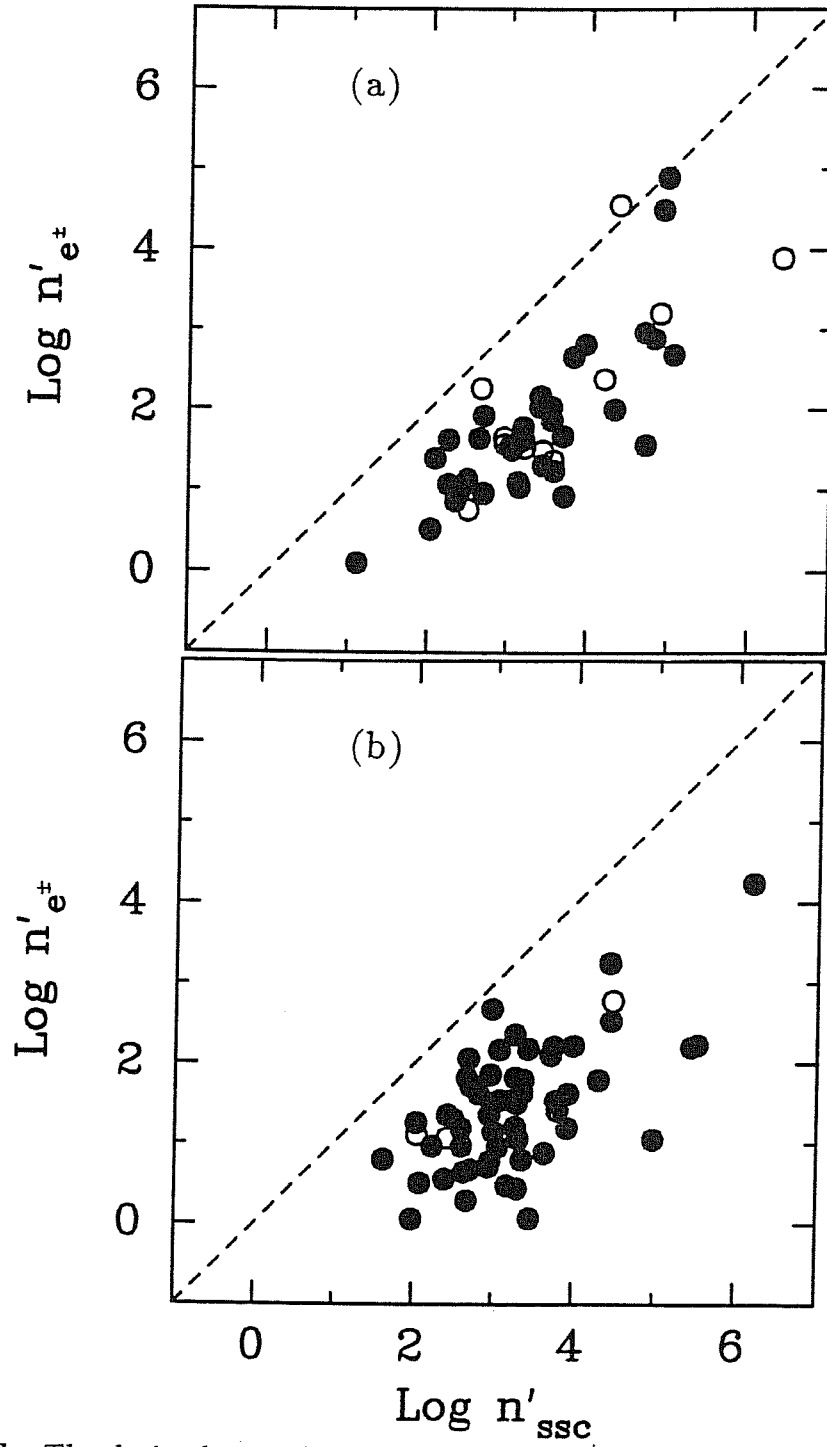


**Fig. 5.9.** The number of Compton scatterings,  $N_{scatt}$  from  $R$  to infinity as a function of  $R/R_0$  (from eq. (5.13)). The assumed parameters are  $R_0 = 10^{14}$  cm,  $\Gamma_0 = \sqrt{3/2}$ . Separate curves are shown for several values of  $\tau_0$ .  $N_{scatt} = 1$  and  $8/3$  are the values appropriate to our definitions of  $R_{tr}$  and  $R_a$  respectively (§5.4.2). It is clear that  $R_{tr} > R_a$  for all values of  $\tau_0$  considered. It can be seen that the higher annihilation rate for higher  $\tau_0$  gives rise to similar values of  $R_{tr}$  and  $R_a$  over a large range of  $\tau_0$ .



**Figs. 5.10a,b.** The derived particle density from the  $e^{\pm}$  pair-jet model ( $n'_{e^{\pm}}$ ) against that from SSC theory ( $n'_{SSC}$ ) for our sample of sources, for  $R_0 = 10^{14}$  cm,  $\tau_0 = 10$ ,  $\alpha = 0.75$  and  $\Gamma_{tr} = \Gamma_0 x_{tr}$  (see eq. (5.19)). The dashed line represents  $n'_{e^{\pm}} = n'_{SSC}$ .

Filled symbols distinguish those sources with measured VLBI diameter,  $\theta_d$ , from those with only an upper limit (open). Objects for which superluminal motion has not been reported are shown in (a), superluminal sources are shown in (b).

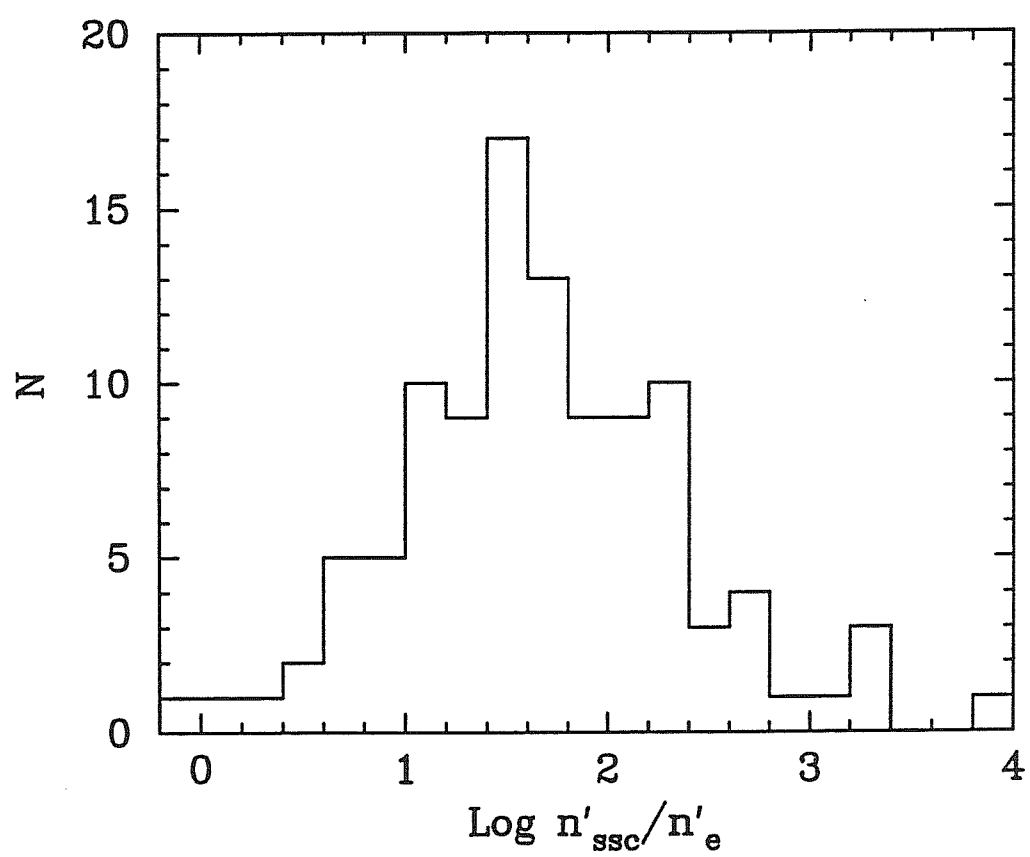
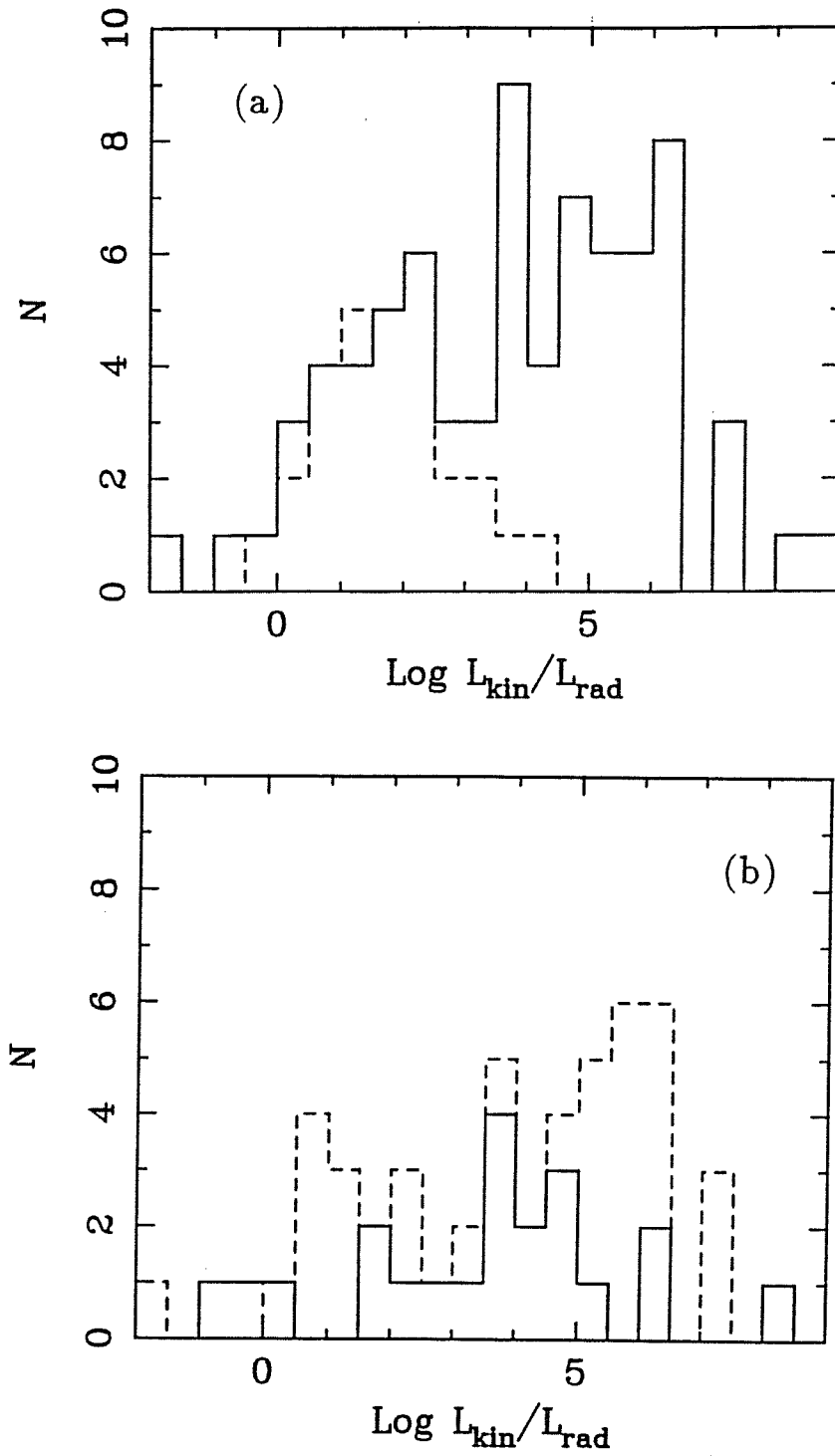
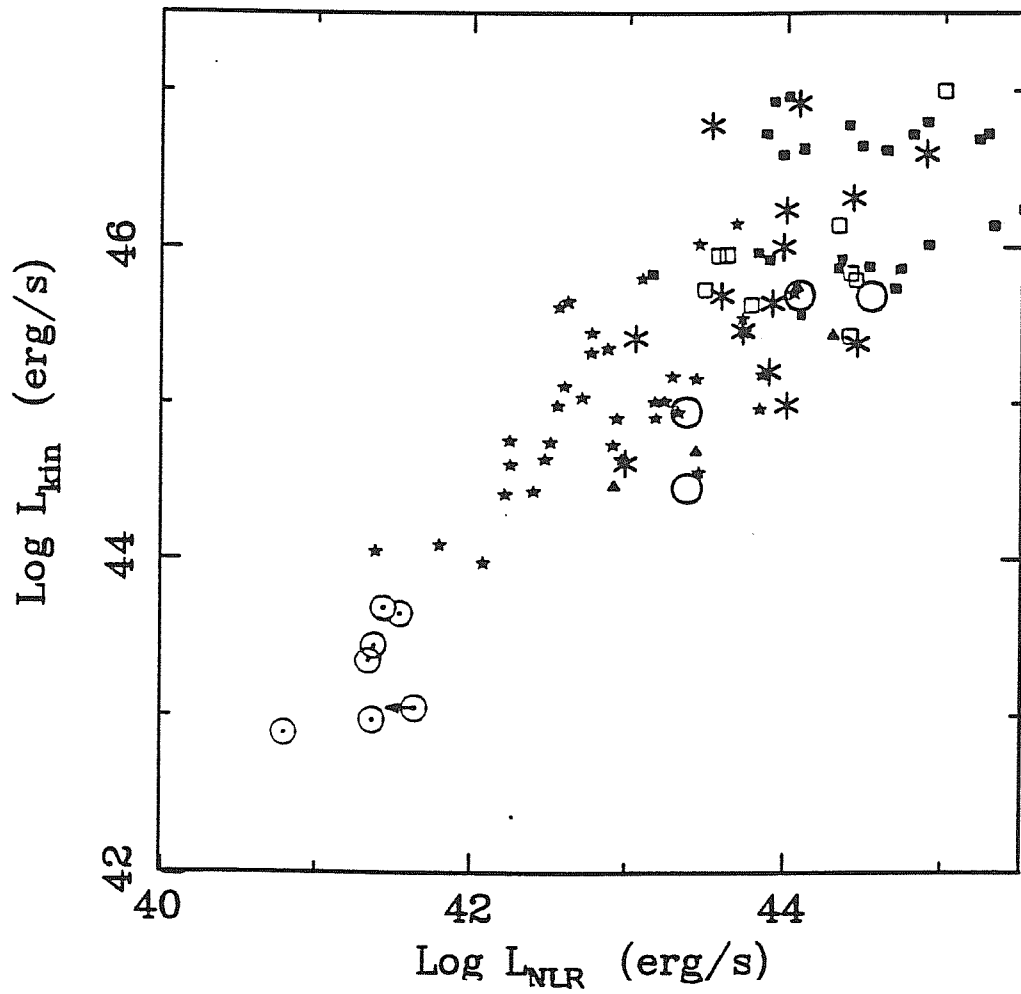


Fig. 5.11. Histogram of the logarithm of the ratio  $n'_{SSC}/n'_{e\pm}$ .



**Figs. 5.12a,b.** (a) Histogram of the logarithm of the ratio  $L_{\text{kin}}/L_{\text{rad}}$ . The solid line is for sources with a Doppler factor  $\delta > 1$ , while the dashed line refers to sources with  $\delta < 1$ . (b) The solid line refers to BL Lacs and the dashed one is relative to core-dominated quasars.



**Fig. 5.13.** The diagram of Rawlings and Saunders (1991), showing the kinetic power on large scale vs the narrow line luminosity, with superimposed our data (large symbols), referring to the kinetic luminosity on pc-scale [as from eq. (2.20)]. Open circles (with dot): FR I; stars: FR II at  $z < 0.5$ ; open triangles: broad-line radio galaxies; squares: radio galaxies at  $z > 0.5$ ; filled squares: quasars. Our big circles refer to sources with  $\delta < 1$ , the asterisks to all the rest of our sample.

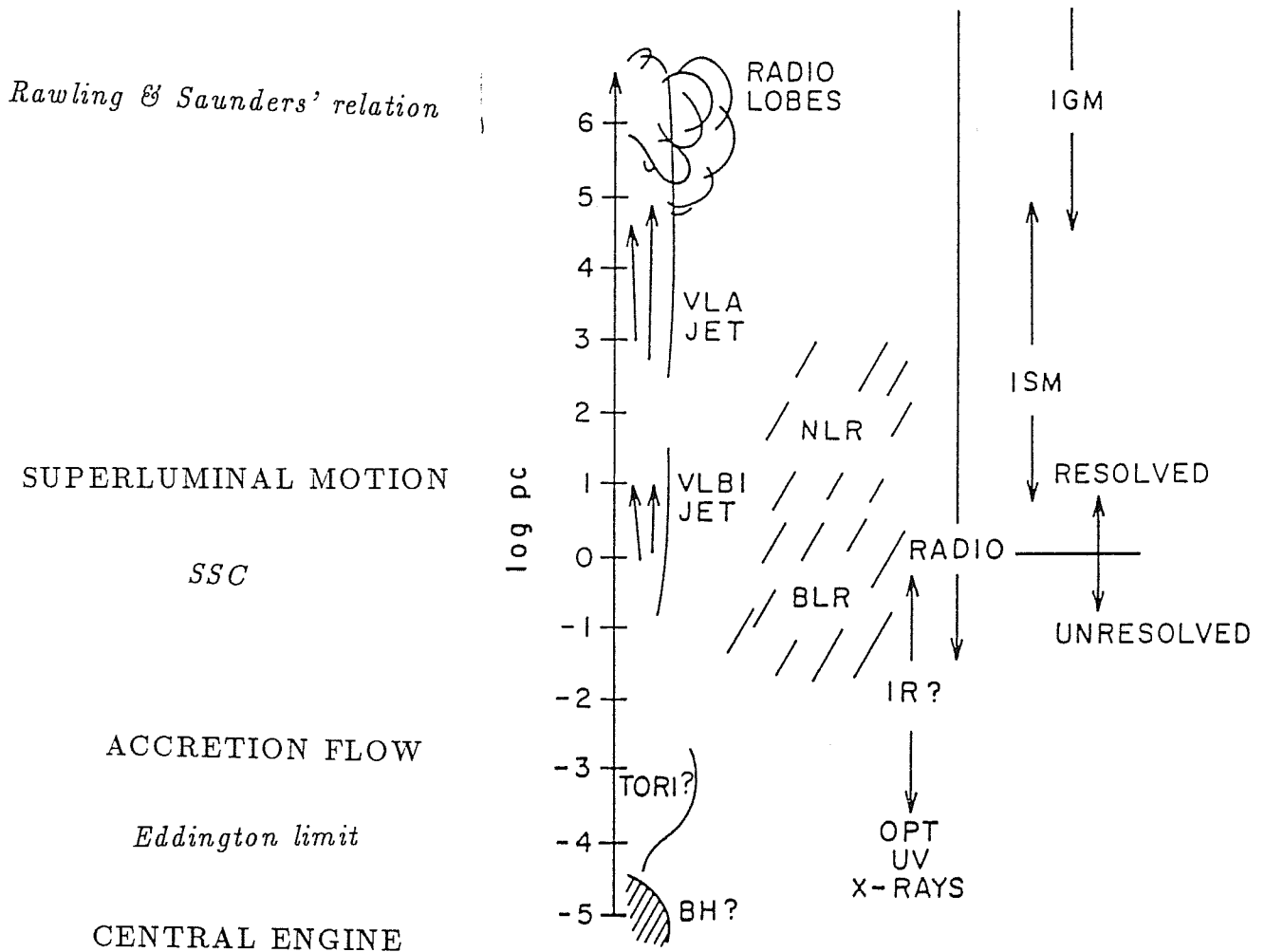


**Fig. 5.14.** Scales of the major features in AGN (Begelman 1989). In particular the regions and constraints we adopt to determine the matter content are indicated: the Eddington accretion rate and the  $e^{\pm}$  pair annihilation limits on the 'central engine' scales, the SSC particle density, the kinetic and radiative luminosities on pc scale and the kinetic power on kpc-Mpc scales.



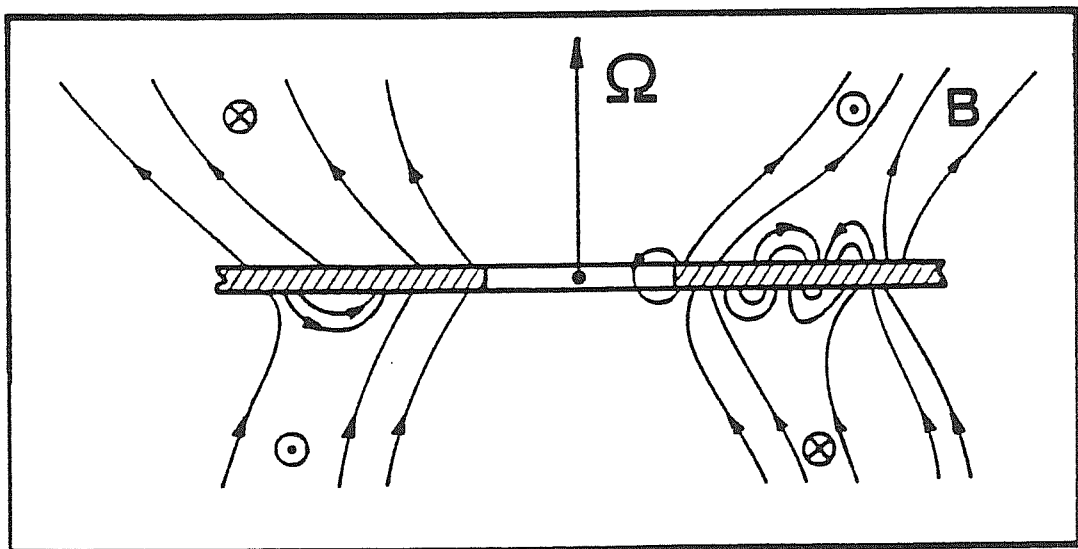


**Fig. 5.15.** Schematic illustration of the field geometry in the inner region of AGN, according to models for the magnetic confinement and acceleration of jets. The structure of the 'loop' lines anchored onto the accretion disc can be also responsible for the confinement of the cold clouds. Finally, reconnection of field lines has been proposed to be responsible for particle acceleration and 'flares' in the high energy emission. From Blandford (1990).

## Chapter 6. Unified model for BL Lac Objects

The statistical consequences of the beaming hypothesis for BL Lac objects are considered. In particular we use spectral and number density information to support the idea that FR I radio galaxies, X-ray and radio-selected BL Lacs are the same phenomena observed at a decreasing angle to the jet axis.

### 6.1 UNIFICATION MODELS

Unification schemes are an attempt to understand the ‘essence’ of AGN, by trying to separate the basic physical phenomena from orientational effects. On the other hand they are compelling: if anisotropic emission occurs in a class of sources there should exist other sources (‘parent population’) intrinsically identical but observed at different orientation and consequently showing different properties.

The current unification models (*e.g.* Lawrence 1987; Urry, Maraschi & Phinney 1990; Lawrence 1992), invoke two basic causes for anisotropy: obscuration and relativistic beaming. Obscuration is due to the presence of a geometrically and optically thick torus (or a warped disk) between the BLR and the NLR. Part of the optical and broad line emission in misaligned sources would be scattered along the line of sight and X-rays would be absorbed (*e.g.* Lawrence & Elvis 1982; Antonucci & Miller 1985; Krolik & Begelman 1988; Phinney 1989). This phenomenon is thought to be responsible for the different appearance of type 1 (strong continuum and broad line emission) and type 2 (weak continuum and only narrow lines) radio-quiet sources (Seyfert 1/Seyfert 2 galaxies). However differences in radio, far IR, narrow line and hard X-ray emission seem to suggest a further dependence on luminosity (Lawrence 1992; Tadhunter 1992).

For the unification of radio-loud objects and blazars also relativistic beaming is invoked. Statistical limits can be also imposed on the number of expected superluminal sources in a randomly selected sample (*e.g.* Cawthorne 1991).

Various unification schemes have been discussed in the literature, identifying a beamed and the related parent population: radio-loud and radio-quiet quasars (Scheuer

& Readhead 1979), flat and steep spectrum radio sources (Orr & Browne 1982). Some difficulties seem to arise with these models (*e.g.* Alexander 1992) but it should be stressed that the identification of the parent population is strongly affected by the intrinsic dispersion of physical quantities, selection effects and evolution. More recently Barthel (1989) suggested that powerful radio galaxies (FR II type) are the parent population of steep spectrum quasars (observed typically at angles smaller than  $45^\circ$ ) and flat-spectrum quasars (for angles of view less than  $\sim 14^\circ$ , Padovani & Urry 1992). FR II present narrow lines and weaker radio core and jets, requiring an obscuring torus as well as beaming effects.

### 6.1.1 FR I radio galaxies and BL Lacs

At lower power FR I radio galaxies have been suggested as the ‘parent population’ of BL Lac objects (Wardle, Moore & Angel 1984; Browne 1989; Woltjer 1989; Ulrich 1989).

Circumstantial evidence for this unification model includes the power and morphology of the extended radio emission (supposedly unbeamed) of BL Lacs (Antonucci & Ulvestad 1985; Perlman & Stocke 1992), the properties of their host galaxies (Ulrich 1989; but see Abraham, McHardy & Crawford 1991), the line emission, the estimate of the incident continuum in highly ionized filaments in the FR I radio galaxy Cen A (Morganti *et al.* 1992), the orientation of the line of sight with respect to the beaming direction predicted by the beaming indicators (as discussed in §5.3), the comparison of the luminosity functions (LF) of the parent and beamed populations (see below). Recent observations however show that few radio-selected BL Lacs (Kollgaard *et al.* 1992) have an extended radio emission of FR type II. It is possible that these highly luminous sources are intrinsically line objects, whose line emission is swamped by a highly enhanced continuum.

Recently, two complete samples of BL Lacs have become available, one selected on the basis of the radio flux, the other on the basis of the X-ray flux. These samples showed conclusively that the broad band energy distributions of the two groups differ systematically, the X-ray-selected objects having considerably smaller radio and optical luminosities relative to their X-ray luminosity (§1.1.2.b). Notably, the radio-selected objects have X-ray luminosities comparable to the X-ray-selected ones. The two classes of sources can be distinguished on the basis of the radio–X-ray spectral index  $\alpha_{rx}$  (Figs. 6.1, 1.3). In the following we will call them radio type (RBL) and X-ray (XBL) type BL Lacs, *independently* of the selection band.

X-ray selection of BL Lac objects should be unbiased with respect to the radio properties. The fact that it yet produces only (or mostly) radio weak objects indicates that radio weak X-ray-selected objects represent the majority of the population. Furthermore

Impey & Tapia (1990) suggest that the optical emission is beamed (but less than the radio one), on the basis of the correlation between the core dominance parameter  $R_{CD}$  and the optical polarization. Finally recent observations seem to indicate a lower value of  $R_{CD}$  for XBL type sources (Perlman & Stocke 1992).

These results may be considered to imply the existence of two different classes of BL Lac objects, with different bulk Lorentz factors. However it was proposed early on (based on the then available information on the different properties of X-ray-selected and radio-selected BL Lac objects) that *the relative numbers and the different energy distributions of XBL and RBL could be understood at the same time*, if in the same object the X-ray emission was more isotropic than the radio emission (Maraschi *et al.* 1986). Observers at large and small angles would see similar X-ray fluxes but only observers at small angles would see a strong relativistically enhanced radio flux. Consequently the ratio of the radio to the X-ray flux (measured by  $\alpha_{rx}$ ), would change according to the viewing angle  $\Theta$ : RBL are the ones observed with small viewing angles, while XBL correspond to sources observed at large angles. In particular Ghisellini & Maraschi (1989) discussed a model in which the flow velocity of the relativistic plasma in the jet (described in §4.1.2) increases (accelerates) with radial distance, so that relativistic beaming is mild in the X-ray emitting region of the jet but strong in the radio emitting region. In this model the angular distribution of the observed radiation is related to the value of the bulk Lorentz factor. In order to explain the observed energy distributions a smooth acceleration of the plasma in the jet was required from  $\Gamma \sim 1$  in the inner (X-ray emitting) region to  $\Gamma \sim 4 - 5$  in the outer (radio emitting) parts.

From the two BL Lac samples the respective luminosity functions have been computed (Stickel *et al.* 1991; Morris *et al.* 1991). Therefore it is now possible to use the absolute space densities to test and constrain beaming models. In a recent series of papers, Urry and Padovani tested the hypothesis that *all* BL Lacs are low luminosity radio galaxies (FR I galaxies) beamed at us. They considered separately and independently the X-ray and radio luminosity functions of the parent population (FR I) and derived the parameters of the beaming model by comparing the counts ( $\log N - \log S$ ) of BL Lac objects predicted from the X-ray or radio luminosity functions with the observed ones (Padovani & Urry 1990; Urry, Padovani & Stickel 1991). They found that the scheme is successful if the X-ray-selected objects have a bulk Lorentz factor  $\Gamma \simeq 3 - 4$  and the radio-selected ones have  $\langle \Gamma \rangle = 7.4$  with a power law distribution extending up to  $\Gamma = 40$ .

Padovani & Urry (1992) applied the same scheme for the unification (in the radio band) of flat radio spectrum, steep radio spectrum quasars, and FR II radio galaxies. A range of  $\Gamma$  was necessary to obtain a good fit, with  $\langle \Gamma \rangle \simeq 11$ .

The above model does not address the question of which physical acceleration mechanism could work on the appropriate scale, a factor  $10^2 - 10^3$  at least in distance from the core. Furthermore it may be difficult to account for large amplitude and rapid

luminosity variations observed in the X-ray band (§1.1.2.b) without invoking relativistic beaming. For these reasons we explore an alternative picture, in which the bulk velocity is constant but the collimation of the jet increases with distance, *i.e.* the solid angle subtended by the velocity vectors of the outflow decreases along the jet (Maraschi, Celotti & Ghisellini 1991). It is interesting to note that large scale radio jets indeed appear to become more collimated with increasing distance (Begelman 1992). We call this model the ‘wide jet’ model.

Here (Celotti *et al.* 1992) we show that the LF predicted by the wide jet model is consistent with the assumption that BL Lacs are FR I galaxies beamed at us in a similar way as discussed by Padovani and Urry for the accelerating jet model. In fact, from the ‘statistical’ point of view the two models are substantially equivalent. But in addition we focus on the *joint* constraints on the luminosity functions provided by the knowledge of the radio fluxes of the XBL and X-ray fluxes of RBL. In fact in our hypothesis statistical information about the relative number of XBL and RBL fixes the relative degree of anisotropy in the X-ray and radio bands, *i.e.* the collimation of the jet. Furthermore the spectral information (*i.e.* the different radio luminosity of XBL and RBL) constraints the relative Doppler amplification in the radio band, *i.e.* the bulk Lorentz factor.

We find that the suggested picture is consistent with the idea that we would observe a FR I radio galaxy, an XBL or a RBL, according with the (decreasing) angle of view, but with different relative behaviour in the X-ray and radio bands. The model seems to reflect the analogous unified scheme for FR II, steep spectrum and flat spectrum radio quasar.

## 6.2 THE LUMINOSITY FUNCTION OF ‘WIDE’ JET OBJECTS

Let us consider a collimated plasma flow with constant bulk Lorentz factor  $\Gamma$ , beamed luminosity  $L$  and intrinsic luminosity  $\mathcal{L}$ , as viewed by an observer comoving with the flow. The line of sight makes an angle  $\Theta$  with the jet axis. The radiation emitted by each element of the plasma is therefore beamed in a cone of half-angle corresponding to  $\sin \Theta_c = 1/\Gamma$ . If the velocity vectors of the streamlines of the flow are parallel, the angular dependence of the observed luminosity  $L(\Theta)$  is given by the usual relation  $L(\Theta) = \delta^n(\Theta)\mathcal{L}$  ( $n$  is assumed to be  $n = 3 + \alpha$ ).

The relativistic beaming affects the form of the luminosity function of the beamed objects. Urry & Shafer (1984) and Urry & Padovani (1991) develop the formalism to infer the luminosity function of the beamed objects as a function of the parent population luminosity function and the Doppler factor (assumed constant for all the objects), for a random orientation of the jets in the sky. The relative number of the parents and beamed objects is a function of luminosity. Indeed it is possible that in some fixed luminosity interval beamed objects are more numerous than the parent population, because they

derive from parents of lower luminosity (which are therefore more numerous). In fact because at each intrinsic luminosity  $\mathcal{L}$  corresponds a range of values of beamed luminosity  $L$ , angularly distributed like  $\delta(\Theta)$ , the luminosity function can not be obtained simply by multiplying the luminosities of the parent LF by  $\delta^n$ .

If the LF of the parent population is a power-law  $\Phi_u(\mathcal{L}) = \Phi_0 \mathcal{L}^{-B}$ , between  $\mathcal{L}_{min}$  and  $\mathcal{L}_{max}$ , the beamed one,  $\Phi(L)$ , is a broken power-law, with the same slope  $B$  above  $L = \delta^n \mathcal{L}_{min}$  and flatter, with slope  $(1+1/n)$  below this value. In fact at each  $\mathcal{L}$  corresponds a range of values of  $L$ , with probability  $P(L, \mathcal{L})dL = P(\delta)d\delta = d(\cos \theta)$ . Substituting  $d \cos \theta / d\delta = \delta^{-2}(\Gamma^2 - 1)^{-1/2}$  and  $d\delta/dL \propto L^{(1/n-1)}/\mathcal{L}^{1/n}$ , then  $P(L, \mathcal{L}) \propto L^{(-1-1/n)}$ .

The flat part of the beamed luminosity function, which depends on the spectral index, can generate a  $\log N - \log S$  flatter than the euclidean value 1.5, without involving evolution (Cavaliere, Giallongo & Vagnetti 1986).

If the flow velocities are spread in a cone of half-angle  $\Theta_j$  larger than  $\Theta_c$  (wide jet), the effects of relativistic beaming is diluted. We now derive expressions for the observed flux at different angles (§6.2.1), and we compute the predicted LF (§6.2.2.), comparing it with the case of parallel velocity flow (Urry & Shafer 1984) in some limiting cases. In §6.2.3 the model is applied to the unification scheme of FR I, XBL and RBL and in §6.3 the observational constraints on the model parameters are presented. The results are discussed in §6.4.

### 6.2.1 The luminosity enhancement

Consider a relativistic flow with fixed bulk Lorentz factor  $\Gamma$  but with velocity directions uniformly spread in a cone of semiaperture  $\Theta_j$ , larger than the critical semiaperture angle for relativistic beaming  $\Theta_c$ .

In this case the relation between the intrinsic and the observed luminosity at an angle  $\Theta$  with the jet axis is

$$L(\Theta) = \mathcal{L} R(\Theta) \equiv \frac{\mathcal{L}}{\Delta \Omega_j} \int_0^{\Theta_j} \sin \theta d\theta \int_0^{2\pi} \delta^n(\Theta, \theta, \phi) d\phi \quad (6.1)$$

with

$$\delta(\Theta, \theta, \phi) = \frac{1}{\Gamma [1 - \beta_b (\sin \Theta \sin \theta \cos \phi + \cos \Theta \cos \theta)]} \quad (6.2)$$

where  $R(\Theta)$  is the enhancement factor due to beaming, defined by eq. (6.1), and the beaming factor  $\delta(\Theta, \theta, \phi)$  is a function of the polar coordinates  $\theta$  and  $\phi$  within the cone of half angle  $\Theta_j$ :  $\phi$  is the azimuthal coordinate and  $\theta$  is measured from the jet axis (Fig. 6.2).  $R(\Theta)$  involves the integration of the contribution from each part of the jet flow: the integrand therefore depends on the angle, call it  $\chi$ , between the line of sight

and the velocity direction of each volume of the jet, the position of which is identified by the two angular coordinates  $\theta$  and  $\phi$ . The combination of sinusoidal functions multiplying  $\beta_b$  in eq. (6.2) is just the cosine of  $\chi$ . The solid angle subtended by the wide jet is  $\Delta\Omega_j = 2\pi(1 - \cos\Theta_j)$ .

For  $\Theta = 0$ , the integral in eq. (6.1) simplifies and the result is

$$L(0) = \mathcal{L} \frac{2\pi}{\Delta\Omega_j} \frac{(1 + \beta_b)^{n-1}}{\beta_b(n-1)} \Gamma^{n-2} [1 - [\Gamma^2(1 + \beta_b)(1 - \beta_b \cos\Theta_j)]^{1-n}] \quad (6.3)$$

In general, eq. (6.1) has to be calculated numerically, but for integer values of  $n$  there exist analytical solutions, which are derived in Appendix B.

Let us now derive  $R(\Theta)$  in some simple limits with approximate but intuitive arguments.

At first we estimate the observed luminosity at  $\Theta < \Theta_j$ . The behaviour of  $R(\Theta)$  can be understood considering that, for  $\Theta < \Theta_j$ , the radiation reaching the observer is mainly produced by plasma in a little cone of angle  $\Theta_c$  around the line of sight and there is always a little cone pointing at the observer. Therefore we expect  $L(\Theta)$  to be almost constant with a value approaching  $L(0)$  (Fig. 6.3, see below).

Furthermore the number  $N$  of small cones of half angle  $\Theta_c$  within the  $\Theta_j$  cone is simply the ratio of the subtended solid angles:  $N = (1 - \cos\Theta_j)/(1 - \cos\Theta_c) = (1 + \beta_b)(1 - \cos\Theta_j)\Gamma^2$ . Therefore

$$L(\Theta) \simeq \frac{\mathcal{L}}{N} \delta^n(0) \sim \frac{2\pi}{\Delta\Omega_j} \mathcal{L} (1 + \beta_b)^{n-1} \Gamma^{n-2}; \quad \Theta < \Theta_j \quad (6.4)$$

$\mathcal{L}/N$  being the rest frame luminosity fraction emitted by particles with velocity direction within  $\Theta_c$ ,  $\delta^n(0)$  being the enhancement of the flux observed at zero angle with respect to the small cone. Eq. (6.4) differs from the value given by eq. (6.3) by the factor  $(n-1)$ , in the limit of large  $\Gamma$ .

Comparing with the value obtained in the case of parallel velocities, for which  $L(0) = \mathcal{L}\delta^n(0) \sim (2\Gamma)^n \mathcal{L}$ , for  $\Gamma \gg 1$ , we see that the maximum observed luminosity from a wide angle jet is smaller than that because only the fraction  $(1/N) \sim 1/2[\Gamma^2(1 - \cos\Theta_j)]$  of the jet is beamed exactly towards the observer, and therefore  $L(0) \propto \Gamma^{n-2}$ .

By the same approximate arguments, we can derive the observed luminosity at  $\Theta > \Theta_j$ . In this case the plasma contributing the most is in the ‘ $1/\Gamma$ ’ little cone at an angle between  $\Theta - \Theta_j$  and  $\Theta - \Theta_j - 1/\Gamma$ , on the border of the jet. Taking  $\Theta - \Theta_j$  as the relevant angle we have

$$L(\Theta) \sim \frac{\mathcal{L}}{N} \delta^n(\Theta - \Theta_j) = \frac{2\pi}{\Delta\Omega_j} \mathcal{L} \frac{1}{(1 + \beta_b)\Gamma^{n+2}[1 - \beta_b \cos(\Theta - \Theta_j)]^n}; \quad \Theta > \Theta_j \quad (6.5)$$

The minimum luminosity corresponds to  $\Theta = \pi/2$ . At this value of  $\Theta$  eq. (6.5) has to be compared with  $L(\pi/2) = \mathcal{L}/\Gamma^n$  obtained in the case of parallel velocities. Depending on  $\Theta_j$  and  $\Gamma$ , eq. (6.5) can yield smaller or greater values than those obtained for parallel velocities.

In the previous calculations we have assumed that *all* the radiation is beamed. More generally, the observed luminosity  $L(\Theta)$  can be the sum of two components: an unbeamed part,  $\mathcal{L}$ , due to stationary plasma, and a beamed one,  $L_b(\Theta)$ . Suppose further that the rest frame luminosity of the moving plasma is a fraction  $f$  of the unbeamed luminosity (Urry and Shafer 1984). In this case  $L(\Theta) = \mathcal{L} + L_b(\Theta) = \mathcal{L} + f\mathcal{L}R(\Theta) = \mathcal{L}[1 + fR(\Theta)]$ . Assuming also that  $f$  is independent of  $\mathcal{L}$  and constant for all sources, we can define

$$\bar{R}(\Theta) = 1 + fR(\Theta) \quad (6.6)$$

Therefore the enhancement factor  $\bar{R}(\Theta)$  represents the ratio of the total observed luminosity to the unbeamed luminosity.

Fig. 6.3 shows the enhancement factor  $\bar{R}(\Theta)$ , which is a monotonic (decreasing) function of  $\Theta$ , for a fixed value of  $\Gamma = 10$ ,  $f = 1$  and  $n = 3$  and for different values of  $\Theta_j$ . For comparison, we also plot the amplification factor for the case of parallel velocities,  $\delta^3(\Theta)$ , for the same  $\Gamma$ . The spread of the velocity vectors produces a smooth ‘step’ function: at all angles inside  $\Theta_j$  the amplification is dominated by the contribution of the small cone along the line of sight. This relative contribution, which is inversely proportional to the number of such cones, decreases with increasing the jet angle. It appears that the wide angle cone profile can be ‘similar’ adopting a lower  $\Gamma$  in the parallel velocity scheme.

### 6.2.2 The luminosity function

Given the relation between the intrinsic and observed luminosity for a single source [eqs. (6.1) and (6.6)], we can compute the luminosity function (LF) for the population of ‘beamed’ objects  $\Phi(L)$ , from the luminosity function of the parent population,  $\Phi_u(\mathcal{L})$ . This procedure was first developed by Urry and Shafer (1984). In this scheme the beamed objects are distinguished from the parent objects by the value of  $\bar{R}$ , and an object is defined as *beamed* if  $\bar{R} \geq 2$ , *i.e.* if the object is observed at an angle such that  $L_b(\Theta) \geq \mathcal{L}$ .



For a random distribution of jet directions in the sky, the probability  $P(L, \mathcal{L})$  of observing a source with a given  $L(\Theta)$  is distributed as the solid angle corresponding to that  $\Theta$ , which for double sided jets is

$$P(L, \mathcal{L})dL = \frac{P(\Theta)}{2\pi}d\Theta = \sin \Theta d\Theta \quad (6.7)$$

If the intrinsic luminosities have a distribution  $\Phi_u(\mathcal{L})$ , between  $\mathcal{L}_{min}$  and  $\mathcal{L}_{max}$ , the observed luminosity function is

$$\Phi(L) = \int_{\mathcal{L}_{min}}^{\mathcal{L}_{max}} \Phi_u(\mathcal{L})P(L, \mathcal{L})d\mathcal{L} \quad (6.8)$$

Changing variable, from  $\mathcal{L}$  to  $\Theta$ , and noting that

$$d\mathcal{L} = -\frac{L}{\bar{R}^2(\Theta)} \frac{d\bar{R}(\Theta)}{d\Theta} d\Theta \quad (6.9)$$

we obtain

$$\Phi(L) = - \int_{\Theta_1}^{\Theta_2} \Phi_u \left( \frac{L}{\bar{R}(\Theta)} \right) \frac{\sin \Theta}{\bar{R}(\Theta)} d\Theta \quad (6.10)$$

where  $\Theta_1, \Theta_2$  are the limiting angles for which there are objects, with intrinsic luminosity  $\mathcal{L}_{min} < \mathcal{L} < \mathcal{L}_{max}$ , which have an observed luminosity  $L$ .  $\Theta_1$  and  $\Theta_2$ , which must range between 0 and  $\pi/2$ , can be found by solving the equations

$$\begin{aligned} L - \mathcal{L}_{max} \bar{R}(\bar{\Theta}_2) &= 0 & \Theta_2 &= \min(\bar{\Theta}_2, \pi/2) \\ L - \mathcal{L}_{min} \bar{R}(\bar{\Theta}_1) &= 0 & \Theta_1 &= \max(\bar{\Theta}_1, 0) \end{aligned} \quad (6.11)$$

Note that eq. (6.10) is very general, and can be used in all cases in which the emitted luminosity is anisotropic. For instance, it can be used in the case of thin disks, where  $L(\Theta) = L(0) \cos \Theta$ , (also spiral galaxies are thin disks), or in the case of thick disks, where the presence of the funnel makes the emitted luminosity very anisotropic.

Due to the complexity of the function  $\bar{R}(\theta)$  we use some crude approximations to have some analytical insights in the behaviour of  $\Phi(L)$  [eq. (6.10)]. In fact, the approximate information about the behaviour of  $L(\Theta)$  derived in §6.2.1 can be used to qualitatively construct the observed luminosity function.

Consider a parent populations of objects with same luminosity  $\mathcal{L}$ . In Urry & Shafer's scheme, the probability to observe a luminosity  $L$  is  $P(L, \mathcal{L}) \propto L^{-(1+1/n)}$  in the entire allowed luminosity range. Here, instead, we must distinguish between viewing angles greater than the cone angle (corresponding to low observed luminosities), and viewing angles inside the jet angle (corresponding to high luminosities).

In the former case [ $L(\Theta > \Theta_j)$ ], we have, from eq. (6.5)

$$\frac{dL}{d(\Theta - \Theta_j)} = n\beta_b \Gamma \delta^{n+1} (\Theta - \Theta_j) \frac{\mathcal{L}}{N} \sin(\Theta - \Theta_j); \quad \Theta > \Theta_j \quad (6.12)$$

Then, using eqs. (6.5) and (6.7), we have

$$P(L, \mathcal{L}) = \frac{1}{n\Gamma\beta_b} \left( \frac{\mathcal{L}}{N} \right)^{1/n} L^{-(1+1/n)}; \quad \Theta > \Theta_j \quad (6.13)$$

Once substituting  $\mathcal{L}$  with  $\mathcal{L}/N$ , eq. (6.13) is the same as eq. (2) of Urry and Shafer, although it is applicable in a restricted luminosity range. Substituting eq. (6.13) into eq. (6.8) we can derive the observed luminosity function. If the parents have a power-law LF, the beamed LF will approximately be a power-law with a flatter slope, as in the case of Urry & Shafer, in the luminosity range  $L(\Theta > \Theta_j)$ .

For viewing angles  $\Theta < \Theta_j$ , the enhancement of the luminosity is almost constant, and approaches the value  $\bar{R}(0)$ . Therefore objects with luminosity  $L \sim \mathcal{L}\bar{R}(0)$  can be seen for almost all lines of sight inside the jet angle. This corresponds to a probability to see objects of luminosity  $L \sim \mathcal{L}\bar{R}(0)$  greater than in the Urry & Shafer case. Therefore, in our model,  $P(L, \mathcal{L})$  is not a power law in the entire luminosity range, but shows an excess in the high luminosity end.

For  $\Theta < \Theta_j$  we can directly derive the approximate luminosity function by setting  $\bar{R}(\Theta) = \bar{R}(0) = \text{const}$  in eq. (6.10), and integrating in the range  $[0, \Theta_j]$

$$\Phi(L) \sim \Phi_u(\mathcal{L}) \frac{(1 - \cos \Theta_j)}{\bar{R}(0)}; \quad \Theta < \Theta_j \quad (6.14)$$

Since the limit in the viewing angles corresponds to a limit in observed luminosities, eq. (6.14) is valid for  $L > L_3 \equiv \mathcal{L}_{min}\bar{R}(0)$ . As in the Urry & Shafer case, the LF of the beamed objects has the same slope of the parent in the high luminosity end.

Consider the case of a power-law LF of the parents:  $\Phi_u(\mathcal{L}) = \Phi_0 \mathcal{L}^{-B}$ . The LF of the beamed objects will be a power-law with slope flatter than  $B$  for  $L \ll L_3$ , it will show an excess for  $L \lesssim L_3$ , and it will be a power-law of slope  $B$  above  $L_3$ .

It is interesting to evaluate the ratio between the parent and the beamed LF at  $L_3$ , in the case of a power-law. From eq. (6.14) we derive

$$\frac{\Phi(L_3)}{\Phi_u(L_3)} = (1 - \cos \Theta_j) \bar{R}(0)^{B-1} \quad (6.15)$$

This ratio can be used to put constraints on the choice of the parameters, once we identify a particular class of sources as the parent population of BL Lacs.

### 6.2.3 Spectra and number densities in the X-ray and radio bands

In this section we apply the above formalism to construct a unification model for FR I radio galaxies, XBL and RBL objects.

Very schematically suppose that the inner jet, producing the X-rays, has an opening angle ( $=\Theta_x$ ) much greater than the  $\Theta_c$ , and that  $\Theta_j$  decreases along the jet, possibly reaching  $\Theta_c$  in the outer, radio emitting, parts (*i.e.*,  $\Theta_r \sim \Theta_c$ ). For  $\Theta \lesssim \Theta_r$  both the X-ray and the radio luminosities are enhanced and these objects would be classified as beamed in both bands. All the RBLs should belong to this group. For  $\Theta_r \lesssim \Theta \lesssim \Theta_x$ , the X-ray luminosity is still enhanced and approximately constant, but the radio luminosity is less beamed: these objects would appear as beamed only if observed in X-rays. We identify these sources as the XBL. The angle  $\Theta_r$  would therefore distinguish between XBL and RBL and also determines the maximum luminosity amplifications for the XBL in the radio band. Finally, for  $\Theta_x \lesssim \Theta \lesssim 90^\circ$ , both the X-ray and the radio luminosity are dimmed by beaming, and (depending on  $f$ ) only the intrinsic (isotropic) luminosity can be observed. These could be FR I sources. For simplicity we refer to the angle  $\Theta_x$  to distinguish between FR I and beamed objects (XBL): this gives an easy estimate of the number density of objects, but we note that the angle  $\Theta_{max}$  for which  $\bar{R}(\Theta_{max}) = 2$  does not exactly coincide with  $\Theta_x$ .

In order to illustrate how the model works we show in Fig. 6.4 the radio to X-ray luminosity ratio as a function of the viewing angle: the shape of the curve is due to the different dependence of the radio and the X-ray luminosities on the viewing angle. At very large angles the unbeamed luminosity dominates ( $\bar{R}(\Theta) \simeq 1$ ) in both bands, then decreasing the viewing angle, at  $\Theta \sim \Theta_x$ , the X-ray emission increases more rapidly than the radio luminosity, which remains almost constant (and dominated by the unbeamed luminosity). When  $\Theta$  approaches  $\Theta_r$ ,  $L_x$  remains almost constant (the line of sight is within the large X-ray jet), but  $L_r$  increases until  $\Theta \sim 0^\circ$ .

This behaviour also explains the ‘L’ shape of the curve in Fig. 6.7, in the plane  $\log L_x$  vs  $\log L_r$ . A decreasing angle of view corresponds to move along the curve, starting from the bottom left toward the top right.

In Figs. 6.5 the predicted luminosity functions in the X-ray (Fig. 6.5a) and radio (Fig. 6.5b) bands are shown for both X-ray type (*i.e.* observed at angles  $\Theta_r < \Theta < \Theta_x$ ) and radio type ( $\Theta < \Theta_r$ ) BL Lacs. Their LF's have been computed assuming a simple X-ray and radio LF's of the parent population,  $\Phi_u \propto \mathcal{L}^{-2}$  (with arbitrary normalization),  $\Gamma = 10$ ,  $\Theta_x = 30^\circ$  and  $f_r = f_x = 0.1$ .

In the X-ray band, Fig. 6.5a, the LF's of XBL and RBL extend to the same maximum luminosity because the emission is dominated by the contribution of one small cone, with identical amplification inside the whole  $\Theta_x$ . A deficit of sources with respect to the parallel flow model is expected at luminosities just below the ‘break’ luminosity  $L_3$ , corresponding

to sources which in the parallel velocity scheme are observed between  $\Theta_r$  and  $\Theta_x$ . In our model these sources appear all with luminosity  $L_3$ , giving rise to a ‘excess’ in the LF, compared to the parallel flow model. Note that our definition of XBL includes only objects at  $\Theta < \Theta_x$ . Finally the wider solid angle in the X-ray band implies a larger number of XBL with respect to RBL.

A different behaviour is expected in the radio band (Fig. 6.5b). The luminosity of RBL objects is more amplified than the XBL and, as in the case of parallel velocity, a break in their LF is visible, below which sources not maximally beamed are visible. The X-ray objects are more numerous, but their radio amplification is low: therefore they dominate at low radio luminosities, while above the break in the LF of the RBL, radio-selected sources appear to be more numerous.

Consequently the model predicts that for a fixed luminosity XBL type sources are more numerous than RBL in the X-ray band, while the opposite is predicted at high radio luminosities.

### 6.3 OBSERVATIONAL CONSTRAINTS

We now examine the constraints imposed on the model by the properties of FR I, XBL and RBL. In particular we consider the LFs of radio-selected and X-ray-selected BL Lacs *both* in the radio and X-ray band.

#### 6.3.1 Luminosity functions of FR I radio galaxies and BL Lac objects

The differential LF of FR I radio galaxies in the X-ray (0.3–3.5 keV) and radio (5 GHz) bands have been computed by Urry & Padovani (1990) and Urry, Padovani & Stickel (1991).

In the X-ray band we adopt their analytical fit  $\Phi_x(\mathcal{L}_x) = 3.2 \times 10^{-36} \mathcal{L}_x^{-2.1} [\text{Gpc}^{-3} \mathcal{L}_x^{-1}]$  between  $\mathcal{L}_{min} = 2.6 \times 10^{40}$  and  $\mathcal{L}_{max} = 1.6 \times 10^{44} [\text{erg s}^{-1}]$ . In the radio band we consider the LF as derived from the 2 Jy sample (Wall & Peacock 1985),  $\Phi_r(\mathcal{L}_r) = 2 \times 10^{-26} \mathcal{L}_r^{-2.33} [\text{Gpc}^{-3} \mathcal{L}_r^{-1}]$ , between  $\mathcal{L}_{min} = 7.9 \times 10^{29}$  and  $\mathcal{L}_{max} = 6.3 \times 10^{33} [\text{erg s}^{-1}]$ . Due to the uncertainty in the low luminosity bins we assume as  $\mathcal{L}_{min}$  the lowest luminosity datum which is also consistent with the LF estimated by Franceschini *et al.* (1988) (see Urry, Padovani & Stickel 1991 for further discussion).

The X-ray and radio LF of BL Lacs have been estimated from the X-ray and radio-selected samples presented by Morris *et al.* (1991) and Stickel *et al.* (1991), respectively. We refer to their articles for a description of the sample selection criteria.

The X-ray sample contains 22 objects with known redshift and measured VLA (5 GHz) flux (we adopt  $\alpha_r = 0$ ). The radio sample include 34 sources, 25 of with measured  $z$  and 9 with a lower limit on it (inferred by the stellar appearance). We adopt this limit as a true value (adopting an average value of  $z = 0.56$  does not significantly modify the derived LF). 28 sources have X-ray flux (Padovani 1992) and from those we compute the X-ray LF.

Because of the clear distinction in the  $\alpha_{rx}$  spectral index of sources belonging to the two samples, we identify the X-ray and radio-selected BL Lacs with XBL and RBL type objects.

We consider the same evolution for the two groups and in order to minimize the number of assumptions we adopt the minimal evolution consistent with the confidence intervals of the evolution parameters, as determined by Stickel *et al.* (1991) and Morris *et al.* (1991). Thus we assume no-evolution in the radio band and a pure luminosity evolution of the form  $L(z) = L(0)(1+z)^{-1.5}$  in the X-ray band (the exponent is in the  $2\sigma$  confidence range).

The radio LF of XBL and the X-ray LF of RBL are calculated using the maximum distance at which an object could have been detected, as derived from the luminosity and flux limit in the band of selection, being the complete sample defined in that band.

The LFs estimated are shown in Figs. 6.6a,b, for the X-ray and radio band respectively. In both bands open circles refer to the Morris *et al.* (1991) sample of XBL, while filled circles indicate the Stickel *et al.* (1991) sample of RBL. Dash-dotted lines represent the LFs of the FR I radio galaxies. All the LFs indicate the local LF (de-evolved at  $z = 0$ ). The error bars are determined as Poissonian errors (as tabulated by Gehrels 1986). The LF are slightly dependent on the bin size in the band of selection, while are more sensible in the ‘other’ band.

### 6.3.2 Constraints on parameters

The comparison between the prediction of the model and the observed LFs is not straightforward. Our distinction in FR I, XBL and RBL type objects is based on the spectral index  $\alpha_{rx}$  as a consequence of the difference in the angle of observation (Fig. 6.4).

On the other hand, the selection criteria for the sample of XBL and RBL do not correspond to the model classification and the extension of the LFs are strongly dependent on the flux limits and the volumes explored in the surveys. Due to the lack of a clear and unique criteria to define the LF corresponding to the model predictions, we use the observed LF as a first attempt to constrain the model parameters.

It is worth to specify that the observed luminosities of BL Lacs are computed assuming isotropic emission. The ‘ $4\pi$ ’ factor is however already included in our definition of beamed

luminosity as given by eq. (6.1).  $\mathcal{L}$  represent in fact the isotropic luminosity of the parent population and  $L(\Theta)$  results  $4\pi$  times the luminosity emitted per unit solid angle along the direction  $\Theta$ .

Given the LFs of the parent population in the radio and X-ray bands the model parameters are: the beaming factor  $\Gamma$ , the opening angle  $\Theta_x$  and the ratio between  $\mathcal{L}$  and the beamed luminosity in both bands, *i.e.*  $f_x$  and  $f_r$ .  $\Theta_r$  is assumed to be  $\Theta_r = 2\Theta_c$  (*i.e.* the sum of the opening angle of the velocity vectors and the angle of beaming).

### 6.3.2.a Relative number of XBL and RBL

The relative number of XBL and RBL observed in X-ray and radio surveys is a crucial constraint for the model. The (unbiased) X-ray searches found almost only XBL type objects (or optically-selected sources), indicating that their number density at a given flux limit exceeds the number density of RBL.

As already discussed, according to our model the X-ray luminosity functions of XBL and RBL are substantially identical in their extension, and differ only for a normalization factor. Following the intuitive description of §6.2.2, in the X-ray band the emission is dominated by the narrow cone (with semiaperture angle  $\Theta_c$ ) pointing at us, no matter if it is inside or outside  $\Theta_r$ . The only difference between XBL and RBL is therefore the X-ray and radio solid angles, *i.e.* the total number of sources which can be observed.

Consequently, *in the X-ray band*, we can use the relative number of XBL over RBL, call it  $R_N$ , to constraint the model parameters.

$$R_N = \frac{1 - \cos(\Theta_x)}{1 - \cos(\Theta_r)} - 1 \quad (6.16)$$

This ratio has to be  $\sim 10$ , according to the X-ray LF functions for XBL and RBL (Fig. 6.6a). However it should be noted that a X-ray survey is expected to detect both XBL and RBL. Therefore the observed LF of the X-ray sample should be compared with the sum of the XBL and RBL luminosity functions.

On the other hand radio surveys revealed mainly RBL type sources, but this fact can be attributed to the higher enhancement factor inside  $\Theta_r$ , *i.e.* to the greater number density of RBL *at high* radio luminosities. Therefore in the radio band a strong dependence on luminosity should be taken into account to estimate the relative number of RBL and XBL from observations.

### 6.3.2.b Relative number of FR I and BL Lacs

As shown in §6.2.2, the ratio  $R_\Phi$  of the luminosity functions of the parent and the beamed populations, evaluated at the luminosity  $L_3$ , is given by [eq. (6.15)],

$$R_{\Phi_{r,x}} \sim [1 + f_{r,x}R(0)]^{B_{r,x}-1}(1 - \cos \Theta_{r,x}) \quad (6.17)$$

where the subscripts refer to the two spectral bands. The observational constraints impose  $R_{\Phi,x} = 20$  and  $R_{\Phi,r} = 2$ .

### 6.3.2.c Maximum luminosity of the beamed population

The ratio of the maximum luminosities of the parent and the beamed populations in the radio and X-ray bands could be another constraint on the parameters. From eq. (6.3) the maximum beamed luminosity is  $L_{max_{r,x}} = \mathcal{L}_{max_{r,x}}[1 + f_{r,x}R(0)]$ . In the limit of  $\Gamma \gg 1$  we have

$$\frac{L_{max_{r,x}}}{\mathcal{L}_{max_{r,x}}} \equiv R_{L_{r,x}} = 1 + \frac{f_{r,x}}{1 - \cos \Theta_{r,x}} \frac{2^{n_{r,x}-1}}{(n_{r,x} - 1)} \Gamma^{n_{r,x}-2} \quad (6.18)$$

However we retain that this constraint is not well defined. As already mentioned, it is expected that both the flux limit and the area covered by the surveys strongly affect this limits. Furthermore there are recent indications that high luminosity RBL can be associated with FR II radio galaxies (§6.1.1). If some high luminosity BL Lacs are actually HPQs the continuum of which is so beamed to swamp the lines, then the maximum luminosity of the ‘real’ BL Lacs is lower.

Interestingly a break appears in the radio LF of XBL objects around  $L_r \sim 10^{32}$  erg s<sup>-1</sup>. We stress that a sharp break is a characteristic feature expected in the LF of a population of beamed sources and it can be of relevance if confirmed with higher statistical significance. The luminosity of the break,  $L_{break} = \delta^n(0)\mathcal{L}_{min}$  is predicted to be given by

$$\frac{L_{break}}{\mathcal{L}_{min}} \equiv R_{L_r} = 1 + \frac{2f_r}{1 - \cos \Theta_r} \Gamma \quad (6.19)$$

and we impose this fourth condition on the parameters. It should be remembered however that a smoother break in the LF of radio sources (Dunlop & Peacock 1991) is an ‘ubiquitous’ feature.

## 6.4 RESULTS AND DISCUSSION

In Figs. 6.6a,b we show the differential LF in the X-ray and radio bands computed from the model, accordingly to the constraints described. Continuous lines refer to XBL, dashed

lines to RBL. We also report the observed LF: FR I radio galaxies are represented by the dash-dotted lines, while XBL are indicated by open circles and RBL by filled circles.

The main features of the LF of RBL and XBL predicted by our model and already discussed are clearly illustrated in the figures. In the X-ray band, the LF of RBL is a factor  $R_N$  below the LF of XBL, corresponding to the ratio of the solid angles of the X-ray and radio jets. They extend roughly to same maximum luminosity, given by the amplification of the maximum luminosity of the parent population in a X-ray small cone. In the radio band, instead, beyond the different normalization, the LF of RBL extends at greater luminosities, due to the stronger beaming enhancement in the radio cone. Note that the amplification is estimated from eq. (6.1) also in the radio band (for  $\Theta_r = 2\Theta_c$ ) and it is consequently smaller than the enhancement obtained in the case of parallel velocity flow.

On the basis of the results of §5.3 we assumed a bulk Lorentz factor  $\Gamma = 10$ . We found that it is not possible to satisfy all the conditions imposed, unless we allow the possibility that only a fraction of the FR I radio galaxies are active and give rise to the BL Lac phenomenon. In this case we find that it is possible to satisfy the above constraints for  $\Gamma = 10$ ,  $f_r = 0.2$ ,  $f_x = 0.5$  and  $\Theta_x = 41^\circ$  (in agreement with the typical angle of view found in §5.3), if only 1/10 of FR I radio galaxies are presently active. Vice versa if all the FR I are misaligned BL Lacs, the derived parameters are:  $\Gamma = 29$ ,  $\Theta_x = 13^\circ$ ,  $f_r = 0.006$  and  $f_x = 0.005$ . For consistency we verify that all the sources observed inside  $\Theta_r$  and  $\Theta_x$  are ‘beamed’ objects (*i.e.*  $\bar{R} > 2$ ).

We would like to mention some important uncertainties in the simple procedure we followed and other ‘complications’:

(i) The hypothesis that  $f$  is constant for all sources may be wrong, and some of the beamed object, instead of having a large  $\Gamma$ , may be characterized by a large  $f$ . Similarly this simple picture can be extended to include the possibility of a distribution rather than a single value of  $\Gamma$  (Urry & Padovani 1991). It is also possible that the beaming phenomenon is present only above some threshold luminosity of the parent sources.

(ii) We neglected the effects of evolution.

(iii) The LF of FR I, XBL and RBL sources are based on small samples. In particular the minimum luminosity of the parent LF (which is not well determined) is crucial, since it determines the normalization of the beamed LF, and the position of the break.

Another way to illustrate the predictions of our model is to compare the X-ray and radio luminosities of BL Lacs with those of FR I radio galaxies. In Fig. 6.7 we report the X-ray vs 5 GHz radio luminosity for the FR I galaxies in the 3C sample (Fabbiano *et al.* 1984) and for the samples of BL Lacs derived from the lists of Morris *et al.* (1991) and Stickel *et al.* (1991).



In Fig. 6.7 we also show the curves predicted by our scheme corresponding to indicative parameters ( $\Gamma = 10$ ,  $\Theta_x = 45^\circ$ ,  $f_r = f_x = 1$ ). According to the viewing angle, the ‘L’ curves connect FR I sources with XBL and RBL, as described in §6.2.3, and are suggestive of the unifying picture discussed here.

As already mentioned the basic requirement for both our and the model of Urry and Padovani is that the degree of beaming increases with decreasing frequency. However a significant different prediction is that in our picture the X-rays are also strongly affected by relativistic effects and consequently we would expect that even small variations of the intrinsic luminosity can result in rapid variations of the observed luminosity, unlikely the Urry and Padovani’s scheme.

As mentioned in the introduction the hypothesis that the increase of beaming with decreasing energy band is due to the change in the degree of collimation of the jet has the advantage not to require an acceleration mechanism operating over some order of magnitude in distance, as requested for an accelerating flow. A physical description of the re-collimation mechanism is above the aim of this work. The jet can be pressure-confined by external gas (but see §5.5), assuming a parabolic shape with a jet angle given by  $\tan \Theta_j = \epsilon(r/r_0)^{1-1/\epsilon}$  (§4.1). Alternatively an increasing collimation can be obtained because the plasma moving at large angles suffers more Compton drag than plasma at small angles and only the inner part of the jet can survive during the propagation. Or the geometry of the magnetic field could determine the collimation (Begelman 1992).

At last we stress that the LF shown in Figs. 6.6 and the parameters derived are just indicative of the predictions of the model, which at present cannot be further constrained. A larger and unbiased complete sample of BL Lacs observed in X-rays and radio bands, to find the relative density of XBL and RBL in both bands would obviously allow a deeper insight into the reality and relationship between the bimodal spectral distribution of BL Lacs.

The basic results of our description are:

- The possibility to include in the unification model for BL Lacs and FR I radio galaxies the existence of two populations of BL Lac objects. Our model accounts in a natural way for the fact that XBL result to be more abundant than RBL in X-ray surveys, while the opposite is found from radio searches and *at the same time* for the different spectral distributions.
- The presence of a break feature in the radio LF of XBL.
- The parallelism between FR II/CDQ/LDQ and FR I/XBL/RBL, as shown in Fig. 5.8. However there are some indications, mentioned in the introduction, which are suggestive of the fact that the two ‘groups’ could correspond to a sequence in increasing power responsible for the different radio morphology and line properties.

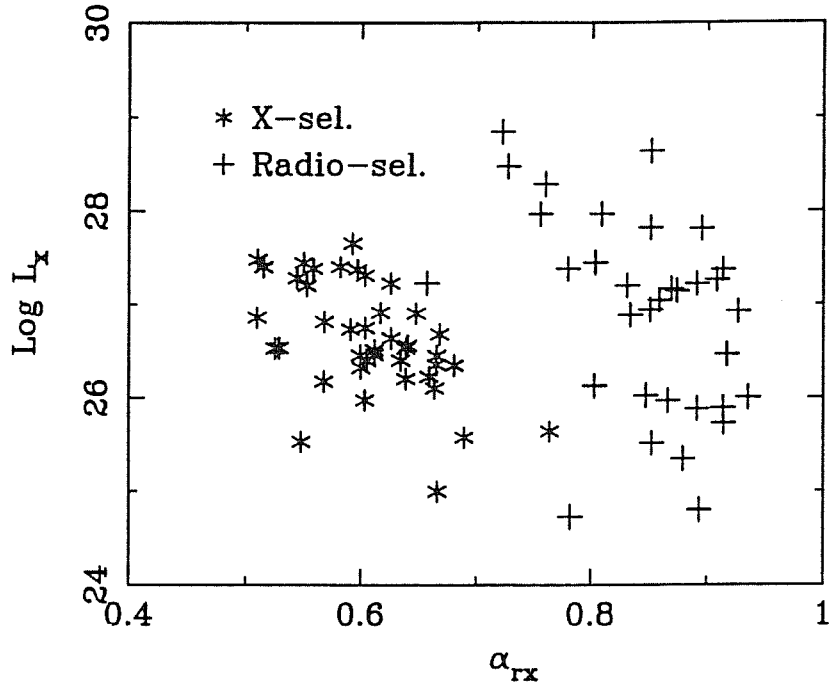


**Fig. 6.1** The X-ray luminosity vs the radio-X spectral index  $\alpha_{rx}$  (between 5 GHz and 2 keV) for X-ray selected (stars) and radio-selected (crosses) BL Lacs. The two classes show a bimodal spectral behaviour.

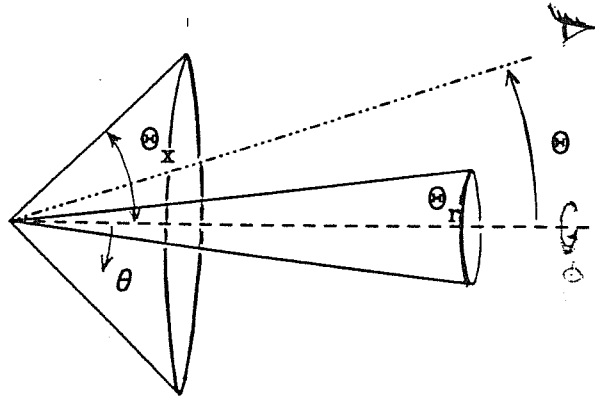


**Fig. 6.2** A schematic representation of the 'wide' jet.  $\Theta_j$  is the jet opening angle and  $\Theta$  the angle between the jet axis and the line of sight.  $\phi$  and  $\theta$  are the azimuthal and the polar coordinates (the latter measured from the jet axis), which identify the position of a portion of the fluid.

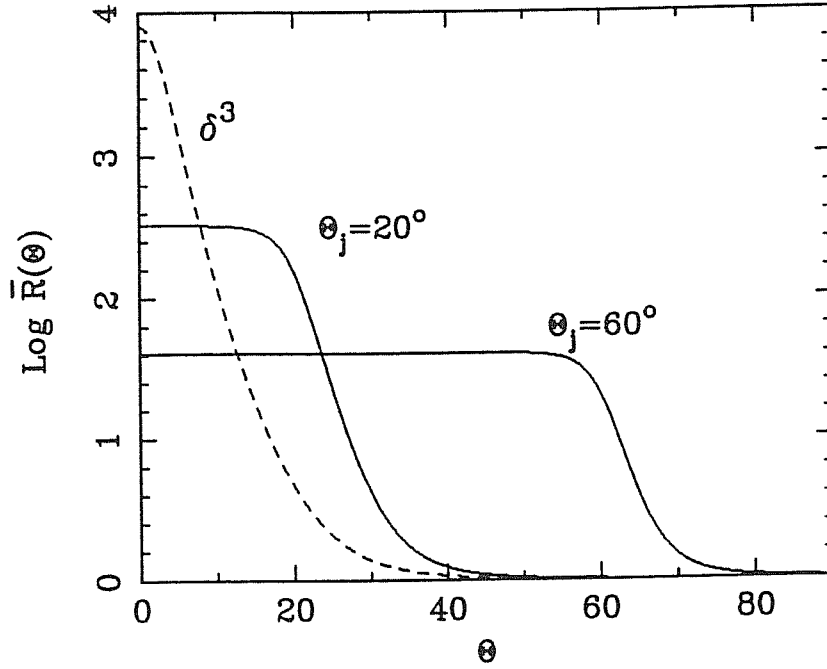


Fig. 6.3. Intensity distribution as a function of the angle between the line of sight and the jet axis, represented by the enhancement factor  $\bar{R}(\theta)$  of the 'wide' jet model. It is calculated for  $\Gamma = 10$ ,  $n = 3$ ,  $f = 1$  and values of the semiaperture angle of the jet  $\Theta_j = 20^\circ$  and  $60^\circ$ . The dashed line represents  $\delta^n$  for the same  $\Gamma$ .

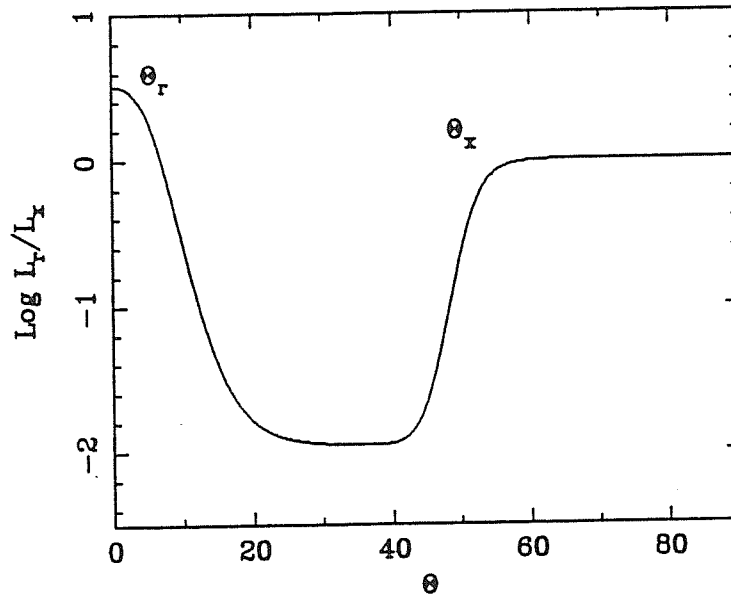
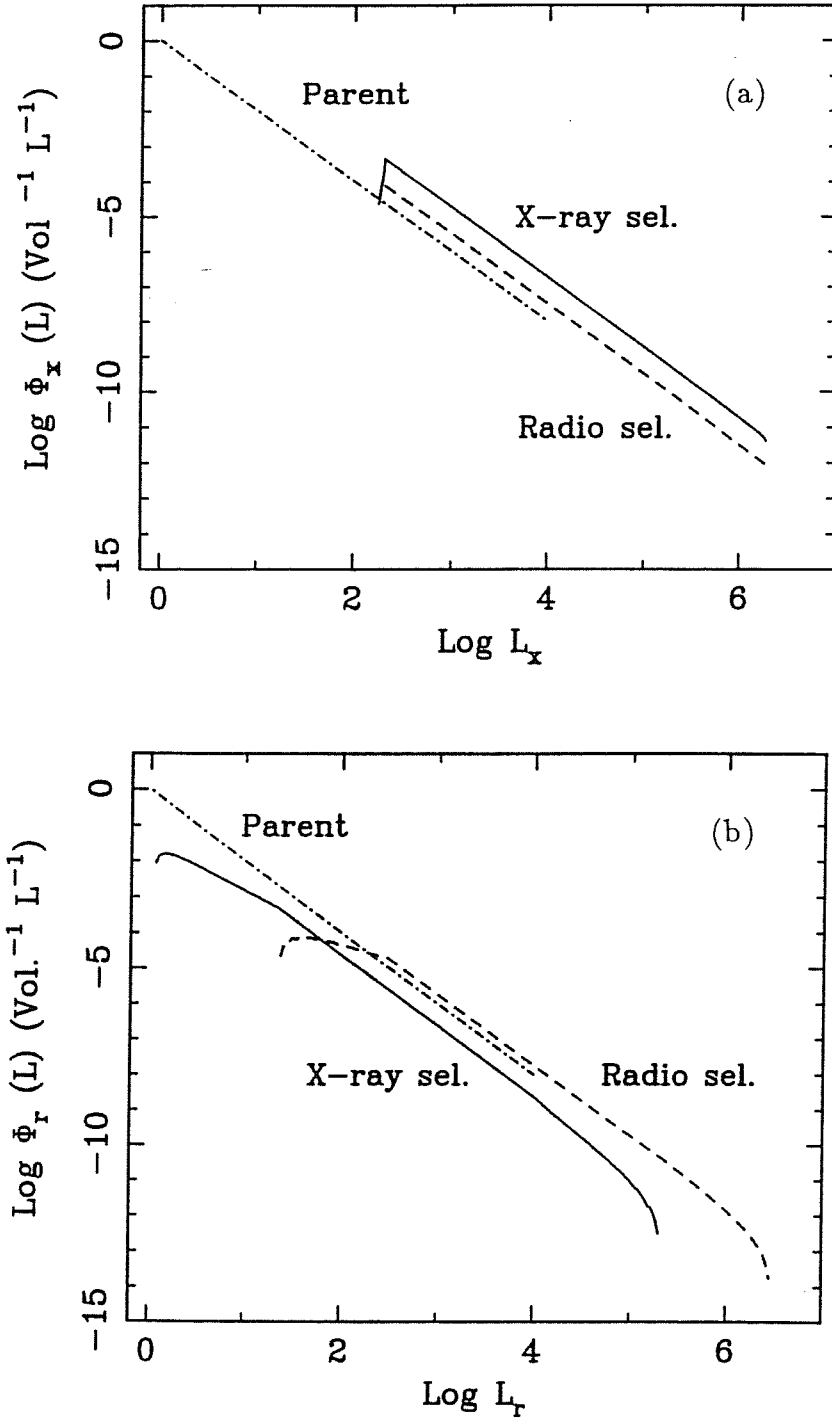
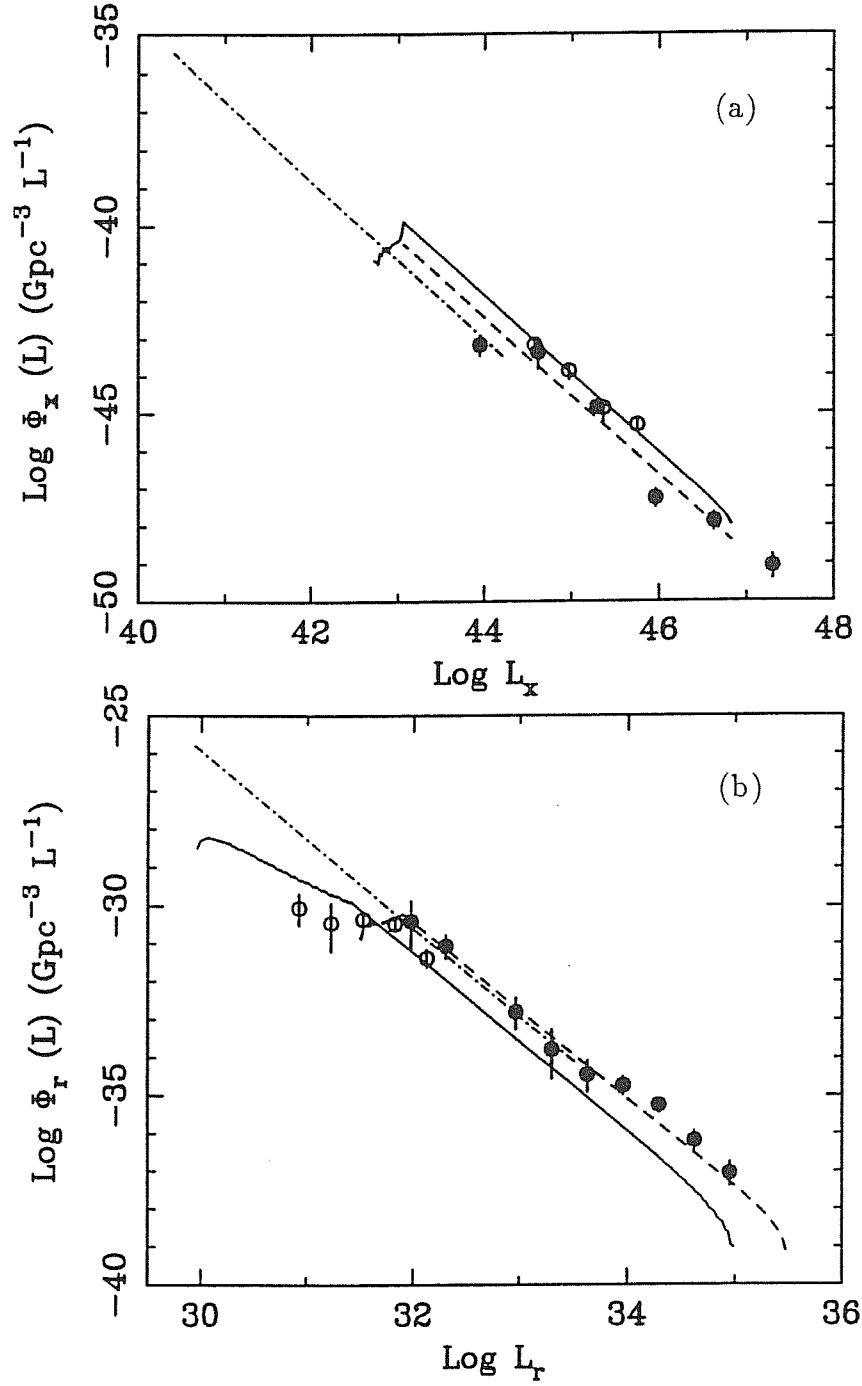


Fig. 6.4 The relative ratio of X-ray to radio luminosity as a function of the viewing angle  $\Theta$  according to the wide jet model. The adopted parameters are:  $\Gamma = 10$ ,  $f_x = f_r = 0.1$ ,  $\Theta_x = 45^\circ$ . The corresponding jet angles are also shown. At large angle we are observing out of the X-ray cone and therefore we can see the unbeamed luminosity. For smaller  $\Theta > \Theta_r$  we start to see a beamed X-ray luminosity and decreasing further the angle, also the radio luminosity is beamed, while the X-ray one remains almost constant.



Figs. 6.5a,b Luminosity functions in the X-ray (a) and radio (b) band for XBL and RBL as predicted by the model. The parent populations have been assumed to be of the form  $\Phi_u \mathcal{L} = \mathcal{L}^{-2}$  and the model parameters are  $\Gamma = 10$ ,  $\Theta_x = 30^\circ$ ,  $f_x = f_r = 0.1$ .



**Figs. 6.6a,b** (a) The differential X-ray luminosity function of BL Lacs calculated assuming FR I radio galaxies as parent population (the LF of which is shown as dot-dashed line), for  $\Gamma = 29$ ,  $\Theta_x = 13^\circ$ ,  $f_x \simeq f_r \simeq 5 \times 10^{-3}$ . The continuous and dashed lines represent the XBL and RBL luminosity functions derived from the model, respectively. The LFs of XBL [from the Morris *et al.* (1991) sample] and RBL [from the Stickel *et al.* (1991) sample] are represented as open and filled circles, respectively. They have been computed assuming a minimum evolution consistent with their data. (b) As Fig. 6.6a, in the radio band, where we assumed no evolution for both samples.

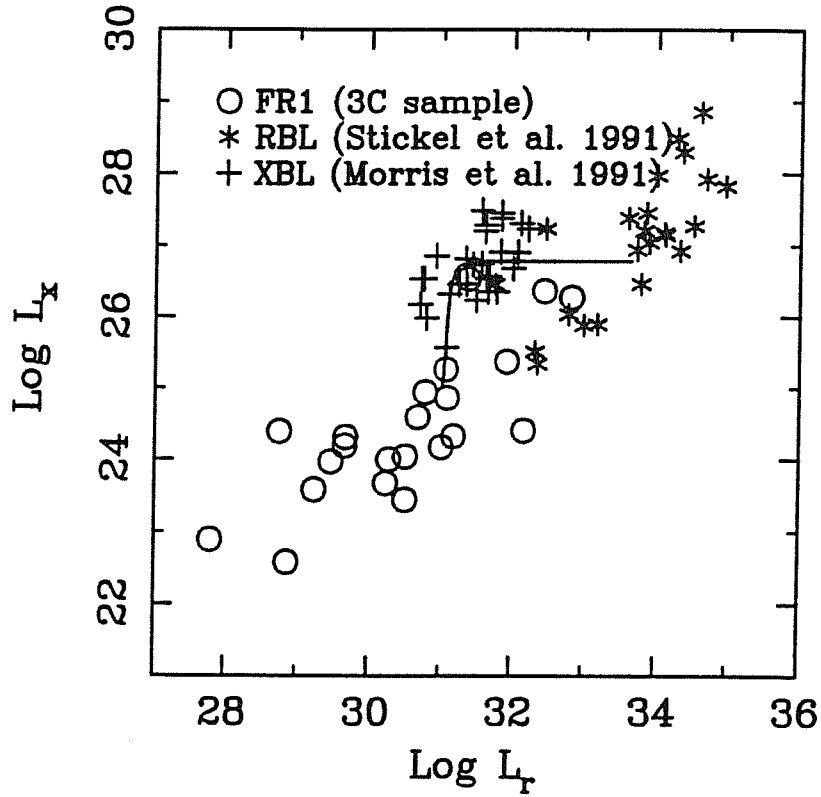


**Fig. 6.7** X-ray luminosity at 2 keV vs. the (core) radio luminosity at 5 GHz for FR I sources (circles), X-ray selected (crosses) and radio selected (stars) BL Lacs from the 3C sample, the Morris *et al.* (1991) and the Stickel *et al.* (1991) samples, respectively. The ‘L’ shaped curve corresponds to changing the line of sight direction according to the ‘wide’ jet model, as explained in §6.2.3. It is calculated using  $\Theta_x = 45^\circ$ ,  $\Gamma = 10$ ,  $p_r = p_x = 3$  and  $f_x = f_r = 1$ . Moving along the curve RBL, XBL and FR I sources are observed.

## Summary and future work

Magnetic fields are likely to play an important rôle in the physics of AGN. High energy emission from compact sources requires an efficient particle (re)acceleration mechanism, operating on very short timescales. One of the most plausible hypothesis is that electric fields are generated by variable magnetic fields, storing an energy density at least comparable with that of the radiation. Similarly, an equipartition magnetic field can be expected if the extraction of the spinning energy of a black hole is an efficient primary power production mechanism. On larger scales, magnetic fields are largely invoked to explain the collimation and acceleration of jets. It is tantalizing to imagine that magnetic configurations anchored in an accretion flow both give rise to the ordered large scale structures and reconnect on the disc surface generating flares of high energy emission.

We have therefore considered the implications of the presence of a strong magnetic field. In particular, we studied the properties of synchrotron and self-Compton emissions, which can be the dominant cooling mechanisms for relativistic electrons in the inner X-ray emitting region(s) and in relativistic jets. It appears that the emission from the inner regions in radio-quiet sources is completely reprocessed from surrounding material while in radio-loud objects the relativistically beamed radiation dominates the observed spectrum.

Here we schematically summarize the main results and outline possible directions for future work.

- Synchrotron and self-Compton emissions are a valid primary radiation processes in the compact emitting region of AGN. At least in radio-quiet sources, most of this primary emission is reprocessed and possibly equally redistributed through the different spectral bands.

In particular an equipartition magnetic field can confine at very high densities a fraction of the cold matter expected to be present. This matter can be in thermal equilibrium at a quasi-blackbody temperature of  $\sim 10^5$  K and in pressure equilibrium with the magnetic field. Furthermore, due to the radiation pressure it can be squeezed enough to become optically thin to Thomson scattering. It can cover, like a blanket, a large fraction of the SSC emitting region(s), with a small filling factor. In these conditions

the cold material can absorb through free-free interaction most of the primary radiation up to the optical-UV band, not affecting the X-ray emission.

A more detailed analysis of the thermal and dynamical evolution of the cold matter toward this equilibrium state, the detailed quasi-blackbody spectrum reemitted from the clouds and the possible effects of clouds interaction, possibly generating sudden and localized ‘burst’ of emission will be considered in future work.

The picture proposed can account both for simultaneous variability at optical and UV frequencies and the lack of spectral features and polarization expected from the (standard) accretion disc model. However, an accretion disc, possibly supporting the magnetic field and reflecting part of the X-ray radiation can also be present, even if its radiative contribution due to viscous dissipation could be small.

Simultaneous observations in the optical-UV and X-ray bands are a crucial test for the proposed picture, as well as accurate measurements of the intrinsic soft X-ray absorption, which can further constrain the clouds properties.

The primary radiation in compact source is most probably also affected by reprocessing due to pair production; models predict a break in the hard X-ray spectrum due to downscattering and a turnover in the  $\gamma$ -rays. Pair reprocessing in SSC models, taking into account the effect of a reacceleration mechanism, are under consideration, looking forward to future GRO results to test the model predictions.

- Relativistic effects dominate the emission from blazars. We have shown that the continuum spectra up to the  $\gamma$ -rays and the high energy variability can be explained in terms of SSC emission from an inhomogeneous relativistic jet model.

At a general level we have shown that a perturbation/shock wave moving along the jet produces an increase of the amplitude of variability and a decrease in the timescales with increasing frequencies and a larger amplitude of variability at smaller angles with the line of sight.

The variable  $\gamma$ -ray emission of 3C 279 implies that the high energy radiation is relativistically beamed, in order to avoid  $\gamma$ -ray absorption by photon-photon  $e^\pm$  pair production. A ‘mapping’ of the structure of the jet can be obtained from simultaneous variability studies, in particular at  $\gamma$ -ray energies, which sometimes dominate the luminosity output, and UV frequencies, where the most rapid variability is expected to be seen. A detailed comparison of simulated light curves with observations at different frequencies will provide a crucial test for the model. A month-long coordinated campaign for the multifrequency observation of 3C 279 from radio to  $\gamma$ -rays is already scheduled.

Possibly the model applies to the blazar class at large and is particularly relevant due to the increasing number of sources observed above 100 MeV. This emission can also provide a significant contribution to the diffuse  $\gamma$ -ray background.



- We then considered important physical parameters of pc-scale jets (*i.e.* Doppler factors, velocities, emitting particle density and magnetic field intensity) from the SSC theory.

The beaming picture is supported by the quantitative correlation, in a large sample of sources with VLBI data, among different indicators: Doppler factors, brightness temperatures, superluminal speeds, core-dominance parameters and the predictions of the unified models. Further important constraints can be obtained from high sensitivity maps to reveal counter-jets on pc-scale and measurements of expansion velocities in radio galaxies.

- Jets are probably composed of an electron-proton plasma and the emitting electron are steadily heated to a typical temperature of  $\sim 50$  MeV. This conclusion is basically suggested by two requirements. On one hand the number flux of SSC electrons should not exceed the number flux of particles which can be continuously supplied from the central source. Estimates of the proton flux can be obtained from the matter accretion rate onto the black hole, while limits on the  $e^\pm$  pair flux are set from the efficient annihilation during the outflow from the compact region. On the other hand the kinetic power in pc-scale jets should exceed both their radiative dissipation and the kinetic power on kpc-scale, if the bulk motion power is the major way of supplying energy to the extended radio structures.

- The jet power output is in fact dominated by the bulk kinetic energy, which intriguingly is comparable with the beamed luminosity, and a correlation between the (isotropic) narrow line luminosity and kinetic energy has been found. Interestingly, it is consistent with the analogous correlation found for jets on large scales.

A deeper insight into the central engine can be derived from the understanding of the relative amount of kinetic and radiative powers and in particular the presence of relativistic outflows in high redshift (radio-quiet) quasars can indicate that matter outflows are indeed the dominant power loss mechanism in AGN.

- Magnetic fields estimated on pc-scale are unimportant for the dynamics of the plasma flow, although they can still be dominant on the much smaller collimation and acceleration regions.

We are studying the radiative effects on the jet kinematic due to free-free opacity (particularly in SS433).

- Finally the statistical consequences of beaming have been considered for BL Lac objects. We have proposed a model which can account for the different spectral energy distributions and relative number densities of radio and X-ray-selected BL Lacs by assuming an increase in the collimation of the relativistic jet. We have used joint constraints

from the X-ray and radio luminosity functions of these sources and shown that the model can include RBL and XBL in the unification scheme of BL Lacs and FR I radio galaxies, in a sequence RBL/XBL/FR I which corresponds to the increasing angle between the line of sight and the jet axis. This is somewhat parallel to the ‘unification’ sequence for SSQ/FSQ/FR II. The parallelism and/or continuity between these two groups of sources has to be further investigated.

## Appendix A

In §4.1.3 simple analytic expressions for the total monochromatic luminosity are given, on the assumption of a homogeneous perturbed region and neglecting the shift in the range of frequencies between the perturbed and the stationary emission.

These approximations are critical mainly in the case *ii*), of a conical perturbed region with increasing thickness, because the frequency range can be quite different in different parts of the emitting volume. Here we give the correct expressions for the luminosities  $L^1$  and  $L^2$ , appearing in eqs. (4.9a), which are used in the numerical computation of the spectra and the light curves.

The volume elements for a parabolic slab (case *i*) and a conical (case *ii*) perturbed regions are given respectively by

$$dV_p = \pi R_0^3 x^{2\epsilon} dx \quad dV_c = \pi R_0^3 \left\{ [x - (x^* - \Delta x^*)] \frac{x^{*\epsilon}}{\Delta x^*} \right\}^2 dx \quad (A.1)$$

Let us consider three volumes: the volume of the perturbed region

$$V^*(t) = \int_{x^* - \Delta x^*}^{x^*} dV_i \quad (A.2)$$

where with  $dV_i$  we indicate the appropriate volume element given in eq. (A.1); the volume  $V(\nu)$  of the parabolic stationary jet emitting at the given frequency

$$V(\nu) = \int_{x_1(\nu)}^{x_2(\nu)} \pi R_0^3 x^{2\epsilon} dx \quad (A.3)$$

and finally the perturbed volume emitting at frequency  $\nu$

$$V^*(\nu, t) = \int_{x_1^{**}(\nu)}^{x_2^{**}(\nu)} dV_i \quad (A.4)$$

where

$$\begin{aligned} x_1^{**}(\nu, t) &= \max[x^* - \Delta x^*, x_1^*(\nu)] \\ x_2^{**}(\nu, t) &= \min[x^*, x_2^*(\nu)] \end{aligned} \quad (A.5)$$

and  $x_1, x_2$  and  $x_1^*, x_2^*$  are obtained inverting eqs.(4.4a) and (4.7a) respectively (in the range  $[1, x_{max}]$ ).

Thus for the synchrotron luminosity we have:

$$L^1(\nu, t) = \int_{x_1^{**}(\nu)}^{x_2^{**}(\nu)} 4\pi^2 R_0^3 \epsilon^* x^{2\epsilon} dx \quad \text{case } i$$

or

$$L^1(\nu, t) = \int_{x_1^{**}(\nu)}^{x_2^{**}(\nu)} 4\pi^2 R_0^3 \epsilon^* \left\{ [x - (x^* - \Delta x^*)] \frac{x^{*\epsilon}}{\Delta x^*} \right\}^2 dx \quad \text{case } ii \quad (A.6)$$

and for  $L^2(\nu, t)$

$$L^2(\nu, t) = L^{st}(\nu) - \int_{\hat{x}_1(\nu)}^{\hat{x}_2(\nu)} 4\pi^2 R_0^3 \epsilon x^{2\epsilon} dx \quad \text{case } i$$

or

$$L^2(\nu, t) = L^{st}(\nu) - \int_{\hat{x}_1(\nu)}^{\hat{x}_2(\nu)} 4\pi^2 R_0^3 \epsilon \left\{ [x - (x^* - \Delta x^*)] \frac{x^{*\epsilon}}{\Delta x^*} \right\}^2 dx \quad \text{case } ii \quad (A.7)$$

where the last integral is extended to the perturbed part of  $V(\nu)$  and the extremes are given by

$$\begin{aligned} \hat{x}_1(\nu, t) &= \max[x^* - \Delta x^*, x_1(\nu)] \\ \hat{x}_2(\nu, t) &= \min[x^*, x_2(\nu)] \end{aligned} \quad (A.8)$$

Analogous expressions are used for Compton emission with the appropriate values of the integration limits.

## Appendix B

In this appendix we find analytically the factor  $R(\Theta)$  of eq. (6.1), for integer values of  $p$ .

We first solve the integral, let call it  $I(\theta, \Theta)$ , in the variable  $\phi$ . We have

$$I(\theta, \Theta) \equiv \int_0^{2\pi} \frac{d\phi}{[1 - \beta_b(\sin \Theta \sin \theta \cos \phi + \cos \Theta \cos \theta)]^p} = \frac{2}{b^p} \int_0^\pi \frac{d\phi}{[a - \cos \phi]^p} \quad (B.1)$$

where

$$\begin{aligned} b &\equiv \beta_b \sin \Theta \sin \theta \\ c &\equiv 1 - \beta_b \cos \Theta \cos \theta \\ a &\equiv c/b \end{aligned} \quad (B.2)$$

The calculation of the integral  $I(\theta, \Theta)$  can be reduced to the calculation of  $I_1$ :

$$I(\theta, \Theta) = \frac{2}{b^p} \frac{1}{(1-p)(2-p)\dots(-1)} \frac{d^{p-1} I_1}{da^{p-1}}$$

where

$$I_1 = \int_0^\pi \frac{d\phi}{(a - \cos \phi)} \quad (B.3)$$

With the two changes of variable

$$\begin{aligned} \cos \phi &= \frac{1 - t^2}{1 + t^2} \\ x &= t \left( \frac{a+1}{a-1} \right)^{1/2} \end{aligned} \quad (B.4)$$

we obtain

$$I_1 = \frac{4}{\sqrt{a^2 - 1}} \left[ \arctg \left( \sqrt{\frac{a+1}{a-1}} \sqrt{\frac{1 - \cos \phi}{1 + \cos \phi}} \right) \right]_0^\pi = \frac{2\pi}{\sqrt{a^2 - 1}} \quad (B.5)$$

Substituting in eq. (B.3) we obtain, for  $p = 3$

$$I(\theta, \Theta) = \frac{1}{2} \frac{1}{b^3} \frac{d^2}{da^2} I_1 = \frac{\pi}{b^3} \frac{2a^2 + 1}{(a^2 - 1)^{5/2}} = \pi \frac{(b^2 + 2c^2)}{(c^2 - b^2)^{5/2}}, \quad p = 3 \quad (B.6)$$

while, for  $p = 4$ , we have

$$I(\theta, \Theta) = -\frac{1}{6} \frac{1}{b^4} \frac{d^3}{da^3} I_1 = \frac{\pi}{b^4} \frac{a(2a^2 + 3)}{(a^2 - 1)^{7/2}} = \pi c \frac{(3b^2 + 2c^2)}{(c^2 - b^2)^{7/2}}, \quad p = 4 \quad (B.7)$$

The last two equalities in eqs. (B.6) and (B.7) avoid the vanishing of the denominator at  $\Theta = 0$ .

We do not report the analytic integration of  $I(\theta, \Theta)$  in the variable  $\theta$ . It reduces to the integration of rational functions  $f_3(\cos \theta) = Q_1(\cos \theta)/Q_2^{5/2}(\cos \theta)$  (for  $p=3$ ) and  $f_4(\cos \theta) = Q_3(\cos \theta)/Q_4^{7/2}(\cos \theta)$  (for  $p=4$ ), where  $Q_i(\cos \theta)$  are second order polynomials, which can be solved substituting  $t \equiv \cos \theta - \cos \Theta/\beta_b$ .

## List of symbols

A list of the symbols is given in alphabetical order (latin and greek). We report only symbols used in more than one Chapter (or which can create ambiguity).

We use the conventional notation  $A_n \equiv 10^{-n}A$  and the masses  $M$  are expressed in solar mass units  $M_\odot = 2 \times 10^{33}$  gr. c.g.s. units. are used. Primed quantities are measured in the comoving frame.

$B$	magnetic field intensity
$d_L$	luminosity distance
$f$	ratio of the beamed and unbeamed luminosities
$F_m$	flux at the self-absorption frequency
$F_x$	X-ray flux
$J$	jet-counterjet flux ratio
$j_{s,C}$	monochromatic synchrotron, Compton emissivities
$l$	typical travel path
$\ell$	compactness parameter
$L$	source luminosity
$L_E$	Eddington luminosity $L_E \equiv 2\pi m_p c^3 R_s / \sigma_T$
$K$	normalization of the non-thermal distribution of emitting particles
$M$	black hole mass
$m_e, m_p$	electron, proton mass
$n$	power law exponent for $K$ in the jet model
$n$	exponent for the Doppler amplification of the flux ( $\propto \delta^n$ )
$n_{e,p,e^\pm,+}$	particle density: electron, protons, $e^\pm$ , positrons, respectively
$n_{SSC}$	density of SSC emitting particles
$N_H$	hydrogen column density
$p$	exponent of the non-thermal distribution of emitting particles
$R_0$	typical source dimension
$R$	radial (or jet axis) coordinate
$R_s$	Schwarzschild radius, $R_s \equiv 2GM/c^2$
$R_{CD}$	core dominance parameter
$r_L$	Larmor radius $r_L \equiv m\beta c/eB$
$T_B$	brightness temperature
$T_{bb}$	blackbody temperature
$T_C$	Compton temperature

$T_v$	virial temperature
$U_B$	magnetic field energy density
$U_{e,p}$	electron (proton) energy density
$U_r$	radiation energy density
$v_{ff}$	free fall velocity
$v_{in}$	infall velocity
$x$	photon energy in units of electron mass energy, $x \equiv h\nu/m_e c^2$
$x$	distance along the jet in units of $x = R/R_0$ (Chs. 4, 5)
$\alpha$	energy spectral index [ $F(\nu) \propto \nu^{-\alpha}$ ]
$\beta_b c$	bulk velocity
$\beta_a c$	apparent superluminal velocity
$\beta_p c$	perturbation velocity
$\beta_1 c, \beta_2 c, \beta_s c$	up-, down-stream fluid and shock front velocities (observer frame)
$\gamma$	particle Lorentz factor
$\gamma_{min,max}$	extremes of the non-thermal distribution of emitting particle
$\gamma_t$	$\gamma_t \equiv (3\nu_t/4\nu_B)^{1/2}$
$\Gamma$	bulk Lorentz factor
$\Gamma_p$	'perturbation' Lorentz factor
$\gamma_1, \gamma_2, \gamma_s$	up-, down-stream fluid and shock front Lorentz factors (observer frame)
$\delta$	Doppler factor
$\Delta t$	variability timescale, $\Delta t \equiv L/(dL/dt)$
$\eta$	accretion efficiency $L = \eta \dot{M} c^2$
$\kappa$	synchrotron absorption coefficient
$\theta$	angle between the jet axis and the line of sight (except Ch. 6)
$\theta$	polar coordinate in the wide jet (Ch. 6)
$\theta_d$	VLBI angular diameter
$\Theta$	angle between the jet axis and the line of sight (Ch. 6)
$\nu_B$	cyclotron frequency
$\nu_{bb}$	blackbody peak frequency
$\nu_t$	synchrotron self-absorption frequency
$\xi$	pair yield
$\sigma_T$	Thomson cross section
$\sigma_{KN}$	Klein-Nishina cross section
$\tau_{e^\pm}$	$e^\pm$ optical depth
$\tau_r$	Thomson optical depth in relativistic particles
$\tau_s$	synchrotron absorption optical depth
$\tau_T$	Thomson optical depth
$\tau_{\gamma\gamma}$	pair production optical depth (by photon-photon interaction)



## References

- Abraham, R.G., McHardy, I.M., & Crawford, C.S., 1991. *Mon. Not. R. astr. Soc.*, **252**, 482.
- Abramowicz, M.A., Calvani, M. & Nobili, L., 1980. *Astrophys. J.*, **242**, 772.
- Abramowicz, M.A., Bao, G., Lanza, A. & Zhang, X.-H., 1989. In "Proc. 23<sup>th</sup> ESLAB Symp: X-ray Astronomy", ESA SP-296, p. 871.
- Alexander, P., 1992. In Proc. of "The Nature of Compact Objects in Active Galactic Nuclei", Cambridge, July 1992, in press.
- Aller, H.D., Aller, M.F., Latimer, G.E. & Hodge, P.E., 1985. *Astrophys. J. Suppl.*, **59**, 513.
- Angel, J.R.P. & Stockman, H.S., 1980. *Ann. Rev. Astr. Astrophys.*, **18**, 321.
- Antonucci, R.R.J., 1984. *Astrophys. J.*, **278**, 499.
- Antonucci, R.J. & Miller, J.S., 1985. *Astrophys. J.*, **297**, 621.
- Antonucci, R.J. & Ulvestad, J.S., 1985. *Astrophys. J.*, **294**, 158.
- Antonucci, R. R. J., Hickson, P., Olszewski, E. W. & Miller, J. S., 1986. *Astron. J.*, **92**, 1.
- Arnaud, K.A., Branduardi-Raymont, G., Culhane, J.L., Fabian, A.C., Hazard, C., McGlynn, T.A., Shafer, R.A., Tennant, A.F. & Ward M.J., 1985. *Mon. Not. R. astr. Soc.*, **217**, 105.
- Arnaud, K.A., Johnston, R.M., Fabian, A.C., Crawford, C.S., Nulsen, P.E., Shafer, R.A. & Mushotzky, R.F., 1987. *Mon. Not. R. astr. Soc.*, **227**, 241.
- Baath, L.B. *et al.*, 1991. *Astron. Astrophys.*, **241**, L1.
- Baity, W.A., Mushotzky, R.F., Worrall, D.M., Rothschild, R.E., Tennant, A.F. & Primini, F.A., 1984. *Astrophys. J.*, **244**, 429.
- Balonek, T.J., 1982. *Astrophys. J. Lett.*, **240**, L3.
- Barbieri, C., Vio, R., Cappellaro, E. & Turatto, M., 1990. *Astrophys. J.*, **359**, 63.
- Barr, P. & Mushotsky, R.F., 1986. *Nature*, **320**, 421.
- Barr, P., Giommi, P., Pollock, A., Tagliaferri, G., Maccagni, D. & Garilli, B., 1989. In "BL Lac Objects", eds. L. Maraschi, T. Maccacaro & M-H. Ulrich (Springer-Verlag), p. 290.
- Barthel, P.D., 1989. *Astrophys. J.*, **336**, 606.
- Barthel, P.D., Pearson, T.J. & Readhead, A.C.S., 1988. *Astrophys. J. Lett.*, **329**, L51.
- Barthel, P.D., Pearson, T.J., Readhead, A.C.S. & Canzian, B.J., 1986. *Astrophys. J. Lett.*, **310**, L7.
- Barthel, P.D., Hooimeyer, J.R., Schilizzi, R.T., Miley, G.K. & Preuss, E., 1989. *Astrophys. J.*, **336**, 601.
- Barvainis, R., 1990. *Astrophys. J.*, **353**, 419.

- Bassani, L., Dean, A.J., Di Cocco, G. & Perotti, F., 1985. In *"Active Galactic Nuclei"*, ed. J. Dyson (Manchester University Press), p. 252.
- Baum, S.A., O'Dea, C.P., Murphy, D.W. & de Bruyn, A.G., 1990. *Astron. Astrophys.*, **232**, 19.
- Begelman, M.C., 1989. In *"Active galactic Nuclei"*, IAU Symp. 134, eds. D.E. Osterbrock & J.S. Miller (Reidel, Dordrecht), p. 141.
- Begelman, M.C., 1992. In *"Jets in Extragalactic Radio Sources"*, eds. H.-J. Röser *et al.*, Springer, Berlin, in press.
- Begelman, M.C. & DeKool, M., 1990. In *"Variability of Active Galactic Nuclei"*, eds. H.R. Miller & P.W. Wiita (Cambridge University Press), p. 198.
- Begelman, M.C., Blandford, R.D. & Rees, M.J., 1984. *Rev. of Mod. Phys.*, **56**, 255.
- Biermann, P.L. & Strittmatter, P.A., 1987. *Astrophys. J.*, **322**, 643.
- Biermann, P.I., Kühr, H., Snyder, W.A. & Zensus, J.A., 1987. *Astron. Astrophys.*, **185**, 9.
- Bignami, G.F., Fichtel, C.E., Hartman, R.C. & Thompson, D.J., 1979. *Astrophys. J.*, **232**, 649.
- Bignami, G.F. *et al.*, 1981. *Astron. Astrophys.*, **93**, 71.
- Biretta, J.A. & Cohen, M.H., 1987. In *"Superluminal Radio Sources"*, eds. A. Zensus & T. Pearson (Cambridge University Press), p. 40.
- Biretta, J.A. & Owen, F.N., 1990. In *"Parsec-Scale Radio Jets"*, eds. J.A. Zensus & T.J. Pearson (Cambridge University Press), p. 125.
- Biretta, J.A., Stern, C.P. & Harris, D.E., 1991. *Astron. J.*, **101**, 1632.
- Blandford, R.D., 1990. In *"Active Galactic Nuclei"*, 20<sup>th</sup> SAAS-FEE Course, eds. T.J.-L. Courvoisier & M. Mayor (Berlin: Springer-Verlag).
- Blandford, R.D., 1992. In Proc. of *"Astrophysical Jets"*, Baltimore, May 1992, in press.
- Blandford, R.D. & Eichler, D., 1987. *Phys. Reports*, **154** 1.
- Blandford, R.D. & Königl, A., 1979. *Astrophys. J.*, **232**, 34.
- Blandford, R.D. & McKee, C.F., 1976. *Phys. Fluids*, **19**, 1130.
- Blandford, R.D. & Payne, D.G., 1982. *Mon. Not. R. astr. Soc.*, **199**, 883.
- Blandford, R.D. & Rees, M.J., 1974. *Mon. Not. R. astr. Soc.*, **169**, 395.
- Blandford, R.D. & Rees, M.J., 1978. In *"Pittsburgh Conference on BL Lac Objects"*, ed. A.N. Wolfe (Pittsburgh University Press), p. 328.
- Blandford, R.D. & Rees, M.J., 1992. In *"Testing the AGN Paradigm"*, AIP Conference Proc. 254, eds. S. Holt, S.G. Neff & C.M. Urry, p. 3.
- Blandford, R.D., McKee, C.F. & Rees, M.J., 1977. *Nature*, **267**, 211.
- Bloom, S.D. & Marscher, A.P., 1991. *Astrophys. J.*, **366**, 16.
- Blumenthal, G.R. & Gould, R.J., 1970. *Rev. Mod. Phys.*, **42**, 237.
- Boksenberg, A. *et al.*, 1992. *Astron. Astrophys.*, in press.
- Boyd, T.J.M. & Sanderson, J.J., 1969. *"Plasma Dynamics"* (New York: Barnes & Noble).
- Brainerd, J.J., 1992. *Astrophys. J. Lett.*, **394**, L33.
- Branduardi-Raymont, G., 1989. In *"Active galactic Nuclei"*, IAU Symp. 134, eds. D.E. Osterbrock & J.S. Miller (Reidel, Dordrecht), p. 177.
- Bregman, J.N., 1990. *Astron. Astrophys. Rev.*, **2**, 125.
- Bregman, J.N. & Hufnagel, B.R., 1989. In *"BL Lac Objects"*, eds. L. Maraschi, T. Maccacaro & M.-H. Ulrich (Springer-Verlag), p. 159.

- Bregman, J.N., Maraschi L. & Urry, M., 1987. In *"Exploring the Universe with I.U.E."*, ed. Y. Kondo (Dordrecht: D. Reidel), p. 685.
- Bregman, J. N., Glassgold, A. E., Huggins, P. J. & Kinney, A. L., 1985. *Astrophys. J.*, **291**, 505.
- Bregman, J.N., *et al.*, 1984. *Astrophys. J.*, **276**, 454.
- Bregman, J.N., *et al.*, 1986. *Astrophys. J.*, **301**, 708.
- Bregman, J.N., *et al.*, 1990. *Astrophys. J.*, **352**, 574.
- Bridle, A.H., 1991. In *"Testing the AGN Paradigm"*, AIP Conference Proc. 254, eds. S. Holt, S.G. Neff & C.M. Urry, p. 386.
- Brodie, J., Bowyer, S. & Tennant, A., 1987. *Astrophys. J.*, **318**, 175.
- Brown, L.M.J. *et al.*, 1989. *Astrophys. J.*, **340**, 129.
- Browne, I.W.A., 1987. In *"Superluminal Radio Sources"*, eds. A. Zensus & T. Pearson (Cambridge University Press), p. 129.
- Browne, I.W.A., 1989. In *"BL Lac Objects"*, eds. L. Maraschi, T. Maccacaro & M-H. Ulrich (Springer-Verlag), p. 401.
- Browne, I.W.A. & Murphy, D.W., 1987. *Mon. Not. R. astr. Soc.*, **226**, 601.
- Browne, I.W.A. & Perley, R.A., 1986. *Mon. Not. R. astr. Soc.*, **222**, 149.
- Burbridge, G. & Hewitt, A., 1989. In *"BL Lacs objects"*, eds. L. Maraschi, T. Maccacaro & M-H. Ulrich, p. 412.
- Canizares, C. & Kruper, J., 1984. *Astrophys. J. Lett.*, **278**, L99.
- Cawthorne, T.V., 1991. In *"Beams and Jets in Astrophysics"*, ed. P.A. Hughes (Cambridge University Press), p. 187.
- Cawthorne, T.V. & Wardle, J.F.C., 1988. *Astrophys. J.*, **332**, 696.
- Cavaliere, A., 1982. In *"Plasma Astrophysics"*, SP-161, ESA, p. 97.
- Cavaliere, A. & Morrison, P., 1980. *Astrophys. J. Lett.*, **238**, L64.
- Cavaliere, A., Giallongo, G. & Vagnetti, F., 1986. *Astron. Astrophys.*, **156**, 33.
- Celotti, A., 1991. *Master Thesis*, I.S.A.S., Trieste, Italy.
- Celotti, A., 1992, in preparation.
- Celotti, A., Fabian, A.C. & Rees, M.J., 1991. *Mon. Not. R. astr. Soc.*, **255**, 419.
- Celotti, A. & Fabian, A.C., 1992a. In Proc. of *"Astrophysical Jets"*, Baltimore, May 1992, in press.
- Celotti, A. & Fabian, A.C., 1992b, in preparation.
- Celotti, A., Ghisellini, G. & Fabian, A.C., 1991. *Mon. Not. R. astr. Soc.*, **251**, 529.
- Celotti, A., Ghisellini, G. & Fabian, A.C., 1991. In Proc. of *"The Physics of Active Galactic Nuclei"*, Heidelberg, June 1991, in press.
- Celotti, A., Maraschi, L. & Treves, A., 1989. In *"BL Lac Objects"*, eds. L. Maraschi, T. Maccacaro & M-H. Ulrich (Springer-Verlag), p. 332.
- Celotti, A., Maraschi, L. & Treves, A., 1991. *Astrophys. J.*, **377**, 403.
- Celotti, A., Maraschi, L., Ghisellini, G. & Caccianiga, A., 1992, in preparation.
- Charlot, P., 1990. *Astron. Astrophys.*, **229**, 51.
- Chini, R., Kreysa, E. & Biermann, P.L., 1989. *Astron. Astrophys.*, **219**, 87.
- Christiansen, W.A., 1989. In *"Hot Spots in Extragalactic Radio Sources"*, eds. K. Meisenheimer & H.-J. Röser (Springer-Verlag), p. 291.
- Clavel, J. *et al.*, 1991. *Astrophys. J.*, **336**, 64.
- Clavel, J. *et al.*, 1992. *Mon. Not. R. astr. Soc.*, in press.

- Clavel, J., Wamstaker, W. & Glass, I.S., 1989. *Astrophys. J.*, **337**, 236.
- Clegg, P.E. *et al.*, 1983. *Astrophys. J.*, **273**, 58.
- Cohen, R.D., 1986. In "*Highlights of Modern Astrophysics*", eds. S.L. Shapiro & S.A. Teukolsky (New York: Wiley), p. 299.
- Cohen, M.H., 1989. In "*BL Lacs Objects*", eds. L. Maraschi, T. Maccacaro & M-H Ulrich (Springer-Verlag), p. 13.
- Cohen, M.H., & Vermeulen, R.C., 1991. In Proc. of In Proc. of "*Extragalactic Radio Sources: from Beams to Jets*", Paris, July 1991, in press.
- Cohen, R.D., Smith, H.E., Junkkarinen, V.T. & Burbidge, E.M., 1987. *Astrophys. J.*, **318**, 577.
- Collin-Souffrin, S., 1991. *Astron. Astrophys.*, **249**, 344.
- Collin-Souffrin, S., 1992. In Proc. of "*The Nature of Compact Objects in Active Galactic Nuclei*", Cambridge, July 1992, in press.
- Coppi, P.S., Kartje, J.F. & Königl, A., 1992. In "*180 Meeting of the A.A.S.*", June 1992, Columbus.
- Courvoisier, T.J.-L., 1992. In Proc. of "*Recent Advances in High Energy Astronomy*", Toulouse, March 1992. in press.
- Courvoisier, T.J.-L. & Clavel, J., 1991. *Astron. Astrophys.*, **248**, 389.
- Courvoisier, T.J.-L. *et al.*, 1987. *Astron. Astrophys.*, **176**, 197.
- Courvoisier, T.J.-L. *et al.*, 1990. *Astron. Astrophys.*, **234**, 73.
- Davidson, K. & Netzer, H., 1979. *Rev. Mod. Phys.*, **51**, 715.
- Davies, R.J., Unwin, S.C. & Muxlow, T.W.B., 1991, *Nature*, **354**, 374.
- Della Ceca, R., Palumbo, G.G.C., Persic, M., Boldt, E.A., De Zotti, G. & Marshall, E.E., 1990. *Astrophys. J. Suppl.*, **72**, 471.
- Dent, W.A., 1965. *Science*, **148**, 1458.
- Dermer, C.D., Schlickeiser, R. & Mastichiadis, A., 1992. *Astron. Astrophys.*, **256**, L27.
- Done, C. & Fabian, A.C., 1989. *Mon. Not. R. astr. Soc.*, **240**, 81.
- Done, C., Ghisellini, G. & Fabian, A.C., 1990. *Mon. Not. R. astr. Soc.*, **245**, 1.
- Done, C., Madejski, G.M., Mushotzky, R.F., Turner, T.J., Koyama, K. & Kunieda, H., 1992. In "*Testing the AGN Paradigm*", AIP Conference Proc. 254, eds. S. Holt, S.G. Neff & C.M. Urry, p. 83.
- Done, C., Ward, M.J., Fabian, A.C., Kunieda, H., Tsuruta, S., Lawrence, A., Smith, M.G. & Wamsteker, W., 1990. *Mon. Not. R. astr. Soc.*, **243**, 713.
- Dulzin-Hacyan, D., 1992. In Proc. of "*The Nature of Compact Objects in Active Galactic Nuclei*", Cambridge, July 1992, in press.
- Dunlop, J.S. & Peacock, J.A., 1990. *Mon. Not. R. astr. Soc.*, **247**, 19.
- Eckart, A., Witzel, A., Biermann, P., Johnston, K.J., Simon, R., Shalinski, C. & Kühr, H., 1987. *Astr. Ap. Supp.*, **67**, 121.
- Edelson, R.A., 1992. In Proc. of "*The Nature of Compact Objects in Active Galactic Nuclei*", Cambridge, July 1992, in press.
- Edelson, R.A. & Malkan, M.A., 1987. *Astrophys. J.*, **323**, 516.
- Edelson, R.A., Saken, J.M., Pike, G.F., Urry, C.M., George, I.M., Warwick, R.S., Miller, H.R., Carini, M.T. & Webb, J.R., 1991. *Astrophys. J. Lett.*, **372**, L9.
- Elvis, M., Wilkes, B.J. & McDowell, J.C., 1990. In "*Extreme Ultraviolet Astronomy*", eds. R.F. Malina & S. Bowyer (New York: Pergamon).

- Fabbiano, G., Miller, L., Trinchieri, G., Longair, M. & Elvis, M., 1984. *Astrophys. J.*, **277**, 115.
- Fabian, A.C., 1979. *Proc. R. Soc. Lond. A.*, **366**, 449.
- Fabian, A.C., 1986. In *"The Physics of Accretion onto Compact Objects"*, eds. Mason, K.O., Watson, M.G. & White, N.E. (Springer-Verlag), p. 229.
- Fabian, A.C., 1989. In *Proc. 23<sup>th</sup> ESLAB Symp: "X-ray Astronomy"*, ESA SP-296, p. 1097.
- Fabian, A.C., 1992a. In *"X-ray Emission from AGN and the Cosmic X-ray Background"*, eds. W. Brinkmann & J. Trümper, MPE Report, March 1992, p. 22.
- Fabian, A.C., 1992b. In *Proc. of "The Nature of Compact Objects in Active Galactic Nuclei"*, Cambridge, July 1992, in press.
- Fabian, A.C., Rees, M.J., Stella, L. & White, N.E., 1988. *Mon. Not. R. astr. Soc.*, **238**, 729.
- Fanaroff, B.L. & Riley, J.M., 1974. *Mon. Not. R. astr. Soc.*, **167**, 31P.
- Feigelson, E.D. *et al.*, 1986. *Astrophys. J.*, **302**, 337.
- Ferland, G.J. & Persson, S.E., 1989. *Astrophys. J.*, **347**, 656.
- Ferland, G.J. & Rees, M.J., 1988. *Astrophys. J.*, **332**, 141.
- Ferland, G.J., Korista, K.T., & Peterson, B.M., 1990. *Astrophys. J. Lett.*, **363**, L21.
- Fichtel, C.E. *et al.*, 1979. *Astrophys. J.*, **222**, 833.
- Fichtel, C.E. *et al.*, 1992a. *IAU Circ.* 5460.
- Fichtel, C.E. *et al.*, 1992b. *Astron. Astrophys.*, in press.
- Fiore, F., Massaro, E. & Barone, P., 1992. *Astron. Astrophys.*, in press.
- Fiore, F., Massaro, E., Perola, G.C. & Piro, L., 1989. *Astrophys. J.*, **347**, 171.
- Franceschini, A., Danese, L., De Zotti, G. & Toffolatti, L., 1988. *Mon. Not. R. astr. Soc.*, **233**, 157.
- Fugmann, W., 1988. *Astron. Astrophys.*, **205**, 86.
- Gabuzda, D.C., Wardle, J.F.C. & Roberts, D.H., 1989. *Astrophys. J. Lett.*, **336**, L59.
- Gabuzda, D.C., Cawthorne, T.V., Roberts, D.H., & Wardle, J.F.C. 1992, *Astrophys. J.*, **388**, 40.
- Garrington, S.T., Leahy, J.P., Conway, R.G. & Laing, R.A., 1988. *Nature*, **331**, 147.
- Gehrels, N., 1986. *Astrophys. J.*, **303**, 336.
- Gehrels, N., 1992. In *Proc. of "Recent Advances in High Energy Astronomy"*, Toulouse, March 1992. in press.
- George, I.M. & Fabian, A.C., 1991. *Mon. Not. R. astr. Soc.*, **249**, 352.
- George, I.M., Warwick, R.S. & Bromage, G.E., 1988. *Mon. Not. R. astr. Soc.*, **232**, 793.
- George, I.M., Warwick, R.S. & McHardy, I.M., 1988. *Mon. Not. R. astr. Soc.*, **235**, 787.
- Ghisellini, G., 1987. *Ph. D. Thesis*, I.S.A.S., Trieste.
- Ghisellini, G., 1989a. *Mon. Not. R. astr. Soc.*, **236**, 341.
- Ghisellini, G., 1989b. *Mon. Not. R. astr. Soc.*, **238**, 449.
- Ghisellini, G. & Maraschi, L., 1989. *Astrophys. J.*, **340**, 181.
- Ghisellini, G., George, I.M. & Done, C., 1989. *Mon. Not. R. astr. Soc.*, **241**, 43P.
- Ghisellini, G., Guilbert, P.W. & Svensson, R., 1988. *Astrophys. J. Lett.*, **334**, L5.
- Ghisellini, G., Maraschi, L. & Treves, A., 1985. *Astron. Astrophys.*, **146**, 204.
- Ghisellini, G., Bodo, G., Trussoni, E. & Rees, M.J., 1990. *Astrophys. J. Lett.*, **362**, L1.

- Ghisellini, G., Celotti, A., George, I.M. & Fabian, A.C., 1992a. *Mon. Not. R. astr. Soc.*, in press.
- Ghisellini, G., Maraschi, L., Tanzi, E. & Treves, A., 1986. *Astrophys. J.*, **310**, 317.
- Ghisellini, G., Padovani, P., Celotti, A. & Maraschi, L., 1991. In “*Testing the AGN Paradigm*”, AIP Conference Proc. 254, eds. S. Holt, S.G. Neff & C.M. Urry, p. 398.
- Ghisellini, G., Padovani, P., Celotti, A. & Maraschi, L., 1992b. *Astrophys. J.*, , submitted.
- Ginzburg, V.L. & Syrovatskii, S.I., 1965. *Ann. Rev. Astr. Ap.*, **3**, 297.
- Giommi, P., Barr, P., Garilli, B., Maccagni, D. & Pollock, A.M.T., 1990. *Astrophys. J.*, **356**, 432.
- Giommi, P., Barr, P., Garilli, B., Gioia, I.M., Maccacaro, T., Maccagni, D., & Schild, R.E., 1987, *Astrophys. J.*, **322**, 662.
- Giommi, P. *et al.*, 1989. In “*BL Lac Objects*”, eds. L. Maraschi, T. Maccacaro & M-H. Ulrich (Springer-Verlag), p. 231.
- Giovanoni, P.M. & Kazanas, D., 1990. *Nature*, **345**, 319.
- Guilbert, P.W. & Rees, M.J., 1988. *Mon. Not. R. astr. Soc.*, **233**, 475.
- Guilbert, P.W. & Stepney, S., 1985. *Mon. Not. R. astr. Soc.*, **212**, 523.
- Guilbert, P.W., Fabian, A.C., & McCray, R., 1983. *Astrophys. J.*, **266**, 466.
- Guilbert, P.W., Fabian, A.C., & Rees, M.J., 1983. *Mon. Not. R. astr. Soc.*, **205**, 593.
- Guilbert, P.W., Fabian, A.C., & Ross, R.R., 1982. *Mon. Not. R. astr. Soc.*, **199**, 763.
- Guilbert, P.W., Fabian, A.C., & Stepney, S., 1982. *Mon. Not. R. astr. Soc.*, **199**, 19P.
- Hackney, R.L., Hackney, K.R., & Kondo, Y., 1982. In “*Advances in UV Astronomy: Four Years of IUE*”, (NASA CP2238), p. 335.
- Hartman, R.C. *et al.*, 1992a. *Astrophys. J. Lett.*, **385**, L1.
- Hartman, R.C. *et al.*, 1992b. *IAU Circ.* 5477.
- Hartman, R.C. *et al.*, 1992c. *IAU Circ.* 5519.
- Henri, G. & Pelletier, G., 1991. *Astrophys. J. Lett.*, **383**, L7.
- Henriksen, M.J., Marshall, F.E. & Mushotzky, R.F., 1984. *Astrophys. J.*, **284**, 491.
- Hewitt, A. & Burbridge, G. 1987. *Astrophys. J. Suppl.*, **63**, 1.
- Hooimeyer, J.R.A., Schilizzi, R.T., Miley, G.K., & Barthel, P.D., 1992a. *Astron. Astrophys.*, , submitted.
- Hooimeyer, J.R.A., Barthel, P.D., Schilizzi, R.T., & Miley, G.K., 1992b. *Astron. Astrophys.*, , submitted.
- Hooimeyer, J.R.A., Schilizzi, R.T., Miley, G.K., & Barthel, P.D., 1992c. *Astron. Astrophys.*, , submitted.
- Hooimeyer, J.R.A., Barthel, P.D., Schilizzi, R.T., & Miley, G.K., 1992d. *Astron. Astrophys.*, , submitted.
- Hough, D.H. & Readhead, A.C.S., 1987. *Astrophys. J. Lett.*, **321**, L11.
- Hough, D.H., Readhead, A.C.S., Wood, D.A., Jr. & Feldmeier, J.J., 1992. JPL Astrophysics preprint n. 215.
- Hoyle, F.R.S., Burbidge, G.R. & Sargent, W.L.W., 1966. *Nature*, **209**, 751.
- Hughes, P.A., Aller, H.D. & Aller, M.F., 1985. *Astrophys. J.*, **298**, 301.
- Hughes, P.A., Aller, H.D. & Aller, M.F., 1989. *Astrophys. J.*, **341**, 54.
- Hunter, S.D., *et al.*, 1992. *IAU Circ.* 5549.

- Icke, V., 1991. In *"Beams and Jets in Astrophysics"*, ed. P.A. Hughes (Cambridge University Press), p.232.
- Impey, C.D., 1992. In Proc. of *"The Nature of Compact Objects in Active Galactic Nuclei"*, Cambridge, July 1992, in press.
- Impey, C.D. & Neugebauer, G., 1988. *Astron. J.*, **95**, 307.
- Impey, C.D. & Tapia, S., 1990. *Astrophys. J.*, **354**, 124.
- Impey, C.D., Lawrence, C.R. & Tapia, S., 1991. *Astrophys. J.*, **375**, 46.
- Jackson, N. & Browne, I.W.A., 1991. *Mon. Not. R. astr. Soc.*, **250**, 414.
- Jagers, W.J., 1987. *Astr. As. Suppl.*, **71**, 75.
- Jenkins, C.R., 1982. *Mon. Not. R. astr. Soc.*, **200**, 705.
- Jones, T.W., 1988. *Astrophys. J.*, **332**, 678.
- Jones, T.W. & O'Dell, S.L., 1977. *Astron. Astrophys.*, **61**, 291.
- Jones, T.W. & Stein, W.A., 1990. *Astrophys. J.*, **349**, 443.
- Jones, T.W., O'Dell, S.L. & Stein, W.A., 1974. *Astrophys. J.*, **188**, 353.
- Jones, T.W., O'Dell, S.L. & Stein, W.A., 1974. *Astrophys. J.*, **192**, 261.
- Jones, D.L. *et al.*, 1986. *Astrophys. J.*, **305**, 684.
- Johnson, J., 1992. In Proc. of *"Recent Advances in High Energy Astronomy"*, Toulouse, March 1992. in press.
- Jourdain, *et al.*, 1991. *Astrophys. J.*, , submitted.
- Junkkarinen, V.T., Marscher, A.P. & Burbidge, E.M., 1982. *Astron. J.*, **87**, 845.
- Kaastra, J.S. & Barr, P., 1989. *Astron. Astrophys.*, **226**, 59.
- Kanbach, G. *et al.*, 1992. *IAU Circ.* 5431.
- Kii, T. *et al.*, 1991. *Astrophys. J.*, **367**, 455.
- Kinman, T.D., 1976. *Astrophys. J.*, **205**, 1.
- Kippenhahn, R. & Schluter, A., 1957. *Z. Astrophys.*, **43**, 36.
- Kollgaard, R.I., Wardle, J.F.C., Roberts, D.H. & Gabuzda, D.C., 1992. In *"180 Meeting of the A.A.S."*, June 1992, Columbus.
- Königl, A., 1980. *Phys. Fluids*, **23**, 1083.
- Königl, A., 1981. *Astrophys. J.*, **243**, 700.
- Königl, A., 1989. In *"BL Lac Objects"*, eds. L. Maraschi, T. Maccacaro & M-H. Ulrich (Springer-Verlag), p. 321.
- Königl, A. & Ruden, S.P., 1992. Preprint
- Koratan, A.P. & Gaskell, C.M., 1991. *Astrophys. J. Lett.*, **370**, L61.
- Krichbaum, T.P. *et al.*, 1990. *Astron. Astrophys.*, **237**, 3.
- Krolik, J.H. & Begelman, M.C., 1988. *Astrophys. J.*, **329**, 702.
- Krolik, J.H., McKee, C.F. & Tarter, C.B., 1981. *Astrophys. J.*, **249**, 422.
- Krolik, J.H., Kallmann, T.R., Fabian, A.C. & Rees, M.J., 1985. *Astrophys. J.*, **295**, 104.
- Ku, W.H.-M., Helfand, D.J. & Lucy, L.B., 1980. *Nature*, **288**, 323.
- Kühr, H. & Schmidt, G.D., 1990. *Astron. J.*, **99**, 1.
- Kühr, H., Witzel, A., Pauliny-Toth, I.I.K & Nauber, U., 1981, *Astr. Ap. Suppl.* **45**, 367.
- Kunieda, H., Turner, T.J., Awaki, H., Koyama, K., Mushotzky, R. & Tsusaka, Y., 1990. *Nature*, **345**, 786.
- Laing, R.A., 1988. *Nature*, **331**, 149.
- Laing, R.A., 1992. In Proc. of *"Astrophysical Jets"*, Baltimore, May 1992, in press.

- Landau, R., Jones, T.W., Epstein, E.E., Neugebauer, G., Soifer, B.T., Werner, M.W., Puschell, J.J. & Balonek, T.J., 1983. *Astrophys. J.*, **268**, 68.
- Landau, R. *et al.*, 1986. *Astrophys. J.*, **308**, 78.
- Laor, A. & Netzer, H. & Piran, T., 1990. *Mon. Not. R. astr. Soc.*, **242**, 560.
- Lawrence, A., 1987. *Pub. Astron. Soc. Pacific*, **99**, 309.
- Lawrence, A., 1992. Preprint.
- Lawrence, A. & Elvis, M.S., 1982. *Astrophys. J.*, **256**, 410.
- Lawrence, A., Pounds, K.A., Watson, M.G. & Elvis, M.S., 1985. *Mon. Not. R. astr. Soc.*, **217**, 685.
- Lawrence, A., Pounds, K.A., Watson, M.G. & Elvis, M.S., 1987. *Nature*, **325**, 692.
- Lawrence, C.R. *et al.*, 1985. *Astrophys. J.*, **296**, 458.
- Lawson, A.J., Turner, M.J.L., Williams, O.R., Stewart, G.C. & Saxton, R.D., 1992. *Mon. Not. R. astr. Soc.*, in press.
- Leahy, J.P., 1991. In *"Beams and Jets in Astrophysics"*, ed. P.A. Hughes (Cambridge University Press), p. 100.
- Ledden, J.E. & O'Dell, S.L., 1985. *Astrophys. J.*, **298**, 630.
- Lightman, A.P. & White, T.R., 1988. *Astrophys. J.*, **335**, 57.
- Lightman, A.P. & Zdziarki, A., 1987. *Astrophys. J.*, **319**, 643.
- Lightman, A.P., Giacconi, R. & Tananbaum, H., 1978. *Astrophys. J.*, **224**, 375.
- Lightman, A.P., Zdziarski, A.A. & Rees, M.J., 1987. *Astrophys. J. Lett.*, **315**, L113.
- Lind, K.R. & Blandford, R.D., 1985. *Astrophys. J.*, **295**, 358.
- Linfield, R.P., *et al.*, 1989. *Astrophys. J.*, **336**, 1105.
- Linfield, R.P., *et al.*, 1990. *Astrophys. J.*, **358**, 350.
- Liu, R. & Pooley, G., 1991. *Mon. Not. R. astr. Soc.*, **249**, 343.
- Longair, M.S. & Ryle, S.M., 1979. *Mon. Not. R. astr. Soc.*, **188**, 625.
- Luty, V.M., 1977. *Sov. Astr.*, **21** 655.
- Macchetto, F., 1991. In Proc. of *"The Physics of Active Galactic Nuclei"*, Heidelberg, June 1991, in press.
- Madau, P., Ghisellini, G. & Persic, M., 1987. *Mon. Not. R. astr. Soc.*, **224**, 257.
- Madejski, G. & Schwartz, D., 1989. In *"BL Lac Objects"*, eds. L. Maraschi, T. Maccacaro & M.-H. Ulrich (Springer-Verlag), p. 267.
- Madejski, G., Mushotzky, R.F., Weaver, K.A., Arnaud, K.A. & Urry, C.M., 1991. *Astrophys. J.*, in press.
- Maisak, M., *et al.* 1992. *Astron. Astrophys.*, in press.
- Makino, F., Fink, H.H., & Clavel, J., 1991. In *Nagoya Conference proceedings*, p. 1.
- Makino, F. *et al.*, 1989. *Astrophys. J. Lett.*, **347**, L9.
- Makino, F. *et al.*, 1987. *Astrophys. J.*, **313**, 662.
- Makino, F. *et al.*, 1990. In Proc. of *"Variability of Active Galactic Nuclei"*, Atlanta, Georgia, in press.
- Malkan, M.A., 1983. *Astrophys. J.*, **268**, 582.
- Mannheim, K. & Biermann, P.L., 1992. *Astr. Ap.*, **253**, L21.
- Maraschi, L., 1992. In *"Variability in blazars"*, eds. E. Valtaoja & M. Valtonen (Cambridge University Press), p. 447.
- Maraschi, L. & Maccagni, D., 1988. *Mem. Soc. Astron. It.*, **59**, 277.



- Maraschi, L., Celotti, A. & Ghisellini, G., 1991. In *"The Physics of Active Galactic Nuclei"*, Heidelberg, June 1991, in press.
- Maraschi, L., Celotti, A. & Treves, A., 1989. In *Proc. 23<sup>th</sup> ESLAB Symp: "X-ray Astronomy"*, ESA SP-296, p. 825.
- Maraschi, L., Ghisellini, G. & Celotti, A., 1991. In *"Testing the AGN Paradigm"*, AIP Conference Proc. 254, eds. S. Holt, S.G. Neff & C.M. Urry, p. 439.
- Maraschi, L., Ghisellini, G. & Celotti, A., 1992. *Astrophys. J. Lett.*, in press.
- Maraschi, L., Ghisellini, G., Tanzi, E.G. & Treves, A., 1986, *Astrophys. J.*, **310**, 325.
- Maraschi, L., Tagliaferri, G., Tanzi, E. & Treves, A., 1986. *Astrophys. J.*, **304**, 637.
- Maraschi, L., Tanzi, E., Tarengi, M. & Treves, A., 1983. *Astron. Astrophys.*, **125**, 117.
- Maraschi, L., Chiappetti, L., Falomo, R., Garilli, B., Malkan, M., Tagliaferri, G., Tanzi, E.G. & Treves, A., 1991. *Astrophys. J.*, **368**, 138.
- Marscher, A.P., 1977. *Astrophys. J.*, **216**, 244.
- Marscher, A.P., 1980. *Astrophys. J.*, **235**, 386.
- Marscher, A.P., 1987. In *"Superluminal Radio Sources"*, eds. A. Zensus & T.J. Pearson (Cambridge University Press), p. 280.
- Marscher, A.P., 1992. In *Proc. of "Astrophysical Jets"*, Baltimore, May 1992, in press.
- Marscher, A.P. & Broderick, J.J., 1985. *Astrophys. J.*, **290**, 735.
- Marscher, A.P. & Gear, W.K., 1985. *Astrophys. J.*, **298**, 114.
- Marshall, N., Warwick, R.S. & Pounds, K.A., 1981. *Mon. Not. R. astr. Soc.*, **194**, 987.
- Mathews, W.G. & Ferland, G.J., 1987. *Astrophys. J.*, **323**, 456.
- Matsuoka, M., Piro, L., Yamauchi, M. & Murakami, T., 1990. *Astrophys. J.*, **361**, 440.
- Matt, G., Perola, G.C. & Piro, L., 1991. *Astron. Astrophys.*, **247**, 25.
- McAlary, C.W. & Rieke, G.H., 1988. *Astrophys. J.*, **333**, 1.
- McAlary, C.W., McLaren, R.A., McGonagal, R.J. & Maza, J., 1983. *Astrophys. J. Suppl.*, **52**, 341.
- McBreen, B., 1979. *Astr. Ap.*, **71**, L19.
- McHardy, I.M., 1988. In *Mem. Soc. Astr. It.*, **59**, 239.
- McHardy, I., 1989. In *"BL Lac Objects"*, eds. L. Maraschi, T. Maccacaro & M.H. Ulrich (Springer-Verlag: Berlin), p. 189.
- McHardy, I.M., Marscher, A.P., Gear, W.K., Muxlow, T., Letho, H.J. & Abraham, R.G., 1990. *Mon. Not. R. astr. Soc.*, **246**, 305.
- Mead, A.R.G., Ballard, K.R., Brand, P.W.J.L., Hough, J.H., Brindle, C. & Bailey, J.A., 1990. *Astron. Astrophys. Suppl.*, **83**, 183.
- Meisenheimer, K. & Heavens, A.F., 1986. *Nature*, **323**, 419.
- Melia, F. & Königl, A., 1989. *Ap. J.*, **340**, 162.
- Michelson, P.F. *et al.*, 1992. *IAU Circ.* 5470.
- Miller, J.S. 1989. In *"BL Lac Objects"*, eds. L. Maraschi, T. Maccacaro & M.H. Ulrich (Springer-Verlag: Berlin), p. 395.
- Mirabel, I.F., Rodriguez, L.F., Cordier, B., Paul, J. & Lebrun, F., 1992. *Nature*, **258**, 215.
- Mittaz, J.P.D. & Branduardi-Raymont, G., 1989. *Mon. Not. R. astr. Soc.*, **238**, 1029.
- Moffet, A.T., Gubbay, J. Robertson, D.S & Legg, A.J., 1972. In *"External Galaxies and Quasi-Stellar Objects"*, IAU Symp. 44, ed. D.S. Evans (Reidel), p. 228.
- Molendi, S., Maraschi, L. & Stella, L., 1992. *Mon. Not. R. astr. Soc.*, **255**, 27.
- Moore, R.L. & Stockman, H.S., 1984. *Astrophys. J.*, **279**, 465.

- Moore, R.L. *et al.*, 1982. *Astrophys. J.*, **260**, 415.
- Morganti, R., Fosbury, R.A.E., Hook, R.N., Robinson, A. & Tsvetanov, Z., 1992. *Mon. Not. R. astr. Soc.*, **256**, 1P.
- Morini, M., Chiappetti, L., Maccagni, D., Maraschi, L., Molteni, D., Tanzi, E.G., Treves, A. & Wolter, A., 1986. *Astrophys. J. Lett.*, **306**, L71.
- Morris, S.L., Stocke, J.T., Gioia, I.M., Schild, R.E., Wolter, A., Maccacaro, T. & Della Ceca, R., 1991. *Astrophys. J.*, **380**, 49.
- Mutel, R.L., 1990. In "*Parsec-Scale Radio Jets*", eds. J.A. Zensus & T.J. Pearson (Cambridge University Press), p. 98.
- Mutel, R.L., Phillips, R.B., Su, B. & Bucciferro, R.R., 1990. *Astrophys. J.*, **352**, 81.
- Nandra, K., 1991. *Ph. D. Thesis*, University of Leicester.
- Nandra, K., Pounds, K.A., 1992. *Nature*, in press.
- Nandra, K., Pounds, K.A., Stewart, G.C., Fabian, A. & Rees, M.J., 1989. *Mon. Not. R. astr. Soc.*, **236**, 39P.
- Nandra, K., Pounds, K.A., Stewart, G.C., George, I.M., Hayashida, K., Makino, F. & Ohashi, T., 1991. *Mon. Not. R. astr. Soc.*, **248**, 760.
- Nandra, K., *et al.*, 1992. *Mon. Not. R. astr. Soc.*, in press..
- Netzer, H., 1990. In "*Active Galactic Nuclei*", 20<sup>th</sup> SAAS-FEE Course, eds. T.J.-L. Courvoisier & M. Mayor (Berlin: Springer-Verlag).
- Neugebauer, G., Green, R.F., Matthews, K., Schmidt, M., Soifer, B.T. & Bennet, J., 1987. *Astrophys. J. Suppl.*, **63**, 615.
- O'Dea, C.P., Barvainis, R. & Challis, P.M., 1988. *Astron. J.*, **96**, 435.
- O'Dea, C.P., Baum, S.A. & Stanghellini, C., 1991. *Astrophys. J.*, **380**, 66.
- O'Dell, S.L., 1988. *Astrophys. J.*, **327**, 60.
- O'Dell, S.L., Dennison, B., Broderick, J.J., Altschuler, D.R., Condon, J.J., Payne, H.E., Mitchell, K.J., Aller, H.D., Aller, M.F. & Hodge, P.E., 1988. *Astrophys. J.*, **326**, 668.
- Ohashi, T., 1989. In "*BL Lac Objects*", eds. L. Maraschi, T. Maccacaro & M.H. Ulrich (Springer-Verlag: Berlin), p. 296.
- Ohashi, T., Tashiro, M., Makishima, K., Kii, T., Makino, F., Turner, M.J.L. & Williams, O.R., 1992. *Astrophys. J.*, in press.
- Orr, M.J.L. & Browne, W.A., 1983. *Mon. Not. R. astr. Soc.*, **200**, 1067.
- Ostriker, J.P. & Vietri, M., 1985. *Nature*, **318**, 446.
- Owen, F.N. & Laing, R.A., 1989. *Mon. Not. R. astr. Soc.*, **238**, 357.
- Owen, F.N., Helfand, D.J. & Spangler, S.R., 1981. *Astrophys. J. Lett.*, **250**, L55.
- Pacholczyk, A.G., 1970. "*Radio Astrophysics*", (Freeman & Company).
- Padovani, P., 1992. *Mon. Not. R. astr. Soc.*, **257**, 404.
- Padovani, P. & Rafanelli, P., 1988. *Astron. Astrophys.*, **205**, 53.
- Padovani, P. & Urry, C.M., 1990. *Astrophys. J.*, **356**, 75.
- Padovani, P. & Urry, C.M., 1992. *Astrophys. J.*, **387**, 449.
- Pan, H.-C., Stewart, G.C. & Pounds, K.A., 1990. *Mon. Not. R. astr. Soc.*, **242**, 177.
- Parkes Catalogue 1990, Australia Telescope National Facility.
- Pauliny-Toth, I.I.K., Preuss, E., Witzel, A., Graham, D., Kellerman, K.I. & Ronnang, B., 1981. *Astron. J.*, **86**, 371.
- Peacock, J.A., 1981. *Mon. Not. R. astr. Soc.*, **196**, 135.

- Pearson, T.J., & Readhead, A.C.S., 1988. *Astrophys. J.*, **328**, 114.
- Penston, M.V., Penston, M.J., Selmes, R.A., Becklin, E.E. & Neugebauer, G., 1974. *Mon. Not. R. astr. Soc.*, **169**, 357.
- Peréz-Fournon, I., Colina, L., Gonzáles-Serrano, J.I. & Biermann, P.L., 1988. *Astrophys. J. Lett.*, **329**, L81.
- Perley, R.A., Bridle, A.H. & Willis, A.G., 1984. *Astrophys. J. Suppl.*, **54**, 292.
- Perley, R.A., Dreher, J.W. & Cowan, J.J., 1984. *Astrophys. J. Lett.*, **285**, L35.
- Perlman, E.S. & Stocke, J.T., 1992. In "180 Meeting of the A.A.S.", June 1992, Columbus.
- Perola, G.C., Piro, L., Altamore, A., Fiore, F., Boksenberg, A., Penston, M.V., Snijders, M.A.J., Bromage, G., Clavel, J., Elvius, A., & Ulrich, M.H., 1986. *Astrophys. J.*, **306**, 508.
- Peterson, B.M., 1992. In Proc. of "The Nature of Compact Objects in Active Galactic Nuclei", Cambridge, July 1992, in press.
- Phillips, R.B. & Mutel, R.L., 1988. In "The Impact of VLBI on Astronomy and Geophysics", IAU Symp. 129, eds. M.J. Reid & J.M. Moran (Kluwer), p.103.
- Phinney, E.S., 1983. *Ph. D. Thesis*, University of Cambridge.
- Phinney, E.S., 1986. In *Astrophysics of Active Galaxies and Quasi Stellar Objects*, ed. Miller, p. 453.
- Phinney, E.S., 1987. "Superluminal Radio Sources" (Cambridge University Press), p. 301.
- Phinney, E.S., 1989. In "Theory of Accretion Discs", ed. F. Meyer *et al.* (Kluwer), p. 457.
- Phinney, E.S., 1992. In Proc. of "Astrophysical Jets", Baltimore, May 1992, in press.
- Piro, L., Yamauchi, M. & Matsuoka, M., 1990. *Astrophys. J. Lett.*, **360**, L35.
- Pollock, A., Brand, P.W.J.L., Bregman, J.N. & Robson, E.I., 1985. *Spa. Sci. Rev.*, **40**, 607.
- Pomphrey, R.B., 1976. *Astron. J.*, **81**, 489.
- Porcas, R.W., 1987. In *Superluminal Radio Sources*, eds. Zensus, A. & Pearson, T. (Cambridge University Press), p. 12.
- Potash, R.I. & Wardle, J.F.C., 1980. *Astrophys. J.*, **239**, 42.
- Pounds, K.A., 1992. In Proc. of "Recent Advances in High Energy Astronomy", Toulouse, March 1992. in press.
- Pounds, K.A., & McHardy, I.M., 1988. In "Physics of Neutron Stars and Black Holes", ed. Y. Tanaka (Univ. Acad. Press, Tokyo), p. 285.
- Pounds, K.A., Nandra, K., Stewart, G.C., George, I.M. & Fabian, A.C., 1990. *Nature*, **344**, 132.
- Preston, R.A. *et al.*, 1989. *Astron. J.*, **98**, 1.
- Priest, E.R., Hood, A.W. & Anzer, U., 1989. *Astrophys. J.*, **344**, 1010.
- Pringle, J.E. & Rees, M.J., 1972. *Astron. Astrophys.*, **21**, 1.
- Punch, M., *et al.*, 1992. *Nature*, **358**, 477.
- Quirrenbach, A., Witzel, A., Kian, S.J., Kricjbaum, T., Hummel, C.A. & Alberdi, A., 1989. *Astron. Astrophys.*, **226**, L1.
- Rawlings, S.G. & Saunders, R.D.E., 1991. *Nature*, **349**, 138.
- Readhead, A.C.S, Pearson, T.J. & Unwin, S.C., 1984. In "VLBI and compact radio sources", IAU Symp. 110, eds. Fanti, R., Kellerman, K. & Setti, G., p. 131.
- Readhead, A.C.S, Hough, D.H., Ewing, M.S., Walker, R.C. & Romney, J.D., 1983. *Astrophys. J.*, **265**, 107.

- Rees, M.J., 1966. *Nature*, **211**, 468.
- Rees, M.J., 1967. *Mon. Not. R. astr. Soc.*, **137**, 429.
- Rees, M.J., 1971. *Nature*, **229**, 312.
- Rees, M.J., 1981. In "*Plasma Astrophysics*", (ESA SP-161), p. 267.
- Rees, M.J., 1984. In "*VLBI and Compact Radio Sources*", IAU Symp. 110, eds. R. Fanti *et al.* (Dordrecht: Reidel), p. 207.
- Rees, M.J., 1984. *Ann. Rev. Astr. Astroph.*, **22**, 471.
- Rees, M.J., 1987. *Mon. Not. R. astr. Soc.*, **228**, 47P.
- Rees, M.J., 1992. In "*X-ray Emission from AGN and the Cosmic X-ray Background*", eds. W. Brinkmann & J. Trümper, MPE Report, March 1992, p. 255.
- Rees, M.J., Netzer, H. & Ferland, G.J., 1989. *Astrophys. J.*, **347**, 640.
- Reichert, G.A., Polidan, R.S., Wu, C.-C. & Carone, T.E., 1988. *Astrophys. J.*, **325**, 671.
- Remillard, R.A., Grossan, B., Bradt, H.V., Ohashi, T., Hayashida, K., Makino, F. & Tanaka, Y., 1991. *Nature*, in press.
- Reynolds, S.P., 1982. *Astrophys. J.*, **256**, 13.
- Roberts, D.H., Gabudza, D.C. & Wardle, J.F.C., 1987. *Astrophys. J.*, **323**, 536.
- Roberts, D.H. *et al.*, 1990. In "*Parsec-Scale Radio Jets*", eds. J.A. Zensus & T.J. Pearson (Cambridge University Press), p. 110.
- Robson, E.I., Gear, W.K., Brown, L.M.J., Courvoisier, T. L.-J., Smith, M.G., Griffin, M.J. & Blecha, A., 1986. *Nature*, **323**, 134.
- Ross, R.R., Fabian, A.C. & Mineshige, S., 1992. *Mon. Not. R. astr. Soc.*, in press.
- Rothschild, R.E., Mushotzky, R.F., Baity, W.A., Gruber, D.E., Matteson, J.L. & Peterson, L.E., 1983. *Astrophys. J.*, **269**, 423.
- Rudnik, L. & Edgar, B.K., 1984. *Astrophys. J.*, **279**, 74.
- Rudy, R.J., 1984. *Astrophys. J.*, **284**, 33.
- Rusk, R. & Seaquist, E.R., 1985. *Astron. J.*, **90**, 30.
- Rybicki, G. & Lightman, A., 1979. "*Radiative Processes in Astrophysics*" (Wiley-Interscience Publ.).
- Salvati, M. & Fanti, R., 1983. *Astron. Astrophys.*, **128**, 165.
- Sanders, D.B., Phinney, E.S., Neugebauer, G., Soifer, G.T. & Matthews, K., 1989. *Astrophys. J.*, **347**, 29.
- Saunders, R., 1991. In Proc. of "*Extragalactic Radio Sources: from Beams to Jets*", Paris, July 1991, in press.
- Saunders, R., Baldwin, J.E., Pooley, G.G. & Warner, P.J., 1989. *Mon. Not. R. astr. Soc.*, **197**, 287.
- Schalinski, C.J., Witzel, A., Krichbaum, T.P., Hummel, C.A., Quirrenbach, A. & Jonstone, K.J., 1992. In "*Variability in blazars*", eds. E. Valtaoja & M. Valtonen (Cambridge University Press), p. 221.
- Scheuer, P.A.G., 1974. *Mon. Not. R. astr. Soc.*, **166**, 513.
- Scheuer, P.A.G. & Readhead, A.C.S., 1979. *Nature*, **277**, 182.
- Schreier, E.J., Feigelson, E., Delvaille, J., Giacconi, R., Grindlay, J., Schwartz, D.A. & Fabian, A.C., 1979. *Astrophys. J. Lett.*, **234**, L39.
- Schneider, P., & Kirk, J.G., 1989. *Astron. Astrophys.*, **217**, 344.

- Schwartz, D.A., Brissenden, R.J.V., Tuohy, I.R., Feigelson, E.D., Hertz, P.L. & Remillard, R.A., 1989. In *"BL Lac Objects"*, eds. L. Maraschi, T. Maccacaro & M.H. Ulrich (Springer-Verlag: Berlin), p. 209.
- Sembay, S., Warwick, S.R.S., Urry, C.M., Sokoloski, J., George, I.M., Makino, F. & Phashi, T., 1992. Preprint.
- Shakura, N.I. & Sunyaev, R.A., 1973. *Astron. Astrophys.*, **24**, 337.
- Shapiro, S.L., Lightman, A.P. & Eardley, D.M., 1976. *Astrophys. J.*, **204**, 187.
- Shields, G.A., 1978. *Nature*, **272**, 706.
- Sikora, M., Kirk, J.G., Begelman, M.C. & Schneider, P., 1987. *Ap. J. (Letters)*, **320**, L81.
- Sitko, M.L., Schmidt, G.D. & Stein, W.A., 1985. *Astrophys. J. Suppl.*, **59**, 323.
- Smith, M.L. & Sitko, M.L., 1991. *Astrophys. J.*, **383**, 580.
- Snyder, W.A. & Wood, K.S., 1984. In *"X-ray and UV Emission from Active Galactic Nuclei"*, MPE Report 184, ed. W. Brinkman & J. Trümper, p. 114.
- Steiner, J.E., 1981. *Astrophys. J.*, **250**, 469.
- Stickel, M., Padovani, P., Urry, C.M., Fried, J.W. & Kühr, H., 1991. *Astrophys. J.*, **374**, 431.
- Stoche, J.T., Liebert, J., Schmidt, G., gioia, I., Maccacaro, T., Schield, R., Maccagni, D. & Arp, H., 1985. *Astrophys. J.*, **298**, 619.
- Stockman, H.S., Moore, R.L. & Angel, J.R.P., 1984. *Astrophys. J.*, **279**, 485.
- Stockton, A. & MacKenty, J.W., 1987. *Astrophys. J.*, **316**, 584.
- Sun, W.-H. & Malkan, M.A., 1989. *Astrophys. J.*, **346**, 68.
- Sunyaev, R., 1992. In Proc. of *"Recent Advances in High Energy Astronomy"*, Toulouse, March 1992. in press.
- Svensson, R., 1984. In *"X-ray and UV emission from Active Galactic Nuclei"*, eds. Trumper, J. & Brinkmann, W., Max Planck, Garching, p. 152.
- Svensson, R., 1986. In *"Radiation-Hydrodynamics in Stars and Compact Objects"*, IAU Coll. 89, eds. D. Mihalas & K.-H.A. Winkler (Springer-Verlag), p. 325.
- Svensson, R., 1987. *Mon. Not. R. astr. Soc.*, **227**, 403.
- Svensson, R., 1990. In *"Physical Processes in Hot Cosmic Plasmas"*, eds. W. Brinkmann, A.C. Fabian & F. Giovannelli (Kluwer Academic Publishers), p. 357.
- Tadhunter, C.N., 1992. In Proc. of *"The Nature of Compact Objects in Active Galactic Nuclei"*, Cambridge, July 1992, in press.
- Tadhunter, C.N. & Tsvetanov, Z., 1989. *Nature*, **341**, 422.
- Tagliaferri, G., Stella, L., Maraschi, L., Treves, A. & Celotti, A., 1991. *Astrophys. J.*, **380**, 78.
- Tanaka, Y., 1991. In *"Iron line Diagnostic in X-ray sources"*, eds. A. Treves, G.C. Perola & L. Stella (Springer-Verlag), p. 98.
- Tanzi, E.G., Barr, P., Bouchet, P., Chiappetti, L., Cristiani, S., Falomo, R., Giommi, P., Maraschi, L. & Treves, A., 1986. *Astrophys. J. Lett.*, **311**, L13.
- Tennant, A.F., Mushotzky, R.F., Boldt, E.A. & Swank, J.H., 1981. *Astrophys. J.*, **251**, 15.
- Terlevich, R., 1990. In *"New Windows to the Universe"*, eds. F. Sanchez & M. Vasquez (Cambridge University Press), p. 211.
- Treves, A., Maraschi, L. & Abramowicz, M., 1989. In *"Accretion"*. *Advanced Series in Astrophysics and Cosmology. Vol. 5.* (World Scientific).

- Treves, A., Perola, G.C. & Stella, L., 1991. *"Iron Line Diagnostic in X-ray Sources"* (Springer-Verlag)
- Treves, A., Bonelli, G., Chiappetti, L., Falomo, R., Maraschi, L., Tagliaferri, G. & E.G. Tanzi, E.G., 1990. *Astrophys. J.*, **359**, 98.
- Treves, A., Morini, M., Chiappetti, L., Fabian, A., Falomo, R., Maccagni, D., Maraschi, L. Tanzi, E.G. & Tagliaferri, G., 1989, *Astrophys. J.*, **341**, 733.
- Tucker, W.H., 1975. *"Radiation Processes in Astrophysics"* (MIT Press).
- Turner, M.J.L., 1992. In Proc. of *"The Nature of Compact Objects in Active Galactic Nuclei"*, Cambridge, July 1992, in press.
- Turner, M.J.L. *et al.*, 1990. *Mon. Not. R. astr. Soc.*, **244**, 310.
- Turner, T.J. & Pounds, K.A., 1989. *Mon. Not. R. astr. Soc.*, **240**, 833.
- Ulrich, M-H., 1989. In *"BL Lac Objects"*, eds. L. Maraschi, T. Maccacaro & M-H. Ulrich (Springer-Verlag), p. 45.
- Ulrich, M.-H., 1989. In *"Theory of Accretion Disks"*, eds. F. Mayer *et al.* (Kluwer Academic Publisher), p. 3.
- Ulrich, M.-H., 1990. In *"Structure and Emission Properties of Accretion Disks"*, Proc. IAU Coll. 129, Paris 1990, eds. C. Bertout *et al.* (Edition Frontieres).
- Ulrich, M.-H., *et al.*, 1991. *Astrophys. J.*, **382**, 483.
- Ulvestad, J., Johnston, K., Perley, R., & Fomalont, E., 1981. *Astron. J.*, **86**, 1010.
- Unwin, S.C., Cohen, M.H., Biretta, J.A., Pearson, T.J., Seielstad, G.A., Walker, R.C., Simon, R.S. & Linfield, R.P., 1985. *Astrophys. J.*, **289**, 109.
- Urry, M., 1984. *Ph. D. Thesis*, University of Maryland.
- Urry, M., 1986. In *"The Physics of Accretion onto Compact Objects"*, eds. K.O. Mason, M.G. Watson & N.E. White (Springer-Verlag), p. 357.
- Urry, M.C. & Mushotzky, R.F., 1982. *Astrophys. J.*, **253**, 38.
- Urry, C.M. & Padovani, P., 1991. *Astrophys. J.*, **371**, 60.
- Urry, C.M. & Shafer, R.A., 1984. *Astrophys. J.*, **280**, 569.
- Urry, C.M., Padovani, P. & Stickel, M., 1991. *Astrophys. J.*, **382**, 501.
- Urry, C.M., Maraschi, L. & Phinney, S.E., 1990. *Comm. Ap.*, in press.
- Valtaoja, E., Lainela, M. & Teräsranta, H., 1989. In *"BL Lac Objects"*, eds. L. Maraschi, T. Maccacaro & M.H. Ulrich (Springer-Verlag), p. 39.
- Valtaoja, E. *et al.*, 1985. *Nature*, **314**, 148.
- van der Laan, H., 1966. *Nature*, **211**, 1131.
- Véron-Cetty, M.-P. & Véron, P., 1991. *A Catalogue of Quasars and Active Nuclei*, ESO Scientific Report, N. 10.
- Visvanathan, N., 1973. *Astrophys. J.*, **179**, 1.
- Visvanathan, N. & Elliot, J.L., 1976. *Astrophys. J.*, **179**, 721.
- Waggett, P.C., Warner, P.J. & Baldwin, J.E., 1977. *Mon. Not. R. astr. Soc.*, **181**, 465.
- Walker, R.C., Benson, J.M. & Unwin, S.C., 1987. *Astrophys. J.*, **316**, 546.
- Walker, R.C., Walker, M.A. & Benson, J.M., 1988. *Astrophys. J.*, **335**, 668.
- Wall, J.V. & Peacock, J.A., 1985. *Mon. Not. R. astr. Soc.*, **216**, 173.
- Wandel, A. & Urry, C.M., 1989. In *"BL Lac Objects"*, eds. L. Maraschi, T. Maccacaro & M.H. Ulrich (Springer-Verlag: Berlin), p. 388.
- Ward, M., Elvis, M., Fabbiano, G., Carleton, N.P., Willner, S.P. & Lawrence, A., 1987. *Astrophys. J.*, **315**, 74.

- Wardle, J.F.C., 1977. *Nature*, **269**, 563.
- Wardle, J.F.C. & Roberts, D.H., 1988. In *"The Impact of VLBI on Astrophysics and Geophysics"*, IAU Coll. 129, eds. M.J. Reid & J.M. Moran (Kluwer), p. 143.
- Wardle, J.F.C., Moore, R.L. & Angel, J.R.P., 1984. *Astrophys. J.*, **279**, 93.
- Wardle, J.F.C., Roberts, D.H., Brown, L.F., Kollgaard, R.I. & Gabuzda, D.C., 1990. In *"Parsec-Scale Radio Jets"*, eds. J.A. Zensus & T.J. Pearson (Cambridge University Press), p. 20.
- Warwick, R.S., Barstow, M.A. & Yaqoob, T. 1989. *Mon. Not. R. astr. Soc.*, **238**, 917.
- Wehrle, A.E. & Cohen, M., 1989. *Astrophys. J. Lett.*, **346**, L69.
- Wehrle, A.E., Marshall, H., Cohen, M.H. & Unwin, S.C., 1990. *Astrophys. J. Lett.*, **351**, L1.
- Weiler, K.W. & Johnston, K.J., 1980. *Mon. Not. R. astr. Soc.*, **190**, 269.
- Weinberg, S., 1972. *"Gravitation and Cosmology"* (New York: Wiley & Son).
- White, N.E., Fabian, A.C. & Mushotzky, R.F., 1984. *Astron. Astrophys.*, **133**, L9.
- Wiita, P.J., 1991. In *"Beams and Jets in Astrophysics"*, ed. P.A. Hughes (Cambridge University Press), p. 379.
- Wilkes, B.J., 1992. In Proc. of *"The Nature of Compact Objects in Active Galactic Nuclei"*, Cambridge, July 1992, in press.
- Wills, B.J., Netzer, H. & Wills, D., 1985. *Astrophys. J.*, **288**, 94.
- Whitney, A.R. *et al.*, 1971. *Science*, **173**, 225.
- Woltjer, L., 1989. In *"BL Lac Objects"*, eds. L. Maraschi, T. Maccacaro & M.-H. Ulrich (Springer-Verlag), p. 460.
- Woltjer, L., 1990. In *"Active Galactic Nuclei"*, 20<sup>th</sup> SAAS-FEE Course, eds. T.J.-L. Courvoisier & M. Mayor (Berlin: Springer-Verlag).
- Worral, D.M. & Wilkes, B.J., 1990. *Astrophys. J.*, **360**, 396.
- Yaqoob, T. & Warwick, R.S., 1991. *Mon. Not. R. astr. Soc.*, **248**, 773.
- Yee, H.K.C., 1980. *Astrophys. J.*, **241**, 894.
- Zdziarski, A., 1991. Preprint
- Zdziarski, A., 1992. In *"Testing the AGN Paradigm"*, AIP Conference Proc. 254, eds. S. Holt, S.G. Neff & C.M. Urry, p. 291.
- Zdziarski, A. & Coppi, P.S., 1991. *Astrophys. J.*, **376**, 480.
- Zdziarski, A., Ghisellini, G., George, I.M., Svensson, R., Fabian, A.C. & Done, C., 1990. *Astrophys. J. Lett.*, **363**, L1.
- Zensus, T., 1989. In *"BL Lac Objects"*, eds. L. Maraschi, T. Maccacaro & M.H. Ulrich (Springer-Verlag), p. 3.
- Zensus, T. & Pearson, T., 1987. *"Superluminal Radio Sources"* (Cambridge University Press).
- Zhang, F.J. & Baath, L.B., 1990. *Astron. Astrophys.*, **236**, 47.

